Dissertation

submitted to the

Combined Faculties for the Natural Sciences and for Mathematics

of the Ruperto-Carola University of Heidelberg, Germany

for the degree of

Doctor of Natural Sciences

presented by

Diplom-Physikerin Irina Golombek

born in Aschaffenburg, Germany

Oral examination: October 16, 2008

# Numerical Simulations

of

# Magnetic fields and cosmic rays

in

# Galaxy Clusters

Referees:    Prof. Dr. Matthias Bartelmann
Prof. Dr. Ralf Klessen

# Numerische Simulationen von Kosmischer Strahlung und Magnetfeldern in Galaxienhaufen

## Zusammenfassung

Wir untersuchen die numerische Modellierung relativistischer Protonen in einem magnetisierten Plasma. Dazu kombinieren wir erstmals zwei unterschiedliche Komponenten eines kosmologischen Simulationscodes welche zuvor nur getrennt voneinander getestet und erfolgreich eingesetzt wurden. Mit Hilfe von Stoßrohrrechnungen überprüfen wir die physikalisch korrekte Wiedergabe eines analytisch lösbaren magnetohydrodynamischen Riemannproblems in einem Gas mit einem konstanten Anteil relativistischer Teilchen. Dazu leiten wir einen analytischen Ausdruck für die Ausbreitungsgeschwindigkeiten der magnetosonischen (Schock-)Wellen her. Das Gleichungssystem welches sich aus dem Riemannproblem ergibt lösen wir in einem iterativen Näherungsverfahren. Aus dem Vergleich der analytischen mit der numerischen Lösung verschiedener Stoßrohrprobleme erhalten wir eine realistische Abschätzung der physikalischen Genauigkeit des Simulationscodes.

Nach der erfolgreichen Testphase simulieren wir die Strukturentstehung von drei Galaxienhaufen, wobei wir die Entwicklung der intergalaktischen Magnetfelder und die Erzeugung relativistischer Teilchen konsistent mitbehandeln. Mit Hilfe analytischer Modelle berechnen wir die Röntgen- und Radioemission der Galaxienhaufen und zeigen den zeitlichen Zusammenhang zwischen beiden Beobachtungsgrößen auf. Durch einen Vergleich mit dem Wirkungsquerschnitt für den starken Linseneffekt belegen wir, dass die beobachtbare Radioemission von Galaxienhaufen mit dem Auftreten von Substrukturen korreliert und somit durch Schocks beim Einfall großer Materieklumpen erzeugt wird.

# Numerical Simulations of Cosmic Rays and Magnetic Fields in Galaxy Clusters

## Abstract

We investigate the numerical modelling of relativistic protons, so-called cosmic rays, in a magnetised plasma. For the first time we combine two different components of a cosmological simulation code that so far have only been tested and employed independently of each other. By means of magnetohydrodynamic shock tube calculations in a gas that contains a constant fraction of relativistic particles we check for the correct physical behaviour of the combined numerical models. For this purpose we derive an analytical expression for the magnetosonic shock and rarefaction waves in the MHD Riemann problem and solve for the resulting system of equations using an iterative scheme. Comparing the theoretical and numerical solutions of a number of shock tube calculations we assess the physical correctness of the simulation.

After successful testing we simulate the structure formation of three galaxy clusters including the consistent modelling of magnetic fields and cosmic rays. By means of analytical models we compute the X-ray and radio emission of the simulated clusters and reveal the temporal correlation between both quantities. Through a comparison with the strong lensing cross sections we demonstrate that the observable radio emission of galaxy clusters is directly connected to the occurrence of substructure in their dark matter halos and is thus triggered by strong merger shocks.

# Contents

# List of Figures

# Introduction

<div style="text-align: right; font-size: 2em;">1</div>

Galaxy clusters are the largest bound systems in the Universe. They sit on top of a hierarchy of objects that had time to collapse under their own gravity since the beginning of structure formation. Because of their large extents, the closest clusters can actually be seen as agglomerations of galaxies on photographs of the sky.

Before astronomers had a full grasp for the distances of other galaxies, clusters were mistaken for special groups of nebulae. After the invention of the wide-field Schmidt telescope in 1930, imaging surveys covered significant portions of the sky and quickly revealed some of the most famous clusters of galaxies, including Virgo, Coma, and Hydra. On the basis of vast numbers of photographic plates, catalogues of galaxies and clusters were produced, among those the comprehensive cluster collection by Zwicky et al. (1968) and the famous Abell catalogue (Abell 1958). Due to the reliance on the human eye these catalogues were biased towards centrally-concentrated clusters at low redshifts ($z \lesssim 0.15$). Moreover, they contained a number of inhomogeneities caused by photometric errors and strong sensitivity variations of the plate material. Nevertheless, despite all deficiencies, Abell's catalogue remained the most cited and utilised resource for both galaxy population and cosmological studies with clusters over the last four decades.

Modern galaxy cluster surveys are based on multi-wave band observations in the optical, X-ray and radio frequency range. While the optical light originates from the stars in the galaxies, the X-ray emission is most consistent with thermal bremsstrahlung from the hot intracluster gas. In contrast, large-scale diffuse radio halos are caused by the synchrotron emission of high energy electrons of non-thermal origin in the cluster magnetic field. Extended radio sources have only been observed in massive and highly unrelaxed clusters that appear to have recently undergone a merger event. The observations revealed a strong correlation between the radio power in cluster halos and the X-ray luminosity and temperature of clusters. This correlation might be explained if the radio emitting electrons are injected by merger shocks and turbulent acceleration, and if the high X-ray luminosities are due to the transient boosts which occur during mergers (Randall et al. 2002).

Detailed numerical simulations are the most important tool for the theoretical study of the formation of galaxy clusters and the evolution of the intracluster medium. High-performance cosmological simulation codes include detailed models of gas physics, magnetic fields, and relativistic particles. The numerical models allow for the analysis of the

complex physical processes that take place in the interplay of the different cluster components. Tracing the evolution of the intracluster plasma might help us to understand the evolution of observable quantities such as X-ray and radio emission and their relation to cluster dynamics from the beginning of cluster formation to the currently observed state.

In this thesis, we develop a method for testing the numerical modelling of shock fronts in a magnetised plasma that contains a population of relativistic particles. On the basis of the test results we evaluate the code performance under cosmological conditions. We carry out numerical simulations of cluster formation and investigate the evolution of the thermal and non-thermal cluster properties, as well as their connection to merger activity. The outline of the thesis is as follows:

In Chapter 1 we give a short introduction to the basics of cosmology, including the current concordance model of the Universe and the concept of distance measures.

In order to illustrate the process of structure growth from small fluctuations in the initial density field to the large-scale matter distribution we observe today we present the Newtonian approach to structure formation in Chapter 2.

In Chapter 3 we review some fundamental properties of galaxy clusters. After presenting theoretical models for their internal structure, we discuss the effects of matter accretion shocks on the intracluster medium. We furthermore give a description of the observable quantities that will be important in the course of this work.

In Chapter 4 we give an overview of the numerical methods used in the simulation code with the focus on the modeling of gas physics, magnetic fields and relativistic particles.

Chapter 5 addresses the problem of combining the numerical models of magnetic fields and cosmic rays. We present a novel analytical solution to the general MHD Riemann problem in presence of a relativistic cosmic ray component. We construct an iterative two-fluid MHD Riemann solver which we use to check the physical accuracy of the simulation results in a number of shock tube tests.

In Chapter 6 we present numerical simulations of three galaxy clusters including magnetic fields and a population of cosmic rays. We trace the evolution of the simulated X-ray and radio luminosities over a wide range of redshifts and investigate the influence of cluster dynamics, especially merger events on the thermal and non-thermal activity in the intracluster medium. In a systematic comparison of the X-ray and radio luminosities and the lensing properties we reveal the correlation between radiation and merger activity.

# Cosmology

<div style="text-align: right; font-size: large;">2</div>

The term "cosmology" denotes our attempts to understand the Universe as a whole through scientific observation and the laws of physics. Difficulties arise from the fact that the Universe exhibits temporal evolution and is not in steady state. Due to large cosmic time scales and the enormous dimension of space we have a very restricted view onto cosmic history. Most of our knowledge therefore runs in parallel with the development of large telescopes and sensitive detectors. The great deal in the observational cosmology of the past century was the detection of the cosmic microwave background (CMB) by Penzias & Wilson (1965). Two decades before the CMB had been predicted as the thermal relict of the Big Bang by Gamow, Alpher, and Herman (Alpher et al. 1948; Alpher & Herman 1949). Since then, the existence of the Big Bang is considered certain.

The aspect that distinguishes modern cosmology from previous efforts to understand the Universe is that we have developed a consistent theoretical framework which agrees quantitatively with the existing observational data. Furthermore, the access to computational resources has enabled the numerical study of non-linear processes. In this manner great progress has been made in understanding the formation and distribution of matter on large-scales. On the other hand, recent hypotheses such as the existence of dark matter and vacuum energy are still controversial, partly due to the fact that the related research fields are still in their infancy.

In what follows we will give a short introduction to the basics of cosmology. The first part of the chapter deals with the aspects of homogeneous cosmology in which the Universe is treated as a homogeneous, uniformly expanding fluid. From this simplified model the dynamics of the overall expansion are derived and assumptions about the geometry and energy content are made. The first section closes with the introduction of the common cosmological distance measures. In the second part we will present the theory of structure formation which provides an explanation how the observable structure has developed starting from small primordial inhomogeneities in the density field. The formation can be divided into a linear and a non-linear phase and ends with the collapse of gravitationally bound objects.
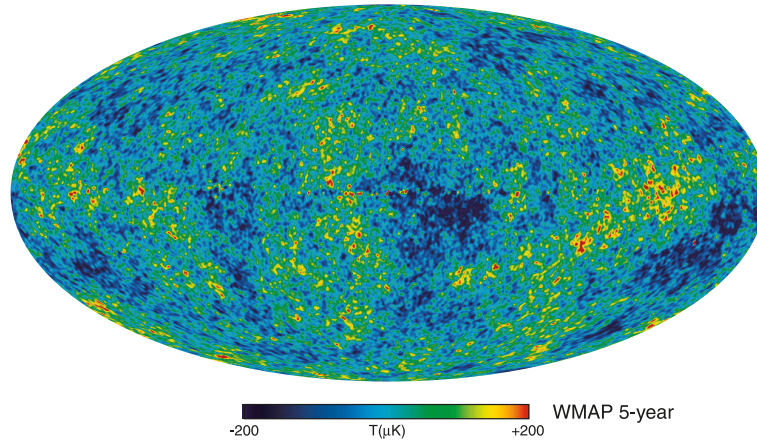
Figure 2.1: Temperature anisotropies of the cosmic microwave background from the 5-year
Wilkinson Microwave Anisotropy Probe (WMAP) data seen over the full sky
(Hinshaw et al. 2008). The colours represent the temperature fluctuations
where red regions are warmer and blue regions are colder by about $2 \cdot 10^{-5} \, \mathrm{K}$.
The average temperature is $2.725 \, \mathrm{K}$.

## 2.1 Friedmann model of the Universe

The standard model of the Universe is based on the fundamental assumptions that, when
averaged over sufficiently large scales, there exists a mean motion of radiation and matter
and that for all fundamental observers co-moving with that mean motion, all observable
properties are isotropic. Both conditions are linked to what is called the cosmological
principle.

Observations support the idea that the Universe is both isotropic and homogeneous
on scales above $\sim 100 \, \mathrm{Mpc}$. The clearest modern evidence for the cosmological principle
is measurements of the cosmic microwave background (shown in Figure 2.1). The CMB
is an image of the photons emitted from the early Universe. Isotropy and homogeneity
are reflected in the smoothness of the temperature and in the random appearance of the
background radiation.

### 2.1.1 The metric

In the framework of general relativity, the postulate that for a fundamental observer the
Universe looks the same at any time in any direction implies that all three-dimensional
spatial hypersurfaces with $t = \mathrm{const}$ in space-time are homogeneous and isotropic. The
hypersurfaces can be scaled by a function $a(t)$ which only depends on time. In cosmology
$a(t)$ is called scale factor and denotes the factor by which the relative distance between
constant spatial coordinates is growing in the course of expansion. Aside from isotropy
and homogeneity, general relativity requires that locally (e.g. near the origin) the line

element be invariant under Lorentz transformations:

$$\mathrm{d}s^2 = \mathrm{d}t - \mathrm{d}\vec{x}^2 \,. \tag{2.1}$$

Thus we arrive at Friedmann-Robertson Walker (FRW) metric, which is the most general space-time metric fullfilling the cosmological principle:

$$\mathrm{d}s^2 = -c^2\mathrm{d}t^2 + a^2(t)\left[\mathrm{d}w^2 + f_{\mathrm{K}}^2(w)\left(\mathrm{d}\theta^2 + \sin^2\theta\mathrm{d}\phi^2\right)\right]\,, \tag{2.2}$$

where spherical polar coordinates $(w, \theta, \phi)$ are chosen to make the symmetries of space-time self-evident. The time coordinate $t$, which is the proper time as measured by a co-moving observer (one at constant spatial coordinates), is referred to as cosmic time. The geometry of spatial sections is determined by the radial function $f_{\mathrm{K}}(w)$ which is either trigonometric, linear, or hyperbolic in $w$:

$$f_{\mathrm{K}}(w) = \begin{cases} K^{-1/2}\sin(K^{1/2}w) & (K > 0) \\ w & (K = 0) \,, \\ |K|^{-1/2}\sinh(|K|^{1/2}w) & (K < 0) \end{cases} \tag{2.3}$$

where $K$ describes the constant curvature of the spatial slices. $K = +1$ corresponds to positively curved spatial sections (locally isometric to 3-spheres), $K = 0$ corresponds to local flatness, and $K = -1$ corresponds to negatively curved (locally hyperbolic) spatial sections. Concerning the scale factor $a(t)$, the convention is such that $a(t_0) = a_0 = 1$ today. Hence, if the co-moving distance today is $x_0$, the physical distance between two points at some earlier time $t$ was $a(t)x_0$.

Another useful form of the RW metric is obtained by a change of variables in the radial coordinate which then yields (see, e.g. Carroll 2004)

$$\mathrm{d}s^2 = -c^2\mathrm{d}t^2 + a^2(t)\left[\frac{\mathrm{d}r^2}{1 - Kr^2} + r^2\left(\mathrm{d}\theta^2 + \sin^2\theta\mathrm{d}\phi^2\right)\right]\,. \tag{2.4}$$

### 2.1.2 Expansion and redshift

To quantify the rate of cosmic expansion and its relation to the energy one introduces the Hubble parameter

$$H(t) \equiv \frac{\mathrm{d}a/\mathrm{d}t}{a}\,, \tag{2.5}$$

which measures how rapidly the scale factor changes with time. The value of the Hubble parameter at the present epoch $t_0$ is the Hubble constant $H_0$. Current measurements indicate that $H_0 = 70.1 \pm 1.3\,\mathrm{km\,s^{-1}\,Mpc^{-1}}$ (Komatsu et al. 2008). Since there is some uncertainty in this value, the Hubble constant is often parameterised as

$$H_0 = 100\,h\,\mathrm{km\,s^{-1}\,km^{-1}}\,, \tag{2.6}$$

so that $h \approx 0.7$.

Due to the uniform expansion of space any object moving with the Hubble flow is receding from us. The light emitted from a distant object is consequently stretched out to larger wavelengths $\lambda$ according to

$$\frac{\lambda_{\mathrm{obs}}}{\lambda_{\mathrm{emit}}} = \frac{1}{a} \equiv 1 + z \,, \tag{2.7}$$

where $\lambda_{\mathrm{emit}}$ and $\lambda_{\mathrm{obs}}$ are the wavelengths at the source and the observer, respectively. The stretching factor $z$ that was introduced in the last equation is known as the redshift. Since the scale factor $a_0$ at present time is set to 1 we have $z_0 = 0$.

### 2.1.3 The Friedmann equations

Since we have required isotropy and homogeneity, the dynamics of the metric is governed by the dynamics of the scale factor $a(t)$. The evolution equations are derived applying the Einstein equations

$$R_{\mu\nu} - \frac{1}{2} R g_{\mu\nu} = \frac{8\pi G}{c^2} T_{\mu\nu} + \Lambda g_{\mu\nu} \,, \tag{2.8}$$

to the RW metric, where $R_{\mu\nu}$ and $R$ are the Ricci tensor and the Ricci scalar, respectively. Equation (2.8) also contains the cosmological constant $\Lambda$ which was originally introduced by Einstein in order to obtain a static cosmological model and which nowadays plays a crucial role in the standard cosmological model.

Using the perfect fluid form for the energy-momentum tensor of cosmological matter,

$$T_{\mu\nu} = (\rho + p) U_\mu U_\nu + p g_{\mu\nu} \,, \tag{2.9}$$

where $U^\mu$ is the fluid four-velocity, and $\rho$ and $p$ are the energy density and the pressure in the rest frame of the fluid, one arrives at the following two differential equations for the scale factor $a(t)$:

$$H^2 = \left(\frac{\dot{a}}{a}\right)^2 = \frac{8\pi G}{3} \rho - \frac{Kc^2}{a^2} + \frac{\Lambda}{3} \,, \tag{2.10}$$

$$\frac{\ddot{a}}{a} = -\frac{4\pi G}{3} \left(\rho + \frac{3p}{c^2}\right) + \frac{\Lambda}{3} \,. \tag{2.11}$$

The overdot denotes a derivative with respect to cosmic time $t$. The last two equations are known as Friedmann's equations and the corresponding RW metric is named Friedmann-Lemaitre-Robertson Walker metric.

In the special case of $K = 0$ and $\Lambda = 0$, which separates eternally expanding world models from those that will re-collapse in the future, the Universe has a current density called critical density $\rho_{\mathrm{crit}}$ which can be inferred from (2.11):

$$\rho_{\mathrm{crit}}(t) = \frac{3H(t)^2}{8\pi G} \,, \qquad \text{where} \qquad \rho_{\mathrm{crit},0} = \frac{3H_0^2}{8\pi G} \,. \tag{2.12}$$

The actual density of the Universe is then conveniently expressed in terms of the dimensionless density parameter

$$\Omega(t) = \frac{8\pi G}{3H(t)^2} \rho(t) = \frac{\rho(t)}{\rho_{\mathrm{crit}}(t)} \,, \tag{2.13}$$

which is one of the central cosmological parameters.

### 2.1.4 Constituents of the Universe and the standard cosmological model

The Friedmann equation (2.10) and (2.11) can be combined to yield the adiabatic equation

$$\frac{\mathrm{d}}{\mathrm{d}t}(a^3\rho c^2) + p\frac{\mathrm{d}}{\mathrm{d}t}(a^3) = 0\,. \tag{2.14}$$

The first term is proportional to the change of energy contained in a fixed co-moving volume and thus has the meaning of an internal energy while the second term corresponds to the pressure work. Equation (2.14) thus states the first law of thermodynamics in a cosmological context. The energy-conservation equation can be re-written in the following way:

$$\dot{\rho} + 3H(\rho + \frac{p}{c^2}) = 0\,. \tag{2.15}$$

One can solve this equation for the different constituents of the Universe to determine the evolution of the corresponding energy density with time. Within the fluid approximation used here, the equation of state is given by $p_i = p_i(\rho_i)$, where $i$ indexes all different possible types of energy in the Universe. It is then convenient to introduce an equation of state parameter $w$ defined by

$$p = w\rho c^2\,. \tag{2.16}$$

Replacing $p$ in (2.15) the conservation of energy equation becomes

$$\frac{\dot{\rho}}{\rho} = -3(1+w)\frac{\dot{a}}{a}\,. \tag{2.17}$$

If $w = p/\rho$ is a constant, this can be integrated to yield

$$\rho \propto a^{-3(1+w)}\,. \tag{2.18}$$

A universe in which most of the energy density is in the form of radiation is known as **radiation-dominated**. This was the case in our Universe at early times when the temperature was much higher than it is today. For a gas of photons or highly relativistic particles $w = 1/3$ and from equation (2.17) we have

$$\rho_{\mathrm{r}}(t) = \rho_{\mathrm{r},0}a^{-4}\,. \tag{2.19}$$

In contrast, non-relativistic matter which is also known as dust can be approximated by a pressure-free fluid, $p = 0$. The energy density in matter then falls of as

$$\rho_{\mathrm{m}}(t) = \rho_{\mathrm{m},0}a^{-3}\,, \tag{2.20}$$

which is simply the decrease in the number density of particles as the Universe expands. A universe whose energy is mostly due to matter is called **matter-dominated**. Since the energy density in radiation falls off slightly faster than that in matter, matter starts dominating the cosmic expansion when $\rho_{\mathrm{m}} = \rho_{\mathrm{r}}$.

There is strong observational evidence for a third component of yet unknown nature (Riess et al. 1998; Perlmutter et al. 1999). The so-called vacuum or **dark energy** also

takes the form of a perfect fluid with an equation of state $p = -\rho c^2$. Since its energy density appears to be constant,

$$\rho_\Lambda = \rho_{\Lambda,0}\, a^0 \,, \tag{2.21}$$

it is usually denoted by $\Lambda$, referring to Einstein's cosmological constant. There are indications that the dark energy component started dominating around $z = 1$ and is since then driving the accelerating expansion of the Universe. Several theorists claim that the dark energy is not constant, but is evolving with time. For a comprehensive overview of the most common dark energy models see Copeland (2007).

Analogous to equation (2.13) one defines the density parameter of the $i$th species,

$$\Omega_i = \frac{\rho_i}{\rho_{\mathrm{crit}}} \,, \tag{2.22}$$

where the critical density as a function of time is given by (2.12). Summing up the density parameters of all constituents we can rewrite the Friedmann equation (2.10) as follows:

$$\sum_i \Omega_i - 1 = \frac{Kc^2}{H^2 a^2} \,. \tag{2.23}$$

From the knowledge of the total density parameter $\Omega = \sum_i \Omega_i$ one can thus infer the global geometry of the three-dimensional spatial hypersurfaces via

$$\begin{aligned} \Omega_{\mathrm{tot}} > 1 &\iff K > 0 \\ \Omega_{\mathrm{tot}} = 1 &\iff K = 0 \\ \Omega_{\mathrm{tot}} < 1 &\iff K < 0 \,. \end{aligned} \tag{2.24}$$

The determination of $\Omega$ has become possible only quite recently from combined measurements of the CMB, supernovae of type Ia, and the large-scale distribution of matter in the Universe. The observations have shown that the current universe is very close to a spatially flat geometry. Most recent values for the cosmological parameter are given in the paper by Komatsu et al. (2008).

The current concordance model of cosmology is a spatially flat universe with a cosmological constant, referred to as $\Lambda$CDM. The abbreviation CDM stands for "cold dark matter", a collisionless form of matter that does not interact with electromagnetic radiation and can therefore not be seen. The term "cold" refers to the velocity dispersion of the dark matter particles which is negligibly small compared to the speed of sound. Dark matter seems to account for more than 90 % of the matter content in the Universe. Its existence has been proclaimed on the basis of galactic rotation curves and the masses of galaxy clusters that could not be explained by the baryonic matter alone (e.g. Markevitch et al. 2004; Clowe et al. 2006). The $\Lambda$CDM model is characterised by the parameters $\Omega_{\mathrm{m}} = \Omega_{\mathrm{dm}} + \Omega_{\mathrm{b}} = 0.279$, $\Omega_{\mathrm{b}} = 0.0462$, $\Omega_\Lambda = 0.721$, and $h = 0.701$.

### 2.1.5  Distance measures

An important concept related to observational tools in an expanding background is associated to the definition of a distance. While in Euclidian space the separation between

two points is unambiguously defined, this is no longer the case for an arbitrary curved space-time. Large distances in cosmology are usually expressed in terms of the redshift, and the distance measures inferred from these redshifts differ, depending on the measuring prescriptions.

The **proper distance** $D_{\mathrm{prop}}$ is the separation between events on radial null trajectories, that is, trajectories of photons which terminate at the observer. The time required for light to propagate from a source at $z_{\mathrm{s}}$ to an observer at $z_{\mathrm{o}}$ translates into an integration over $\mathrm{d}D_{\mathrm{prop}} = -c\mathrm{d}t = -c\mathrm{d}a/\dot{a}$ along the photon trajectory. This yields

$$D_{\mathrm{prop}}(z_{\mathrm{o}}, z_{\mathrm{s}}) = \frac{c}{H_0} \int_{a(z_{\mathrm{s}})}^{a(z_{\mathrm{a}})} \frac{\mathrm{d}a}{\dot{a}} = \frac{c}{H_0} \int_{a(z_{\mathrm{s}})}^{a(z_{\mathrm{a}})} \frac{\mathrm{d}a}{aE(a)}, \qquad (2.25)$$

where we have introduced the function

$$E(a) \equiv \sqrt{\Omega_{\mathrm{r}} \, a^{-4} + \Omega_{\mathrm{m}} \, a^{-3} + \Omega_{\Lambda}}, \qquad (K = 0), \qquad (2.26)$$

which relates the Hubble parameter at earlier time to its present value

$$H(a) =: H_0 \, E(a). \qquad (2.27)$$

The proper distance is especially important since in the specified time interval $\Delta t$ no information could have propagated further.

The **co-moving distance** is the distance on the spatial hypersurface at $t = t_0$ between the world-lines of a source and an observer locked into the Hubble flow. It is obtained by integrating over $\mathrm{d}D_{\mathrm{com}}(z) = -c\mathrm{d}a/a\dot{a}$:

$$D_{\mathrm{com}}(z_{\mathrm{o}}, z_{\mathrm{s}}) = \frac{c}{H_0} \int_{a(z_{\mathrm{s}})}^{a(z_{\mathrm{o}})} \frac{\mathrm{d}a}{a\dot{a}} = \frac{c}{H_0} \int_{a(z_{\mathrm{s}})}^{a(z_{\mathrm{a}})} \frac{\mathrm{d}a}{a^2 E(a)} := w(z_{\mathrm{o}}, z_{\mathrm{s}}). \qquad (2.28)$$

In contrast to the physical distance the co-moving distance stays constant over time for a source and an observer co-moving with the mean cosmic flow.

A classical distance measure in cosmology is the **angular diameter distance** which is defined as the ratio of an object's physical transverse size to its angular size in radians: $D_{\mathrm{ang}}^2 = \delta A/\delta\omega$. It is used to convert angular separations in telescope images into proper separations at the source. The size and solid angle of the object relate to that of the full sphere according to

$$\frac{\mathrm{d}\omega}{4\pi} = \frac{\delta A}{4\pi a(z_{\mathrm{s}})^2 f_{\mathrm{K}}^2[w(z_{\mathrm{o}}, z_{\mathrm{s}})]}, \qquad (2.29)$$

where we have used the scaling function $f_{\mathrm{K}}^2(w)$ given in (2.3). It follows that

$$D_{\mathrm{ang}}(z_{\mathrm{o}}, z_{\mathrm{s}}) = \left(\frac{\delta A}{\delta\omega}\right)^{1/2} = a(z_{\mathrm{s}}) f_{\mathrm{K}}[w(z_{\mathrm{o}}, z_{\mathrm{s}})]. \qquad (2.30)$$

For the flat Universe we obtain $D_{\mathrm{ang}} = a(z_{\mathrm{s}})w(z_{\mathrm{o}}, z_{\mathrm{s}}) = D_{\mathrm{com}}(1 + z_{\mathrm{s}})^{-1}$. The angular diameter distance is therefore not increasing indefinitely as $z \to \infty$. It turns over at $z \sim 1$ and thereafter more distant objects appear larger in angular size.

Another way of inferring distances in cosmology is to measure the flux $S$ from an object of known bolometric luminosity $L$. The **luminosity distance** is then defined by

$$D_{\text{lum}} \equiv \left( \frac{L}{4\pi S} \right)^{1/2} .$$

(2.31)

The surface brightness of a receding object is reduced by a factor $[a(z_{\text{s}})/a(z_{\text{o}})]^4$ and the angular area goes down as $D_{\text{ang}}^{-2}$. This yields

$$D_{\text{lum}}(z_{\text{o}}, z_{\text{s}}) = \left[ \frac{a(z_{\text{o}})}{a(z_{\text{s}})} \right]^2 D_{\text{ang}}(z_{\text{o}}, z_{\text{s}}) .$$

(2.32)

All four distance-redshift relations depend on the cosmological parameters and are larger in a universe with a cosmological constant than in one without. The fact that the Hubble expansion rate can be determined from the luminosity distance of far-off supernovae with common absolute magnitudes $M$ led to the famous discovery of accelerating expansion and dark energy (Riess et al. 1998; Perlmutter et al. 1999).

## 2.2 Structure formation

The homogeneity of the Universe is a reasonable assumption on large scales. However, in the observable universe, there exists a significant degree of inhomogeneity in the form of galaxies, clusters and large filaments (see Figure 2.2). The temperature fluctuations in the CMB indicate that these structures have grown out of small seeds around $z \approx 1000$, possibly the quantum fluctuations of a scalar field.

The description of the different stages of structure formation from small primordial density fluctuations to the cosmic web we observe today requires the study of the growth of inhomogeneities in an otherwise smooth universe. As long as these inhomogeneities are small, their growth can be studied by the linear perturbation around a background Friedmann universe. Once the deviations from the smooth universe become large, linear theory fails and we have to switch to a non-linear description. To ultimately understand the late non-linear phases of structure growth we have to rely on numerical simulations.

### 2.2.1 Linear evolution

Jeans was the first who formulated a linear theory for the evolution of small fluctuations in the density and velocity in a non-expanding homogeneous and isotropic "mean" fluid. The corresponding formalism is therefore named Jeans' Theory. Linear structure growth in an expanding background must be treated within the framework of general relativity. However, on scales much smaller than the Hubble radius and as long as the gravitational fields are weak we can introduce a valid Newtonian approximation to the relativistic theory. This implies the restriction to non-relativistic matter such as CDM and baryons.

An important quantity in the theory of linear structure formation is the density contrast $\delta$, defined by

$$\delta(\vec{r}) = \frac{\delta\rho(\vec{r})}{\bar{\rho}} = \frac{\rho(\vec{r}) - \bar{\rho}}{\bar{\rho}} ,$$

(2.33)
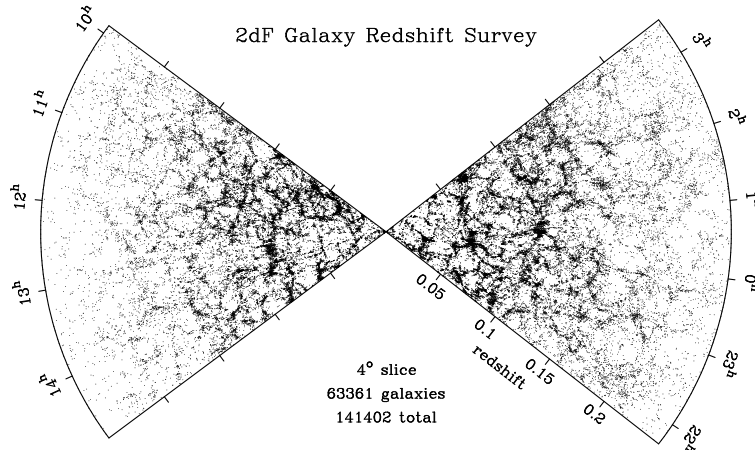
Figure 2.2: Distribution of galaxies in the Two Degree Field Galaxy Redshift Survey (2dF) drawn from a total of 141,402 galaxies (Peacock et al. 2001). The galaxy sample probes the structure in the Universe out to $z = 0.3$, corresponding to distances up to $1000\,h^{-1}\,\mathrm{Mpc}$ away from us (located at the centre).

where $\vec{r} = a(t)\vec{x}$ where $\vec{x}$ is the co-moving coordinate. The mean density $\bar{\rho}$ drives the Hubble expansion while a fluctuation with $\rho(\vec{r}) - \bar{\rho} > 0$ produces an additional gravitational field that slows down the expansion in the concerned area. The density contrast will therefore grow over time. Likewise, in an underdense region where $\rho(\vec{r}) - \bar{\rho} < 0$ the density drops faster than the cosmic mean and $\delta$ will become more negative as time evolves. Structure growth therefore is a self-amplifying process.

We start with a description of the initial fluctuations in the mean density, pressure, velocity and gravitational fields by small linear perturbations to the background values

$$\rho(\vec{r}, t) \quad \rightarrow \quad \rho(t) + \delta\rho(\vec{r}, t)\,, \tag{2.34}$$

$$p(\vec{r}, t) \quad \rightarrow \quad p(t) + \delta p(\vec{r}, t)\,, \tag{2.35}$$

$$\vec{v}(\vec{r}, t) \quad \rightarrow \quad \vec{v}(t) + \delta\vec{v}(\vec{r}, t)\,, \tag{2.36}$$

$$\Phi(\vec{r}, t) \quad \rightarrow \quad \Phi(t) + \delta\Phi(\vec{r}, t)\,. \tag{2.37}$$

The density drops inversely proportional with the cubed scale factor $a$ while the mean velocity is determined by the Hubble expansion law. We can thus use the ansatz

$$\rho(t) = \rho_0 a(t)^{-3}\,, \qquad \vec{v} = \frac{\mathrm{d}\vec{r}}{\mathrm{d}t} = \frac{\dot{a}}{a}\vec{r} = H\vec{r}\,, \tag{2.38}$$

where $\rho_0$ is the background density at a fixed time $t = t_0$. The potential $\Phi$ is defined through the Poisson equation for the Newtonian gravitational potential

$$\nabla^2\Phi = 4\pi G\rho\,. \tag{2.39}$$

Inserting the above definitions into the continuity and the Euler equation and neglecting

all terms non-linear in $\delta\rho$, $\delta\vec{v}$, $\delta p$, and $\delta\Phi$ we arrive at

$$\frac{\partial\delta\rho}{\partial t} \quad + \quad 3H\delta\rho + \vec{v}\cdot\nabla\delta\rho + \rho\nabla\cdot\delta\vec{v} = 0\,, \tag{2.40}$$

$$\frac{\partial\delta\vec{v}}{\partial t} \quad + \quad H\delta\vec{v} + (\vec{v}\cdot\nabla)\delta\vec{v} = -\frac{c_s^2}{\rho}\nabla\delta\rho - \nabla\delta\Phi\,, \tag{2.41}$$

$$\nabla^2\Phi \quad = \quad 4\pi G\delta\rho\,, \tag{2.42}$$

where we have used the definition of the sound velocity $c_s^2 = \delta p/\delta\rho$. Using the total time derivative of $\delta\rho$ and $\delta\vec{v}$

$$\dot{\delta\rho} \equiv \frac{\mathrm{d}\delta\rho}{\mathrm{d}t} = \frac{\partial\delta\rho}{\partial t} + \vec{v}_0\cdot\nabla\delta\rho \qquad \text{and} \qquad \dot{\delta\vec{v}} \equiv \frac{\mathrm{d}\delta\vec{v}}{\mathrm{d}t} = \frac{\partial\delta\vec{v}}{\partial t} + \vec{v}_0\cdot\nabla\delta\vec{v}\,, \tag{2.43}$$

we can express the total time derivative of the density contrast $\delta$ as follows:

$$\rho_0\dot{\delta} \equiv \rho_0\frac{\mathrm{d}\delta}{\mathrm{d}t} = \dot{\delta\rho} + 3H\rho_0\delta\,. \tag{2.44}$$

Now replacing $\delta\rho$ by $\delta$ in (2.40) and going from real to Fourier space

$$\nabla_x = \frac{1}{a}\nabla_r \rightarrow -i\frac{\vec{k}}{a}\,, \tag{2.45}$$

the system of equations (2.40) - (2.42) becomes

$$\dot{\delta}_{\vec{k}} \quad - \quad \frac{i}{a}\vec{k}\vec{v}_{\vec{k}} = 0\,, \tag{2.46}$$

$$\dot{\vec{v}}_{\vec{k}} \quad + \quad H\vec{v}_{\vec{k}} = \frac{i}{a}c_s^2\vec{k}\delta_{\vec{k}} + \frac{i}{a}\vec{k}\Phi_{\vec{k}}\,, \tag{2.47}$$

$$\Phi_{\vec{k}} \quad = \quad -\frac{4\pi G\rho_0}{k^2}a^2\delta_{\vec{k}}\,. \tag{2.48}$$

These three equations can be combined into a single partial differential equation of second order for the density contrast:

$$\ddot{\delta} + 2H\dot{\delta} + \left(\frac{c_s^2 k^2}{a^2} - 4\pi G\rho_0\right)\delta = 0\,. \tag{2.49}$$

The resulting equation yields the damped oscillator equation with the frequency

$$\omega = \sqrt{\frac{c_s^2 k^2}{a^2} - 4\pi G\rho_0}\,, \tag{2.50}$$

provided that the oscillation frequency is much higher than the expansion rate. For a complex $\omega$ the perturbation amplitude will grow exponentially. This applies to wave numbers $k \geq k_J := a\kappa_J = a\sqrt{4\pi G\rho_0}/c_s$ from which we define the co-moving "Jeans length"

$$\lambda_J := \frac{2\pi}{k_J} = 2c_s\sqrt{\frac{\pi}{G\rho_0}}\,. \tag{2.51}$$

The Jeans length marks the length scale above which the density contrast can further increase while smaller perturbations will oscillate. In other words, on scales larger than $\lambda_J$ the infall of material happens faster than the perturbation can be mediated through the medium. At the Jeans length the free-fall time $\tau \sim 1/\sqrt{4\pi G\rho}$ and sound crossing time therefore cancel exactly. Apparently the expansion of the universe has a damping effect on the growth of primordial density fluctuations. From the damping term $2H\dot{\delta}$ we infer that, the faster the expansion proceeds, the slower overdensities will grow.

Equation (2.49) can be solved by Bessel functions. However, for the limiting cases of a universe that is dominated by radiation or matter, simpler solutions can be found:

In the early Universe, during radiation domination, we can neglect the gravitational term. Since we have $H(t) = 1/(2t)$, the oscillator equation then takes the form

$$\ddot{\delta} + \frac{1}{t}\dot{\delta} + \frac{c_s^2 k^2}{a^2}\delta = 0\,. \tag{2.52}$$

For CDM we can also ignore the $c_s$ term since $p \ll \rho$ and thus $c_s \ll 1$. We then obtain

$$\ddot{\delta}_{\text{CDM}} + \frac{1}{t}\dot{\delta}_{\text{CDM}} = 0\,. \tag{2.53}$$

A growing solution exits for $\dot{\delta}_{\text{CDM}} \neq 0$. Nevertheless, perturbations can grow logarithmically:

$$\delta_{\text{CDM}}(t) = \delta_{\text{CDM}}(t_0)\left[1 + a\ln\left(\frac{t}{t_0}\right)\right]\,. \tag{2.54}$$

During radiation domination the background expansion is too fast to allow for the growing of sub-horizon perturbations. Likewise, the coupling between gas and photons will suppress the growth of the baryonic density contrast. Since the sound velocity at this epoch is given by $c_s = \sqrt{1/3}\,c$, the Jeans length yields

$$\lambda_J \sim H^{-1}\,. \tag{2.55}$$

Consequently, all sub-horizon scales are stable and baryonic density fluctuations will not grow during radiation domination.

In the matter-dominated phase, we can assume a so-called Einstein-de Sitter universe with $H(t) = 2/(3t)$ and $\rho_0(t) = (6\pi Gt^2)^{-1}$. Equation (2.49) then reads

$$\ddot{\delta} + \frac{4}{3t}\dot{\delta} - \frac{2}{3t^2}\delta = 0 \qquad \text{for} \qquad k \ll k_J\,. \tag{2.56}$$

Using the ansatz $\delta(t) \propto t^n$ we obtain an increasing and a decaying solution:

$$\delta_+(t) = \delta_+(t_0)\left(\frac{t}{t_0}\right)^{2/3}\,, \tag{2.57}$$

$$\delta_-(t) = \delta_-(t_0)\left(\frac{t}{t_0}\right)^{-1}\,. \tag{2.58}$$
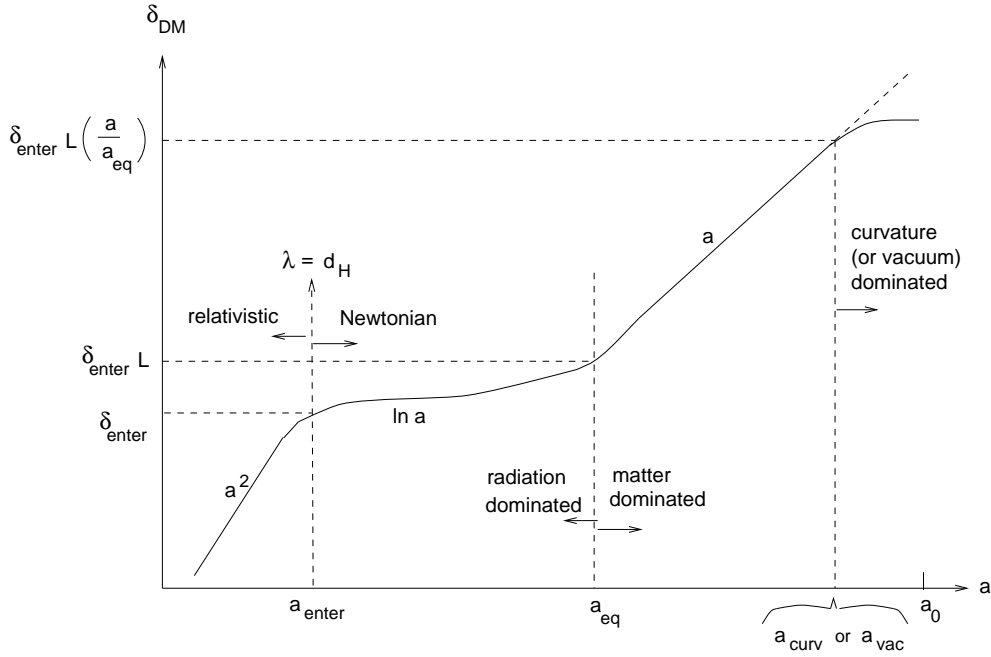
Figure 2.3: Schematic figure showing the growth of linear perturbations in dark matter
(Padmanabhan 1999). The cosmological horizon at early times is very small
so the fluctuations on scales relevant to structure formation are outside the
horizon where they grow as $a^2$. As the universe expands, perturbations on
larger scales enter the Hubble radius. During the radiation dominated phase
fluctuations grow as $\ln a$ while during matter domination they grow as $a$.

The decaying mode quickly becomes irrelevant. The remaining solution is conventionally
called "growth factor" and denoted by $D_+$. Since $t \propto a^{3/2}$, density perturbations in a
matter-dominated universe grow proportional to the scale factor $a$.

The evolution of the dark matter density contrast during the time of radiation and mat-
ter domination is sketched in Figure 2.3. While the CDM density contrast starts growing
at matter-radiation equality, baryonic structures can only form after recombination when
the gas gets decoupled from radiation and its sound velocity drops. The baryonic overden-
sities will later fall into the gravitational potential of the CDM structure that has formed
earlier.

## 2.2.2 Non-linear evolution

When the density contrast of a perturbation reaches $\delta \approx 1$ the linear description of its
evolution breaks down. The overdense regions that have formed out of the primordial seeds
will continue to grow until they collapse under their own gravity and by subsequent infall
of material evolve into the large-scale structure we observe today. The self-gravitating
objects are commonly known as "halos".

Since the gravitational collapse of a halo is a complicated process the study of cosmolog-

ical structure formation usually involves large scale numerical simulations. Nevertheless, we can analyse the non-linear regime using some simple analytic approximations in order to obtain insights into the problem. In what follows we will investigate the evolution of a spherical "top-hat" which approximates the halo by a homogeneous overdense sphere. The model is particularly simple for the $\Omega_m = 1$, matter dominated Einstein-de Sitter universe that is described by the Hubble constant $H = H_0 a^{-3/2}$. We follow the approach presented in Wang & Steinhardt (1998), complementary information can be found in Padmanabhan (1993) and White (1996).

The growth of a density perturbation is slowed down due to the gravitational potential of the local mass concentration. The radius of the overdense sphere will reach a maximum $R_{\mathrm{ta}}$ before the process of expansion is inverted and the halo starts shrinking again. In what follows we use the radius at turn-around to parameterise the radius of the halo according to

$$x := \frac{a}{a_{\mathrm{ta}}}, \quad y := \frac{R}{R_{\mathrm{ta}}}. \tag{2.59}$$

Furthermore we have introduced the parameter $y$ that gives the scale factor of the background expansion in units of the scale factor $a_{\mathrm{ta}}$ at the moment of turn-around. By defining the scaled time

$$\tau := H_{\mathrm{ta}} t = H_0 t a_{\mathrm{ta}}^{-3/2}, \tag{2.60}$$

we can derive the following useful relations:

$$x' := \frac{\mathrm{d}x}{\mathrm{d}\tau} = \frac{1}{H_{\mathrm{ta}}} \frac{\dot{a}}{a_{\mathrm{ta}}} = \frac{H}{H_{\mathrm{ta}}} x = x^{-1/2}, \quad \Longrightarrow \quad \tau = \frac{2}{3} x^{3/2}. \tag{2.61}$$

The sphere obeys the Friedmann equation for cosmic expansion with a different effective $\Omega_0$. Restricting ourselves to CDM with $p = 0$ we obtain the equation of motion

$$\frac{\mathrm{d}^2 R}{\mathrm{d}t^2} = -\frac{GM}{R^2} = -\frac{G}{R^2} \frac{4\pi}{3} \rho_{\mathrm{ta}} R_{\mathrm{ta}}^3, \tag{2.62}$$

where $\rho_{\mathrm{ta}}$ denotes the mean density of the sphere at the time of turn-around. Defining the overdensity of the halo relative to the background at turn-around by $\zeta = \rho_{\mathrm{ta}}/\bar{\rho}(a_{\mathrm{ta}})$ we can re-write $\rho_{\mathrm{ta}}$ as

$$\rho_{\mathrm{ta}} = \frac{3H_{\mathrm{ta}}^2}{8\pi G} \zeta. \tag{2.63}$$

Inserting the last expression into equation (2.62) and re-arranging the terms finally gives

$$\begin{aligned} \frac{1}{H_{\mathrm{ta}}^2} \frac{\mathrm{d}^2}{\mathrm{d}t^2} \left( \frac{R}{R_{\mathrm{ta}}} \right) &= -\frac{1}{2} \zeta \left( \frac{R}{R_{\mathrm{ta}}} \right)^2, \\ y'' &= -\frac{1}{2} \frac{\zeta}{y^2}. \end{aligned} \tag{2.64}$$

which is a differential equation of second order in $y$. Since the overdensity ceases to expand at turn-around when $x = 1$, and under the additional assumption that halo formation sets

in contemporaneously with the beginning of the cosmic expansion at $x = 0$, we obtain the two boundary conditions

$$y|_{x=0} = 0 \,, \quad y'|_{x=1} = 0 \,. \tag{2.65}$$

Integrating equation (2.64) yields

$$\tau = \frac{1}{\sqrt{\zeta}} \left[ \frac{1}{2} \arcsin(2y - 1) - \sqrt{y - y^2} + \frac{\pi}{4} \right] \,, \tag{2.66}$$

and thus the overdensity at turn-around time $\tau = 2/3$ is given by $\zeta = (3\pi/4)^2$.

Expanding expression (2.66) to lowest order in $y$,

$$\tau = \frac{2}{3} x^{2/3} \approx \frac{8}{9\pi} y^{3/2} \left( 1 + \frac{3y}{10} \right) \,, \tag{2.67}$$

and solving for $x$, we obtain the linear density contrast $\delta_{\mathrm{L}}$ of the overdense sphere

$$\delta_{\mathrm{L}} = \left( \frac{\rho}{\bar{\rho}} \right)^3 \zeta - 1 = \left( \frac{x}{y} \right)^3 \zeta - 1 \approx \frac{3y}{5} \,. \tag{2.68}$$

To arrive at the second equality we have inserted the scaling relations for the background density $\bar{\rho} \propto (a_{\mathrm{ta}}/a)^3$ and the mean density of the halo $\rho \propto (R_{\mathrm{ta}}/R)^3$. The density contrast $\delta_{\mathrm{L}}$ can then be linearly extrapolated to the time of turn-around:

$$\delta_{\mathrm{L,ta}} = \frac{a_{\mathrm{ta}}}{a} \delta_{\mathrm{L}} = \frac{\delta}{x} = \frac{3y}{5x} \,. \tag{2.69}$$

Using equations (2.61) and (2.67) we can infer the numerical value:

$$\delta_{\mathrm{L,ta}} = \frac{3}{5} \left( \frac{3\pi}{4} \right)^{2/3} \approx 1.06 \,. \tag{2.70}$$

Theoretically, due to the symmetry in the equations of motion, the sphere should collapse to a single point at twice the time of turn-around when $\tau = \tau_{\mathrm{coll}} = 4/3$ and thus $x = 2^{2/3}$. The linear density contrast inside the halo would then be

$$\delta_{\mathrm{coll}} = 2^{2/3} \delta_{\mathrm{ta}} = \frac{3}{5} \left( \frac{3\pi}{2} \right)^{2/3} \approx 1.69 \,. \tag{2.71}$$

In reality, however, during infall the particles will be scattered by small fluctuations of the gravitational field and virialise in a process which is called "violent relaxation" (Lynden-Bell 1967). At $\tau_{\mathrm{coll}}$ the halo has de facto reached virial equilibrium with $R_{\mathrm{vir}} = (R_{\mathrm{max}}/2)$ and we obtain

$$\frac{\rho_{\mathrm{vir}}}{\bar{\rho}(a_{\mathrm{vir}})} = \left( \frac{2^{2/3}}{1/2} \right)^3 \zeta = 18\pi^2 \approx 178 \,. \tag{2.72}$$

Although the assumption of spherical symmetry in this analysis is in fact inadequate, the last result is commonly used to define the virialised region of a halo to be a sphere with a

mean density which is about $\sim 200$ times the critical density $\rho_c$ at the time of the collapse. In real halos, the time-varying gravitational potential will randomise the velocities of the infalling particles and we would expect a non-symmetric distribution of matter. However, it turns out that a density contrast $\sim 100$ - $200$ is quite successful at defining and hence finding halos in N-body simulations (Navarro et al. 1997).

The oldest agglomerations of matter we know today are the globular clusters with masses that roughly correspond to the estimated baryonic Jeans mass after recombination. The ages and masses of the compact stellar clusters indicate that they were the first objects that formed out of the collapsed overdensities (Peebles & Dicke 1968). In contrast, a large number of the most massive gravitationally bound objects in our Universe, the clusters of galaxies, seem not to have finished the process of relaxation yet. Observations in X-ray and radio as well as data from gravitational lensing reveal a high level of turbulence and asymmetry of their central parts, including the merging of sub-clumps, which suggests that those objects are currently in the process of forming.

# Galaxy clusters

<div style="text-align: right; font-size: 3em;">3</div>

Clusters of galaxies are the largest gravitationally bound objects in the Universe. They are believed to have formed in a hierarchical process during which initially small collapsed objects have collected into galaxies, and later into clusters of galaxies. This evolution spans a significant fraction of the age of the Universe, thereby involving many interacting physical processes. Galaxy clusters typically have masses between $10^{14}\,\mathrm{M_\odot}$ and $10^{15}\,\mathrm{M_\odot}$ and spread over a region of several Mpc.

They consist of three main components: galaxies, gas, and dark matter. Although they contain hundreds of galaxies the matter bound in stars and galaxies contribute the least, at most a few percent, to the total mass (Sarazin 1988). About 10% to 30% of the total mass are made up by the intracluster medium (ICM), diffuse, hot gas at densities between $10^{-4}$ and $10^{-2}\,\mathrm{cm^{-3}}$ and temperatures of $10^7$ to $10^8\,\mathrm{K}$. The largest component seems to be the collisionless, dark matter which is needed to explain the gravitational stability of clusters.

A great advance in the systematic study of the properties of clusters occurred when Abell (1958) compiled an extensive, statistically complete catalogue of rich clusters of galaxies. Until today, this catalogue has been an important resource in the study of galaxy clusters.

## 3.1  Mass profiles

Similar to the spherical halo model which we used in the last chapter to derive the collapse parameters, the most simple approach to the dark matter distribution of a relaxed galaxy cluster is that of an isothermal sphere. The density profile is described by

$$\rho_{\mathrm{DM}}(r) = \frac{\sigma_v^2}{2\pi G r^2}\,, \tag{3.1}$$

where $r$ is the halo radius and $\sigma_v^2$ is the velocity dispersion which is assumed constant and isotropic at every point. The distribution has a singularity at $r = 0$ and the total mass of the halo becomes infinite. One avoids the problem of diverging densities by defining a constant central density $\rho_{\mathrm{c}} = 9\sigma_v^2/(2\pi G r_{\mathrm{c}})$ within a core radius $r_{\mathrm{c}}$ which depends on the object under consideration (see e.g. Shapiro et al. 1999).

Numerical simulations suggest that the CDM halo profiles of relaxed galaxy clusters are indeed approximately isothermal over a large range of radii. Near the centre, however,

the decline appears to be shallower than $r^{-2}$ while close to the virial radius the density declines more rapidly. The resulting density can be described by the generic formula

$$\rho_{\mathrm{DM}}(r) = \frac{\rho_{\mathrm{DM},0}}{(r/r_{\mathrm{s}})^{\gamma}(1 + (r/r_{\mathrm{s}})^{\alpha})^{(\beta-\gamma)/\alpha}} \, , \qquad (3.2)$$

where the parameters $\gamma$ and $\beta$ denote the inner and outer power-law slopes and the scale radius $r_{\mathrm{s}}$ specifies the transition from shallow to steep. The width of the transition region decreases with increasing $\alpha$. This profile appears to be universal, with the same shape for all masses and epochs. However, the exact values of the four parameters are under debate since different groups of authors found different results for the shape of the innermost regions of galaxies and galaxy clusters (Navarro et al. 1996; Fukushige & Makino 1997; Moore et al. 1999). The currently most common choice for the profile of dark matter halos of virialised galaxy clusters is the NFW profile, named after Navarro, Frenk, and White. It has the parameters $(\alpha, \beta, \gamma) = (1, 3, 1)$ and a typical scale radius that ranges between 0.1 and $0.25\,r_{\mathrm{vir}}$ for simulated clusters. Lower-mass objects tend to have smaller scaling radii because they formed earlier in time when the overall density of the universe was larger (Bullock et al. 2001; Eke et al. 2001).

Concerning the distribution of the baryonic gas inside a galaxy cluster, historically, the most popular description is the so-called $\beta$-model. It is based on an isothermal gas model where the density is given in terms of three free parameters $\rho_{\mathrm{gas},0}$, $r_{\mathrm{c}}$, and $\beta$:

$$\rho_{\mathrm{gas}}(r) = \frac{\rho_{\mathrm{gas},0}}{(1 + (r/r_{\mathrm{c}}))^{3\beta/2}} \, . \qquad (3.3)$$

The normalisation parameter $\rho_{\mathrm{gas},0}$ depends on the ratio of the gas mass to the virial mass in the cluster, $f = M_{\mathrm{gas}}/M_{\mathrm{vir}}$, for which Fujita & Takahara (1999) derived the relation $f \propto \rho_{\mathrm{vir}}^{-0.1} M_{\mathrm{vir}}^{0.4}$, where $\rho_{\mathrm{vir}} = M_{\mathrm{vir}}/r_{\mathrm{c}}^3$ is the characteristic density of gravitational matter and $r_{\mathrm{c}}$ is the core radius. The slope parameter $\beta$ as inferred from X-ray observations takes values in the range $\sim 0.4$ - $1.0$, which means that for radii larger than $r_{\mathrm{c}}$ the density profiles range from $\propto r^{-1.2}$ to $\propto r^{-3}$ and are thus more diverse than those of dark matter (Jones & Forman 1984, 1999).

Although the profile (3.3) is still widely used to describe the radial distribution of the intracluster-cluster medium (ICM), the assumption of an isothermal gas is certainly not consistent with observed temperature profiles of galaxy clusters. Non-radiative gas dynamical simulations have shown that, in the absence of additional physics, the ICM of relaxed clusters can be approximately described as a polytropic gas in hydrostatic equilibrium with the gravitational potential created by the dark matter (Ascasibar et al. 2003). An analytical profile has for example been derived by Suto et al. (1998):

$$\rho_{\mathrm{gas}}(r) = \rho_{\mathrm{gas},0} \left[ \frac{T(r)}{T_0} \right]^{1/(\gamma-1)} , \text{ where } \quad \frac{T(r)}{T_0} = 1 - Bf\left(\frac{r}{R_{\mathrm{s}}}\right) . \qquad (3.4)$$

The scale radius $R_{\mathrm{s}}$ and the parameter $B$ relate the temperature profile $T(r)$ of the gas to the underlying dark matter distribution for which we have assumed a NFW profile. Here,

$T_0$ is the central temperature and $\gamma$ denotes the adiabatic index of the thermal gas. The parameter $B$ and the function $f(x)$ are given by

$$B = \frac{4\pi G \mu m_{\rm p}(\gamma - 1)\rho_{\rm DM,0} R_s^2}{\gamma k T_0}\,, \qquad f(x) = 1 - \frac{\ln(1+x)}{x}\,. \qquad (3.5)$$

Unlike the isothermal $\beta$-model the distribution (3.4) provides a physical basis to directly probe the shape of the dark matter halo from the observed temperature profiles of clusters of galaxies. However, since the smooth, radially symmetric density profile is an idealised picture, the dark matter profile might only be inferred if the galaxy cluster is in a state of complete virial equilibrium.

Observations by Jones & Forman (1999) have shown that at least 40 % out of a sample of 368 X-ray detected clusters of galaxies contain substantial substructure. Since the accretion of gas and dark matter is lumpy, not smooth, those substructures are interpreted as evidence of a nonvirialised state, indicating that many clusters are dynamically young systems.

## 3.2 Evolution and dynamics

The formation process of galaxy clusters is classified according to the size and mass of infalling substructures: The accretion of matter lumps with masses smaller than $\sim$5 % of the main halo mass is considered approximately smooth. If the mass of the sub-clump exceeds these 5 % the accretion process is called a **minor merger**, while for the accretion of clumps larger than $\sim 1/3$ of the main halo mass the event is termed a **major merger**. Depending on the type of merger and the observer's line of sight, the shape of the galaxy cluster can significantly deviate from the spherical halo model and instead display a highly irregular shape.

In a major merger event, subclusters collide at velocities of $\sim 2000$ km/s, releasing gravitational binding energies of as much as $\gtrsim 10^{64}$ erg (Feretti et al. 2002). The large energy release makes the cluster mergers the most energetic events in the Universe since the Big Bang. They have strong effects onto the cluster interior, resulting in a remarkable change of observable properties which therefore can significantly differ from that of more relaxed systems.

In the upcoming section, we will present the physical effects that merger events have onto the diffuse hot gas and the intracluster particle population. In the subsequent section, we will introduce some important cluster observables and explain how they relate to the dynamical state of the galaxy cluster.

### 3.2.1 Thermal effects of mergers

The shocks caused by the accretion of matter lumps heat and compress the intracluster medium and raise the cluster's entropy through the dissipation of kinetic energy. Compression and heating depend on the shock strength which can be seen if we re-express the Rankine-Hugoniot jump conditions for thermodynamic shocks (Rankine 1870; Hugoniot

1887, 1889) as functions of the Mach number $M$:

$$\frac{\rho_2}{\rho_1} = \frac{(\gamma+1)M^2}{(\gamma-1)M^2+2}, \tag{3.6}$$

$$\frac{p_2}{p_1} = \frac{2\gamma M^2 - (\gamma-1)}{\gamma+1}, \tag{3.7}$$

$$\frac{T_2}{T_1} = \frac{\left[2\gamma M^2 - (\gamma-1)\right]\left[(\gamma-1)M^2+2\right]}{(\gamma+1)^2 M^2}. \tag{3.8}$$

Here, the quantities $\rho$, $p$, and $T$ denote the density, pressure, and temperature of the gas and the indices 1 and 2 refer to the states ahead and behind the shock front. Since the Mach number is linked to the pre-shock state through $M = v_1/\sqrt{\gamma p/\rho}$, where $v_1$ is the pre-shock velocity relative to the shock front, the heating effect will be largest if the clump falls into cold, low-pressure gas.

The irregular infall of plasma clumps of varying sizes will mix up the ICM in a complex network of shocks that causes turbulence and convective motion on large scales. Since the effectiveness of all important radiative loss mechanisms depend on the density and temperature of the plasma, strong merger shocks will boost the emission of thermal radiation in galaxy clusters (see Section 3.3.3). The observable X-ray emission can thereby be amplified up to a factor of $\sim 10$ in luminosity. Consequently, the thermal signature of a merging galaxy cluster will not only significantly differ in its shape but also in the total power of the emitted radiation from that of a relaxed cluster.

After the merging is completed, turbulent and convective motions in the ICM will gradually run dry until the thermal equilibrium and convective stability are established. A long time after the merger, the cluster is expected to approach the shape of a cluster that has been formed by smooth accretion only. Numerical simulations of the structure formation process have shown that, despite of the irregular infall geometries and the complexity of the shock structure, in the end virialised clusters with nearly self-similar entropy structures are produced (Kay 2004; Voit et al. 2005).

The term entropy used in this context is equivalent to the entropic function $A(s)$, which is given by the constant of proportionality in the adiabatic equation of state $p = A\rho^\gamma$. The entropy is directly related to the temperature through

$$A \equiv \frac{k_{\mathrm{B}}T}{\mu m_{\mathrm{p}}\rho_{\mathrm{gas}}^{2/3}}, \tag{3.9}$$

where $m_p$ is the proton rest mass and $\mu$ is the mean molecular weight. We can define an universal reference entropy for galaxy clusters of different masses if we replace $\rho_{\mathrm{gas}}$ in the above expression by an approximate virial overdensity that is given by the product of the mean density of dark matter within the scale radius $R_{200}$ and the global baryon fraction $f_b = \Omega_{\mathrm{b}}/\Omega_{\mathrm{M}}$. Furthermore, we insert the characteristic halo temperature $T_{200}$ within the
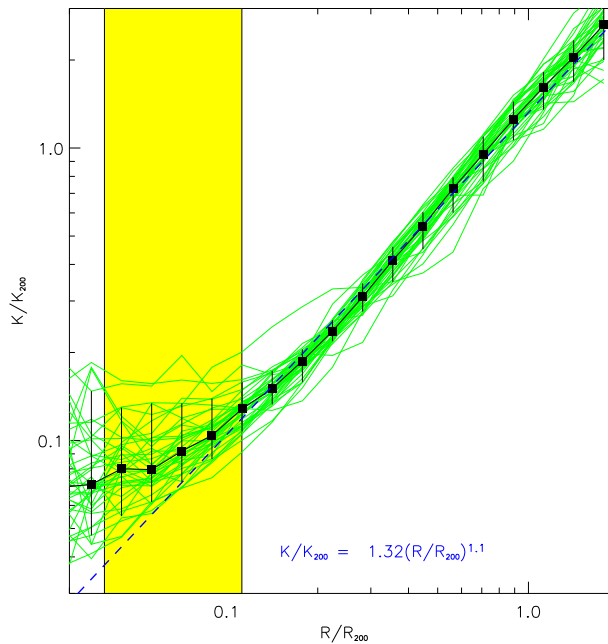
Figure 3.1: Dimensionless entropy $K/K_{200}$ as a function of scale radius $R/R_{200}$ for 40 clusters simulated with the GADGET-code. Black squares show the median profile. The dashed line illustrates the power-law relation $K/K_{200} = 1.32\,(R/R_{200})^{1.1}$ which represents the best fit within the range $0.2 \lesssim R/R_{200} \lesssim 1.0$ (Voit et al. 2005)

same radius:

$$A_{200} \quad = \quad \frac{k_{\mathrm{B}}T_{200}}{\mu m_{\mathrm{p}}(200 f_{\mathrm{b}}\rho_{\mathrm{cr}})^{2/3}} \tag{3.10}$$

$$= \quad \frac{1}{2}\left[\frac{2\pi}{15}\frac{G^2 M_{200}}{f_{\mathrm{b}}H(z)}\right]^{2/3} . \tag{3.11}$$

With the characteristic entropy scale $A_{200}$ we can cast the entropy distribution of different clusters into the dimensionless form $A/A_{200}$.

Figure 3.1 shows the spherically averaged entropy profiles of 40 clusters generated with a numerical simulation of a $\Lambda$CDM cosmology including non-radiative gas physics (Voit et al. 2005). The masses of these clusters range from $5.5 \cdot 10^{14}\,h^{-1}\,M_\odot$ to $8.4 \cdot 10^{14}\,h^{-1}\,M_\odot$. The dimensionless profiles appear to be self-similar within the range $0.2 \lesssim r/R_{200} \lesssim 1.0$, where they can to a good approximation be described by the power law $A(r) \propto r^{1.1}$, depicted by the blue dashed line in the plot. Deviations from the profile appear inside the radius $0.1\,R_{200}$. They are partly due to fact that some of the simulated clusters have nearly isentropic cores, while others do not. Moreover, the results in the cluster cores slightly depend on the hydrodynamical method used in the simulations.

### 3.2.2 Non-thermal effects of mergers

High speed astrophysical shocks in a magnetised plasma lead to a significant production of relativistic particles due to a mechanism that was first described by Fermi (1949). In his original paper, he considered the encounters of charged particles with moving gas clouds that are steeped in tightly bound turbulent magnetic fields. The latter is a reasonable assumption since cosmic magnetic fields easily get stirred by stellar winds, ionisation fronts, or supernova explosions. An energetic particle that enters a cloud gets reflected at the magnetic irregularities through resonances between its gyro-motion and magnetohydrodynamic waves in the plasma. By repeated scattering the particle can be accelerated to very high energies. In the following we will present the underlying mathematical formalism for non-relativistic cloud velocities. For a treatment of relativistic motion see Webb (1987).

First of all, we can make the simplifying assumption that the particle is already sufficiently relativistic so that $E \approx pc$. In the rest frame of the cloud the total particle energy $E_1'$ is then given by

$$E_1' = \gamma E_1 (1 - \beta \cos \theta_1) \,, \tag{3.12}$$

where $\theta_1$ is the incident scattering angle, $\gamma$ denotes the Lorentz factor and $\beta = u/c$ is the cloud's velocity relative to the speed of light. Since the scattering inside the cloud is due to the motion in the magnetic field and does not involve any collisions, we can consider it as elastic: $E_1' = E_2'$. Transforming this energy back to the laboratory frame, we have the energy of the particle after it has escaped the cloud,

$$E_2 = \gamma E_2' (1 + \beta \cos \theta_2') \,. \tag{3.13}$$

Substituting (3.12) into (3.13) we obtain the energy change for the particular encounter characterised by the scattering angles $\theta_1$ and $\theta_2'$:

$$\frac{\Delta E}{E} = \frac{(1 + \beta \cos \theta_2')(1 - \beta \cos \theta_1)}{1 - \beta^2} - 1 \,. \tag{3.14}$$

The mean energy gain $\langle E_2 - E_1 \rangle / E_1$ after a certain number of collisions ultimately depends on the geometry of the scattering system. We can now distinguish between two physical situations that result in different efficiencies of the acceleration process:

**Fermi I acceleration**

We consider a large plane shock front propagating at the supersonic speed $\vec{u}$ that separates the gas into two regions of different flow velocities. The situation is sketched in Figure 3.2. The gas flows away from the shock with a velocity $\vec{v}_2$ relative to the shock front, and $|\vec{v}_2| < |\vec{v}_1|$. Thus in the laboratory frame the gas behind the shock moves to the right with the velocity $\vec{u}_2 = -\vec{v}_1 + \vec{v}_2$. If we furthermore assume that the gas ahead of the front is at rest, its velocity in the reference frame of the shock front will be given by $-\vec{v}_1 = \vec{u}$. Equation (3.14) applies to this situation if we set $\beta = |\vec{u}_2|/c$. To obtain the mean energy gain we now need to average over all possible scattering angles $\theta_1$ and $\theta_2$, such that the
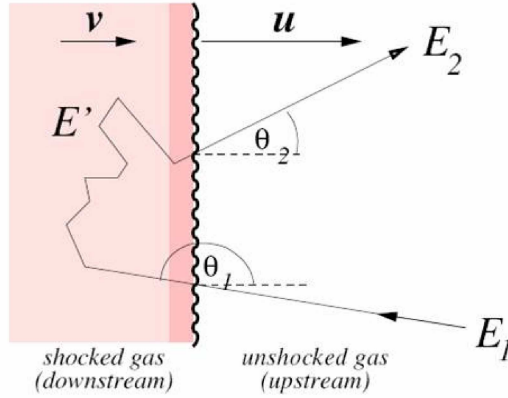
Figure 3.2: Acceleration at a plane shock front (figure from Kolanoski 2007)

particle stays inside the system:

$$\langle \cos \theta_1 \rangle = \frac{\int_{-1}^{0} \cos \theta_1 \mathrm{d} \cos \theta_1}{\int_{-1}^{0} \mathrm{d} \cos \theta_1} = -\frac{1}{2} \,, \quad \langle \cos \theta_2' \rangle = \frac{\int_{0}^{+1} \cos \theta_2' \mathrm{d} \cos \theta_2'}{\int_{0}^{+1} \mathrm{d} \cos \theta_2'} = \frac{1}{2} \,. \qquad (3.15)$$

Inserting (3.15) into (3.14) we arrive at

$$\frac{\langle \Delta E \rangle}{E} = \frac{(1 + \frac{1}{2}\beta)^2}{1 - \beta^2} - 1 \approx \beta \,. \qquad (3.16)$$

Since in merging clusters material falls in with velocities of about $10^4 \,\mathrm{km/s}$ we can safely treat the merger shock as a strong shock for which $M \to \infty$. The simplifying feature of strong shocks is that the density enhancement on crossing the shock front (3.6) yields

$$\frac{\rho_2}{\rho_1} = \frac{(\gamma + 1)}{(\gamma - 1)} \,. \qquad (3.17)$$

For a fully ionised gas $\gamma = 5/3$ and hence $\rho_2/\rho_1 = 4$. If we furthermore take into account the equation of mass conservation over the shock surface, $\rho_1 v_1 = \rho_2 v_2$, we infer that $u = v_1 = 4v_2 = 4(u + u_2)$. Solving for $u_2$ we thus obtain

$$u_2 = -\frac{3}{4}u \,, \qquad (3.18)$$

and hence

$$\beta = \frac{|\vec{u}_2|}{c} \approx \frac{3}{4}\frac{u}{c} \,. \qquad (3.19)$$

The increase in kinetic energy thus depends linearly on the shock velocity. Observations of radio emission from Galactic supernova remnants reveal that at least a few percent of the shock energy is directed into the acceleration of relativistic ions and electrons. Applying these numbers to strong merger shocks in clusters, one would expect that relativistic
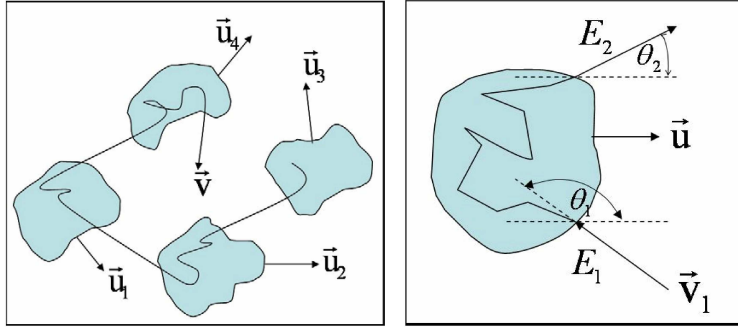
Figure 3.3: Left panel: stochastically distributed plasma clouds allowing for isotropic particle scattering; right panel: acceleration by a moving partially ionised gas cloud (figure from Kolanoski 2007)

particles with a total energy of $E \sim 10^{62}\,\mathrm{erg}$ are produced (Sarazin 2004). Thus, merging clusters should host huge populations of relativistic particles, so-called cosmic rays (see Section 3.3.2).

**Fermi II acceleration**

The second scenario consists of a charged particle with velocity $\vec{v}$ that is caught up in a system of randomly distributed magnetised gas clouds. We suppose that the clouds are moving isotropically at velocity $\vec{u}$ and that the particle gets scattered several times before escaping the system. The situation that was suggested in Fermi's original paper is illustrated in Figure 3.3. The probability of a collision is now proportional to the relative velocity between the cloud and the particle,

$$\frac{\mathrm{d}n}{\mathrm{d}t\,\mathrm{d}\cos\theta_1} \sim v - u\cos\theta_1\,, \tag{3.20}$$

where $n$ is the number of collisions. Averaging over incident scattering angles we have

$$\langle\cos\theta_1\rangle = \frac{\int_{-1}^{+1}\cos\theta_1(v - u\cos\theta_1)d\cos\theta_1}{\int_{-1}^{+1}(v - u\cos\theta_1)d\cos\theta_1} = -\frac{u}{3v} \approx -\frac{\beta}{3}\,. \tag{3.21}$$

The last approximation results from the assumption that the particle is already moving at a relativistic speed, so that $v \approx c$. Due to the isotropy of scattering in the system of clouds the average over the reflection angle $\theta_2'$ yields

$$\langle\cos\theta_2'\rangle = 0\,. \tag{3.22}$$

With these two distributions we obtain for the mean energy of the scattered particle:

$$\frac{\langle E\rangle}{E} = \frac{(1 + \frac{1}{3}\beta^2)}{1 - \beta^2} - 1 \approx \frac{4}{3}\beta^2\,, \tag{3.23}$$

which means that the energy gain is only of the second order in the cloud's velocity. The original version of Fermi's theory is therefore known as second order Fermi acceleration

and is a very slow process. Despite its low efficiency, magnetohydrodynamic simulations indicate that the turbulence generated during cluster mergers may be able to drive significant cosmic ray acceleration in the ICM (Candia et al. 2002; Cassano & Brunetti 2004).

One can deduce the non-thermal energy distribution characteristic of Fermi acceleration in a simple fashion. If we let $\xi$ be the average increase in particle energy per collision, $E = E_0\xi$, and $P$ the constant probability that the particle remains within the accelerating region after one scattering event, then, after $n$ encounters, there will be $N = N_0 P^n$ particles with energies $E = E_0\xi^n$. Eliminating $n$ between these quantities gives

$$\frac{\ln(N/N_0)}{\ln(E/E_0)} = \frac{\ln P}{\ln \xi}\,, \tag{3.24}$$

and hence

$$\frac{N}{N_0} = \left(\frac{E}{E_0}\right)^{-\alpha}, \quad \text{with} \quad \alpha = -\frac{\ln P}{\ln \xi}\,. \tag{3.25}$$

The Fermi mechanism thus leads to a power-law spectrum of cosmic ray energies. Equation (3.25) states that higher energy particles take longer to accelerate than low energy particles. Consequently, the lifetime of the Fermi accelerator limits the maximum energy per particle that can be produced.

## 3.3 Cluster observables

There is firm evidence that the ICM is a mixture of hot gas, magnetic fields, and relativistic particles. While the hot gas results in thermal bremsstrahlung X-ray emission, relativistic electrons and positrons generate non-thermal radio synchrotron emission and possibly hard X-ray emission by inverse Compton processes. Observations in the corresponding wavelengths are used thus to study the thermal and non-thermal properties of galaxy clusters. In contrast, since there is no radiative interaction of the dark matter component, its mass and distribution is investigated via the gravitational lensing effect.

In the next two sections we will give a short introduction to magnetic fields and cosmic rays which are the non-thermal constituents of galaxy clusters. Afterwards, we will describe the physical processes that lead to bremsstrahlung and synchrotron emission. Gravitational lensing as the main tool for inferring the shape of dark matter halos will be treated in the last section.

### 3.3.1 Magnetic fields

The existence of large-scale magnetic fields in the intracluster medium of galaxy clusters is well established through different methods of analysis. While the cosmic magnetic fields are generally tangled chaotically with magnetic fluctuations at scales that range over orders of magnitude, there is often a component of the field that is spatially coherent. Observed coherence lengths of up to $\sim 0.75\,\text{Mpc}$ in some clusters (Clarke et al. 2002) indicate that

the magnetic fields are not associated to the galaxy population or single AGN but are harboured by the diffuse intergalactic plasma.

A variety of observational and numerical efforts are undertaken to determine the morphologies and the strengths of the cluster permeating magnetic fields and to understand their origin. The direct method for quantifying magnetic fields on cosmic scales is the study of the Faraday rotation effect on linearly polarised light emitted by sources behind and inside the galaxy cluster. The linearly polarised light can be decomposed into a right-handed and a left-handed circularly polarised wave that propagate at different phase velocities within the magnetised plasma. The resulting rotation of the polarisation plane of the electromagnetic wave is usually written in terms of the rotation measure $RM$:

$$\Psi_{\mathrm{rot}}(\lambda) = \lambda^2 \, RM = \lambda^2 \, \frac{e^3}{2\pi m_{\mathrm{e}}^2 c^4} \int_0^L n_{\mathrm{e}}(l) \vec{B}_\parallel(l) \mathrm{d}l \,, \qquad (3.26)$$

where $\Psi_{\mathrm{rot}}$ denotes the angle by which the polarisation plane is rotated and $\vec{B}_\parallel$ is the magnetic field component along the line of sight. The integration is carried out along the cluster path length $L$. Since the rotation measure is also a function of the electron density $n_{\mathrm{e}}$ in the ICM, the reliability of the measurement significantly depends on the model for the intracluster gas density distribution. The field strengths inferred from high-resolution $RM$ maps for a galaxy cluster like Coma are of the order of $\sim 1\,\mu\mathrm{G}$, with a significant enhancement of the rotation measure in the central regions. The amplification is even more pronounced in cooling core clusters where field strengths from $\sim 5\,\mu\mathrm{G}$ up to extreme values of $40\,\mu\mathrm{G}$ were found (Carilli & Taylor 2002; Govoni & Feretti 2004), indicating a strong scaling between the magnetic and thermal energy densities in clusters of galaxies.

Magnetic fields are indirectly traceable by the large-scale radio emission that is produced by the gyration of relativistic electrons around the field lines. To estimate the magnetic field strength from the cluster's synchrotron emission one makes use of the equipartition assumption which states that the energy contributions of the magnetic field and the relativistic particles are approximately equal.

A different possibility is to compare the luminosities of the synchrotron and the inverse compton (IC) emission. The IC emissivity is proportional to the energy density in the photon field, $u_{\mathrm{ph}}$, which for the CMB is $\sim 5 \cdot 10^{-13} \, (1+z)^4 \, \mathrm{erg\,cm}^{-3}$, whereas the synchrotron emissivity is proportional to the energy in the magnetic field, $u_B = B^2/8\pi$. This leads to the simple proportionality

$$\frac{L_{\mathrm{sync}}}{L_{\mathrm{IC}}} = \frac{u_B}{u_{\mathrm{ph}}} \,, \qquad (3.27)$$

from which one can obtain an estimate for the energy density of the magnetic field (see Govoni & Feretti 2004 for details). The inferred values for the magnetic energy density lie in the range of a few percent of the thermal energy density.

The drawback of the latter two techniques is that they are only applicable to a small sample of galaxy clusters since the large scale radio halos are not a common property of all clusters but are only observed in a fraction of $\sim$10 % of all objects. For those clusters

displaying a radio halo typical magnetic field values in the range of $0.1\,\mu$G to $1.0\,\mu$G are derived under the assumption that the field entirely fills the radio source volume. It is conceivable that also smaller clusters host radio halos but with surface brightnesses that currently lie below the detection limit. However, with ongoing observational efforts they may become accessible in the near future.

At the present, very little is known about the origin of magnetic fields and, although many plausible explanations of how and when the fields were first generated have emerged, no single theory became widely accepted. One class of models relies on large scale field generation prior to recombination and subsequent field amplification by turbulence and structure formation shocks. The hydrodynamical battery mechanism suggested by Biermann is probably the most famous among those theories (Biermann 1950; Grasso & Rubinstein 2001). In contrast, post-recombination models usually assume a galactic origin like the outflow of fields from active and starburst galaxies and radio jets at high redshift. As in the primordial scenarios, an amplification of the seed fields by structure formation is required to arrive at the observed values of today (Rees 1989; Goldshmidt & Rephaeli 1993).

The evolution of intracluster magnetic fields can be studied with numerical magneto-hydrodynamic simulations. Dolag et al. (1999, 2002) performed simulations of the structure formation of galaxy clusters with the GADGET-2 code. Starting from seed field values of $\sim 10^{-9}$ G at redshift 15 in a $\Lambda$CDM cosmology, they found that the amplification by compression and shear flows during collapse and virialisation resulted in a roughly exponential growth of the mean magnetic field strength with decreasing redshift. At $z = 0$ the magnetic fields had grown by a factor of $\sim 10^3$, displaying profiles similar to that of the thermal gas distribution and thus confirming the existence of a close relation between both components. Last not least, the simulations revealed that violent merger events play a crucial role for the field amplification. In clusters undergoing one or two major mergers the magnetic field was significantly enhanced compared to clusters that formed in a rather smooth accretion process.

### 3.3.2 Cosmic rays

Cosmic Rays were discovered by Hess (1912) and Kohlhörster (1913) in the beginning of the twentieth century through their ionising effect on airtight vessels of glass enclosing two electrodes with a high voltage between them. Since the balloon-mounted detector was measuring an increasing ionising effect as it climbed to higher altitudes the particles were found to originate from outside earth. So the term Cosmic Rays was coined. Soon afterwards their charge was detected since the Earth's magnetic field acted differently on particles coming from different directions.

The relative abundance of elements in the cosmic ray population are to first approximation similar to those of the interstellar medium. Relativistic protons make up the largest part (∼90 %), followed by ionised helium (∼10 %). The rest are heavier elements including essentially all elements in the periodic table with a tendency towards larger atomic numbers at highest energies. Remarkably, the abundances of individual elements such as lithium and beryllium can be up to several orders of magnitude higher compared to
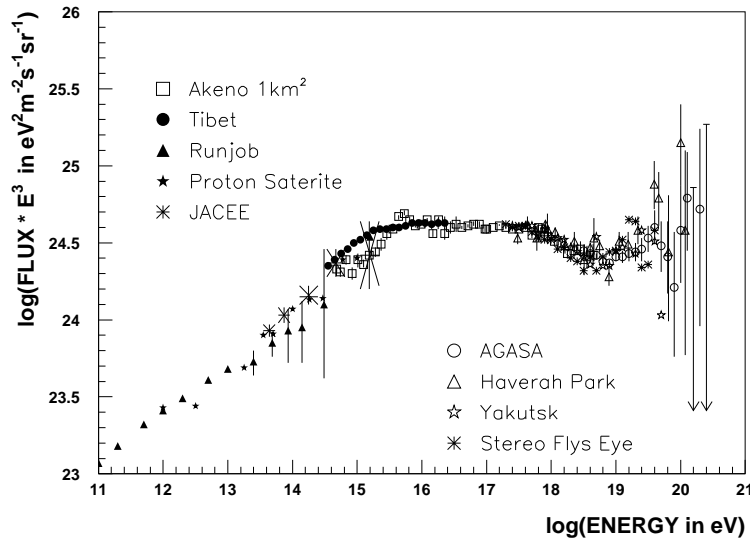
Figure 3.4: The cosmic ray all-particle spectrum observed by different experiments
(Nagano & Watson 2000). The differential flux was multiplied by $E^3$ to project
out the steeply falling character.

those found in the interstellar medium (Wiebel-Sooth et al. 1998). Only a very small fraction ($\sim 1$ %) of the cosmic ray population consists of lighter particles such as relativistic electrons and positrons.

Cosmic rays are observed over eleven decades of energy from $\sim 10^9$ eV to $\geq 10^{20}$ eV. Most experiments agree that the all-particle spectrum above $\sim 10^{10}$ eV is characterised by broken power-laws with a number of breaks while for lower energies the observed spectrum is flat as it is affected by solar modulation. The spectrum observed by different experiments above $10^{11}$ eV is shown in Figure 3.4. In the energy range between $10^{10}$ eV and $3 \cdot 10^{15}$ eV it can be fit by a power-law with slope $\sim 2.7$. The spectral index grows to $\sim 3.1$ at the "knee" around $\sim 10^{15}$ eV. The spectrum displays a second knee at $\sim 10^{17.5}$ eV where the slope changes from $\sim 3.0$ to 3.2. The upper bend is the so-called "ankle" at $\sim 10^{18.5}$ eV. The spectrum above the ankle is not well defined, but might approximately be described by a spectral index of $\sim 2.7$ (Gaisser & Stanev 2009; Bergman & Belz 2007).

At energies around $5 \cdot 10^{19}$ eV the interactions with the CMB should produce a strong cutoff in the observed spectrum, called the GZK-cutoff (Greisen 1966; Zatsepin & Kuz'min 1966). The fact that this cutoff could not be seen at any energy up to the limit of data at $\simeq 3 \cdot 10^{20}$ eV has been one of the most serious problems facing cosmic ray physics until today. Only recently, the detection of GZK-cutoff has been reported by the Pierre Auger Observatory (Yamamoto & for the Pierre Auger Collaboration 2007).

The power law characteristics of the cosmic energy spectrum together with its high

particle energies rule out any conceivable thermal emission process as a source of particle acceleration. It is for that reason that the cosmic ray population is usually referred to as the non-thermal component of the ICM. Possible sites of primary particle acceleration are point sources like supernova remnants, quasars or AGN, as well as large extended structures like clusters of galaxies undergoing gravitational collapse or merger shocks (Blandford & Ostriker 1978; Kang & Jones 2002). It is generally believed that in all of those sources energy injection is generated by first and second order Fermi processes inside the magnetised plasma. With the diffusive shock acceleration mechanism cosmic ray energies up to $E \approx 10^{20}$ eV can be produced in merger shocks.

Due to their high kinetic energies, cosmic rays are essentially unaffected by gravitational forces. The only confinement they experience is due to Lorentz force caused by the magnetic fields in the interstellar and intergalactic medium. At energies above $\sim 3 \cdot 10^{18}$ eV the gyroradii in typical galactic magnetic fields become larger than the size of the galaxy so that the highest energy particles can diffuse into the ICM.

The transport of cosmic rays in clusters of galaxies is dominated by a variety of loss mechanisms. Ionisation losses and spallation are mostly relevant for protons and heavier nuclei in the lower-energy tail of the cosmic ray energy distribution and typically lead to a cutoff at approximately $0.1$ GeV. Furthermore, spallation restricts the distance heavy nuclei can travel without being destroyed to only a few Mpc (Sigl 2006; Harari et al. 2006). Cosmic ray nuclei also interact with photons. Depending on the particle energy, the particle-photon collisions either result in (1) pair production, (2) photoproduction of hadrons (mostly pions), or (3) photodisintegration of the nucleus (for an overview see Mannheim & Schlickeiser 1994).

The most important process in the context of the present work are hadronic collisions between cosmic ray nuclei and the atoms and molecules of the thermal plasma. In this process neutral and charged pions are produced that further decay into gamma rays and "secondary" electrons respectively (Dennison 1980):

$$\begin{aligned} \pi^{\pm} &\rightarrow \mu^{\pm} + \nu_{\mu}/\bar{\nu}_{\mu} \rightarrow e^{\pm} + \nu_e/\bar{\nu}_e + \nu_{\mu} + \bar{\nu}_{\mu} \\ \pi^0 &\rightarrow 2\gamma \,. \end{aligned} \tag{3.28}$$

By the means of the above reaction a large population of secondary electrons can be produced, additionally to the original cosmic ray electron population which will in the following be labelled "primary".

Independent of their origin, due to their small rest masses, the cosmic ray electrons strongly suffer from radiative losses such as synchrotron and inverse compton emission. The associated lifetimes of relativistic electrons in the ICM are thus rather short, within a few $10^8$ years, which limits the distances cosmic ray electrons can travel to about $1$ Mpc. Figure 3.5 shows the lifetimes of cosmic ray electrons under typical cluster conditions calculated in an analytical model by Sarazin (1999). The combined timescale due to the losses by IC scattering, synchrotron emission, Coulomb losses, and Bremsstrahlung reaches a maximum of $\sim 3 \cdot 10^9$ yr for electrons with Lorentz factors $\gamma \sim 300$. This maximum loss time scale is comparable to the Hubble time or the typical age of clusters. For relativistic electrons with either much higher or lower energies, the loss time scale is considerably shorter than the typical age of a cluster.
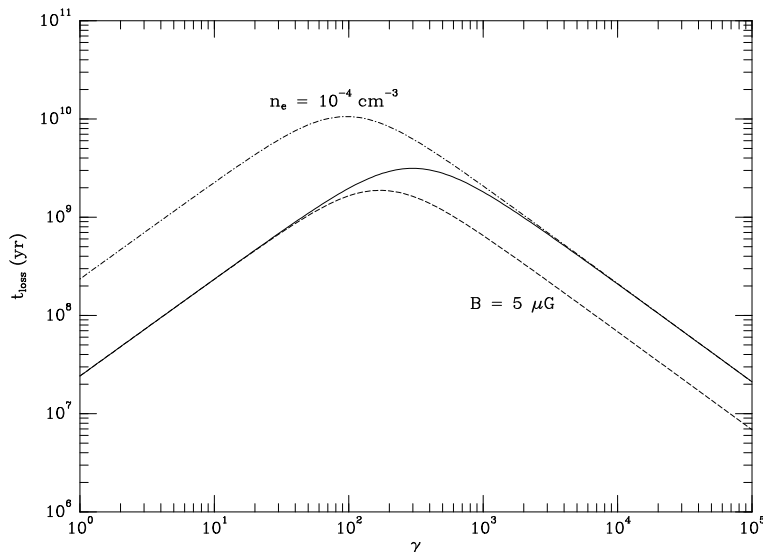
Figure 3.5:  The lifetimes of relativistic electrons as a function of $\gamma$ in a cluster with an electron density $n_e = 10^{-3}\,\mathrm{cm}^{-3}$ and a magnetic field of $B = 1\,\mu\mathrm{G}$ (solid curve), for a magnetic field of $B = 5\,\mu\mathrm{G}$ (dashed curve), and for an electron density of $n_e = 10^{-4}\,\mathrm{cm}^{-3}$ (dot-dashed curve). Figure from Sarazin (1999).

### 3.3.3 Radiation

X-ray emission due to thermal bremsstrahlung is a common property of galaxy clusters. Through its X-ray emission, the ICM yields the highest-quality observational data concerning a cluster's dynamical state. In contrast, radio synchrotron emission from the ICM is only observed in those clusters currently experiencing the largest departures from a virialised state. By studying the X-ray and radio properties of galaxy clusters we can gain important insight into the evolution and distribution of the large-scale structure in our Universe.

#### Bremsstrahlung emission

When a charge is accelerated or decelerated it emits radiation, and bremsstrahlung or free-free emission is the radiation emitted in electromagnetic encounters between the charge and a nucleus of the ambient plasma. The most common situation in which a continuum of radiation is emitted is in the collision of an electron with an atom. In the instantaneous rest frame of the accelerated electron, the total power emitted into all angles is described by Larmor's formula

$$\frac{\mathrm{d}E}{\mathrm{d}t} = \frac{2e^2|\dot{\vec{v}}|}{3c^3}\,, \tag{3.29}$$

where $\dot{\vec{v}}$ is the proper acceleration of the electron. To obtain the spectral distribution of the radiation we make use of Parseval's theorem which tells us that the acceleration $\dot{\vec{v}}(t)$

and its Fourier decomposition $\dot{\vec{v}}(\omega)$ are related by

$$\int_{-\infty}^{\infty} |\dot{\vec{v}}(t)|^2 \mathrm{d}t = \frac{1}{2\pi} \int_{-\infty}^{\infty} |\dot{\vec{v}}(\omega)|^2 \mathrm{d}\omega \, . \tag{3.30}$$

Thus, the total energy radiated in a single collision between an electron and a nucleus is given by

$$\int_{\infty}^{\infty} \frac{\mathrm{d}E}{\mathrm{d}t} \mathrm{d}t = \frac{2e^2}{6\pi c^3} \int_{-\infty}^{\infty} |\dot{\vec{v}}(t)|^2 \mathrm{d}t = \frac{2e^2}{6\pi c^3} \int_{-\infty}^{\infty} |\dot{\vec{v}}(\omega)|^2 \mathrm{d}\omega$$

$$= \frac{4e^2}{3\pi c^3} \int_0^{\infty} |\dot{\vec{v}}(\omega)|^2 \mathrm{d}\omega \, , \tag{3.31}$$

By differentiation we obtain the total energy per unit frequency emitted throughout the duration of the encounter,

$$\frac{\mathrm{d}E}{\mathrm{d}\omega} = \frac{2e^2}{3c^3} |\dot{\vec{v}}(\omega)|^2 \, . \tag{3.32}$$

With these definitions we can now derive the energy radiated by an electron that moves past an ion of charge $Ze$ with impact parameter $b$. Assuming that the electron moves rapidly enough, we can neglect the deviation of its path from a straight line. With Larmor's formula we already have an expression for the acceleration of the electron in the electrostatic field of the ion. From (3.32) we know the frequency distribution of the radiation emitted in the encounter.

To obtain the total spectrum for a medium with ion density $n_i$ and electron density $n_e$ and for a fixed electron speed $v$ we need to integrate over all collision parameters $b$:

$$\frac{\mathrm{d}E}{\mathrm{d}\omega \mathrm{d}V \mathrm{d}t} = n_e n_i 2\pi v \int_{b_{\min}}^{\infty} \frac{\mathrm{d}E(b)}{\mathrm{d}\omega} b \, \mathrm{d}b \, , \tag{3.33}$$

where $b_{\min}$ is the lower limit for the impact parameter. To a very good approximation $\mathrm{d}E(b)/\mathrm{d}\omega$ can be replaced by its asymptotic expression for low frequencies:

$$\frac{\mathrm{d}E(b)}{\mathrm{d}\omega} = \frac{8Z^2 e^6}{3\pi c^3 m^2 v^2 b^2} \, , \quad b \ll v/\omega \, . \tag{3.34}$$

Integration of equation (3.33) then yields

$$\frac{\mathrm{d}E}{\mathrm{d}\omega \mathrm{d}V \mathrm{d}t} = \frac{16e^2}{3c^3 m^2 v} n_e n_i Z^2 \int_{b_{\min}}^{b_{\max}} \frac{\mathrm{d}b}{b} = \frac{16e^2}{3c^3 m^2 v} n_e n_i Z^2 \ln \left( \frac{b_{\max}}{b_{\min}} \right) \, . \tag{3.35}$$

The value for $b_{\min}$ is derived from quantum physics. The maximum velocity acquired by the electron is $\Delta v \approx 2v$ and hence $\Delta p = 2m_e v$. According to the Heisenberg uncertainty principle, the uncertainty in the position is then given by $\Delta x \approx \hbar$ and thus

$$b_{\min} = \frac{\hbar}{2m_e v} \, . \tag{3.36}$$

The upper limit to the impact parameter, $b_{\max}$ will occur when the duration of the collision is of the same order as the period of the electron in the orbit. Thus we only integrate out
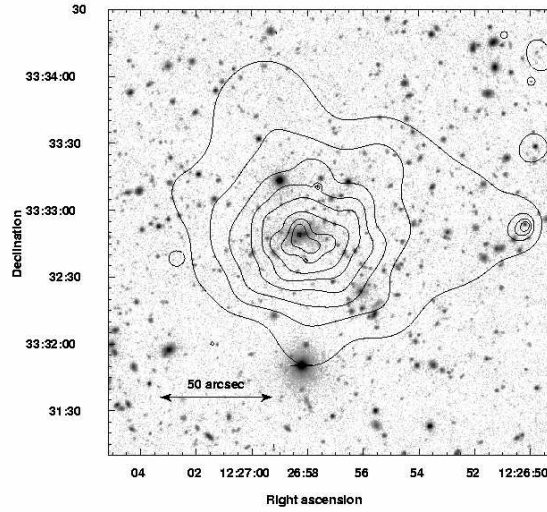
Figure 3.6: RXJ1226.9+3332, a relaxed massive cluster at $z = 0.89$. The contours of X-
ray emission detected by XXM-Newton 0.3 - 8 keV is overlaid on a Subaru
I-band image. Figure from Maughan et al. (2004).

to those values of $b$ for which $\omega b/v = 1$ (see e.g. Longair 1981). The result is conveniently
stated in terms of the Gaunt factor $g_{\mathrm{ff}}(v, \omega)$ such that

$$\frac{\mathrm{d}E}{\mathrm{d}\omega \mathrm{d}V \mathrm{d}t} = \frac{16\pi e^2}{3\sqrt{3}c^3 m^2 v} n_{\mathrm{e}} n_{\mathrm{i}} Z^2 g_{\mathrm{ff}}(v, \omega). \tag{3.37}$$

The Gaunt factor is a function of the electron energy and the frequency of the emission.
Tables and graphs of it can be found in the literature (Karzas & Latter 1961; Bressaard
& van de Hulst 1962).

In order to work out the bremsstrahlung from a gas at temperature $T$, expression (3.37)
must be integrated over a Maxwellian distribution of electron velocities:

$$P(v)\mathrm{d}v = Av^2 \exp\left(-\frac{mv^2}{2k_{\mathrm{B}}T}\right)\mathrm{d}v. \tag{3.38}$$

Performing the integral and using $\mathrm{d}\omega = 2\pi \mathrm{d}\nu$ we arrive at (Rybicki & Lightman 1979)

$$\frac{\mathrm{d}E}{\mathrm{d}\nu \mathrm{d}V \mathrm{d}t} = \frac{2^5 \pi e^6 Z^2}{3mc^2} \sqrt{\frac{2\pi}{3k_{\mathrm{B}}m}}\, T^{-1/2}\, n_{\mathrm{e}}\, n_{\mathrm{i}}\, e^{-h\nu/kT} \bar{g}_{\mathrm{ff}}(T, \nu), \tag{3.39}$$

where $\bar{g}_{\mathrm{ff}}(T, \nu)$ is a velocity averaged Gaunt factor. Most clusters have temperatures be-
tween $2 \cdot 10^7$ K and $10^8$ K and therefore emit in the X-ray regime. From X-ray observations,
one can thus infer the density and temperature of a galaxy cluster.

Figures 3.6 and 3.7 show the X-ray morphologies of the bremsstrahlung emission of
the two galaxy clusters RXJ1226.9+3332 and RX J0152.7-1357. The first object is a
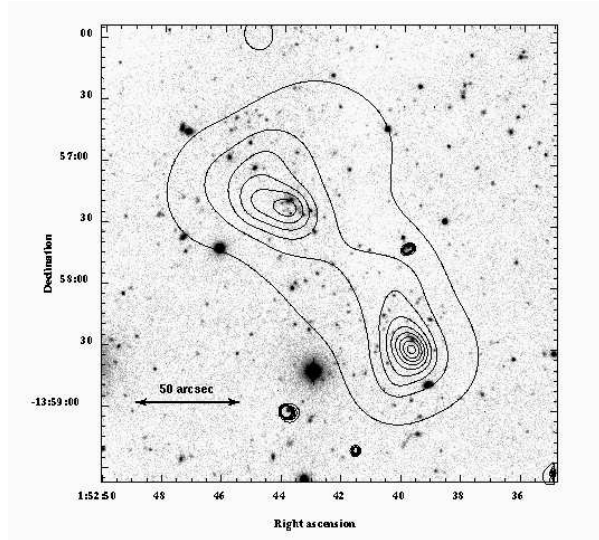
Figure 3.7: The merging cluster RX J0152.7-1357 at $z = 0.83$. The Chandra X-ray contours are overlaid on a Keck II I-band image. Figure from Maughan et al. (2003)

massive relaxed cluster while the second object is a galaxy cluster in an early stadium of a major merger event. A comparison of the two pictures demonstrates how clearly the ICM distribution of a dynamically active cluster differs from that of a virialised one.

**Synchrotron emission**

Synchrotron radiation is generated when relativistic electrons spiral through magnetic fields. The particles are forced on helical orbits around the magnetic field lines by the Lorentz force. Since the force on a particle is perpendicular to the motion, the magnetic field cannot do work on the particle, and so its speed does not change, i.e. $|\vec{v}| = \text{constant}$. The relativistic form of the equation of motion of the particle in the magnetic field can thus be written

$$\gamma m \frac{\mathrm{d}\vec{v}}{\mathrm{d}t} = \frac{q}{c}\vec{v} \times \vec{B} \,, \tag{3.40}$$

where $q$ is the charge of the particle and $\vec{B}$ is the magnetic field vector. Separating components along and normal to $\vec{B}$ we have

$$\frac{\vec{v}_\parallel}{\mathrm{d}t} = 0 \,, \quad \frac{\mathrm{d}\vec{v}_\perp}{\mathrm{d}t} = \frac{q}{m\gamma c}\vec{v}_\perp \times \vec{B} \,. \tag{3.41}$$

The frequency of the resulting helical motion is given by

$$\nu_{\mathrm{g}} = \frac{qB}{2\pi\gamma mc} \,. \tag{3.42}$$

The total emitted power $P$ for the relativistic particle follows from considering the power produced in the frame of the particle (for which Larmor's formula applies) and then transforming to the laboratory frame using the Lorentz transformations (Rybicki & Lightman 1979):

$$P = \frac{2q^2}{3c^3}\gamma^4 \frac{q^2 B^2}{\gamma^2 m^2 c^2} v_\perp^2 \,. \tag{3.43}$$

For an isotropic distribution of velocity vectors we furthermore need to average $v_\perp$ over all pitch angles $\theta$, which are the angles between the magnetic field and the velocity vector,

$$\langle v_\perp^2 \rangle = \frac{v^2}{4\pi}\int_0^\pi (\sin\theta)^2 \mathrm{d}\Omega = \frac{v^2}{2}\int_0^\pi (\sin\theta)^3 \mathrm{d}\theta = \frac{2}{3}v^2 \,. \tag{3.44}$$

The total power emitted at all frequencies may then be written as

$$P = \frac{dE}{dt} = \frac{1}{6\pi}\sigma_T c\gamma^2\beta^2 B \,, \tag{3.45}$$

where we have introduced the Thomson cross section $\sigma_{\mathrm{T}} = 8\pi r_0^2/3$ and the classical electron radius $r_0 \equiv e^2/mc^2$.

   In clusters of galaxies the synchrotron radiation from cosmic ray electrons is the dominant source of non-thermal emission. The spectrum of the IC synchrotron radiation is obtained by integrating over the distribution of cosmic ray electrons, which is approximated by a power-law over a limited range of energies:

$$n(E)dE = CE^{-\alpha}dE, \qquad E_1 < E < E_2 \,, \tag{3.46}$$

where $C$ is a normalisation constant that can vary with the electron pitch angle and the like. The emissivity of an ultra-relativistic electron with energy $E \gg m_{\mathrm{e}}c^2$ and pitch angle $\theta$ in the frequency range $[\nu, \nu + \mathrm{d}\nu]$ is given by (Longair 1981)

$$P(\nu, E, \theta)\mathrm{d}\nu = \frac{\sqrt{3}e^3 B\sin\theta}{mc^2}\frac{\nu\mathrm{d}\nu}{\nu_{\mathrm{c}}}\int_{\nu/\nu_{\mathrm{c}}}^\infty K_{5/3}(\eta)\mathrm{d}\eta \,, \tag{3.47}$$

where $K_{5/3}$ is the Bessel function of order 5/3. Here, $\nu_{\mathrm{c}}$ denotes the critical frequency at which the resulting energy spectrum has a maximum:

$$\nu_{\mathrm{c}} = \frac{3\gamma^2 eB\sin\theta}{4\pi m_{\mathrm{e}}c} \,. \tag{3.48}$$

Integrating the cosmic ray distribution (3.46) times the single electron radiation formula (3.47) over the energy range $(E_1, E_2)$, and using the substitution $E = x^{-1/2}\sqrt{\frac{4\pi m^3 c^5 \nu}{3eB\sin\theta}}$ with $x = \nu/\nu_{\mathrm{c}}$ leads to

$$P_{\mathrm{sync}}(\nu, \theta) = \int_{E_1}^{E_2} P(E, \nu)n(E)dE =$$

$$\frac{\sqrt{3}e^3}{2mc^2}\left(\frac{3e}{4\pi m^3 c^5}\right)^{(\alpha-1)/2} C\,(B\sin\theta)^{(\alpha+1)/2}\nu^{(1-\alpha)/2}G\left(\frac{\nu}{\nu_1}, \frac{\nu}{\nu_2}, \alpha\right) \,. \tag{3.49}$$

In the above expression, $G$ replaces the integral

$$G\left(x_1, x_2, p\right) = \int_{x_2}^{x_1} x^{p-3/2}\, x \int_x^\infty K_{5/3}(x)\mathrm{d}x\,.$$ (3.50)

For a very wide range of frequencies with $\nu_1 \to 0$ and $\nu_2 \to \infty$ we can approximate (3.50) by

$$G\left(\infty, 0, \alpha\right) = \frac{2^{(\alpha-3)/2}}{3}\left(\frac{3\alpha + 7}{\alpha + 1}\right)\Gamma\left(\frac{3\alpha - 1}{12}\right)\Gamma\left(\frac{3\alpha + 7}{12}\right)\,.$$ (3.51)

For an isotropic distribution of particles and orientations of magnetic fields, the averaged emitted power into all spatial directions is obtained by integration, using the isotropic distribution function of the pitch angle:

$$\frac{1}{4\pi}\int_0^\pi (\sin\theta)^k \mathrm{d}\Omega = \frac{1}{2}\int_0^\pi (\sin\theta)^{k+1}\mathrm{d}\theta = \frac{\sqrt{\pi}}{2}\Gamma\left(\frac{k + 2}{2}\right)\Gamma\left(\frac{k + 3}{2}\right)^{-1}\,.$$ (3.52)

With these last two results (3.51) and (3.52) we finally obtain

$$P_{\mathrm{sync}}(\nu) = \frac{\sqrt{3\pi}}{32\pi}\frac{e^3}{m_\mathrm{e}c^2}\left(\frac{3\,e}{2\pi\, m_\mathrm{e}^3\, c^5\, \nu}\right)^{\alpha_\nu}\times$$
$$C\,B^{(\alpha_\nu+1)}\nu^{-\alpha_\nu}\frac{\alpha_\mathrm{e} + \frac{7}{3}}{\alpha_\mathrm{e} + 1}\frac{\Gamma\left(\frac{3\alpha_\mathrm{e}-1}{12}\right)\Gamma\left(\frac{3\alpha_\mathrm{e}+7}{12}\right)\Gamma\left(\frac{\alpha_\mathrm{e}+5}{4}\right)}{\Gamma\left(\frac{\alpha_\mathrm{e}+7}{4}\right)}\,,$$ (3.53)

where the spectral index of the synchrotron spectrum is defined by $\alpha_\nu = (\alpha - 1)/2$. Thus we find that a power-law distribution of relativistic electrons produces a power-law synchrotron spectrum.

Cosmic ray electrons in the ICM of galaxy clusters typically emit in the radio frequency range. Since particle acceleration is significantly enhanced during a merger event, the presence of extended radio sources and halos is a strong indicator for ongoing dynamical activity. Furthermore, large scale radio halos represent a direct probe of the strength and morphology of the intracluster magnetic field. In Figures 3.8 and 3.9 we show observations of two different galaxy clusters in radio and X-ray. The radio contours of the first cluster, Abell 2163, have a rather regular shape while the morphology of the bremsstrahlung emission indicates the infall of a large sub-clump from outside the virial radius. The second example is the cluster Abell 2256. Radio and X-ray emission suggest a major merger in its final stage. Two sub-clumps of nearly equal size close to the centre of the cluster can be seen in the X-ray detection. At the same time, the steep radio profile in the north west clearly reflects the orientation of the shock front and thus reveals the infall geometry.

### 3.3.4 Gravitational lensing

The term gravitational lensing denotes the deflection and time delay of light by a Newtonian gravitational field due to the distortion of the locally flat Minkowski space-time. The
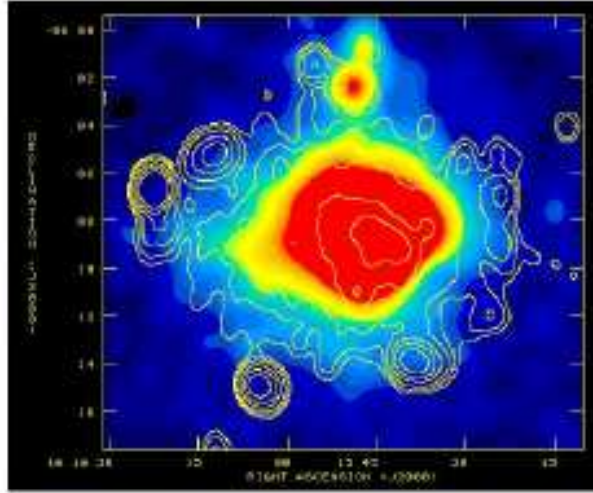
Figure 3.8: The cluster A2163 ($z = 0.2$) in radio and X-ray. The contours represent radio emission at $20\,\mathrm{cm}$, showing an extended radio halo. The colour-scaled image represents the ROSAT X-ray emission. The extended irregular X-ray structure indicates the presence of a recent cluster merger. Figure from Feretti et al. (2004).

null-geodesics of photons that move past a spherical distribution of mass $M$ in the weak field limit ($\Phi \ll c^2$) are described by the line element

$$\mathrm{d}s^2 = \left(1 + \frac{2\Phi}{c^2}\right) c^2 \mathrm{d}t^2 - \left(1 - \frac{2\Phi}{c^2}\right) \mathrm{d}l^2 = 0\,, \tag{3.54}$$

where $\Phi = GM/r$ denotes the gravitational potential and $r$ is the distance of closest approach between the photon and the deflecting object. Since the corrections of order $GM/rc^2$ are small we can, after separating terms in (3.54) and taking the square root, expand both brackets in a power series such that

$$\left(1 + \frac{\Phi}{c^2}\right) c\mathrm{d}t = \left(1 - \frac{\Phi}{c^2}\right) \mathrm{d}l\,. \tag{3.55}$$

The light refraction can now be expressed in terms of an effective speed of light $c'$ which is defined by

$$c' = \frac{\mathrm{d}l}{\mathrm{d}t} = c\left(1 + \frac{\Phi}{c^2}\right) =: \frac{c}{n}\,, \tag{3.56}$$

where

$$n := \left(1 - \frac{\Phi}{c^2}\right) \geq 1 \tag{3.57}$$

is the effective index of refraction defined in analogy to the concepts of geometrical optics. The mass thus acts like a convex lens that deflects the light of a background source
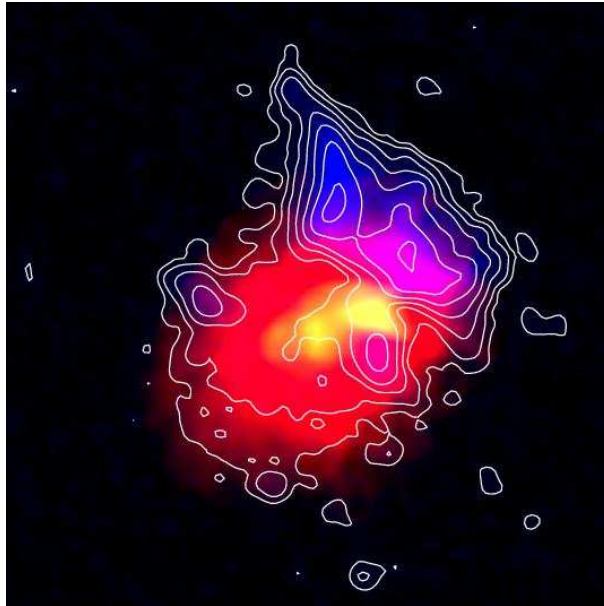
Figure 3.9: Three colour image of the radio and X-ray emission in A2256 ($z = 0.0594$). Contours and blue emission show the 1369 MHz synchrotron emission, while the Chandra X-ray image shown in red and yellow reveals the extended diffuse thermal emission. The two X-ray peaks near the cluster centre indicate a major merger event which is thought to be responsible for creating the diffuse radio emission. Figure from Clarke & Ensslin (2006).

towards its centre. The lensing effect becomes stronger with increasing mass $M$ of the lensing object and with decreasing distances $r$ from its centre.

We can derive the deflection angle using Fermat's principle which states that the integral over the path of a light ray between two fixed points becomes extremal,

$$\delta \int n(\vec{x}) \, \mathrm{d}\vec{x} = 0 \,. \tag{3.58}$$

From the corresponding Euler-Lagrange equations we obtain the change of the tangent vector $\vec{e}$ along the light ray

$$\frac{\mathrm{d}\vec{e}}{\mathrm{d}l} = -\frac{2}{c^2}\vec{\nabla}_\perp\Phi \,, \tag{3.59}$$

where the gradient is taken perpendicular to the light path. Suppose that the deflection produced by the lens is small, the total deflection of the light ray is then given by the angle

$$\hat{\vec{\alpha}} = -\int \vec{\nabla}_\perp n \mathrm{d}l = \frac{2}{c^2}\int \vec{\nabla}_\perp\Phi \mathrm{d}l \,, \tag{3.60}$$

where the integral is taken along the photon trajectory. Nevertheless, since $\hat{\vec{\alpha}}$ is small, the integration can be carried out along an unperturbed, straight light ray.

Furthermore, we can assume that the lens is infinitely thin compared to the distances between the source and the lens and between the lens and the observer. The gravitational lens can thus be considered to be a mass sheet lying in a plane orthogonal to the line of sight that is called the lens plane. Projection of the lensing object along the line of sight yields the surface mass density

$$\Sigma(\vec{\xi}) = \int \rho(\vec{\xi}, z) \, \mathrm{d}z \,, \tag{3.61}$$

in which the integral is taken over the photon path as before. The deflection angle at a certain position $\vec{\xi}$ is then found by summing up the deflection angles of all infinitesimal mass elements in the lens plane:

$$\hat{\vec{\alpha}}(\vec{\xi}) = \frac{4G}{c^2}\int \frac{(\vec{\xi} - \vec{\xi}\,')\Sigma(\vec{\xi}\,')}{|\vec{\xi} - \vec{\xi}\,'|}\mathrm{d}\vec{\xi}\,' \,. \tag{3.62}$$

For the simple case of a spherically symmetric lens the mass projection yields a circular symmetric mass distribution and the deflection angle is given by

$$\hat{\alpha}(\xi) = \frac{4GM(\xi)}{c^2\xi} \,, \quad \text{where} \quad M(\xi) = 2\pi\int_0^\xi \Sigma(\xi\,')\xi\,'\mathrm{d}\xi\,' \,. \tag{3.63}$$

The angle $\hat{\alpha}$ thus points towards the centre of symmetry.

The great virtue of gravitational lensing comes from the fact that, in analogy to geometrical optics, the angular diameters and angular-diameter distances of the lens and the source are related by the simple laws of geometry. The optical axis of the system is defined by the line of sight of the observer through the centre of the lens as sketched in Figure
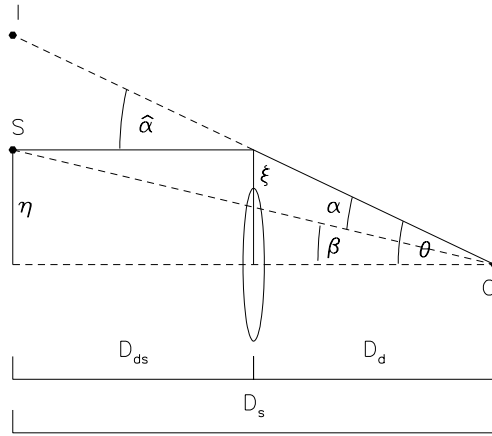
Figure 3.10: The geometry of gravitational lensing. The source S is lensed by a massive object at distance $D_{\mathrm{ds}}$ and produces an image I which is seen by the observer O under the angle $\alpha$ (from Narayan & Bartelmann 1996).

3.10.  Using the angular diameter distance between the lens and the source, $D_{\mathrm{ds}}$, and between the lens and the observer, $D_{\mathrm{s}}$, we can infer the reduced deflection angle which is the angular distance on the sky between a source and its image:

$$\vec{\alpha} = \frac{D_{\mathrm{ds}}}{D_{\mathrm{s}}} \, \hat{\vec{\alpha}} \,. \tag{3.64}$$

From the diagram we also see that

$$\vec{\theta} D_{\mathrm{s}} = \vec{\beta} D_{\mathrm{s}} - \hat{\vec{\alpha}} D_{\mathrm{ds}} \,, \tag{3.65}$$

where $\vec{\beta}$ and $\vec{\theta}$ are the angular positions of the source and the image relative to the optical axis. Therefore, the positions of the source and the image are related through the simple lens equation

$$\vec{\beta} = \vec{\theta} - \vec{\alpha}(\vec{\theta}) \,. \tag{3.66}$$

A characteristic quantity of gravitational lensing is the critical surface mass density $\Sigma_{\mathrm{cr}}$. Integrating over a constant surface mass density in equation (3.63) we obtain the reduced deflection angle

$$\vec{\alpha}(\vec{\theta}) = \frac{D_{\mathrm{ds}}}{D_{\mathrm{s}}} \frac{4G}{c^2 \xi} \left( \Sigma \pi \xi^2 \right) = \frac{4\pi G \, \Sigma}{c^2} \frac{D_{\mathrm{d}} D_{\mathrm{ds}}}{D_{\mathrm{s}}} \, \vec{\theta} \,, \tag{3.67}$$

where we have set $\xi = D_{\mathrm{d}} \vec{\theta}$. The critical surface mass density $\Sigma_{\mathrm{cr}}$ is now defined such that $\vec{\alpha}(\vec{\theta}) = \vec{\theta}$ and $\vec{\beta} = 0$ for any $\vec{\theta}$:

$$\Sigma_{\mathrm{cr}} = \frac{c^2}{4\pi G} \frac{D_{\mathrm{s}}}{D_{\mathrm{d}} D_{\mathrm{ds}}} \,. \tag{3.68}$$

This property corresponds to a perfect lens which brings all light rays to focus at a well-defined focal length. Real gravitational lenses are related to the ideal lens via the convergence $\kappa := \Sigma/\Sigma_{\mathrm{cr}}$. Due to the rotational symmetry of the perfect lens system, a source which lies exactly on the optical axis ($\vec{\beta} = 0$) is imaged as a ring if the lens is supercritical. The corresponding ring radius is named Einstein radius $\theta_{\mathrm{E}}$.

It is useful to define the effective lensing potential $\psi(\vec{\theta})$ which is a weighed projection of the Newtonian potential,

$$\psi(\vec{\theta}) = \frac{D_{\mathrm{ds}}}{D_{\mathrm{d}} D_{\mathrm{s}}} \frac{2}{c^2} \int \Phi(D_{\mathrm{d}}\vec{\theta}, z)\, dz\,. \tag{3.69}$$

The reduced deflection angle can then be written as

$$\vec{\nabla}_{\theta}\psi = D_{\mathrm{d}} \vec{\nabla}_{\xi}\psi = \frac{2}{c^2} \frac{D_{\mathrm{ds}}}{D_{\mathrm{s}}} \int \vec{\nabla}_{\perp}\Phi\, dz = \vec{\alpha}\,. \tag{3.70}$$

Using Poisson's equation for the three-dimensional gravitational potential and inserting definition (3.68), we find that the Laplacian is just twice the convergence in the two-dimensional Poisson equation

$$\nabla_{\theta}^2 \psi = \frac{2}{c^2} \frac{D_{\mathrm{d}} D_{\mathrm{ds}}}{D_{\mathrm{s}}} \int \nabla_{\xi}^2 \Phi\, dz = \frac{2}{c^2} \frac{D_{\mathrm{d}} D_{\mathrm{ds}}}{D_{\mathrm{s}}} \cdot 4\pi G\, \Sigma = 2 \frac{\Sigma(\vec{\theta})}{\Sigma_{\mathrm{cr}}} \equiv 2\kappa(\vec{\theta})\,. \tag{3.71}$$

Real gravitational lenses such as galaxy clusters in general do not only shift the apparent position of a background source but also magnify its apparent luminosity. Moreover, since galaxy clusters usually have a non-spherical shape and may show significant substructure, the image can be strongly distorted. The local properties of the mapping of the source plane onto the image plane are best specified by the Jacobian matrix

$$\mathcal{A} \equiv \frac{\partial\vec{\beta}}{\partial\vec{\theta}} = \left( \delta_{ij} - \frac{\partial^2\psi(\vec{\theta})}{\partial\theta_i \partial\theta_j} \right)\,. \tag{3.72}$$

With equation (3.71) we find that

$$\kappa = \frac{1}{2} \left( \frac{\partial^2\psi}{\partial\theta_1 \partial\theta_1} + \frac{\partial^2\psi}{\partial\theta_2 \partial\theta_2} \right)\,. \tag{3.73}$$

Another important quantity is the shear tensor $\gamma(\vec{\theta})$. Its two components are given by

$$\gamma_1(\vec{\theta}) = \frac{1}{2} \left( \frac{\partial^2\psi}{\partial\theta_1 \partial\theta_1} - \frac{\partial^2\psi}{\partial\theta_2 \partial\theta_2} \right) \equiv \gamma(\vec{\theta}) \cos\left[ 2\phi(\vec{\theta}) \right]\,, \tag{3.74}$$

$$\gamma_2(\vec{\theta}) = \frac{\partial^2\psi}{\partial\theta_1 \partial\theta_2} = \frac{\partial^2\psi}{\partial\theta_2 \partial\theta_1} \equiv \gamma(\vec{\theta}) \sin\left[ 2\phi(\vec{\theta}) \right]\,. \tag{3.75}$$

Inserting these definitions, the transformation matrix $\mathcal{A}$ can be written

$$\mathcal{A} = \begin{pmatrix} 1 - \kappa - \gamma_1 & -\gamma_2 \\ -\gamma_2 & 1 - \kappa + \gamma_1 \end{pmatrix} \tag{3.76}$$

$$= (1 - \kappa) \begin{pmatrix} 1 & 0 \\ 0 & 1 \end{pmatrix} - \gamma \begin{pmatrix} \cos 2\phi & \sin 2\phi \\ \sin 2\phi & -\cos 2\phi \end{pmatrix}\,. \tag{3.77}$$

The meanings of the different terms are now clear from the above decomposition. Convergence alone causes isotropic focussing of light rays, thereby leading to isotropic magnification of a source. The shear terms introduce anisotropic distortions of the image. As an example, a circular source of unit radius will be distorted to an elliptical image with major and minor axes $(1 - \kappa - \gamma)^{-1}$ and $(1 - \kappa + \gamma)^{-1}$, respectively. The magnification is now given by

$$\mu = \frac{1}{\det \mathcal{A}} = \frac{1}{[(1 - \kappa)^2 - \gamma^2]} \,. \tag{3.78}$$

So-called critical lines form at locations where $1 - \kappa \pm |\gamma| = 0$ and the mapping between the source and image plane becomes singular. The corresponding curves in the source plane are called caustics. Near the caustics the shape of the images gets strongly distorted, producing near-circular giant arcs which can be very bright.

One distinguishes between the weak and strong lensing regime, depending on whether the shape of high redshifted objects is only slightly deformed or whether the sources are strongly distorted and amplified. In the latter case multiple images can be produced.

In observational cosmology, strong lensing is used to probe the mass distribution in the central parts of galaxy clusters while weak lensing distortions of background galaxies are used to trace the mass distributions in the cluster periphery. Since the images produced by cluster lensing are usually highly complex, considerable modelling is needed to infer the underlying mass distribution.

# Numerical Methods

<div style="text-align: right; font-size: 3em;">4</div>

The numerical simulations of the formation of galaxy clusters were carried out with the GADGET-2 code, a massively parallel cosmological code designed by Volker Springel (Springel 2005). The code is capable of following a collisionless fluid with the N-body method, calculating the gravitational forces through the combination of a TreePM algorithm and Fourier techniques. In the extended code version also gas physics is integrated.

In what follows we will present the numerical method that is used in the code for describing the behaviour of a baryonic gas. We first introduce the concepts of smoothed particle hydrodynamics that appears to be the method of choice for most astrophysical applications. In the subsequent section we will demonstrate how the numerical description is extended to yield smooth particle magnetohydrodynamics. Finally, a simplified model for the description of cosmic ray physics is presented that self-consistently accounts for the dynamical effects of the relativistic particles during structure formation.

## 4.1 Smoothed particle hydrodynamics

Smoothed particle hydrodynamics (SPH) was first implemented by Gingold & Monaghan (1977) and Lucy (1977) as a new numerical technique for describing stellar gas dynamics. In contrast to the conventional grid-based methods that split the computational domain into a mesh of grid cells over which the physical variables need to be averaged (particle-mesh, PM) or interpolated (finite difference/volume methods, (Godunov 1959; Colella & Woodward 1984)), SPH is designed to trace the motions of individual fluid elements. The fluid continuum is approximated by so-called SPH-particles of preassigned masses for which the equations of motion are solved, provided the conservation of energy, momentum, and angular momentum. Consequently, the force that acts on a single particle is the sum of the forces exerted by all other particles.

Due to its Lagrangian nature, in situations where a high resolution inside a large-scale system is required, SPH offers numerical advantages over the grid-based representations. While in the Eulerian grid approach small, but dynamically important regions must be treated by a subgrid model, the resolution in a SPH representation is naturally increased due to the intrinsically higher number of particles in high-density regions. In astrophysics and cosmology one often deals with systems that exhibit important features over several orders of magnitude (e.g. turbulent motion inside galaxy clusters) or objects that change

their sizes on short timescales (e.g. gravitational collapse of gas clouds). SPH is particularly suited to follow the gravitational growth of structure and to automatically increase the resolution in the central regions of galaxy clusters, which are the regions of primary interest for the study of non-thermal radio and X-ray emission.

An important disadvantage of the SPH discretisation is that the fluid quantities can only vary on the smallest length scale, namely the radius of a SPH particle, and discontinuities such as shock fronts are therefore not resolved. To cure this problem, an artificial viscosity is introduced which spreads out the discontinuity such that it can be resolved and furthermore supplies the required entropy injection in non-isentropic shocks.

### 4.1.1  Basic concepts

The concepts of SPH are derived from the simple identity

$$A(\vec{r}) = \int_{\mathbb{R}^3} A(\vec{r}\,')\delta(|\vec{r} - \vec{r}\,'|)\mathrm{d}\vec{r}\,' \,, \tag{4.1}$$

where $A$ is any variable defined on the spatial coordinates $\vec{r}$ and $\delta$ is the Dirac delta distribution. We introduce a smoothing kernel $W$ that has the properties

$$\lim_{h \to 0} W(|\vec{r} - \vec{r}\,'|, h) = \delta(|\vec{r} - \vec{r}\,'|) \quad \text{and} \quad \int_{\mathbb{R}^3} W(|\vec{r} - \vec{r}\,'|, h)\mathrm{d}\vec{r}\,' = 1 \,. \tag{4.2}$$

For $h > 0$ the integral is thus approximated by

$$A(\vec{r}) \approx \int_{\mathbb{R}^3} A(\vec{r}\,')W(|\vec{r} - \vec{r}\,'|, h)\mathrm{d}\vec{r}\,' \,. \tag{4.3}$$

To switch from the continuum description to the discretised picture, the integral is replaced by a summation over all SPH-particles

$$A_{\mathrm{S}}(\vec{r_i}) = \sum_{j=1}^{N} m_j \frac{A_j}{\rho_j} W(|\vec{r_i} - \vec{r_j}|, h_j) \,, \tag{4.4}$$

where the volume element $d\vec{r}\,'$ has been replaced by the volume $V_j = m_j/\rho_j$ of the $j$th particle and the quantity $A_{\mathrm{S}}(\vec{r_i})$ is now defined at the location of the $i$th particle. The length $h_j$ in the argument of the kernel function is identified with the particle radius. The essential point about (4.4) is that, by using a differentiable kernel, the derivative of the hydrodynamic variable $A_{\mathrm{S}}$ reduces to the analytic differentiation of the kernel:

$$\nabla A_{\mathrm{S}}(\vec{r_i}) = \sum_{j=1}^{N} m_j \frac{A_j}{\rho_j} \nabla W(|\vec{r_i} - \vec{r_j}|, h_j) \,. \tag{4.5}$$

In GADGET-2, instead of the Gaussian kernel that was originally proposed by Gingold & Monaghan (1977), a spline kernel of the form (see Monaghan & Lattanzio (1985))

$$W(r, h) = \frac{8}{\pi h^3} \begin{cases} 1 - 6\left(\frac{r}{h}\right)^2 + 6\left(\frac{r}{h}\right)^3 \,, & 0 \leq \frac{r}{h} \leq \frac{1}{2} \\ 2\left(1 - \frac{r}{h}\right)^3 \,, & \frac{1}{2} < \frac{r}{h} \leq 1 \\ 0 \,, & \frac{r}{h} > 1 \end{cases} \tag{4.6}$$

is used. The smoothing length $h$ is variable and in each time step adjusted such that the total mass of the particles inside the radius of the $i$th particle is nearly equal to a fixed value $M_{\mathrm{sph}}$ for the the estimated density $\rho_i$ and an average particle mass $\bar{m}$:

$$\frac{4\pi}{3}h_i^3\rho_i = M_{\mathrm{SPH}} = \bar{m}N_{\mathrm{SPH}}\,.\tag{4.7}$$

Very often, in SPH calculations we use a symmetrised kernel $\bar{W}_{ij}$ that is the arithmetic average of the two kernels $W(|\vec{r}_i - \vec{r}_j|, h_i)$ and $W(|\vec{r}_j - \vec{r}_i|, h_j)$,

$$\bar{W}_{ij} = \frac{1}{2}\left[W(|\vec{r}_i - \vec{r}_j|, h_i) + W(|\vec{r}_j - \vec{r}_i|, h_j)\right]\,.\tag{4.8}$$

Using this kernel together with (4.4), the density at the centre of each particle can be expressed as

$$\rho_i = \sum_{j=1}^{N} m_j \bar{W}_{ij}\,.\tag{4.9}$$

It is always instructive to rewrite the divergence of a quantity with the density placed inside the operator. For the divergence of the velocity for instance we then get

$$(\nabla \cdot \vec{v})_i = \frac{1}{\rho_i}[\nabla_i \cdot (\rho\vec{v})_i - \vec{v}_i \cdot (\nabla\rho)_i] = \frac{1}{\rho_i}\sum_{j=1}^{N} m_j(\vec{v}_j - \vec{v}_i) \cdot \nabla_i W(|\vec{r}_i - \vec{r}_j|, h_i)\,.\tag{4.10}$$

This expression will become useful later on.

### 4.1.2 The fluid equations

Starting from the equations of motion in Lagrangian coordinates, the discretised fluid equations are straightforwardly derived following the formalism presented above. The momentum equation for the $i$th particle in the absence of dissipation is given by

$$\frac{\mathrm{d}\vec{v}}{\mathrm{d}t} = -\frac{\nabla p}{\rho}\,.\tag{4.11}$$

The equation can be directly translated into an SPH equation:

$$\frac{\mathrm{d}\vec{v}_i}{\mathrm{d}t} = \frac{1}{\rho_i^2}\sum_{j} m_j(p_j - p_i)\nabla_i W(|\vec{r}_i - \vec{r}_j|, h_i)\,.\tag{4.12}$$

However, in the present form, the SPH momentum equation violates the conservation of linear and angular momenta. This can be seen when considering an isolated pair of particles with unequal pressures. According to (4.12) both particles would experience an acceleration of the same absolute value but with opposite signs, inducing an unphysical drift velocity of the entire system. By re-expressing the pressure gradient according to

$$\frac{(\nabla p)}{\rho} = \nabla\frac{p}{\rho} + \frac{p}{\rho^2}\nabla\rho\,,\tag{4.13}$$

we can bring the momentum equation (4.11) into a symmetric discretised form:

$$\frac{\mathrm{d}\vec{v}_i}{\mathrm{d}t} = -\sum_{j=1}^{N} m_j \left( \frac{p_j}{\rho_j^2} + \frac{p_i}{\rho_i^2} \right) \nabla_i \bar{W}_{ij} \,. \tag{4.14}$$

The pressure gradient now produces a symmetric central force between pairs of particles and therefore guarantees for the conservation of the linear and angular momentum. The above symmetrised equation of motion has for example been used by Thomas & Couchman (1992) in simulations of galaxy cluster formation. Nevertheless, infinitely many symmetric forms of the SPH momentum equations can be constructed.

The thermal energy equation can be transformed in a similar manner:

$$\frac{\mathrm{d}u}{\mathrm{d}t} = -\left( \frac{p}{\rho} \right) \nabla \cdot \vec{v} = -\nabla \cdot \left( \frac{p\vec{v}}{\rho} \right) + \vec{v} \cdot \nabla \left( \frac{p}{\rho} \right) \,. \tag{4.15}$$

The symmetrised SPH equivalent yields

$$\frac{\mathrm{d}u_i}{\mathrm{d}t} = \frac{1}{2} \sum_{j=1}^{N} m_j \left( \frac{p_j}{\rho_j^2} + \frac{p_i}{\rho_i^2} \right) (\vec{v}_i - \vec{v}_j) \cdot \nabla_i \bar{W}_{ij} \,. \tag{4.16}$$

Integration of the two equations gives the thermodynamic state of the fluid element. In the present form, the equations of motion adequately describe fully reversible hydrodynamic processes. For the capturing of shocks in the simulation, we must account for the broadening of the shock fronts and, where necessary, for the increase of entropy due to energy dissipation. In SPH this is achieved by adding an artificial viscosity term to (4.14) and (4.16) (see Section 4.1.4).

Hernquist (1993) showed that in the presented formulation of SPH the total energy is well conserved while at the same time the entropy conservation is violated, even for purely adiabatic flows. There is the possibility to switch to a different representation of the hydrodynamic equations, but according to Hernquist (1993) and Springel & Hernquist (2002), this will not lead to any improvement.

A fundamentally different approach was suggested by Lucy (1977), Benz & Hills (1987), and Hernquist (1993) who formulated SPH in terms of dynamical equations for the entropy instead of the energy. If an entropy equation is integrated then the entropy is accurately conserved although this time, the total energy is not. However, Springel & Hernquist (2002) accomplished to develop a SPH scheme that manifestly conserves both, energy and entropy. They tested their "conservative entropy approach" against several alternative implementations of SPH for a set of astrophysical problems. The authors point out that the algorithm is particularly suited for cosmological simulations, although the total energy is not conserved accurately for point explosions. The "conservative entropy approach" is also used in the GADGET-2 code.

### 4.1.3 The entropy equation

For an ideal gas undergoing adiabatic compression or expansion, the gas pressure and density are related by

$$p = A(s)\rho^{\gamma}\,,\tag{4.17}$$

where $\gamma$ is the adiabatic index. The thermodynamic state of a SPH particle is defined through the entropic function $A(s)$ which is an exclusive function of the specific entropy $s$ and can therefore be used as an adiabatic invariant of hydrodynamics. From the entropic function the internal energy is inferred:

$$u = \frac{A(s)}{\gamma - 1}\rho^{\gamma - 1}\,.\tag{4.18}$$

Using the last expression, the Lagrangian for the system of SPH particles takes the form

$$\mathcal{L}(\vec{q}, \dot{\vec{q}}, t) = \frac{1}{2}\sum_i m_i \dot{\vec{r}}_i^2 - \frac{1}{\gamma - 1}\sum_i m_i A_i \rho_i^{\gamma - 1}\,,\tag{4.19}$$

where the independent variables $\vec{q} = (\vec{r}_1, \ldots, \vec{r}_N, h_i, \ldots, h_N)$ are the coordinates and smoothing radii of the $N$ particles and the thermal energy acts as the potential that induces the particle motion. The conservative entropy approach requires that the smoothing radii are constrained as stated in (4.7), giving rise to the N holonomic constraints

$$\phi_i \equiv \frac{4\pi}{3}h_i^3\rho_i - M_{\mathrm{SPH}} = 0\tag{4.20}$$

on the coordinates of the Lagrangian. The corresponding $2N$ Euler-Lagrange equations of the first kind are:

$$\frac{\partial\mathcal{L}}{\partial q_i} - \frac{\mathrm{d}}{\mathrm{d}t}\frac{\partial\mathcal{L}}{\partial\dot{q}_i} + \sum_{j=1}^N \lambda_j \frac{\partial\phi_j}{\partial q_i} = 0\,.\tag{4.21}$$

The second half of these equations leads to

$$m_i\frac{p_i}{\rho_i^2}\left(\frac{\partial\rho_i}{\partial h_i}\right) - \left[4\pi h_i^2\rho_i + \frac{4\pi}{3}h_i^3\left(\frac{\partial\rho_i}{\partial h_i}\right)\right]\lambda_i = 0\tag{4.22}$$

and hence the Lagrange multipliers are

$$\lambda_i = \frac{3}{4\pi}\frac{m_i}{h_i^3}\frac{p_i}{\rho_i^2}\left[1 + \frac{3\rho_i}{h_i}\left(\frac{\partial\rho_i}{\partial h_i}\right)^{-1}\right]^{-1}\,.\tag{4.23}$$

Inserting the Lagrange multipliers into the first half of equations (4.21) we obtain the $N$ equations of motion:

$$m_i\frac{\mathrm{d}\vec{v}_i}{\mathrm{d}t} = -\sum_{j=1}^N m_j\frac{p_j}{\rho_j^2}\left[1 - \left(1 + \frac{3\rho_i}{h_i}\frac{\partial h_i}{\partial\rho_i}\right)^{-1}\right]\nabla_i\rho_j\,.\tag{4.24}$$

By re-expressing the density gradient in the last equation according to

$$\nabla_i \rho_j = m_i \nabla_i W(\vec{r}_i - \vec{r}_j, h_j) + \delta_{ij} \sum_{k=1}^{N} m_k \nabla_i W(\vec{r}_k - \vec{r}_i, h_i) \,, \tag{4.25}$$

we get the equations of motion in their final form:

$$\frac{\mathrm{d}\vec{v}_i}{\mathrm{d}t} = -\sum_{j=1}^{N} m_j \left( f_i \frac{p_i}{\rho_i^2} \nabla_i W(\vec{r}_i - \vec{r}_j, h_i) + f_j \frac{p_j}{\rho_j^2} \nabla_i W(\vec{r}_i - \vec{r}_j, h_j) \right) . \tag{4.26}$$

Here, the coefficients $f_i$ are defined by

$$f_i = \left[ 1 + \frac{h_i}{3\rho_i} \frac{\partial \rho_i}{\partial h_i} \right]^{-1} . \tag{4.27}$$

Interestingly, the equation of motion has a intrinsically symmetric form and is very similar to the momentum equation (4.14) derived in the last chapter. Nevertheless, energy and entropy are only conserved when the $f$-factors are included.

## 4.1.4 Shocks and viscosity

Flows of gas easily develop discontinuities and shocks over which the pressure and density of the medium undergo a sudden change. Under ideal conditions, the relaxation time that the system requires to attain equilibrium on microphysical scales is infinitely small. The system then passes through a number of quasi stationary states and the shock is said to be isentropic. In reality however, due to the intrinsic viscosity of any fluid, the thermal equilibrium can never be reached instantaneously. Therefore, the assumption of a quasi stationary process generally does not hold in real gas shocks. Instead, the interactions on microphysical scales dissipate kinetic energy and generate entropy.

   The common method to mimic this non-adiabatic behaviour in SPH is to introduce artificial viscosity. The form of the artificial viscosity term was proposed by Monaghan & Gingold (1983) and later slightly modified by Monaghan (1997). The viscosity tensor that is used in GADGET-2 has the form (Springel 2005):

$$\Pi_{ij} = \begin{cases} -\frac{\alpha}{2}(c_i + c_j - 3w_{ij})w_{ij}/\rho_{ij} \,, & \vec{v}_{ij} \cdot \vec{r}_{ij} < 0 \\ 0 \,, & \vec{v}_{ij} \cdot \vec{r}_{ij} \geq 0 \end{cases} , \tag{4.28}$$

where $c_i$ and $c_j$ are the sound velocities of the two particles $i$ and $j$ and $\vec{v}_{ij}$ and $\vec{r}_{ij}$ denote the arithmetic means of the velocities and position vectors. $w_{ij} = \vec{w}_{ij} \cdot \vec{v}_{ij}/|\vec{r}_{ij}|$ is the relative velocity of the particle approach projected onto the connecting line between the particles. The parameter $\alpha$ is used to adjust the strength of the viscosity with typical values in the range $\alpha \simeq 0.5 - 1.0$. Consequently, the viscosity tensor has the dimension

$$[\Pi] = \frac{[\text{length}]^5}{[\text{mass}][\text{time}]^2} . \tag{4.29}$$

Including artificial viscosity into the momentum equation we obtain

$$\frac{\mathrm{d}\vec{v}_i}{\mathrm{d}t} = -\sum_{j=1}^{N} m_j \left( f_j \frac{P_j}{\rho_j^2} + f_i \frac{P_i}{\rho_i^2} + \Pi_{ij} \right) \nabla_i \bar{W}_{ij}, \tag{4.30}$$

where we have used the symmetrised kernel defined in equation (4.8).

In absence of external sinks and sources of heat the change in the entropic function $A(s)$ is solely generated by shock fronts and depends on the artificial viscosity according to

$$\frac{\mathrm{d}A_i}{\mathrm{d}t} = \frac{1}{2} \frac{\gamma - 1}{\rho_i^{\gamma-1}} \sum_{j=1}^{N} m_j \Pi_{ij} (\vec{v}_i - \vec{v}_j) \cdot \nabla_i \bar{W}_{ij}. \tag{4.31}$$

To illustrate the influence of artificial viscosity on the particle motion we define the viscous pressure acting on the particles $i$ and $j$,

$$p_{\text{visc}} \simeq \frac{1}{2} \rho_{ij}^2 \Pi_{ij} = -\frac{\alpha}{2} \left[ \rho_{ij} c_{ij} w_{ij} + \frac{3}{2} \rho_{ij} w_{ij}^2 \right] \tag{4.32}$$

and relate it to the thermal pressure $p_{\text{therm}} = c_{ij}^2 \rho_{ij}/\gamma$. This gives

$$\frac{p_{\text{visc}}}{p_{\text{therm}}} \simeq \frac{\alpha}{2} \gamma \left[ \frac{w_{ij}}{c_{ij}} + \frac{3}{2} \left( \frac{w_{ij}}{c_{ij}} \right)^2 \right]. \tag{4.33}$$

It appears that the relative viscous pressure grows with the value of the quantity $w_{ij}/c_{ij}$ which can be interpreted as the Mach number of the fluid flow. Hence, artificial viscosity becomes most important where shocks occur and is automatically reduced elsewhere. Since SPH simulations can still be more dissipative than necessary in certain situations (such as shear flows), an additional viscosity switch is implemented in GADGET-2 (see e.g. Morris & Monaghan (1997), Dolag et al. (2005)).

## 4.2 Smoothed particle magnetohydrodynamics (SPMHD)

The cosmic plasma can in good approximation be described as one single, ideally conducting fluid. It mainly consists of freely streaming electrons and ions that quickly straighten out charge imbalances and thus limit the lifetime of cosmic electric fields to very short time scales. In contrast, no free magnetic charges exist to short out cosmic magnetic fields. Once generated through the action of electric currents, due to the quasi infinitely large conductivity, the magnetic fields are "frozen" into the plasma where they can persist for a long time.

The evolutionary equation for magnetic fields is the induction equation which can be written as

$$\frac{\mathrm{d}\vec{B}}{\mathrm{d}t} = (\vec{B} \cdot \nabla)\vec{v} - \vec{B}(\nabla \cdot \vec{v}). \tag{4.34}$$

Translating this equation into the SPH formalism, using relation (4.10), we obtain

$$\frac{\mathrm{d}B_i^k}{\mathrm{d}t} = \frac{1}{\rho_i} \sum_{j=1}^N m_j (B_i^k(\vec{v}_i - \vec{v}_j) - (\vec{v}_i - \vec{v}_j)^k \vec{B}_i) \cdot \nabla_i W(|\vec{r}_i - \vec{r}_j|, h_i), \qquad (4.35)$$

where $(\vec{v}_j - \vec{v}_i)^k$ is the $k$th component of the relative velocity $\vec{v}_j - \vec{v}_i$. Since the electrically neutral but conducting gas effectively feels only the effects of magnetic forces (and the hydrodynamic forces), we obtain for the Lorentz force density:

$$\rho \frac{\mathrm{d}\vec{v}}{\mathrm{d}t} = \frac{1}{4\pi}(\nabla \times \vec{B}) \times \vec{B} \qquad (4.36)$$

$$= -\frac{1}{8\pi}\nabla\vec{B}^2 + \frac{1}{4\pi}(\vec{B} \cdot \nabla)\vec{B}, \qquad (4.37)$$

where, in the second line, we applied the formula for the expansion of the triple vector product to obtain the two terms for the contributions of the magnetic pressure and the magnetic tension. The right hand side of the Lorentz force density is conveniently written as the divergence of the stress-energy tensor $M^{km}$ of the magnetic field

$$\rho \frac{\mathrm{d}\vec{v}^m}{\mathrm{d}t} = \frac{\partial M^{km}}{\partial x^m}. \qquad (4.38)$$

The components of $M$ are given by

$$M^{km} = \frac{1}{4\pi}\left(\vec{B}^k \vec{B}^m - \frac{1}{2}\vec{B}^2 \delta^{km}\right). \qquad (4.39)$$

The additional term $\vec{B}(\nabla \cdot \vec{B})/\rho$ that appears when evaluating the divergence of the stress-energy tensor vanishes due to $\nabla \cdot \vec{B} = 0$. Equations (4.37) and (4.38) are therefore analytically equivalent. Numerically, however, this is not true since in SPMHD calculations discretisation errors cause $\nabla \cdot \vec{B}$ to grow over time. The resulting unphysical force term must explicitly be subtracted from the Lorentz force in each time step (Børve et al. 2001).

The tensor equation (4.38) has the important advantage that it conserves linear and angular momenta exactly. A disadvantage of the conservation form is that, as shown in calculations by Phillips & Monaghan (1985), the gas motion can become unstable in the presence of strong magnetic fields. In such situations, (4.37) leads to better results.

Dolag et al. (1999) compared the two alternative implementations in cosmological cluster simulations without finding significant differences in the resulting magnetic fields. The reason for this might be that in large-scale cosmological simulations such critical values for the magnetic field are never reached. For the GADGET-simulations we therefore employ the conservative form of the Lorentz force density (4.38), being well aware that difficulties may arise in shock tube tests where the magnetic pressure is comparable to the thermal pressure (see Chapter 5).

Dividing (4.38) by $\rho$, we can derive the Lorentz force term and add it to the SPH momentum equation (4.30):

$$\frac{\mathrm{d}\vec{v}_a^k}{\mathrm{d}t} = \sum_j^N m_j \left(\frac{M_i^{km}}{\rho_i^2} + \frac{M_j^{km}}{\rho_j^2}\right) \cdot \nabla_i^m W(\vec{r}_i - \vec{r}_j, h_i). \qquad (4.40)$$

The term that must be removed afterwards to correct for the erroneous divergence of $\vec{B}$ is calculated according to Børve et al. (2001)

$$\frac{\vec{B}(\nabla \cdot \vec{B})}{\rho} \approx \vec{B}_i \sum_j^N m_j \left( \frac{\vec{B}_i}{\rho_i^2} + \frac{\vec{B}_j}{\rho_j^2} \right) \cdot \nabla_i W(\vec{r}_i - \vec{r}_j, h_i) \,. \tag{4.41}$$

Furthermore, to be in consistency with the SPH momentum equation we need to incorporate the variable smoothing length terms $\nabla h$ into the SPMHD equations. The derivation is presented in Price & Monaghan (2004).

As will be explained in detail in Section 5.1.2, the MHD system allows for a whole set of different types of waves to form, among which are shock and Alfvén waves involving discontinuous changes in the magnetic field. When modelling such waves, high frequency oscillations may occur that are typically damped out as they propagate away from the discontinuity where they were generated. Although the numerical noise does not affect the stability of the simulation, it can lead to a relatively poor representation close to the discontinuities. To counteract this effect, the magnetic field of each SPH particle is smoothed after a fixed temporal interval. The standard smoothing technique is to calculate a corrected magnetic field vector according to Børve et al. (2001):

$$\langle \vec{B} \rangle_i = \frac{\sum_j (m_j \vec{B}_j / \rho_j) W_{ij}}{\sum_j (m_j / \rho_j) W_{ij}} \,, \tag{4.42}$$

and to weight the old magnetic field with the new smoothed estimate:

$$\vec{B}_i^{\text{new}} = q \langle \vec{B} \rangle_i + (1 - q) \vec{B}_i \,. \tag{4.43}$$

In GADGET-2, we set $q = 1$, so that the $\vec{B}$-vector is completely replaced by the smoothed magnetic field vector once every 15 time steps.

## 4.3 The cosmic ray model

The energy density of cosmic rays inside galaxy clusters as inferred from observations is of about a few percent of the thermal energy density. Locally, the amount of cosmic ray energy can vary, in regions of ongoing shock acceleration, the non-thermal fraction of the energy density may rise to up to 20% while in quiet peripheral regions, the amount of energy in relativistic ions and electrons is evanescent.

When including cosmic rays into cosmological SPH simulations, we assume that the relativistic population is effectually coupled to the thermal gas by magnetic fields. The internal energy of an SPH particle is then composed to a large part of thermal gas energy and to a small part of relativistic energy. In consequence, the cosmic ray population contributes to the total pressure and energy density of the fluid particle and thus influences the dynamic behaviour of the simulation. Although the cosmic rays do not drastically modify the physics of structure formation, their integration into cosmological simulations can have measurable effects on observable quantities like the Sunyaev-Zel'dovich effect and

the X-ray emission of galaxy clusters (Jubelgas et al. 2008; Pfrommer et al. 2007). It is therefore purposive to include the cosmic ray physics consistently into the SPH formalism rather than restricting its treatment to the post-processing as was for example done by Miniati et al. (Miniati et al. 2001; Miniati 2002).

The cosmic ray model employed in GADGET-2 was developed by Ensslin et al. (2006) for the purpose of describing the dynamical interplay between cosmic rays and gas dynamics in the context of SPH. To save computational time, the physics of cosmic rays was reduced to the aspects that are of the highest significance for the dynamics of structure formation. Owing to the intrinsic complexity of the various processes that influence the cosmic ray spectrum, the following simplifications were made:

- The model only traces the evolution of the dominant relativistic proton population. Since the contribution of heavier nuclei does not significantly change the dynamical picture, alpha particles and heavier ions are neglected. Furthermore, the population of primary cosmic ray electrons is ignored.

- The momentum spectrum of the protons is approximated by a single power-law with a constant spectral index of $\alpha \in [2,3]$. Since protons with energies below $E_{\mathrm{kin}} = m_{\mathrm{p}}c^2 \approx 1\,\mathrm{GeV}$ are assigned to the thermal population, the lower cutoff of the momentum distribution is initially set to $m_{\mathrm{p}}c$. The steepness of the profile renders a higher cutoff unnecessary.

- Particle acceleration and loss processes are defined in terms of analytic functions that depend on the proton energy. The shapes of those functions are derived from the theory of diffusive shock acceleration and radiative physics and therefore naturally accommodate the fact that the effectiveness of most processes strongly varies with the energy of a cosmic ray particle.

- The network of reactions between cosmic rays and thermal protons is downgraded to single source functions for relativistic electrons and gamma rays, neglecting any intermediate reactions such as pion production and decay.

- The model exclusively accounts for radio emission by secondary electrons.

The resulting algorithm captures the hydrodynamical effects of cosmic rays as well as all important physical processes like the particle injection by diffusive shock acceleration, re-acceleration by plasma waves or modified shock structures. For details, see Ensslin et al. (2006).

### 4.3.1 Basic cosmic ray variables

The differential momentum spectrum of the protons is given by

$$f(p) = \frac{\mathrm{d}N}{\mathrm{d}p\mathrm{d}V} = Cp^{-\alpha}\Theta(p-q), \qquad \alpha \in [2,3]\,, \tag{4.44}$$

where $\Theta$ is the Heaviside step function and the momenta $p$ and $q$ are expressed in dimensionless form in units of $m_{\mathrm{p}}c$. Consequently, the normalisation $C$ has the unit $[\mathrm{length}]^{-3}$.

Since the power-law index $\alpha$ is fixed, the cosmic ray spectrum can only vary through the spatial and temporal dependence of the two dynamical quantities $C = C(\vec{r}, t)$ and $q = q(\vec{r}, t)$. The normalisation and the cut-off are connected to the thermodynamic state of the SPH particle via the thermal gas density. Upon adiabatic compression or expansion the normalisation $C$ and the cutoff $q$ shift according to

$$C(\rho) = (\rho/\rho_0)^{\frac{\alpha+2}{3}} C_0 \ \text{ and } \ q(\rho) = (\rho/\rho_0)^{\frac{1}{3}} q_0 , \tag{4.45}$$

leaving the phase-space density of the cosmic ray population invariant. The reference density $\rho_0$ can be set to any reasonable value (for example to the mean cosmic density), where $C_0$ and $q_0$ denote the corresponding normalisation and cut-off at this density.

From (4.44), the expressions for the cosmic ray state variables are derived. The number density yields

$$n_{\mathrm{CR}} = \int_0^\infty \mathrm{d}p \, f(p) = \frac{C \, q^{1-\alpha}}{\alpha - 1} = \frac{C_0 \, q_0^{1-\alpha}}{\alpha - 1} \frac{\rho}{\rho_0} , \tag{4.46}$$

where we have used (4.45) to obtain the second identity. Integrating over the kinetic energy of a single relativistic proton with momentum $p$,

$$T_{\mathrm{p}}(p) = (\sqrt{1 + q^2} - 1) \, m_{\mathrm{p}} c^2 , \tag{4.47}$$

we get the kinetic energy density of the cosmic ray population:

$$
\begin{aligned}
\epsilon_{\mathrm{CR}} &= \int_0^\infty \mathrm{d}p \, f(p) \, T_{\mathrm{p}}(p) \\
&= \frac{C m_{\mathrm{p}} c^2}{\alpha - 1} \left[ \frac{1}{2} \mathcal{B}_{\frac{1}{1+q^2}} \left( \frac{\alpha - 2}{2}, \frac{3 - \alpha}{2} \right) + q^{1-\alpha} \left( \sqrt{1+q^2} - 1 \right) \right] ,
\end{aligned} \tag{4.48}
$$

where $\mathcal{B}_x(a, b)$ denotes the incomplete beta function and $\alpha > 2$ is assumed. The average kinetic energy of a cosmic ray proton $\epsilon_{\mathrm{CR}}/n_{\mathrm{CR}}$ is then defined by

$$T_{\mathrm{CR}} = \left[ \frac{q^{\alpha-1}}{2} \mathcal{B}_{\frac{1}{1+q^2}} \left( \frac{\alpha - 2}{2}, \frac{3 - \alpha}{2} \right) + \sqrt{1+q^2} - 1 \right] m_{\mathrm{p}} c^2 . \tag{4.49}$$

The cosmic ray pressure acts as an isotropic pressure component that adds to the thermal and magnetic pressure of the SPH particle. It is given by

$$P_{\mathrm{CR}} = \frac{m_{\mathrm{p}} c^2}{3} \int_0^\infty \mathrm{d}p \, f(p) \, \beta \, p = \frac{C \, m_{\mathrm{p}} c^2}{6} \mathcal{B}_{\frac{1}{1+q^2}} \left( \frac{\alpha - 2}{2}, \frac{3 - \alpha}{2} \right) , \tag{4.50}$$

where $\beta = v/c = p/\sqrt{1 + p^2}$ is the dimensionless velocity of a single proton.

Since the cosmic ray spectrum covers a large range of energies, starting from barely super-thermal energies of $E \sim 1 \, \mathrm{GeV}$ and going up to the ultra-relativistic regime of $E \sim 10^{20} \, \mathrm{GeV}$, the adiabatic index is not a constant but is shifting between $\gamma = 5/3$ for an ideal thermal gas and the ultra-relativistic limit of $\gamma = 4/3$. For the local adiabatic exponent of the cosmic ray pressure component we therefore have

$$\gamma_{\mathrm{CR}} \equiv \left. \frac{\mathrm{d} \log P_{\mathrm{CR}}}{\mathrm{d} \log \rho} \right|_s , \tag{4.51}$$
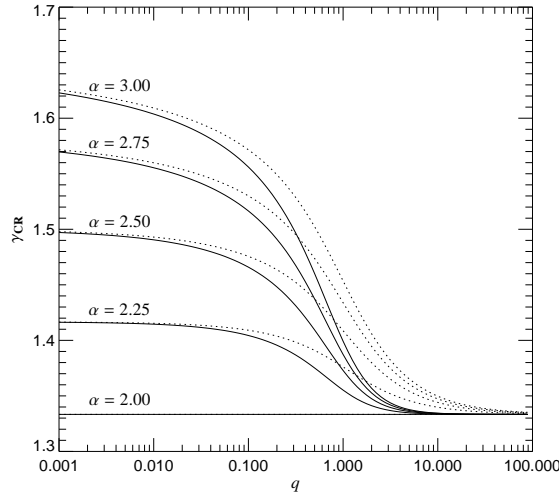
Figure 4.1: Adiabatic index of the cosmic ray population as a function of the momentum
cutoff for different spectral indices. The solid lines show the function (4.52)
while the dotted lines reflect a hypothetical polytropic gas for which the adia-
batic index is defined by $\gamma^*_{\mathrm{eff}} = 1 + P_{\mathrm{CR}}/\epsilon_{\mathrm{CR}}$. (Ensslin et al. 2006)

where the derivative is taken at constant entropy $s$. Using definitions (4.45) and (4.50) we
can rewrite the last equation in the following way:

$$
\begin{aligned}
\gamma_{\mathrm{CR}} &= \frac{\rho}{P_{\mathrm{CR}}} \left( \frac{\partial P_{\mathrm{CR}}}{\partial C} \frac{\partial C}{\partial \rho} + \frac{\partial P_{\mathrm{CR}}}{\partial q} \frac{\partial q}{\partial \rho} \right) \\
&= \frac{\alpha + 2}{3} - \frac{2}{3} q^{2-\alpha} \beta(q) \left[ \mathcal{B}_{\frac{1}{1+q^2}} \left( \frac{\alpha - 2}{2}, \frac{3 - \alpha}{2} \right) \right]^{-1}.
\end{aligned}
\qquad (4.52)
$$

The shifting of the adiabatic index becomes obvious in Figure 4.1 where $\gamma$ is plotted as
a function of $q$ for different spectral indices $\alpha$. Around the lower threshold $q \approx 1$ the
adiabatic exponent takes values between 1.35 and 1.4 for $\alpha$ in the range $2.25 - 3.00$
and adjusts to the relativistic limit for momenta $q \lesssim 10^4$. To account for the different
behaviour of the thermal gas and the cosmic ray component under compression we define
the effective adiabatic index for the compound gas inside the SPH particle:

$$
\gamma_{\mathrm{eff}} \equiv \left. \frac{\mathrm{d} \log(P_{\mathrm{th}} + P_{\mathrm{CR}})}{\mathrm{d} \log \rho} \right|_s = \frac{\gamma_{\mathrm{th}} P_{\mathrm{th}} + \gamma_{\mathrm{CR}} P_{\mathrm{CR}}}{P_{\mathrm{th}} + P_{\mathrm{CR}}}.
\qquad (4.53)
$$

## 4.3.2 Non-adiabatic processes

Once conveniently chosen at the beginning of the cosmological simulation, the evolution of
the two adiabatically invariant parameters $q_0$ and $C_0$ is solely determined by the various
non-adiabatic source and sink processes that shape the CR spectrum. The induced changes

in the particle number and kinetic energy density translate into a change of $q_0$ and $C_0$ according to

$$\begin{pmatrix} \mathrm{d}C_0 \\ \mathrm{d}q_0 \end{pmatrix} = \begin{pmatrix} \partial C_0/\partial n_{\mathrm{CR}} & \partial C_0/\partial \epsilon_{\mathrm{CR}} \\ \partial q_0/\partial n_{\mathrm{CR}} & \partial q_0/\partial \epsilon_{\mathrm{CR}} \end{pmatrix} \begin{pmatrix} \mathrm{d}n_{\mathrm{CR}} \\ \mathrm{d}\epsilon_{\mathrm{CR}} \end{pmatrix}. \tag{4.54}$$

Inserting definitions (4.46) and (4.48) the inverse of the Jacobian is given by

$$\mathrm{d}C_0 = C_0 \frac{\mathrm{d}\epsilon_{\mathrm{CR}} - T_{\mathrm{p}}(q)\,\mathrm{d}n_{\mathrm{CR}}}{\epsilon_{\mathrm{CR}} - T_{\mathrm{p}}(q)\,n_{\mathrm{CR}}}, \tag{4.55}$$

$$\mathrm{d}q_0 = \frac{q_0}{\alpha - 1} \frac{\mathrm{d}\epsilon_{\mathrm{CR}} - T_{\mathrm{CR}}\,\mathrm{d}n_{\mathrm{CR}}}{\epsilon_{\mathrm{CR}} - T_{\mathrm{p}}(q)\,n_{\mathrm{CR}}}. \tag{4.56}$$

We note that these expressions are only applicable when the changes to the cosmic ray population are below a few percent, since otherwise the integration gets very time consuming. For larger changes, the variables $q_0$ and $C_0$ are computed by inverting equations (4.46), (4.48), and (4.49) after applying the principles of particle and energy conservation (see appendix A in Ensslin et al. (2006)).

The non-adiabatic processes that are covered by the cosmic ray model are

- energy injection by structure formation shocks and supernovae,

- diffusive transport,

- Fermi I re-acceleration of mildly relativistic protons,

- radiative losses due to Coulomb scattering,

- hadronic losses due to collisions between cosmic rays and thermal ions and subsequent gamma ray and synchrotron emission.

In what follows, we will dwell upon the description of shock acceleration and synchrotron emission as these two effects play a key role in the presented work. A detailed description of all the processes mentioned above is given in Ensslin et al. (2006).

**Shock acceleration**

Due to the Fermi II mechanism, charged particles of the thermal population can get accelerated to very high energies when crossing a shock wave. Above the relativistic energy threshold, the particles are injected into the non-thermal population. Consequently, at the location of the shock front the cosmic ray population receives a growth in number and energy density.

In the simplified cosmic ray model, this acceleration procedure is treated as an instantaneous process where the particles and energy are inserted according to statistical considerations that allow to compress the complete acceleration process into a few parameters. The presented formalism is a modification of the approach by Miniati et al. (2001).

For a known shock strength, the temperature of the thermal gas behind the shock front, hereafter denoted by $T_{\mathrm{d}}$, can be inferred from the Rankine-Hugoniot jump conditions. The

thermal protons in the high-energy tail of the Maxwellian distribution can only escape back upstream of the shock if their speeds are sufficient to allow them to avoid being trapped by the plasma waves that moderate the shock. We therefore define the momentum threshold $q_{\mathrm{inj}}$ for the thermal protons to be accelerated to be a fixed multiple of the peak thermal value

$$q_{\mathrm{inj}} = x_{\mathrm{inj}} p_{\mathrm{th}} = x_{\mathrm{inj}} \sqrt{\frac{2\,kT_{\mathrm{d}}}{m_{\mathrm{p}} c^2}}\,. \tag{4.57}$$

In the linear regime, the diffusely accelerated protons emerging from the shock are characterised by a power law distribution that smoothly merges into the thermal distribution at the threshold value $q_{\mathrm{inj}}$:

$$f_{\mathrm{CR,lin}}(p) = f_{\mathrm{th}}(q_{\mathrm{inj}}) \left(\frac{p}{q_{\mathrm{inj}}}\right)^{-\alpha_{\mathrm{inj}}} \theta(p - q_{\mathrm{inj}})\,. \tag{4.58}$$

The spectral index $\alpha_{\mathrm{inj}}$ is determined by the shock strength

$$\alpha_{\mathrm{inj}} = \frac{r + 2}{r - 1}\,, \tag{4.59}$$

where $r = \rho_{\mathrm{d}}/\rho_{\mathrm{u}}$ denotes the shock compression ratio. The normalisation of the proton spectrum (4.58) is the value of the Maxwellian gas distribution at momentum $q_{\mathrm{inj}}$:

$$\begin{aligned}
f_{\mathrm{th}}(q_{\mathrm{inj}}) &= 4\pi n_{\mathrm{th}} \left(\frac{m_{\mathrm{p}} c^2}{2\pi kT_{\mathrm{d}}}\right)^{3/2} q_{\mathrm{inj}}^2 \exp\left(-\frac{m_{\mathrm{p}} c^2\,q_{\mathrm{inj}}^2}{2\,kT_{\mathrm{d}}}\right) \\
&= \frac{4}{\sqrt{\pi}}\, n_{\mathrm{th}} \left(\frac{x_{\mathrm{inj}}}{q_{\mathrm{inj}}}\right)^3 q_{\mathrm{inj}}^2 \exp(-x_{\mathrm{inj}}^2)\,,
\end{aligned} \tag{4.60}$$

where the quantity $n_{\mathrm{th}} = n_{\mathrm{d}}$ denotes the number density of particles of the thermal distribution behind the shock front. The number density of freshly injected cosmic ray particles is then found by integrating the spectrum of accelerated protons over the entire momentum space:

$$\Delta n_{\mathrm{CR,lin}}(x_{\mathrm{inj}}, T_{\mathrm{d}}) = \int_0^\infty \mathrm{d}p\, f_{\mathrm{CR,lin}}(p) = \frac{4}{\sqrt{\pi}} n_{\mathrm{th}} \frac{x_{\mathrm{inj}}^3}{\alpha_{\mathrm{inj}} - 1}\, \mathrm{e}^{-x_{\mathrm{inj}}^2}\,. \tag{4.61}$$

Using this expression we get the dynamically relevant injected cosmic ray energy density in the linear regime:

$$\Delta \epsilon_{\mathrm{CR,lin}}(\alpha_{\mathrm{inj}}, x_{\mathrm{inj}}, T_{\mathrm{d}}) = \Delta n_{\mathrm{CR,lin}}(T_{\mathrm{d}})\, T_{\mathrm{CR}}(\alpha_{\mathrm{inj}}, q_{\mathrm{inj}})\,, \tag{4.62}$$

where $T_{\mathrm{CR}}$ is the average kinetic cosmic ray proton energy defined in (4.49).

The injection constant $x_{\mathrm{inj}}$ for diffusive shock acceleration in (4.57) is inferred from theoretical studies of supernova remnants to lie in the range of 3.3 to 3.6, which typically results in a momentum cutoff in the sub-relativistic regime. Since Coulomb cooling is very efficient at these low energies, a large part of the newly injected cosmic rays is

immediately re-thermalised. The model accounts for this fact by increasing the cutoff from $q_{inj}$ to $q_{Coulomb} \sim 0.03$. For the effectively injected cosmic ray energy we then obtain

$$\Delta\epsilon_{CR,lin,Coulomb} = \Delta n_{CR,lin}T_{CR}(\alpha_{inj}, q_{Coulomb})\left(\frac{q_{Coulomb}}{q_{inj}}\right)^{1-\alpha_{inj}}. \qquad (4.63)$$

The post-shock temperature $T_d$ and the spectral index $\alpha_{inj}$ are inferred from the shock strength. Assuming a dominant thermal gas component, $\alpha_{inj}$ can expressed in terms of the Mach number of the shock by solving

$$M = \sqrt{\frac{2(2+\alpha_{inj})}{1+2\alpha_{inj}-3\gamma}}. \qquad (4.64)$$

Since $\gamma = 5/3$, the spectral index $\alpha_{inj}$ can have a maximum value of 2.

The presented analytical description applies to the regime of linear cosmic ray acceleration. The theory of diffusive shock acceleration permits an upper limit of 50 % of the shock energy to be injected into the relativistic particle population for infinitely high Mach numbers. To extend the presented model to the non-linear regime, these saturation effects must be taken into account. Details are presented in Ensslin et al. (2006).

**Synchrotron emission**

The secondary electron population is a reaction product of the hadronic collisions between cosmic rays and thermal nuclei in the ICM. Above the kinematic threshold of $q_{thr}m_pc^2 = 0.78$GeV neutral or charged pions are produced that further decay into gamma rays or electrons and protons respectively. The pion production rate and the decay into the stable end products can be described by analytical functions that are motivated from accelerator experiments and known reaction kinematics (Dermer (1986a), Dermer (1986b), Mannheim & Schlickeiser (1994)). Appropriately combining the source functions for the pion production and the pion decay we obtain a single source function for the end products of the reaction chain.

For a power-law distribution of relativistic protons the resulting source function of secondary electrons is given by

$$s_e(\vec{r}, E_e) = \frac{16}{3}2^{2-\alpha_P}c\,n_N(\vec{r})C(\vec{r})\sigma_{pp}^\pi\frac{1}{GeV}\left(\frac{8E_e}{GeV}\right)^{-\alpha_P}, \qquad (4.65)$$

where $\sigma_{pp}^\pi \simeq 32 \cdot \left(0.96 + e^{4.4-2.4\alpha}\right)$ mbarn is the effective cross section (see Pfrommer & Enßlin (2004)) and $n_N$ is the nucleon density of the ICM. The spectral index $\alpha_P$ corresponds to the power-law index of the proton spectrum introduced in Section 4.3.1. For a better distinction in what follows we denote it with the index p.

To obtain the stationary spectrum of secondary electrons the energy losses due to the ubiquitous cooling by synchrotron and IC emission must be taken into account:

$$-\dot{E}_e(\vec{r}, E_e) = \frac{4\sigma_T c}{3m_e^2c^4}(\epsilon_B + \epsilon_{CMB}). \qquad (4.66)$$

Here, $\epsilon_B = B^2/(8\pi)$ is the local magnetic energy density, and $\epsilon_{\mathrm{CMB}} = B_{\mathrm{CMB}}^2/(8\pi)$ is the energy density of the cosmic microwave background (CMB) that can be expressed by an equivalent field strength of $B_{\mathrm{CMB}} = 3.24\,(1+z)^2\mu\mathrm{G}$. The steady-state spectrum of secondary electrons can then be described by the following continuity equation:

$$\frac{\partial}{\partial E_{\mathrm{e}}}\left(\dot{E}_{\mathrm{e}}(\vec{r}, E_{\mathrm{e}}), f_{\mathrm{e}}(\vec{r}, E_{\mathrm{e}})\right) = s_{\mathrm{e}}(\vec{r}, E_{\mathrm{e}})\,. \tag{4.67}$$

The equation is solved for the spectral function $f_{\mathrm{e}}(\vec{r}, E_{\mathrm{e}})$ according to

$$f_{\mathrm{e}}(\vec{r}, E_{\mathrm{e}}) = \frac{1}{|\dot{E}_{\mathrm{e}}(\vec{r}, E_{\mathrm{e}})|} \int_{E_{\mathrm{e}}}^{\infty} \mathrm{d}E_{\mathrm{e}}' s_{\mathrm{e}}(\vec{r}, E_{\mathrm{e}}')\,. \tag{4.68}$$

If we insert (4.65) and (4.66) into the above expression and carry out the integration we arrive at

$$f_{\mathrm{e}}(\vec{r}, E_{\mathrm{e}}) = \frac{16^{1-\alpha_{\mathrm{p}}}}{\alpha_{\mathrm{p}} - 1}\, \frac{\sigma_{\mathrm{pp}}\, m_{\mathrm{e}}^2\, c^4}{\sigma_{\mathrm{T}}\, \mathrm{GeV}}\, \frac{n_{\mathrm{N}}(\vec{r})C(\vec{r})}{\epsilon_B + \epsilon_{\mathrm{ph}}}\, \frac{1}{\mathrm{GeV}} \left(\frac{E_{\mathrm{e}}}{\mathrm{GeV}}\right)^{-(\alpha_{\mathrm{p}}+1)}\,. \tag{4.69}$$

The calculation shows that from the hadronic interactions of a power-law distribution of cosmic ray protons with the thermal nuclei we obtain a power-law spectrum of secondary electrons. Using Dermer's model we set $\alpha_{\mathrm{e}} = \alpha_{\mathrm{p}} + 1$. The distribution of relativistic electrons (above a GeV) is thus described by

$$f_{\mathrm{e}}(\vec{r}, E_{\mathrm{e}}) = \frac{C_{\mathrm{e}}(\vec{r})}{\mathrm{GeV}} \left(\frac{E_{\mathrm{e}}}{\mathrm{GeV}}\right)^{-\alpha_{\mathrm{e}}}\,, \tag{4.70}$$

$$\text{and}\quad C_{\mathrm{e}}(\vec{r}) = \frac{16^{2-\alpha_{\mathrm{e}}}}{\alpha_{\mathrm{e}} - 2}\, \frac{\sigma_{\mathrm{pp}}\, m_{\mathrm{e}}^2\, c^4}{\sigma_{\mathrm{T}}\, \mathrm{GeV}}\, \frac{n_{\mathrm{N}}(\vec{r})C(\vec{r})}{\epsilon_B + \epsilon_{\mathrm{ph}}} \left(\frac{m_{\mathrm{p}}c^2}{\mathrm{GeV}}\right)^{\alpha_{\mathrm{e}}-1}\,. \tag{4.71}$$

The synchrotron emissivity $j_{\mathrm{sync}}(\nu)$ at frequency $\nu$ and per steradian of such a cosmic electron population located in an isotropic distribution of magnetic fields is calculated according to

$$j_{\mathrm{sync}}(\nu) = \frac{P_{\mathrm{sync}}(\nu)}{4\pi} = \frac{1}{4\pi} \int_{E_1}^{E_2} P(E_{\mathrm{e}}', \nu)\, f_{\mathrm{e}}(E_{\mathrm{e}}')\mathrm{d}E_{\mathrm{e}}'\,, \tag{4.72}$$

where $P(E_{\mathrm{e}}, \nu)$ is the power emitted by each single electron at energy $E_{\mathrm{e}}$ and frequency $\nu$. If we assume an isotropic distribution of electron pitch angles the integration yields:

$$j_{\mathrm{sync}}(\nu) = A_{E_{\mathrm{syn}}}(\alpha_{\mathrm{e}})\, C_{\mathrm{e}} \left[\frac{\epsilon_B}{\epsilon_{B_{\mathrm{c}}}}\right]^{(\alpha_{\nu}+1)/2} \propto \epsilon_{\mathrm{CRe}}\, B^{\alpha_{\nu}+1}\nu^{-\alpha_{\nu}}\,, \tag{4.73}$$

with the frequency dependent characteristic magnetic field strength

$$B_{\mathrm{c}} = \sqrt{8\pi\,\epsilon_{B_{\mathrm{c}}}} = \frac{2\pi\, m_{\mathrm{e}}^3\, c^5\, \nu}{3\, e\, \mathrm{GeV}^2} \simeq 31 \left(\frac{\nu}{\mathrm{GHz}}\right)\, \mu\mathrm{G}\,, \tag{4.74}$$

and the coefficient

$$A_{E_{\mathrm{syn}}} = \frac{\sqrt{3\pi}}{32\pi}\, \frac{B_{\mathrm{c}}\, e^3}{m_{\mathrm{e}}c^2}\, \frac{\alpha_{\mathrm{e}} + \frac{7}{3}}{\alpha_{\mathrm{e}} + 1}\, \frac{\Gamma\left(\frac{3\alpha_{\mathrm{e}}-1}{12}\right)\Gamma\left(\frac{3\alpha_{\mathrm{e}}+7}{12}\right)\Gamma\left(\frac{\alpha_{\mathrm{e}}+5}{4}\right)}{\Gamma\left(\frac{\alpha_{\mathrm{e}}+7}{4}\right)}\,. \tag{4.75}$$

Here, $\Gamma(a)$ denotes the $\Gamma$-function and $\alpha_{\nu}$ is given by $(\alpha_{\mathrm{e}} - 1)/2 = \alpha_{\mathrm{p}}/2$.

### 4.3.3 Mach number estimation

To adequately account for the gas heating due to energy dissipation and the injection of cosmic rays in simulations of cosmological structure formation, Pfrommer et al. (2006) developed a formalism that allows for the identification of shocks and the accurate estimation of the related Mach numbers.

In the entropy formulation of SPH, the shock strength is deduced from the jump in the entropic function $A(s)$ a fluid particle experiences when passing through the shock:

$$\frac{A_\mathrm{d}}{A_\mathrm{u}} = \frac{A_\mathrm{u} + \Delta A_\mathrm{u}}{A_u}, \qquad (4.76)$$

where the indices u and d refer to the quantities of the upstream and downstream flow. Since shock fronts in the SPH formalism are no sharp discontinuities, the crossing of the particle will take a finite time. The quantity $\Delta A_\mathrm{u}$ can thus be approximated by $\Delta A_\mathrm{u} \simeq \Delta t\, \mathrm{d}A_\mathrm{u}/\mathrm{d}t$, where $\Delta t$ is the time it takes the SPH particle to diffuse over the shock. Since the shock front is spread out over a length scale comparable to the SPH particle radius we get

$$\Delta t = f_h h / v_\mathrm{u}, \qquad (4.77)$$

where $v_\mathrm{u}$ is the pre-shock gas velocity in the reference frame of the shock front and $f_h \sim 2$ is a factor found by calibration against shock tubes. Replacing $\Delta t$ in (4.76) we thus obtain

$$\frac{A_\mathrm{d}}{A_\mathrm{u}} = 1 + \frac{f_h h}{v_\mathrm{u} A_\mathrm{u}} \frac{\mathrm{d}A_\mathrm{u}}{\mathrm{d}t}. \qquad (4.78)$$

Using the adiabatic equation (4.17) we furthermore have

$$\frac{A_\mathrm{d}}{A_\mathrm{u}} = \frac{P_\mathrm{d}}{P_\mathrm{u}} \left(\frac{\rho_\mathrm{u}}{\rho_\mathrm{d}}\right)^\gamma. \qquad (4.79)$$

The jump in the adiabatic function solely depends on the shock strength. Using the Rankine-Hugoniot jump conditions for hydrodynamic shocks we can rewrite the entropy jump as a function of the Mach number $M = v_\mathrm{u}/c$:

$$\frac{A_\mathrm{d}}{A_\mathrm{u}} = \frac{2\gamma M^2 - (\gamma - 1)}{\gamma + 1} \left[\frac{(\gamma - 1)M^2 + 2}{(\gamma + 1)M^2}\right]^\gamma \equiv f_A(M). \qquad (4.80)$$

To obtain the Mach number of the SPH particle we therefore need to solve the equation

$$[f_A(M) - 1]\, M = \frac{f_h h}{c_1 A_\mathrm{u}} \frac{\mathrm{d}A_\mathrm{u}}{\mathrm{d}t}, \qquad (4.81)$$

where we have replaced $v_\mathrm{u}$ with $M c_\mathrm{u}$. The right hand side of the equation can be calculated from (4.31).

In the above derivation we have implicitly assumed an ideal thermal gas. Nevertheless, the equations can be extended to allow for the Mach number detection inside a composite of a thermal gas and a cosmic ray component. Due to the additivity of the individual

pressure components we can define the effective entropic function of the compound gas according to

$$A_{\text{eff}} = (P_{\text{th}} + P_{\text{CR}}) \rho^{-\gamma_{\text{eff}}} . \tag{4.82}$$

Assuming that, because of their relativistic energies, the cosmic rays are only adiabatically compressed over the shock front the derivative of the entropic function yields

$$\frac{dA_{\text{eff}}}{dt} = \frac{dA_{\text{th}}}{dt} \rho^{\gamma_{\text{th}} - \gamma_{\text{eff}}} . \tag{4.83}$$

In analogy to the case of the thermal gas we thus obtain the equation for the jump in the entropic function in a medium that is composed of a thermal gas and cosmic rays:

$$\frac{A_{\text{eff,d}}}{A_{\text{eff,u}}} = \frac{\left( P_{\text{CR,d}} + P_{\text{th,d}} \right) \rho_{\text{d}}^{-\gamma_{\text{eff,d}}}}{\left( P_{\text{CR,u}} + P_{\text{th,u}} \right) \rho_{\text{u}}^{-\gamma_{\text{eff,u}}}} = 1 + \frac{f_h h}{M c_{\text{u}} A_{\text{eff,u}}} \frac{dA_{\text{eff,u}}}{dt} . \tag{4.84}$$

The equation can be transformed via the modified Rankine-Hugoniot jump conditions to yield a system of two equations that depend on the density and pressure jumps over the shock front. The root is determined with a two-dimensional Newton-Raphson iteration. From the known density jump the Mach number is calculated according to:

$$M = \sqrt{\frac{(P_{\text{d}} - P_{\text{u}})\rho_{\text{d}}/\rho_{\text{u}}}{\rho_{\text{u}} c_{\text{u}}^2 (\rho_{\text{d}}/\rho_{\text{u}} - 1)}} . \tag{4.85}$$

In cosmological simulations, the crossing time $\Delta t$ over the shock front must be adapted to account for the cosmic expansion. Furthermore, in the regime of strong shocks ($M \geq 3$) the shock broadening is more pronounced and $f_h = 2$ is not valid anymore. We then use an empirically determined formula for the Mach number (Pfrommer et al. 2006).

### 4.3.4 Integration into SPH

To arrange for the consistent integration of the cosmic ray model into the SPH formalism we introduce the number of relativistic protons per unit gas mass and momentum of the $i$th particle

$$\hat{f}_i(p) = \frac{dN_{\text{CR}}}{dp \, dm} = \frac{1}{\rho(\vec{r}_i)} \frac{dN_{\text{CR}}}{dp \, dV} = \frac{1}{\rho(\vec{r}_i)} f_i(p) , \tag{4.86}$$

where $f_i(p)$ is the cosmic ray proton distribution given in (4.44). Consequently, the normalisation constant of the re-defined spectrum yields $\hat{C}_i = C_i/\rho_i$.

Similarly, we define the cosmic ray energy per unit mass $\hat{\epsilon}_{\text{CR}i} = \epsilon_{\text{CR}i}/\rho_i$ which is incorporated into the discretised Lagrangian of the system of particles (4.19), yielding

$$\mathcal{L}(\vec{q}, \dot{\vec{q}}, t) = \frac{1}{2} \sum_i m_i \dot{\vec{r}}_i^2 - \sum_i m_i \hat{\epsilon} . \tag{4.87}$$

Here, we have introduced the total energy per unit mass of the $i$th particle, $\hat{\epsilon} = \hat{\epsilon}_{\text{th},i} + \hat{\epsilon}_{\text{CR},i}$, where the thermal component $\hat{\epsilon}_{\text{th}i}$ is given by (4.18). The equations of motion are then

found in analogy to the derivation presented in Section 4.1.3, where the constraints (4.20) for the smoothing radii were taken into account. In the case of the compound gas this leads to the Lagrange multipliers

$$\lambda_i = \frac{3}{4\pi} \frac{m_i}{h_i^3} \frac{\partial \hat{\epsilon}_i}{\partial \rho_i} \left[ 1 + \frac{3\rho_i}{h_i} \left( \frac{\partial \rho_i}{\partial h_i} \right)^{-1} \right]^{-1} .$$  (4.88)

Using the definition for the thermodynamic pressure at constant entropy

$$p = - \left( \frac{\partial E}{\partial V} \right)_s ,$$  (4.89)

where $s = s_i$ denotes the entropy of a SPH particle volume element of size $V = V_i = \rho_i/m_i$ and internal energy $E = m_i \hat{\epsilon}_i$, we deduce the derivative of the SPH particle energy with respect to the local density:

$$\frac{\partial (m_i \hat{\epsilon}_i)}{\partial \rho_i} = m_i \frac{p_i}{\rho_i^2} = m_i \frac{p_{\text{th},i} + p_{\text{CR},i}}{\rho_i^2} .$$  (4.90)

The resulting equation of motion thus retains the form given in (4.26), with the only difference that the thermal pressure has been replaced with the total pressure of the thermal and the cosmic ray component.

# Code Testing

<span style="float: right; font-size: 3em;">5</span>

Since the release of the public versions GADGET-1 in 2000 (Springel et al. 2001) and GADGET-2 in 2005 (Springel 2005) the code has constantly been improved and its functionality has been enhanced. Additionally, a number of modules that go beyond gravity and ordinary gas physics have been developed that are not contained in the public version. The inclusion of extra modules describing for example the formation of stars, cooling and feedback is important to increase our understanding of astrophysical processes and how their interaction influences the cosmic structure we observe today.

Before a new module can be included into GADGET-2, its reliability must be verified through standard tests. Moreover, the smooth and consistent interplay of all code sub-components activated in a single simulation must be guaranteed, which usually requires additional compatibility checks. So far, the SPMHD algorithm and the cosmic ray model presented in the last chapter have only separately been tested and successfully used in cosmological simulations. Since in our studies of the non-thermal emission of galaxy clusters we for the first time employ both components simultaneously, we have to perform numerical tests that are mandatory for the interpretation of our later results.

In this chapter we will introduce a standard test for MHD codes, the coplanar Riemann shock tube problem. After some theoretical considerations we will present the algorithm that is used to find an analytical solution to the test problems. The Riemann solver and the performance of the GADGET-2 code will be tested by means of five different Riemann problems with well-known solutions. After successful testing the analytical MHD Riemann solver should provide a solid basis for the upgrade to the more complex situation of a two-component fluid consisting of a thermal gas and a cosmic ray component. The goal is to find an analytical solution that can serve as a benchmark for numerical shocktubes including SPMHD and the cosmic ray module. In the second part of this chapter we will therefore present an enhancement of the Riemann solver, which allows for the prediction of simulation results of MHD shock tubes performed with the compound gas. In the subsequent section the results of numerical tests are presented. Finally, problems and implications for cluster simulations are discussed.

## 5.1 MHD shock tubes with thermal gas

The MHD Riemann problem plays a crucial role in astrophysics where many applications fundamentally depend on the presence of magnetic fields and an ionised, conducting character of the medium under investigation. For known analytical solutions, the shock tube problem can be used to check the performance of MHD codes. However, due to the intrinsic complexity of the MHD flows, finding the analytical solution is not straightforward.

### 5.1.1 The magnetohydrodynamic equations

The equations of magnetohydrodynamics give a continuum description of a conducting fluid interacting with a magnetic field. Analogous to ordinary hydrodynamics they are derived from the conservation laws of mass, energy, and momentum, additionally taking into account Maxwell's equations of electrodynamics. By neglecting electrostatic force, displacement current, internal friction, and thermal conduction one obtains the following equations of ideal MHD (see e.g. Courant & Friedrichs 1976):

$$\frac{\partial \rho}{\partial t} + \nabla \cdot (\rho \vec{v}) = 0 \,, \tag{5.1}$$

$$\rho \frac{\partial \vec{v}}{\partial t} + \rho (\vec{v} \cdot \nabla) \vec{v} + \nabla p - \frac{1}{\mu_0} (\nabla \times \vec{B}) \times \vec{B} = 0 \,, \tag{5.2}$$

$$\frac{\partial}{\partial t} \left( \frac{\rho \vec{v}^2}{2} + \rho \epsilon + \frac{\vec{B}^2}{2\mu_0} \right) + \nabla \cdot \left[ \rho \left( \frac{\vec{v}^2}{2} + \omega \right) \vec{v} + \frac{1}{\mu_0} (\vec{B} \times (\vec{v} \times \vec{B})) \right] = 0 \,, \tag{5.3}$$

$$\frac{\partial \vec{B}}{\partial t} - \nabla \times (\vec{v} \times \vec{B}) = 0 \,. \tag{5.4}$$

The hydrodynamic continuity equation stays unaltered. An additional term $\vec{j} \times \vec{B}$ must be added to the Euler equation (5.2) that describes the Lorentz force density on the induced charge current $\vec{j} = c/\mu_0 \nabla \times \vec{B}$. A similar extension applies to the energy conservation (5.3) where the magnetic energy density and the Poynting vector come into play. Here, $\epsilon$ and $w$ are the energy and enthalpy per mass. The induction equation (5.4) determines the transport of the magnetic field with the fluid flow. The system is closed by an equation of state that connects $p$ to $\rho$ and $\epsilon$,

$$p = (\gamma - 1)\rho \epsilon \,, \tag{5.5}$$

with $\gamma = 5/3$ for an ideal gas.

As in ordinary gas dynamics the above equations of magnetohydrodynamics form a system of hyperbolic equations. If we assume that all variables depend on the time $t$ and only one spatial dimension $x$ the system (5.1) - (5.4) in conservative form yields

$$\frac{\partial}{\partial t} \vec{U} + \frac{\partial}{\partial x} \vec{F}(\vec{U}) = 0 \,, \tag{5.6}$$

where we defined the the state vector

$$\vec{U} = \begin{pmatrix} \rho, & \rho v_x, & \rho v_y, & \rho v_z, & B_y, & B_z, & E \end{pmatrix}^{\mathrm{T}} \tag{5.7}$$

and the flux function

$$\vec{F}(\vec{U}) = \begin{pmatrix} \rho v_x \\ \rho v_x^2 + P - B_x^2 \\ \rho v_x v_y - B_x B_y / \mu_0 \\ \rho v_x v_z - B_x B_z / \mu_0 \\ B_y v_x - B_x v_y \\ B_z v_x - B_x v_z \\ (E + P) v_x - B_x / \mu_0 (B_x v_x + B_y v_y + B_z v_z) \end{pmatrix}. \tag{5.8}$$

Here, the total pressure and the total energy density are given by

$$P = p + \frac{1}{2\mu_0}(B_x^2 + B_y^2 + B_z^2), \tag{5.9}$$

$$E = \frac{1}{2}\rho(v_x^2 + v_y^2 + v_z^2) + \frac{p}{\gamma - 1} + \frac{1}{2\mu_0}(B_x^2 + B_y^2 + B_z^2). \tag{5.10}$$

Equation (5.6) can be written in the quasilinear form

$$\frac{\partial}{\partial t}\vec{U} + \mathbf{A}\frac{\partial}{\partial x}\vec{U} = 0, \tag{5.11}$$

where $\mathbf{A}$ is the $7 \times 7$ Jacobian matrix $\mathbf{A}(\vec{U}) = \partial \vec{F}/\partial \vec{U}$. The original flow differential equations (5.1) - (5.4) have thus been reduced to a set of seven partial differential equations (PDEs) of hyperbolic type. The eigenvalues of the matrix $\mathbf{A}$ are the velocities of the seven families of characteristics that occur in magnetohydrodynamics (see e.g. Ryu & Jones 1995):

$$\begin{aligned} \lambda_{1/7} &= v_x \mp c_f, \\ \lambda_{2/6} &= v_x \mp c_a, \\ \lambda_{3/5} &= v_x \mp c_s, \\ \lambda_4 &= v_x, \end{aligned} \tag{5.12}$$

where $c_a = \sqrt{B_x^2/\mu_0\rho}$ is the Alfvén speed and

$$c_{\mathrm{f}} = \left( \frac{1}{2}\left[ a^2 + \frac{B_x^2 + B_y^2 + B_z^2}{\mu_0\rho} + \sqrt{\left( a^2 + \frac{B_x^2 + B_y^2 + B_z^2}{\mu_0\rho} \right)^2 - 4a^2\frac{B_x^2}{\mu_0\rho}} \right] \right)^{1/2} \tag{5.13}$$

$$c_{\mathrm{s}} = \left( \frac{1}{2}\left[ a^2 + \frac{B_x^2 + B_y^2 + B_z^2}{\mu_0\rho} - \sqrt{\left( a^2 + \frac{B_x^2 + B_y^2 + B_z^2}{\mu_0\rho} \right)^2 - 4a^2\frac{B_x^2}{\mu_0\rho}} \right] \right)^{1/2} \tag{5.14}$$

are the fast and slow magnetosonic velocities respectively. In the above definitions the sound speed enters as $a = \sqrt{\gamma p / \rho}$. The system of equations is strictly hyperbolic if the eigenvalues of matrix $\mathbf{A}$ are non-degenerate. Nevertheless, some wave speeds will coincide when either $B_x$ or $B_\perp = \sqrt{B_y^2 + B_z^2}$ vanishes. The system is therefore called non-strictly hyperbolic.

### 5.1.2 Waves and discontinuities

A wave in a medium is defined to be a disturbance which propagates at a finite speed. Consequently, there must be an advancing wave front separating the region through which the disturbance has passed from the region it is about to enter. The eigenvalues (5.12) of the Jacobian matrix that we derived from the MHD equations in the last section can be interpreted as the velocities of such "disturbance waves". Corresponding to the plus or minus sign, they are propagating forwards or backwards relative to the fluid motion.

In the above formulation of the conservation equations in differential form (5.1) - (5.4), we implicitly assumed a steady flow, i.e. that the characteristic fields are continuously differentiable everywhere. This steadiness can be broken when waves fronts occur. Transforming into the reference frame of the wave front, the region of gas infall is called the front side or upstream flow, the other the back side or downstream flow respectively. As the influence of a disturbance is propagated into the medium through sound waves, the type of jump over the wave front will depend on the ratio of the infall velocity $v_{\mathrm{up}}$ to the upstream speed of sound $a_{\mathrm{up}}$.

In the case $v_{\mathrm{up}} < a_{\mathrm{up}}$, the upstream gas will always "see" the disturbance before its crossing. The singularity at the wave front is then confined to a discontinuity of the derivatives of the solution and the front is a surface of **weak discontinuity**. When the discontinuities occur in the first order derivatives of the dependent variables the solution will experience a discontinuity in slope. If the discontinuities occur in the higher order derivatives then the wave form appears to be smooth. The corresponding waves are called "simple magnetohydrodynamic waves" and the variation of physical quantities across the front is described by a set of differential equations that can be derived from the general Riemann invariants (see, e.g. Jeffrey 1966).

If the velocity of the perturbation is growing, triggered for example by the motion of an accelerating piston, later influences of the disturbance travel faster and tend to overtake those sent out earlier. The wave front gets steeper and steeper and becomes vertical above the sonic limit when $v_{\mathrm{up}} > a_{\mathrm{up}}$. The character of the resulting discontinuity is similar to the breaking of a water wave that steepens as more slowly progressing parts are overtaken by faster ones. The wave transforms into a shock front involving jumps in all dependent variables. Shock fronts are **strong discontinuities**. A different type of strong discontinuity solely arising in MHD are the Alfvén discontinuities. The associated Alfvén waves are linear waves, involving no compression but a rotation in the transversal magnetic field and the transversal velocity.

By looking at the eigenvalues (5.12) we can identify the different types of waves that result from the MHD system of equations. The waves corresponding to $\lambda_{3/5}$ and $\lambda_{1/7}$ are the slow and fast "magneto-sonic" waves, because they are compressible like sound waves

in hydrodynamics. There are two Alfvén waves that are moving at $v_x \mp c_a$. The last eigenvalue, $\lambda = v_x$ relates to the entropy mode, where the density and entropy undergo jumps when crossing the wave front. As there is no discontinuity in velocity or pressure, no fluid particles can cross the front and the fluids on adjacent sides of the wave front cannot mix. For this reason, these wave fronts are usually called contact discontinuities.

The mathematical treatment of strong discontinuities is conveniently done in terms of Lagrangian mass coordinates. The Lagrangian coordinate is defined as the location of an infinitesimal mass element $dm \equiv \rho dV$ inside an infinitesimal volume $dV$ moving with the fluid. Introducing the operator $\frac{d}{dt} \equiv \frac{\partial}{\partial t} + \vec{v} \cdot \nabla$ and the specific volume $1/\rho$ we can rewrite the one-dimensional MHD equations as functions of $t$ and the mass coordinate $m$:

$$\frac{d}{dt}\left(\frac{1}{\rho}\right) - \frac{\partial}{\partial m} u_x = 0 \,, \tag{5.15}$$

$$\frac{d}{dt} u_x + \frac{\partial}{\partial m}\left(P - \frac{B_x^2}{\mu_0}\right) = 0 \,, \tag{5.16}$$

$$\frac{d}{dt} u_y - \frac{\partial}{\partial m}\left(\frac{B_x B_y}{\mu_0}\right) = 0 \,, \tag{5.17}$$

$$\frac{d}{dt} u_z - \frac{\partial}{\partial m}\left(\frac{B_x B_z}{\mu_0}\right) = 0 \,, \tag{5.18}$$

$$\frac{d}{dt}\left(\frac{B_y}{\rho}\right) - \frac{\partial}{\partial m}\left(B_x u_y\right) = 0 \,, \tag{5.19}$$

$$\frac{d}{dt}\left(\frac{B_z}{\rho}\right) - \frac{\partial}{\partial m}(B_x u_z) = 0 \,, \tag{5.20}$$

$$\frac{d}{dt}\left(\frac{E}{\rho}\right) - \frac{\partial}{\partial m}\left(v_x P - \frac{Bx}{\mu_0}(B_x y_x + B_y v_y + B_z v_z)\right) = 0 \,. \tag{5.21}$$

Integrating the above equations over the discontinuities yields the jump conditions:

$$W\left[\frac{1}{\rho}\right] = -\left[v_x\right] \,, \tag{5.22}$$

$$W\left[v_x\right] = \left[P - \frac{B_x^2}{\mu_0}\right] \,, \tag{5.23}$$

$$W\left[v_y\right] = -\frac{B_x}{\mu_0}\left[B_y\right] \,, \tag{5.24}$$

$$W\left[v_z\right] = -\frac{B_x}{\mu_0}\left[B_z\right] \,, \tag{5.25}$$

$$W\left[\frac{B_y}{\rho}\right] = -B_x\left[v_y\right] \,, \tag{5.26}$$

$$W\left[\frac{B_z}{\rho}\right] = -B_x\left[v_z\right] \,, \tag{5.27}$$

| 1 | 2 | 3 | 4 | 5 | 6 | 7 | 8 |
|---|---|---|---|---|---|---|---|

fast              rotational       slow          contact/           slow          rotational       fast
structure   discontinuity   structure    tangential      structure   discontinuity   structure
                                                     discontinuity
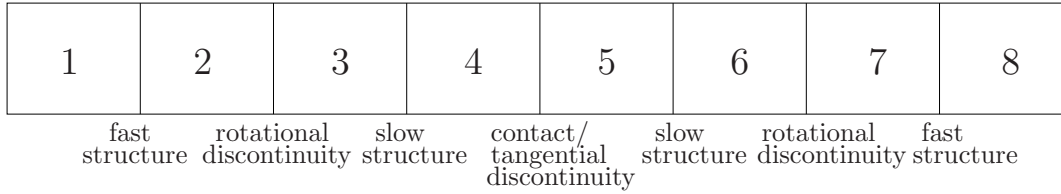
Figure 5.1: The MHD Riemann problem at $t > 0$. The initial zones 1 and 8 are separated by six intermediate states and seven waves and/or discontinuities.

$$W \left[ \frac{E}{\rho} \right] = [v_x P] - \frac{B_x}{\mu_0} [B_x v_x + B_y v_y + B_z v_z] \; , \tag{5.28}$$

where the brackets $[X] = X_\mathrm{d} - X_\mathrm{u}$ stand for the difference between the downstream and upstream values of a quantity $X$, and $W = \rho_\mathrm{u}(v_\mathrm{disc.} - v_\mathrm{u})$ is the speed of the discontinuity surface in Lagrangian coordinates. The wave speed is negative when the discontinuity propagates in the negative $m$-direction.

### 5.1.3  The MHD Riemann problem

The Riemann problem is a special initial value problem consisting of two constant states with a single discontinuity. Except for the normal component of the magnetic field, which is subject to the divergence criterion, any field variable may vary in the absolute value as well as the direction in the two halfspaces. Consequently, in the one-dimensional case, one has to solve the system of hyperbolic equations (5.11) for initial conditions of the form

$$\vec{U}(x,0) = \begin{cases} \vec{U}_\mathrm{L} & x < x_0 \\ \vec{U}_\mathrm{R} & x > x_0 \end{cases} . \tag{5.29}$$

In general, at $t > 0$, seven wave fronts will emerge from the initial boundary, consisting of the four types of waves we came to know in the last section. The slow, fast, and Alfvén waves appear in pairs, each one consisting of one wave propagating in positive, and one wave propagating in negative $x$-direction relative to the fluid motion. As $c_\mathrm{f} > c_\mathrm{A} > c_\mathrm{s}$, the fast waves are the outermost structures on each side, followed by the Alfvén waves and, behind that, the slow waves. The boundary itself is identified with the structure of the entropy mode. Consequently, the original setup is separated into eight constant states including the original pair, as sketched in Figure 5.1.

Since the MHD equations form a non-strictly hyperbolic system, up to five out of the seven eigenvalues of the Jacobian matrix may coincide and the system may admit non-regular waves, like compound waves and overcompressive intermediate shocks. One example for the occurrence of a compound wave is the Brio & Wu shock tube (Brio & Wu 1988) which is a well-established test problem for MHD codes and will be presented in a later section. Except for this one prominent example we will stick to the regular case of the MHD Riemann problem and not take the special waves into account. However, in certain cases, they might have a physical relevance. Details about the special wave phenomena can e.g. be found in the papers by Wu (1990) and Myuong & Roe (1997a,b).

A first analytical solution to the MHD Riemann problem was provided by Dai & Woodward who solved the system of equations iteratively by Newton's method (Dai & Woodward 1994). Although they used a simplified approach in which they approximated all waves by strong discontinuities and thus neglected the detailed structure of emerging simple waves, they computed reasonable solutions for a set of test cases. The efficiency of their algorithm was confirmed when Ryu & Jones refined it to accurately include rarefaction waves over which the pressure and density decrease steadily (Ryu & Jones 1995). They only found minor differences ($\lesssim 1\%$) to the results by Dai & Woodward.

For the performance tests of the GADGET-2 code, we employ the Riemann solver by Dai & Woodward. Since the correct description of rarefaction waves involves the inclusion of a number of unwieldy equations while improving the exactness of the Riemann solver by only a small factor, this simplification is justified.

### 5.1.4 Construction of the MHD Riemann solver

We present the key steps taken by Dai and Woodward to develop a non-linear MHD Riemann solver. For a comprehensive description, see the original paper by Dai & Woodward (1994) or the advanced approach by Ryu & Jones (1995).

**Basic principles**

Starting from the regular MHD Riemann problem, we can already infer the number and types of waves we expect and in which order they will appear (see Figure 5.1). By restricting ourselves to strong discontinuities we also know that the initial setup will be split into eight constant states consisting of the two initial zones 1 and 8 at the boundaries and six unknown intermediate states. If we were able to predict the propagation speed of each of the seven waves we could directly evaluate the field variables in each zone by starting from the boundary states and piecewise calculating the variables of the adjacent zones via the jump conditions (5.22) - (5.28). The discontinuity between the regions 4 and 5 must then fulfil the conditions for a contact discontinuity:

$$v_{x4} = v_{x5} , \qquad (5.30)$$
$$v_{y4} = v_{x5} , \qquad (5.31)$$
$$v_{z4} = v_{x5} , \qquad (5.32)$$
$$p_4 = p_5 . \qquad (5.33)$$

The Riemann solver obeys the same principle. Before we can start the solving procedure we need to derive analytical expressions for the seven wave speeds.

For simplicity, we set $\mu_0 = 1$. The entropy mode simply follows the fluid motion and therefore $v_{\mathrm{d}} = v_x$, the Alfvén velocity equals $\sqrt{B_x^2/\rho}$. The propagation speed of the slow and fast waves can be expressed as a function of the upstream quantities and the jump in the tangential magnetic field components over the discontinuity, $[B_\perp] = B_{\perp\mathrm{d}} - B_{\perp\mathrm{u}}$, where $B_\perp = \sqrt{B_y^2 + B_z^2}$. This is achieved by using equations (5.22) - (5.27) to eliminate all downstream variables except for $B_y$ and $B_z$ and replacing them in the last jump condition

(5.28), which then has to be solved for $W$. The procedure is straightforward but tedious since it involves a lot of nested functions. The result is (Ryu & Jones 1995)

$$W_{f,s}^2 = \frac{1}{2}\frac{1}{1+S_0}\left[(C_s^2 + C_f^2 + S_1) \pm \sqrt{(C_s^2 + C_f^2 + S_1)^2 - 4(1+S_0)(C_s^2 C_f^2 - S_2)}\right], \quad (5.34)$$

where $C_f = \rho C_f$ and $C_s = \rho C_s$. The upper and lower signs refer to fast and slow waves respectively. The coefficients $S_0, S_1, S_2$ are given by

$$S_0 = -\frac{1}{2}(\gamma - 1)\frac{[B_\perp]}{B_\perp}, \quad (5.35)$$

$$S_1 = \frac{1}{2}\left(-(\gamma-2)C_\perp^2\frac{[B_\perp]}{B_\perp} + 2C_0^2 - (\gamma-4)C_\perp^2 - 2\gamma C_a^2\right)\frac{[B_\perp]}{B_\perp}, \quad (5.36)$$

$$S_2 = \frac{1}{2}\left(\rho C_a^2([B_\perp]^2) + \sqrt{\rho}(\gamma+2)C_\perp C_a^2[B_\perp] + C_\perp^2 C_a^2(\gamma+1) + (\gamma+1)C_a^4 - 2C_0^2 C_a^2\right)\frac{[B_\perp]}{B_\perp}. \quad (5.37)$$

If we consider the zones 1 and 8 in the Riemann problem as two pre-shock states, the upstream quantities for the fast wave speeds are defined through the initial conditions. The only indefinite variables left are the downstream transverse components of the magnetic field.

## Step 1

We start the solving procedure with an initial guess for one transverse magnetic field component (e.g., $y$-component) $B_{y2}$, $B_{y4}$, and $B_{y7}$ in the regions 2, 4, and 7, and the common orientation of the transverse part of the magnetic field $\psi = \arctan(B_{z3}/B_{y3})$ in regions 3, 4, 5, and 6.

## Step 2

Inserting the upstream quantities and the guess for the corresponding downstream $B_y$-component into equation (5.34), we can calculate the two fast shock speeds, one for the wave moving to the right, the other for the wave moving to the left. We subsequently apply the jump conditions (5.22) - (5.27) with these shock speeds and the values for $B_{y2}$ and $B_{y7}$ respectively to obtain the complete post-shock states in regions 2 and 7.

## Step 3

States 2 and 7 now serve as the upstream states for the Alfvén waves. Since Alfvén discontinuities are non-compressive we have

$$\rho_d = \rho_u, \quad p_d = p_u, \quad v_{xd} = v_{xu}, \quad (5.38)$$

and the Alfvén speed can directly be determined. With the initial guess for $\psi$ we perform the rotations according to

$$B_{y\mathrm{d}} = \cos(\psi)\sqrt{B_{y\mathrm{u}}^2 + B_{z\mathrm{u}}^2}\,, \tag{5.39}$$

$$B_{z\mathrm{d}} = \sin(\psi)\sqrt{B_{y\mathrm{u}}^2 + B_{z\mathrm{u}}^2}\,, \tag{5.40}$$

$$u_{y\mathrm{d}} = u_{y\mathrm{u}} - \frac{B_x}{\sqrt{B_x^2/\rho}}(B_{y\mathrm{d}} - B_{y\mathrm{u}})\,, \tag{5.41}$$

$$u_{z\mathrm{d}} = u_{z\mathrm{u}} - \frac{B_x}{\sqrt{B_x^2/\rho}}(B_{z\mathrm{d}} - B_{z\mathrm{u}})\,, \tag{5.42}$$

to obtain the field variables in zones 3 and 6, respectively.

## Step 4

We repeat the procedure in Step 2 for the slow shocks and inserting our initial guess for $B_{y4}$ to get the states in 4 and 5.

## Step 5

Since we only made an estimate for the quantities $B_{y2}$, $B_{y4}$, $B_{y7}$, and $\psi$, the states in regions 4 and 5 will not satisfy the conditions for the contact discontinuity (5.30) - (5.33). Nevertheless, for an educated guess, the deviations should be small.

To improve the guess for $B_{y2}$, $B_{y4}$, $B_{y7}$, and $\psi$, we use a Newton-Raphson scheme to find the root of the following system of functions:

$$\begin{align}
F_1 &= v_{x5}(B_{y2}, B_{y4}, \psi) - v_{x4}(B_{y4}, B_{y7}, \psi)\,, \tag{5.43}\\
F_2 &= v_{y5}(B_{y2}, B_{y4}, \psi) - v_{y4}(B_{y4}, B_{y7}, \psi)\,, \tag{5.44}\\
F_3 &= v_{z5}(B_{y2}, B_{y4}, \psi) - v_{z4}(B_{y4}, B_{y7}, \psi)\,, \tag{5.45}\\
F_4 &= p_5(B_{y2}, B_{y4}, \psi) - p_4(B_{y4}, B_{y7}, \psi)\,. \tag{5.46}
\end{align}$$

For the evaluation of the functions $F_1$ - $F_4$ we have to repeat Steps 1 - 4 for each iteration. The associated Jacobian matrix is numerically approximated. If the initial guess is reasonable, usually only a couple of iterations leads to very good convergence.

The success of the Newton-Raphson iteration sensitively depends on the initial guess for $B_{y2}$, $B_{y4}$, $B_{y7}$, and $\psi$. In some Riemann problems, even a minor deviation in one of the parameters will cause negative radicants in the shock speed (5.34), and the iteration will fail. Several methods for finding an appropriate initial guess are described in **Dai & Woodward (1994)** and **Ryu & Jones (1995)**. The efficiency of a particular approach varies with the number of emerging weak and strong discontinuities. Unfortunately, whether the solution of a given Riemann problem only consists of strong discontinuities or also involves compression and/or rarefactions waves is a priori not known. To avoid the difficulties, we perform our numerical shock tube tests with some of the Riemann problems presented in the paper by Ryu & Jones, from which we can borrow the proper values for $B_{y2}$, $B_{y4}$, $B_{z4}$, and $B_{y7}$.

### 5.1.5 Numerical tests

The following shock tube tests were carried out with the GADGET-2 code. The simulation volume is an elongated box with side length ratios $x : y : z = 4000 : 1 : 1$. The SPH gas particles have equal masses and were set up in an amorphous glass-like distribution that was produced by simulating a gas of the desired density in a cubic box with gravitational forces switched off. By the time the relative particle motion came to rest the configuration was in hydrostatic equilibrium.

According to the required densities in the shock tube simulations, the number of particles per tube ranges between 220000 and 415400. For a visualisation of the results without disturbing boundary effects, the edges of the boxes in $x$-direction are cut. The remaining domain, $x \in [1500, 2500]$, is divided into 1000 equally spaced bins and rescaled to 1. The hydrodynamic quantities and magnetic fields from the simulation are then averaged over the number of gas particles located in each bin.

The first Riemann problem investigated is the test problem 2a in Ryu & Jones (hereafter R&J) and the first problem in Dai & Woodward (hereafter D&W) respectively. It is set up with the initial states $B_x = 2.0/\sqrt{4\pi}$ and

$$\vec{U}_{\mathrm{L}} = (\rho, v_x, v_y, v_z, B_y, B_z, p)_{\mathrm{L}} = (1.08, 0.01, 0.5, 3.6/\sqrt{4\pi}, 2.0/\sqrt{4\pi}, 0.95) \,,$$
$$\vec{U}_{\mathrm{R}} = (\rho, v_x, v_y, v_z, B_y, B_z, p)_{\mathrm{R}} = (1.0, 0.0, 0.0, 0.0, 4.0/\sqrt{4\pi}, 2.0/\sqrt{4\pi}, 1.0) \,.$$

The iteration was primarily started with the exact values for $B_{y2}$, $B_{y4}$, $B_{y7}$, and $B_{z4}$ taken from R&J. As expected in this case, the solver reports successful convergence after only one iteration step. To check the robustness of the iteration procedure, the initial guess was modified to deviate from the solution by $10 - 20$ %. The iteration then took a few more steps until convergence was obtained. The results are shown in Table 5.1a. The states computed by our Riemann solver perfectly agree with the results given in Ryu & Jones (1995). In Table 5.1b we give the associated Lagrangian velocities of the fast and slow magnetosonic waves together with their Mach numbers. Since all four Mach numbers are larger than 1, the magnetosonic waves are shock waves, albeit the shocks are rather weak.

Figure 5.2 shows a snapshot of the simulation at $t = 0.1$. The averaged hydrodynamic quantities and magnetic fields $\langle \rho(x) \rangle$, $\langle p(x) \rangle$, $\langle v_x(x) \rangle$, $\langle v_y(x) \rangle$, $\langle v_z(x) \rangle$, $\langle B_x(x) \rangle$, $\langle B_y(x) \rangle$, $\langle B_z(x) \rangle$, as well as the Mach numbers $\langle M(x) \rangle$ are plotted as solid black lines. The initial conditions and analytical solutions of our Riemann solver are overlaid as red dotted and red solid lines. The overall agreement between the simulated and analytic solution is very good, except for the Mach numbers which are by $\sim$10 % too large for the two fast and by $\sim$3 % too small for the right-facing slow magnetosonic shock.

The wrong Mach number computation in GADGET-2 is a systematic error which is caused by the different evaluation of the Mach numbers in hydrodynamics and MHD: For a hydrodynamic shock, the Mach number relates the shock speed to the sound speed. In MHD however, the Mach number is defined by the ratio of the shock speed to the characteristic wave speed. For a fast magnetosonic shock, the latter is given by the fast wave speed $c_{\mathrm{f}}$, defined in Equation (5.13). Likewise, for a slow shock, the characteristic

velocity is the slow wave speed $c_s$, given by Equation (5.14). Depending on the strength of the magnetic field, the wave speeds more or less differ from the sound speed $a$, and thus lead to the overestimation of the fast, and the underestimation of the slow shock Mach numbers by the code.

As can be seen in Figure 5.2, the characteristic SPH broadening of the wave fronts is only weakly pronounced at the outer discontinuities whereas the resolution gets poorer at the Alfvén discontinuities and the inner shock fronts. The overshooting in the gas pressure at the contact discontinuity is caused by the initial conditions which are constructed by patching two boxes with different particle densities together without additional smoothing. The particle radii at the junction thus jump abruptly, resulting in a small unphysical amplitude after the SPH interpolation. Since the gas pressure is a product of the two SPH interpolated fields $\rho$ and $u$, this effect is enforced in the $p_g$-diagram. Consequently, for larger differences in the initial densities and therefore higher jumps in the SPH smoothing lengths, we expect the overshoot in $p_g$ to become larger. Concerning the magnetic fields, the oscillations around the magnetic discontinuities are well suppressed by the smoothing algorithm. In the $x$-component a minor deviation from the constant value $B_x = 0.564$ is observable but apparently does not strongly affect the result.

The second shock tube we consider is the Riemann problem 2b in R&J. The longitudinal magnetic field component is $B_x = 3.0/\sqrt{4\pi}$ and the left and right states are given by

$$\begin{aligned}
\vec{U}_L &= (1.0, 0.0, 0.0, 6.0/\sqrt{4\pi}, 0.0, 1.0)\,, \\
\vec{U}_R &= (0.1, 0.0, 0.0, 0.0, 1.0/\sqrt{4\pi}, 0.0, 10.0)\,.
\end{aligned}$$

For the initial guess we took the values $B_{y2} = 3.5$, $B_{y4} = 1.0$, $B_{z4} = 0.2$, and $B_{y7} = 0.2$ which differ from the final values given in R&J by $\sim 10 - 20$ %. The solution found with the Riemann solver after three iteration steps is presented in Table 5.2a, with the corresponding Mach numbers and wave velocities given in Table 5.2b. The Mach numbers indicate that the shock tube consists of two left-facing magnetosonic shocks, the contact discontinuity, and two right-facing rarefactions, each wave pair separated by a rotational discontinuity. Like in the test before, the results of our iteration accurately match the analytical solutions found by R&J.

In Figure 5.3 the result of the GADGET-2 simulation at $t = 0.035$ is plotted. The rarefaction waves are displayed as shock fronts while in the simulation they are naturally broadened. The Alfvén wave in between is significantly smoothed out, whereas all discontinuities in the left halfspace are well resolved. The broadening might partly be explained by the large jumps in the tangential velocities together with the change of sign in the $y$-component which possibly also causes the strong numerical oscillations. Again, as had to be expected, the Mach numbers are computed incorrectly. GADGET-2 found Mach numbers of $M_{-f} \approx 2.25$ and $M_{-s} \approx 1.25$ that differ from the theoretical values in Table 5.2b by 42 % and 20 % respectively.

The third MHD Riemann problem we investigate is the problem VI in D&W which corresponds to test 1a in R&J and has the initial states $B_x = 5.0/\sqrt{4\pi}$ and

$$\begin{aligned}
\vec{U}_L &= (1.0, 10.0, 0.0, 5.0/\sqrt{4\pi}, 0.0, 20.0)\,, \\
\vec{U}_R &= (1.0, -10.0, 0.0, 0.0, 5.0/\sqrt{4\pi}, 0.0, 1.0)\,.
\end{aligned}$$

Since in this set-up the magnetic field at the boundary is continuous, we know from the beginning that the solution will not involve any rotational discontinuities. The iteration was started with the initial guess $B_{y2} = 3.6$, $B_{y4} = 4.2$, $B_{z4} = 5.2$, and $B_{y7} = 0$. This time, the initial values differ from the final solution by only $\sim 5\%$ since any larger deviation resulted in undefined wave speeds. With the specified parameter setting convergence was reached within eight iteration steps. In Table 5.3a we give the final values of the fields in the eight zones. The agreement with R&J is very good. From the Mach numbers in Table 5.3b we infer that, from left to right, the Riemann problem contains a fast shock, a slow rarefaction, the initial contact discontinuity, a slow and a fast shock.

The simulated Mach numbers at $t = 0.02$ are shown in the upper right panel of Figure 5.4. The Mach number of the left shock is in accord with the theoretical one, whereas the Mach number of the fast right-facing shock wave is overestimated by $\sim 35$ %. All other quantities are computed correctly, with minor aberrations due to numerical oscillations and a small deviation from $B_x = 1.41$, caused by the non-vanishing divergence.

As a fourth test we investigate the slightly modified Riemann problem 3b in R&J. Originally, the shock tube has a vanishing longitudinal magnetic field component. In that case only two magnetosonic waves and a contact discontinuity occur. This specific problem demands a particular implementation of the Riemann solver since the modified jump conditions result in a different equation for the wave velocities (see Dai & Woodward (1994)). To avoid a re-implementation of the algorithm we approximate the Riemann problem by adding a small magnetic field in $x$-direction. The initial conditions then yield $B_x = 0.01$ and

$$\begin{aligned}
\vec{U}_{\mathrm{L}} &= (1.0, -1.0, 0.0, 0.0, 1.0, 0.0, 1.0), \\
\vec{U}_{\mathrm{R}} &= (1.0, 1.0, 0.0, 0.0, 1.0, 0.0, 1.0).
\end{aligned}$$

We start the iteration with the values $B_{y2} = 0.5$, $B_{y4} = 0.5$, $B_{y7} = 0.5$, and $B_{z4} = 0$ that approximately correspond to the solution of the Riemann problem given in R&J. Since we have changed the initial conditions of the Riemann problem we expect a slightly different outcome. The solver needs two iteration steps, the results are given in Table 5.4a. Due to continuity of the magnetic field over the initial boundary the shock tube contains no rotational discontinuities. The density drops by almost 50 % over the two outer magnetosonic waves, while the decompression over the inner slow waves is very weak. The corresponding wave speeds and Mach numbers are found in Table 5.4b.

Figure 5.5 shows a snapshot of the simulation at $t = 0.07$. As described in R&J, we observe two strong and identical rarefactions on each side of the tube, while the additional pair of slow rarefactions very close to the central discontinuity is generated by the inclusion of the weak longitudinal magnetic field. Comparing the plot to Figure 3b in R&J we can see that the fading of the $B_x$-component causes the slow waves to coincide with the initial boundary. The degeneracy of the wave speeds is obvious from equations (5.12)-(5.14). The agreement of the analytical and simulated fast wave velocities is not very accurate, leading to slightly lower central densities and tangential magnetic fields and a higher pressure in the simulation. Where the difference arises from is unclear, it might either be a non-unique root of equations (5.43) - (5.46) or a numerical inaccuracy.

The last Riemann problem is the MHD analogue of the Sod shock tube (Sod 1978). It was first described by Brio & Wu (1988) and despite its special wave structure it is nowadays a standard test for most astrophysical MHD codes (Dai & Woodward 1994; Ryu & Jones 1995; Balsara 1998; Dolag et al. 1999). The Brio & Wu shock tube is the fourth problem discussed in D&W and the test 5a in R&J respectively. It has the initial states $B_x = 0.75$ and

$$\begin{aligned} \vec{U}_{\mathrm{L}} &= (1.0, 0.0, 0.0, 1.0, 0.0, 1.0)\,, \\ \vec{U}_{\mathrm{R}} &= (0.125, 0.0, 0.0, 0.0, -1.0, 0.0, 0.1)\,, \end{aligned}$$

where the tangential component of the magnetic field changes sign over the discontinuity. A configuration of that kind results in a so-called compound wave structure which consists of a shock followed by a rarefaction wave of the same family. The existence of compound waves in nature is contested by several authors who argue that such intermediate states might be an artifact of restricting the geometry to one spatial dimension whilst allowing the magnetic field to vary in two dimensions (Barmin et al. 1996; Falle & Komissarov 2001). Nevertheless, although being potentially unphysical, the Brio & Wu shock tube is an interesting test case for our Riemann solver.

The results we found after iterating from the initial values $B_{y2} = 0.5$, $B_{y4} = -0.5$, $B_{y7} = -0.8$, and $B_{z4} = 0$ are shown in Tables 5.5a and 5.5b. They compare well to the analytical solution given in R&J with differences only in the second or third decimal places. According to our solver this Riemann problem involves a fast rarefaction, a rotational discontinuity, a slow shock, a contact discontinuity, a slow shock, and a fast rarefaction.

The simulation however produces a different result. As shown in Figure 5.6 at $t = 0.1$, the Alfvén wave and the slow shock on the left coalesce to a single compound structure. The difference between the analytical and the numerical solution of the Brio & Wu shock tube is intrinsic and has been seen in all previously reported simulations (Brio & Wu 1988; Stone et al. 1992). The other waves in the plot agree with the theoretical prediction except for a minor discrepancy in the velocity of the rightwards propagating slow shock. The theoretical wave speed is slightly smaller than the simulated one, leading to small errors in the subsequent state which is furthermore overlaid by numerical oscillations. The estimated Mach number of the slow shock is rather close to the theoretical value $M_{+s}$ with a relative error of only $\sim 8\%$. The left Mach number in the upper right panel belongs to the compound wave and, according to GADGET-2, has the value $M_{-\mathrm{comp}} \approx 1.25$.

### 5.1.6 Conclusions

Through the examination of five different MHD Riemann problems we have demonstrated that the analytical Riemann solver works correctly and is able to reproduce the results of four shock tube tests described by Ryu & Jones (1995). We found that for a sufficiently accurate initial guess that deviates from the final result by 5 to 20 %, depending on the Riemann problem, the convergence is reached within a maximum of eight iterations. The results of three general Riemann problems agree exactly with those given in Ryu & Jones (1995) while the Brio & Wu shock tube, which is a special case due to its compound wave structure, can be approximated with $\gtrsim 99$ % exactness.
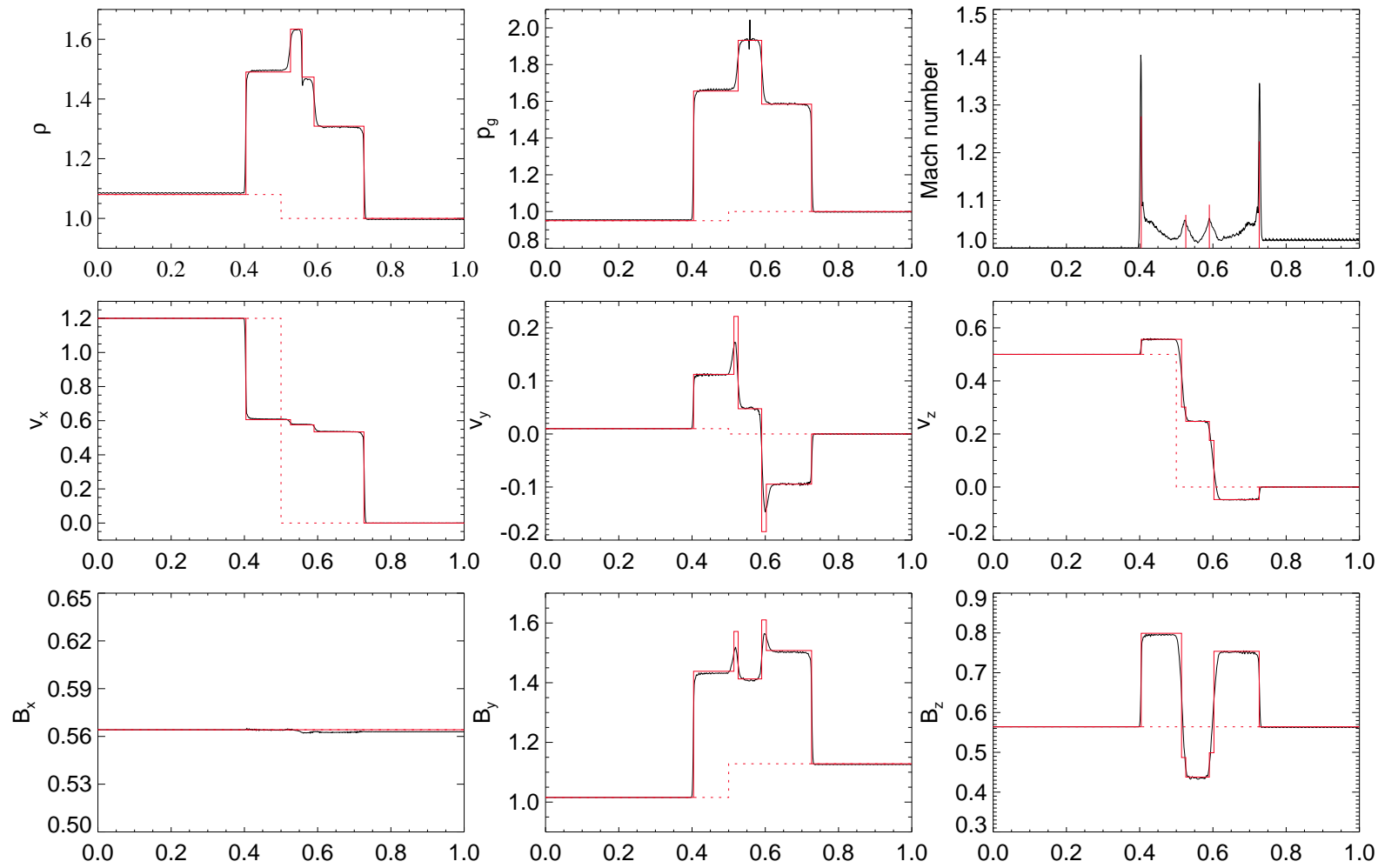
Figure 5.2: Riemann problem 1 (R&J 2a) at $t = 0.1$ with waves from left to right: fast shock, rotational discontinuity, slow shock, contact discontinuity, slow shock, rotational discontinuity, fast shock
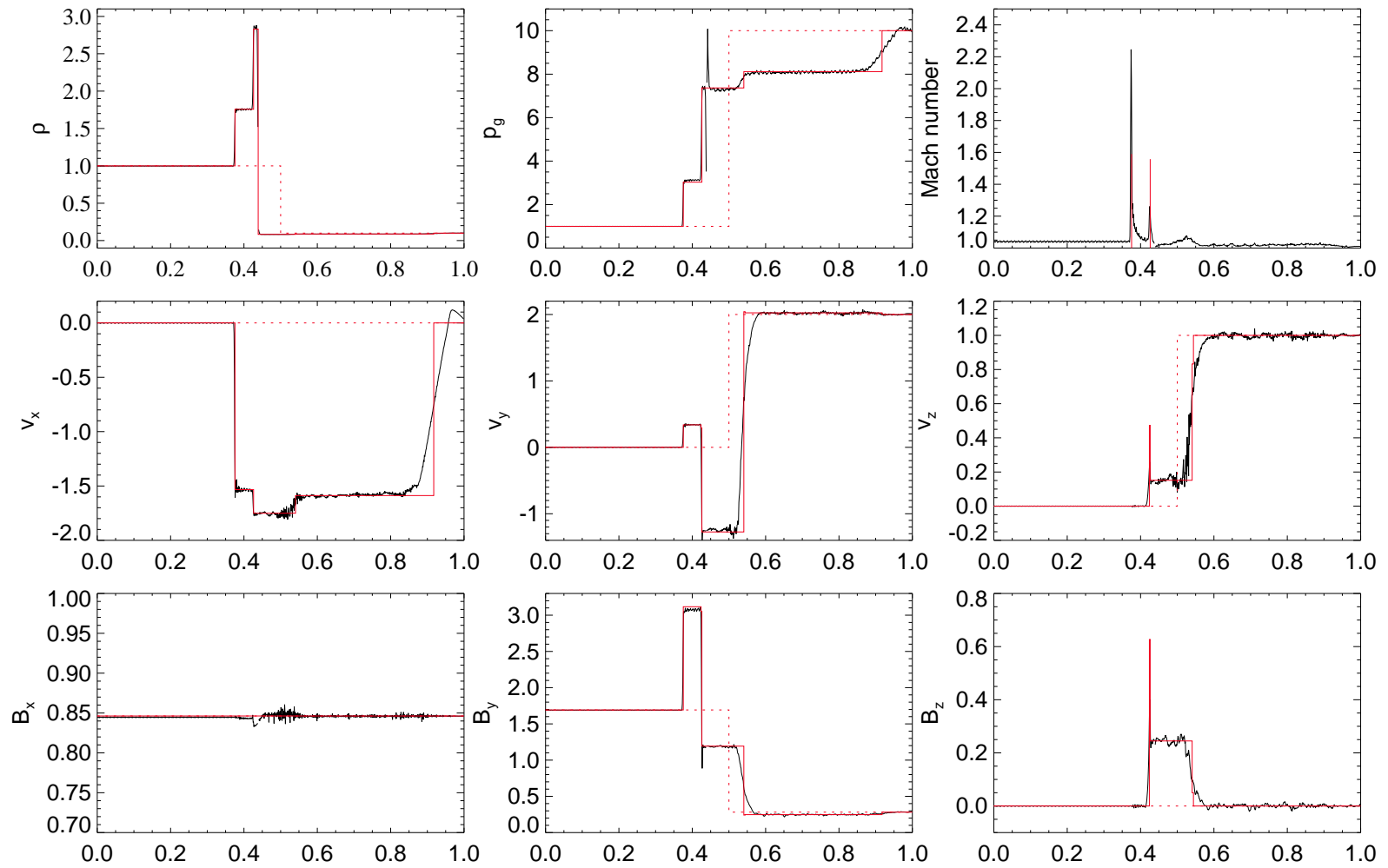
Figure 5.3: Riemann problem 2 (R&J 2b) at $t = 0.035$ with waves from left to right: fast shock, Alfvén wave, slow shock, contact discontinuity, slow rarefaction, Alfvén wave, fast rarefaction
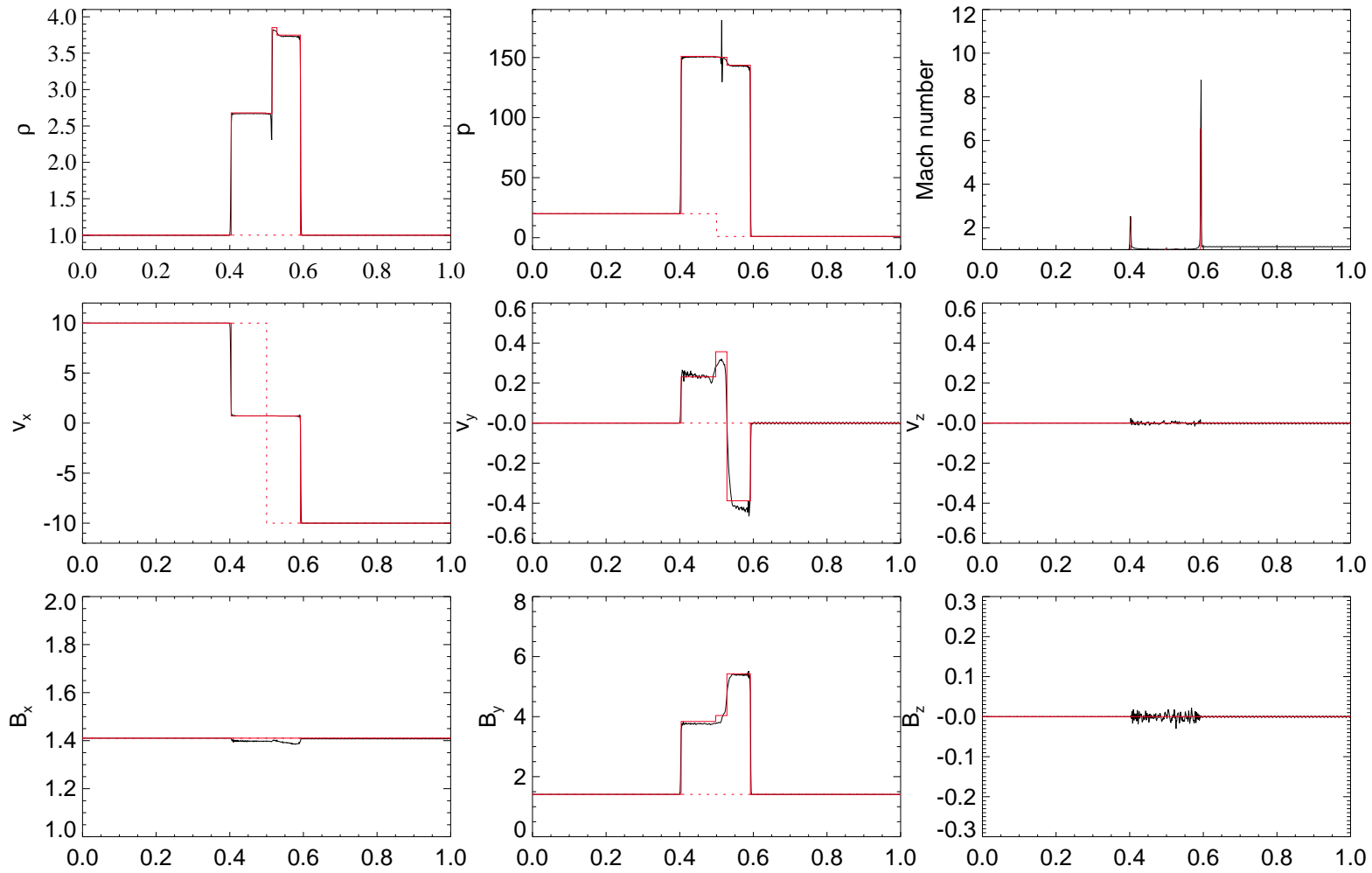
Figure 5.4: Riemann problem 3 (R&J 1a) at $t = 0.02$ with waves from left to right: fast shock, slow rarefaction, contact discontinuity, slow shock, fast shock
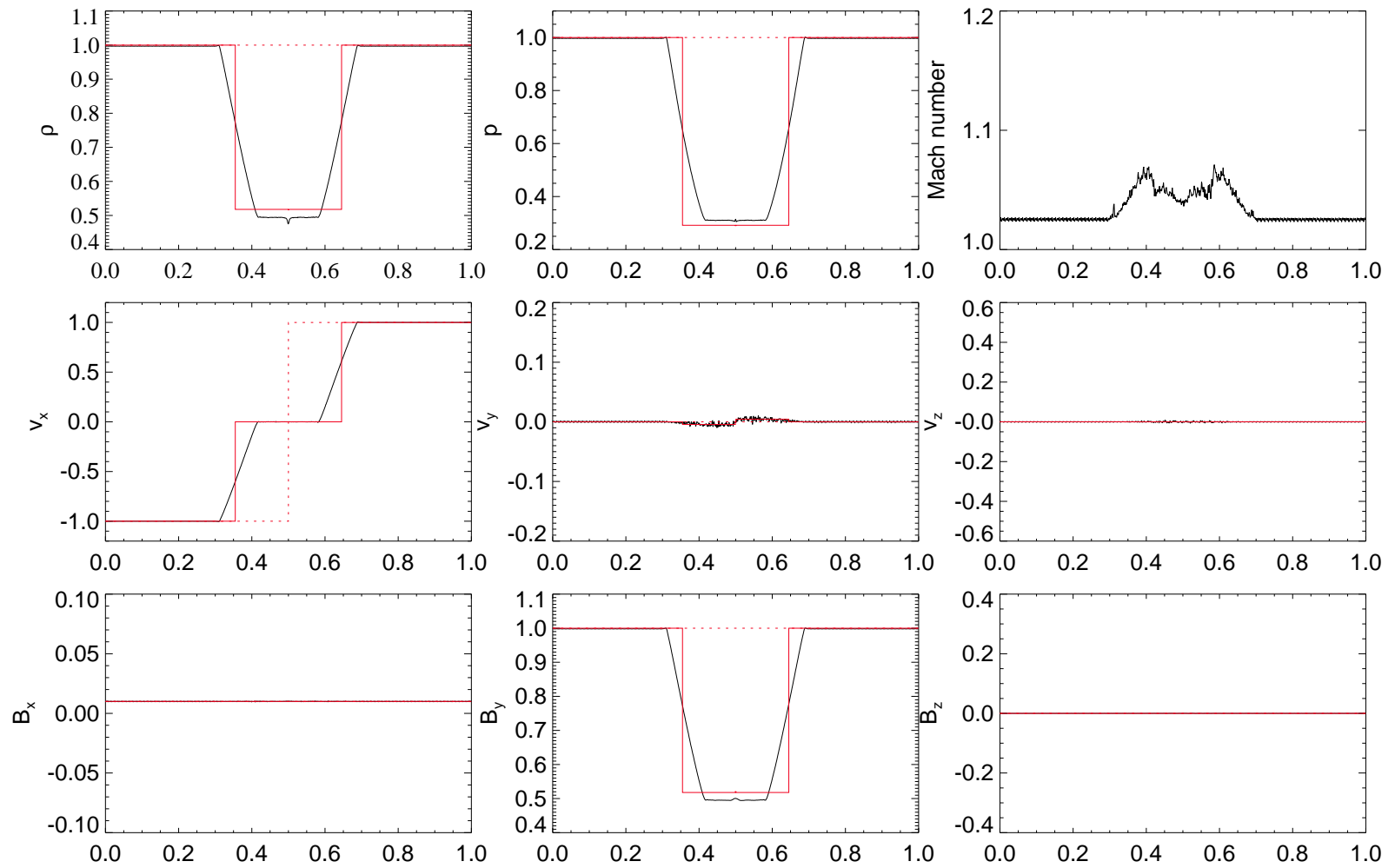
Figure 5.5: Riemann problem 4 (R&J 3b) at $t = 0.07$ with waves from left to right: fast rarefaction, slow rarefaction, tangential discontinuity, slow rarefaction, fast rarefaction
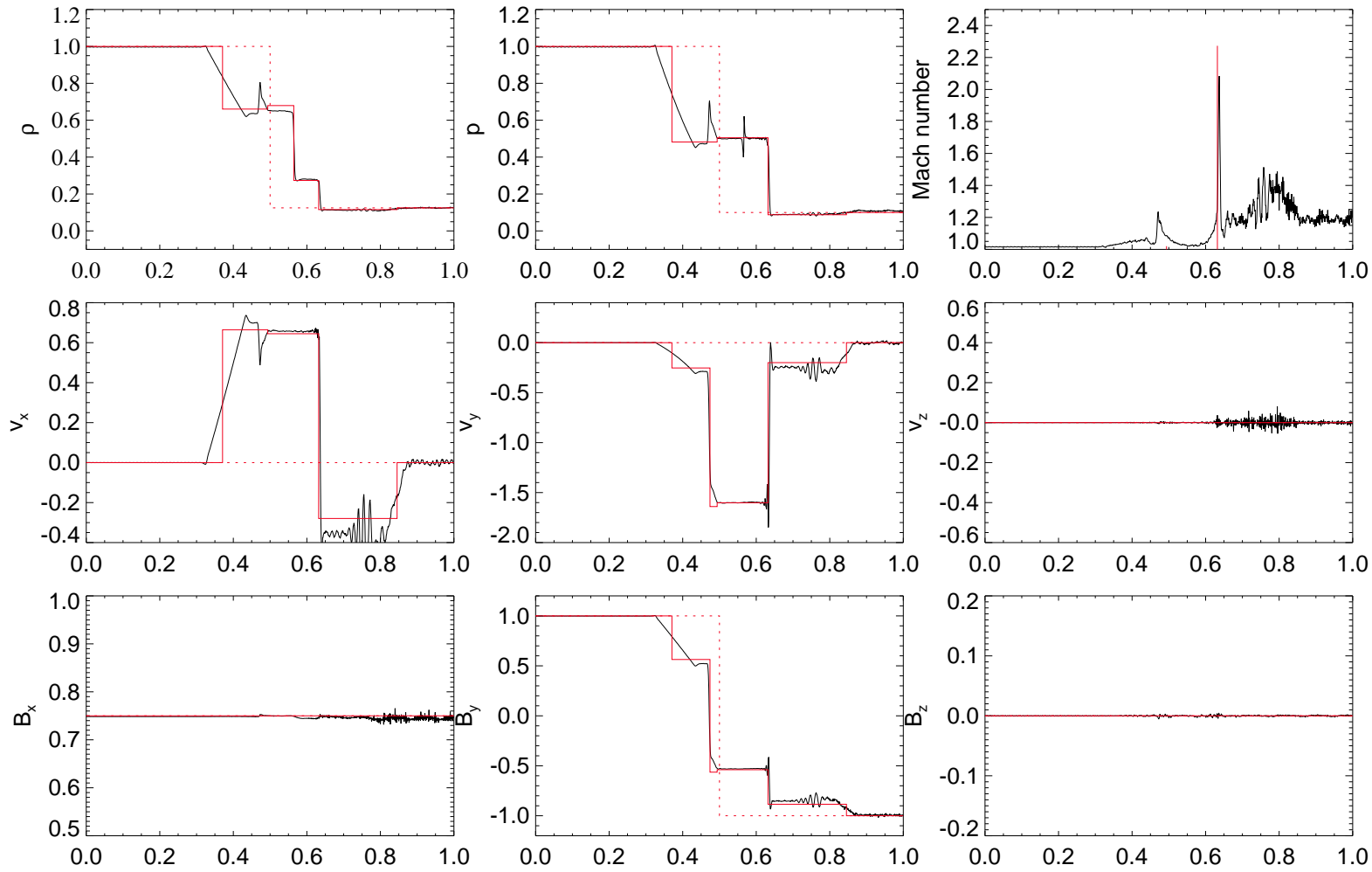
Figure 5.6: Riemann problem 5 (R&J 5a) at $t = 0.1$ with waves from left to right: fast rarefaction, slow compound, contact discontinuity, slow shock, fast rarefaction

Table 5.1a: Solution of Riemann problem 1 (R&J 2a)

| $\rho$ | $v_c$ | $v_y$ | $v_z$ | $B_y$ | $B_z$ | $p$ |
|--------|--------|---------|---------|--------|--------|--------|
| 1.0800 | 1.2000 | 0.0100 | 0.5000 | 1.0155 | 0.5642 | 0.9500 |
| 1.4903 | 0.6059 | 0.1124 | 0.5569 | 1.4383 | 0.7991 | 1.6558 |
| 1.4903 | 0.6059 | 0.2216 | 0.3012 | 1.5717 | 0.4870 | 1.6558 |
| 1.6343 | 0.5754 | 0.0476 | 0.2473 | 1.4126 | 0.4377 | 1.9317 |
| 1.4735 | 0.5754 | 0.0476 | 0.2473 | 1.4126 | 0.4377 | 1.9317 |
| 1.3090 | 0.5343 | −0.1841 | 0.1756 | 1.6103 | 0.4990 | 1.5844 |
| 1.3090 | 0.5343 | −0.0946 | −0.0473 | 1.5078 | 0.7539 | 1.5844 |
| 1.0000 | 0.0000 | 0.0000 | 0.0000 | 1.1284 | 0.5642 | 1.0000 |

Table 5.1b: Lagrangian wave speeds and Mach numbers of Riemann problem 1

| $W_{-\mathrm{f}}$ | $W_{-\mathrm{s}}$ | $W_{+\mathrm{s}}$ | $W_{+\mathrm{f}}$ |
|--------|--------|--------|--------|
| 2.33047 | 0.51594 | 0.48144 | 2.26379 |

| $M_{-\mathrm{f}}$ | $M_{-\mathrm{s}}$ | $M_{+\mathrm{s}}$ | $M_{+\mathrm{f}}$ |
|--------|--------|--------|--------|
| 1.27611 | 1.06985 | 1.09121 | 1.22385 |

Table 5.2a: Solution of Riemann problem 2 (R&J 2b)

| $\rho$ | $v_c$ | $v_y$ | $v_z$ | $B_y$ | $B_z$ | $p$ |
|--------|--------|---------|---------|--------|--------|--------|
| 1.00000 | 0.00000 | 0.00000 | 0.00000 | 1.69257 | 0.00000 | 1.00000 |
| 1.75761 | −1.53351 | 0.33872 | 0.00000 | 3.11650 | 0.00000 | 3.03182 |
| 1.75761 | −1.53351 | 0.29067 | 0.47288 | 3.05279 | 0.62693 | 3.03182 |
| 2.83060 | −1.75055 | −1.27369 | 0.15162 | 1.19260 | 0.24491 | 7.36537 |
| 0.08332 | −1.75055 | −1.27369 | 0.15162 | 1.19260 | 0.24491 | 7.36537 |
| 0.08825 | −1.58801 | 2.04164 | 0.83247 | 0.24235 | 0.04977 | 8.11532 |
| 0.08825 | −1.58801 | 2.02462 | 1.00000 | 0.24741 | 0.00000 | 8.11532 |
| 0.10000 | 0.00000 | 2.00000 | 1.00000 | 0.28210 | 0.00000 | 10.0000 |

Table 5.2b: Lagrangian wave speeds and Mach numbers of Riemann problem 2

| $W_{-\mathrm{f}}$ | $W_{-\mathrm{s}}$ | $W_{+\mathrm{s}}$ | $W_{+\mathrm{f}}$ |
|--------|--------|--------|--------|
| 3.55765 | 1.00632 | 0.242564 | 1.1926 |

| $M_{-\mathrm{f}}$ | $M_{-\mathrm{s}}$ | $M_{+\mathrm{s}}$ | $M_{+\mathrm{f}}$ |
|--------|--------|--------|--------|
| 1.58954 | 1.5579 | 0.96714 | 0.921488 |

Table 5.3a: Solution of Riemann problem 3 (R&J 1a)

| $\rho$ | $v_c$ | $v_y$ | $v_z$ | $B_y$ | $B_z$ | $p$ |
|---|---|---|---|---|---|---|
| 1.00000 | 10.00000 | 0.00000 | 0.00000 | 1.41047 | 0.00000 | 20.00000 |
| 2.67975 | 0.721129 | 0.23138 | 0.00000 | 3.83879 | 0.00000 | 150.98000 |
| 2.67975 | 0.721129 | 0.23138 | 0.00000 | 3.83879 | 0.00000 | 150.98000 |
| 2.67132 | 0.723762 | 0.35684 | 0.00000 | 4.03790 | 0.00000 | 150.19000 |
| 3.85080 | 0.723762 | 0.35684 | 0.00000 | 4.03790 | 0.00000 | 150.19000 |
| 3.74812 | 0.705049 | −0.38803 | 0.00000 | 5.42713 | 0.00000 | 143.56600 |
| 3.74812 | 0.705049 | −0.38803 | 0.00000 | 5.42713 | 0.00000 | 143.56600 |
| 1.00000 | −10.00000 | 0.00000 | 0.00000 | 1.41047 | 0.00000 | 1.00000 |

Table 5.3b: Lagrangian wave speeds and Mach numbers of Riemann problem 3

| $W_{-f}$ | $W_{-s}$ | $W_{+s}$ | $W_{+f}$ |
|---|---|---|---|
| 14.8028 | 2.23848 | 2.63066 | 14.6005 |

| $M_{-f}$ | $M_{-s}$ | $M_{+s}$ | $M_{+f}$ |
|---|---|---|---|
| 2.48652 | 0.997678 | 1.02136 | 6.54282 |

Table 5.4a: Solution of Riemann problem 4 (R&J 3b)

| $\rho$ | $v_c$ | $v_y$ | $v_z$ | $B_y$ | $B_z$ | $p$ |
|---|---|---|---|---|---|---|
| 1.00000 | −1.00000 | 0.00000 | 0.00000 | 1.00000 | 0.00000 | 1.00000 |
| 0.51791 | −0.00003 | −0.00449 | 0.00000 | 0.51789 | 0.00000 | 0.29167 |
| 0.51791 | −0.00003 | −0.00449 | 0.00000 | 0.51789 | 0.00000 | 0.29167 |
| 0.51648 | 0.00000 | 0.00000 | 0.00000 | 0.52047 | 0.00000 | 0.29032 |
| 0.51648 | 0.00000 | 0.00000 | 0.00000 | 0.52047 | 0.00000 | 0.29032 |
| 0.51791 | 0.00003 | 0.00449 | 0.00000 | 0.51789 | 0.00000 | 0.29167 |
| 0.51791 | 0.00003 | 0.00449 | 0.00000 | 0.51789 | 0.00000 | 0.29167 |
| 1.00000 | 1.00000 | 0.00000 | 0.00000 | 1.00000 | 0.00000 | 1.00000 |

Table 5.4b: Lagrangian wave speeds and Mach numbers of Riemann problem 4

| $W_{-f}$ | $W_{-s}$ | $W_{+s}$ | $W_{+f}$ |
|---|---|---|---|
| 1.07426 | 0.00576556 | 0.00576556 | 1.07426 |

| $M_{-f}$ | $M_{-s}$ | $M_{+s}$ | $M_{+f}$ |
|---|---|---|---|
| 0.657845 | 0.998009 | 0.998009 | 0.657845 |

Table 5.5a: Solution of Riemann problem 5 (R&J 5a)

| $\rho$ | $v_c$ | $v_y$ | $v_z$ | $B_y$ | $B_z$ | $p$ |
|---|---|---|---|---|---|---|
| 1.00000 | 0.00000 | 0.00000 | 0.00000 | 1.00000 | 0.00000 | 1.00000 |
| 0.66045 | 0.66468 | $-0.25326$ | 0.00000 | 0.56342 | 0.00000 | 0.48194 |
| 0.66045 | 0.66468 | $-1.63983$ | 0.00000 | $-0.56342$ | 0.00000 | 0.48194 |
| 0.67920 | 0.64462 | $-1.60187$ | 0.00000 | $-0.53913$ | 0.00000 | 0.50496 |
| 0.27378 | 0.64462 | $-1.60187$ | 0.00000 | $-0.53913$ | 0.00000 | 0.50496 |
| 0.11564 | $-0.27951$ | $-0.19969$ | 0.00000 | $-0.88503$ | 0.00000 | 0.08767 |
| 0.11564 | $-0.27951$ | $-0.19969$ | 0.00000 | $-0.88503$ | 0.00000 | 0.08767 |
| 0.12500 | 0.00000 | 0.00000 | 0.00000 | $-1.00000$ | 0.00000 | 0.10000 |

Table 5.5b: Lagrangian wave speeds and Mach numbers of Riemann problem 5

| $W_{-\mathrm{f}}$ | $W_{-\mathrm{s}}$ | $W_{+\mathrm{s}}$ | $W_{+\mathrm{f}}$ |
|---|---|---|---|
| 1.29287 | 0.479982 | 0.185017 | 0.431798 |

| $M_{-\mathrm{f}}$ | $M_{-\mathrm{s}}$ | $M_{+\mathrm{s}}$ | $M_{+\mathrm{f}}$ |
|---|---|---|---|
| 0.758331 | 1.02016 | 2.27309 | 0.944193 |

The shock tube simulations carried out with GADGET-2 reconfirmed the high performance of the code that was independently proven in hydrodynamic shock tubes calculations by Dolag et al. (2005) and Pfrommer et al. (2006), and by Dolag & Stasyszyn (2008) in the MHD Riemann problem. In three general MHD Riemann problems the simulations accurately matched the analytical prediction apart from minor numerical errors that are intrinsic to the SPMHD implementation. In case of a tiny longitudinal magnetic field small discrepancies in the wave speeds were detected. In the Brio & Wu shock tube problem a single compound structure instead of two separate waves evolved which is in accord with shock tube calculations carried out with other MHD codes.

The weak point in the MHD shock tube simulation with GADGET-2 is the prediction of the Mach numbers. While the estimation of the shock strength via the change in the specific entropy (see Section 4.3.3) works properly in hydrodynamical shock tubes, the values that are found in the MHD calculations deviate from the expected Mach numbers on average by about $5-15$ % in both directions. In one case, the fast shock strength is even overestimated by 42 %. The systematically false Mach number detection in presence of magnetic fields is due to the numerical implementation which is solely construed for the hydrodynamic case.

The determination of the shock strength is actually important for calculating the shock injection rate of relativistic particles in cosmological simulations including a cosmic ray component. An incorrect estimation of Mach numbers could have considerable effects on the radio luminosity of simulated galaxy clusters since the synchrotron emissivity of the SPH particles directly depends on the energy and density of the cosmic ray component.

Nevertheless, in consideration of the fact that the magnetic energy of a galaxy cluster only constitutes about 1 % of its thermal energy, with local maxima of ∼10 % under extreme conditions (see Dolag et al. 2001 and references therein), the deviation in the Mach numbers should be small. The inherited errors in the cosmic ray particle injection can thus be neglected.

Concerning the validity of our cosmological simulations it is more important to check whether the inclusion of cosmic rays allows for the correct identification of shocks fronts and whether the post-shock states are accurately calculated. Testing those issues is subject of the next section in which we will repeat the five shock tube calculations including a thermal and a non-thermal gas.

## 5.2 MHD shock tubes for a composite of thermal gas and cosmic rays

In an astrophysical context the assumption that the medium under investigation is a single magnetised plasma is a strong simplification. Shock waves in the interstellar and intracluster medium inevitably come along with particle acceleration due to the Fermi II process (see Section 3.2.2). The charged relativistic particles accumulate in the cosmic structure where they are bound by magnetic fields. For realistic simulations this non-thermal gas component must be taken into account.

To check the code performance we repeat the set of MHD shock tube tests including a fixed fraction of cosmic rays. The associated Riemann problem is analytically solved under simplifying conditions. We will use the analytical solution to check the quality of the simulation and thereby reveal potential weak points in the interplay of the SPMHD and cosmic ray module.

### 5.2.1 Extension of the MHD Riemann solver

The following derivation of an analytical solution for the MHD Riemann problem in presence of a non-thermal cosmic ray component is based on the work by Christoph Pfrommer who developed a two-fluid formalism for a thermal and a relativistic gas in the purely hydrodynamic case (see Pfrommer et al. 2006).

For the analytical derivation, we have to make the fundamental assumption that no particle acceleration takes place over the shock front. This rather unphysical simplification is necessary since any energy transfer to the cosmic ray population inevitably affects the properties of the downstream thermal gas. Consequently, the post-shock states of cosmic ray-modified shocks cannot be derived from the jump conditions anymore but need to be integrated time-dependently or calculated from nonlinear methods. This can only be achieved numerically (see Kang & Jones 2005).

As a second simplification, we set the cosmic ray adiabatic index to the constant value $\gamma_{\mathrm{CR}} = 1.38$ over the shock tube. In contrast to the thermal gas, the cosmic rays do not undergo a shock compression over supersonic wave fronts. Since relativistic particles themselves move at supersonic velocities, the cosmic rays are merely adiabatically compressed

or expanded,

$$p_{\mathrm{CRd}} = p_{\mathrm{CRu}} \left( \frac{\rho_{\mathrm{d}}}{\rho_{\mathrm{u}}} \right)^{\gamma_{\mathrm{CR}}}, \quad \epsilon_{\mathrm{CRd}} = \epsilon_{\mathrm{CRu}} \left( \frac{\rho_{\mathrm{d}}}{\rho_{\mathrm{u}}} \right)^{\gamma_{\mathrm{CR}}}. \tag{5.47}$$

To consistently include the cosmic rays in our MHD Riemann solver, we need to replace the pressure $P$ and total energy density $E$ in the jump conditions by the combined quantities $P^* = P + p_{\mathrm{CR}}$ and $E^* = E + \epsilon_{\mathrm{CR}}$:

$$P^* = p + p_{\mathrm{CR}} + \frac{1}{2}(B_x^2 + B_y^2 + B_z^2), \tag{5.48}$$

$$E^* = \frac{1}{2}\rho(v_x^2 + v_y^2 + v_z^2) + \frac{p}{\gamma - 1} + \epsilon_{\mathrm{CR}} + \frac{1}{2}(B_x^2 + B_y^2 + B_z^2), \tag{5.49}$$

where we have again set $\mu_0 = 1$.

### Derivation of the magnetosonic wave speeds

With the modified jump conditions it is not any longer possible to write the fast and slow shock speeds as functions of the upstream state and solely two downstream quantities, namely $B_{y\mathrm{d}}$ and $B_{z\mathrm{d}}$, as we did in Section 5.1.4. Since the downstream density appears in the exponent of the CR adiabatic equation, after replacing all downstream hydrodynamic variables, jump condition (5.28) cannot analytically be solved for $W$ anymore. We therefore retain the density jump in the terms for the downstream CR pressure and density and arrive at the following quadratic equation in $W^2$:

$$W^4 A + W^2 B^{\pm} + C = 0, \tag{5.50}$$

where the three coefficients $A, B^{\pm}, C$ can be written as

$$A = (By_{\mathrm{d}} - By_{\mathrm{u}})^2 \gamma - (By_{\mathrm{d}}^2 - By_{\mathrm{u}}^2), \tag{5.51}$$

$$B^{\pm} = \mp B_{y\mathrm{d}}(B_{y\mathrm{d}}^2 B_{y\mathrm{u}}(\gamma - 2) - 2B_{y\mathrm{u}} \left[ B_{z\mathrm{d}}^2 + \epsilon_{\mathrm{CRu}} \left( \frac{\rho_{\mathrm{d}}}{\rho_{\mathrm{u}}} \right) + p_{\mathrm{CRu}} \left( \frac{\rho_{\mathrm{d}}}{\rho_{\mathrm{u}}} \right) \right]$$

$$- \left[ 2B_x^2(B_{y\mathrm{d}} - B_{y\mathrm{u}})(B_{y\mathrm{d}}\gamma - B_{y\mathrm{u}}(1 + \gamma)) + B_{y\mathrm{u}}(B_{y\mathrm{u}}^2 + B_{z\mathrm{d}}^2 + B_{z\mathrm{u}}^2 \right.$$

$$\left. + 2(\epsilon_{\mathrm{CRu}} \left( \frac{\rho_{\mathrm{d}}}{\rho_{\mathrm{u}}} \right) + p_{\mathrm{u}}))\gamma + 2B_{y\mathrm{d}}((B_{y\mathrm{u}}^2 + B_{z\mathrm{u}}^2 + \epsilon_{\mathrm{CRu}})(1 - \gamma) + p_{\mathrm{CRu}} - p_{\mathrm{u}}\gamma) \right] )\rho_{\mathrm{u}}, \tag{5.52}$$

with $B^+$ for right-facing, $B^-$ for left-facing shock waves, and

$$C = B_x^2(B_x^2(B_{y\mathrm{d}} - B_{y\mathrm{u}})^2(1 + \gamma) + B_{y\mathrm{d}}(B_{y\mathrm{d}}^3 - 2B_{y\mathrm{u}}(B_{z\mathrm{d}}^2 + \epsilon_{\mathrm{CRu}} \left( \frac{\rho_{\mathrm{d}}}{\rho_{\mathrm{u}}} \right) + p_{\mathrm{CRu}} \left( \frac{\rho_{\mathrm{d}}}{\rho_{\mathrm{u}}} \right))$$

$$+ B_{y\mathrm{d}}^2 B_{y\mathrm{u}}(\gamma - 2) + 2B_{y\mathrm{u}}(\epsilon_{\mathrm{CRu}} \left( \frac{\rho_{\mathrm{d}}}{\rho_{\mathrm{u}}} \right) + p_{\mathrm{u}})\gamma + 2B_{y\mathrm{d}}(\epsilon_{\mathrm{CRu}} \left( \frac{\rho_{\mathrm{d}}}{\rho_{\mathrm{u}}} \right)(1 - \gamma)$$

$$- (B_{y\mathrm{u}}^2 + B_{z\mathrm{u}}^2 + p_{\mathrm{u}})\gamma + p_{\mathrm{CRu}} \left( \frac{\rho_{\mathrm{d}}}{\rho_{\mathrm{u}}} \right)) + (B_{y\mathrm{u}}\gamma + B_{y\mathrm{d}})(B_{y\mathrm{u}}^2 + B_{z\mathrm{d}}^2 + B_{z\mathrm{u}}^2)))\rho_{\mathrm{u}}^2. \tag{5.53}$$

For a given upstream state, equation (5.50) can be solved for $W$ if the downstream density and tangential magnetic field components are known. It must be individually tested which of the two positive solutions matches the correct wave velocity. In the MHD Riemann problem, evidence arises from the fact, that the speed of the fast wave must be larger than the speed of the slow wave.

**Iteration procedure**

We can now proceed with steps 1 to 4 in section 5.1.4, with the difference that, in addition to $B_{y2}$, $B_{y4}$, $B_{y7}$, and $\psi$, we also need to provide an initial guess for the four density jumps

$$r_2 = \frac{\rho_2}{\rho_1}, \quad r_4 = \frac{\rho_4}{\rho_3}, \quad r_5 = \frac{\rho_5}{\rho_6}, \quad r_7 = \frac{\rho_7}{\rho_8}. \tag{5.54}$$

Problems arise in step 5 when a Newton-Raphson-Iteration is used to refine the initial guess until the states in regions 4 and 5 satisfy the jump conditions for the contact discontinuity within a specified precision. Instead of four, the system of functions now depends on eight independent parameters,

$$
\begin{array}{rcl}
F_1 & = & v_{x5}(B_{y2}, B_{y4}, \psi, r_2, r_4) - v_{x4}(B_{y4}, B_{y7}, \psi, r_5, r_7), \tag{5.55} \\
F_2 & = & v_{y5}(B_{y2}, B_{y4}, \psi, r_2, r_4) - v_{y4}(B_{y4}, B_{y7}, \psi, r_5, r_7), \tag{5.56} \\
F_3 & = & v_{z5}(B_{y2}, B_{y4}, \psi, r_2, r_4) - v_{z4}(B_{y4}, B_{y7}, \psi, r_5, r_7), \tag{5.57} \\
F_4 & = & p_5(B_{y2}, B_{y4}, \psi, r_2, r_4) - p_4(B_{y4}, B_{y7}, \psi, r_5, r_7), \tag{5.58}
\end{array}
$$

for which the Newton-Raphson scheme is not applicable since the resulting $4 \times 8$ Jacobian matrix cannot be inverted. We solve the problem by temporarily fixing the four density jumps and performing a nested iteration: Holding the initial guess for $r_2$, $r_4$, $r_5$, and $r_7$ constant, we carry out a Newton-Raphson iteration until convergence is obtained and re-calculate the densities in regions 2 to 6. With the resulting density jumps and final values for $B_{y2}$, $B_{y4}$, $B_{y7}$, and $\psi$, a new Newton-Raphson iteration is started. We repeat this procedure until the total change $\Delta r = |r_{i+1} - r_i|$ in all four density jumps between two Newton-iterations becomes less than 1%.

In Section 5.1.4 we already pointed out that an inappropriate initial guess leads to the break-down of the MHD Riemann solver. We avoided the problem by constraining our shock tube tests to the Riemann problems studied by D&W for which the final values of $B_{y2}$, $B_{y4}$, $B_{y7}$, and $\psi$ are known. To test our algorithm for the composite of a thermal and a relativistic gas, we will study the same Riemann problems, but this time the additional cosmic ray component will change the initial conditions for the pressure and energy density according to (5.48). Consequently, the states given in Ryu & Jones (1995) will not match the solution anymore and finding a good initial guess gets difficult, especially since the two-fluid MHD Riemann solver now depends on eight parameters.

Another drawback of the presented method is that, precisely because of the high dimensionality of the parameter space, the solution to the system (5.55) - (5.58) found by the Riemann solver may not be unique. Starting from an initial guess, the algorithm converges

Table 5.6: The sequence of iterations for the density jumps in Riemann problem 1

| Iteration | $r_2$ | $r_4$ | $r_5$ | $r_7$ |
|---|---|---|---|---|
| 0 | 1.37991 | 1.09662 | 1.12567 | 1.30900 |
| 1 | 1.22420 | 1.02637 | 1.10186 | 1.34326 |
| 2 | 1.20369 | 1.00719 | 1.10255 | 1.35334 |
| 3 | 1.20105 | 1.00279 | 1.10367 | 1.35532 |

to the nearest root, irrespective of whether the solution is physically permitted or not. In some Riemann problems, the co-existing solutions lie very closely to each other. With respect to the performance tests of the GADGET-2 code, this leads to some complicacy.

## 5.2.2 Numerical tests

We use the same numerical set-up as in Section 5.1.5. The initial conditions for the thermal gas are identical to the MHD Riemann problems studied before, but the pressure of the compound gas is enhanced due to the partial pressure of the non-thermal cosmic rays which constitutes between 30 and 200 % of the thermal gas pressure.

This time, we cannot make a theoretical prediction of the shock strengths. The determination of the Mach numbers requires the knowledge of the fast and slow wave speeds which are to be derived from the modified MHD equations, analogous to Section 5.1.1. It turns out that the associated system of equations cannot be analytically solved for the two-fluid problem. We presume that the inclusion of cosmic rays will not further deteriorate the Mach number detection since the Mach finder algorithm already accounts for the presence of a non-thermal component. The error in the simulated Mach numbers should thus mainly be due to the missing magnetic pressure in the fast and slow wave speeds. From the results we obtained in the last section we therefore expect to a deviation by 5 to 40 %.

The first Riemann problem (2a in R&J) contains a relative cosmic ray pressure of $X_L = p_{CR}/p_{th} = 2.0$ on the left side and $X_R = p_{CR}/p_{th} = 1.0$ on the right side. The initial conditions are thus $B_x = 2.0/\sqrt{4\pi}$ and

$$\vec{U}_L = (\rho, v_x, v_y, v_z, B_y, B_z, p)_L = (1.08, 0.01, 0.5, 3.6/\sqrt{4\pi}, 2.0/\sqrt{4\pi}, 2.85),$$
$$\vec{U}_R = (\rho, v_x, v_y, v_z, B_y, B_z, p)_R = (1.0, 0.0, 0.0, 0.0, 4.0/\sqrt{4\pi}, 2.0/\sqrt{4\pi}, 2.0).$$

As starting values for the four density ratios we insert the jumps that were obtained in the thermal shock tube, $r_2 = 1.3799$, $r_4 = 1.0966$, $r_5 = 1.1257$, and $r_7 = 1.309$. We do the same for the magnetic fields, yielding the initial guess $B_{y2} = 1.4383$, $B_{y4} = 1.4126$, $B_{z4} = 1.5078$, and $B_{y7} = 0.4377$. The solver needs three nested iterations until convergence is obtained (see Table 5.6). The solution is given in Table 5.11a with the corresponding wave speeds presented in Table 5.11b. Compared to the thermal case the left-facing fast shock is significantly weaker while the other density jumps are approximately equal.

The result of the GADGET-2 simulation at time $t = 0.1$ is shown in Figure 5.7. In the upper central panel the two partial pressure components are displayed individually as

Table 5.7: The sequence of iterations for the density jumps in Riemann problem 2

| Iteration | $r_2$ | $r_4$ | $r_5$ | $r_7$ |
| --- | --- | --- | --- | --- |
| 0 | 1.75761 | 1.61000 | 0.94417 | 0.90146 |
| 1 | 1.89337 | 1.42281 | 0.93343 | 0.89808 |
| 2 | 1.91107 | 1.40204 | 0.92280 | 0.89571 |
| 3 | 1.91760 | 1.39972 | 0.91233 | 0.89422 |
| 4 | 1.92224 | 1.39956 | 0.90207 | 0.89348 |
| 5 | 1.92600 | 1.39967 | 0.89206 | 0.89339 |
| 6 | 1.92906 | 1.39981 | 0.88231 | 0.89386 |

black dashed and black dotted lines with the analytical solutions overlaid in green and purple. Apparently, the simulation code behaves exactly as predicted by the Riemann solver although the thermal pressure is slightly too small. The numerical errors seen in the plot are explicitly described in section 5.1.5.

The second Riemann problem (2b in R&J) is endowed with a relativistic pressure component of $X_L = p_{CR}/p_{th} = 1.0$ and $X_R = p_{CR}/p_{th} = 0.5$. Accordingly, the initial states for the compound gas yield $B_x = 3.0/\sqrt{4\pi}$ and

$$
\begin{aligned}
\vec{U}_L &= (1.0, 0.0, 0.0, 6.0/\sqrt{4\pi}, 0.0, 2.0), \\
\vec{U}_R &= (0.1, 0.0, 0.0, 0.0, 1.0/\sqrt{4\pi}, 0.0, 15.0).
\end{aligned}
$$

We start the iteration with the density jumps $r_2 = 1.75761$, $r_4 = 1.61000$, $r_5 = 0.94417$, and $r_7 = 0.90146$. The values are again taken from the one-fluid solution whereupon the last ratio had to be slightly increased since otherwise, taken our initial guess for the magnetic fields, $B_{y2} = 3.1166$, $B_{y4} = 1.1924$, $B_{y7} = 0.24732$, and $B_{z4} = 0.24487$, the wave speed of the right-facing fast shock is undefined. In the course of the iteration, $r_7$ must be adjusted upwards several times in order to prevent the Riemann solver from break-down. A stable analytical solution is eventually found after six iteration cycles (see Table 5.7). However, the comparison with the simulation suggests that the analytical solution is not physical since it does not adequately predict the wave velocities. In Tables 5.12a and 5.12b we give the states computed after two Newton-Raphson iterations when the solution is closest to the simulation results. The numbers have to be handled with caution since the density jumps $r_2$, $r_4$, and $r_7$ have then only converged by about 2 % and $r_5$ is even 6 % away from the final value.

The corresponding diagrams and the simulation results at $t = 0.025$ are shown in Figure 5.8. At this stage of the iteration the speed of the leftwards propagating fast discontinuity agrees well with that of the simulated shock wave whereas the rarefactions on the right hand side significantly lag behind the GADGET-2 solution. Comparing the displayed densities with the pressure and the fluid velocities in $x$-direction, the strong sensitivity of the thermodynamic states to the density ratios becomes obvious. In the current shock tube problem the Riemann solver missed the correct value for $r_7$ and converged to a different solution. This problem could certainly have been avoided with a better initial guess.

Table 5.8: The sequence of iterations for the density jumps in Riemann problem 3

| Iteration | $r_2$ | $r_4$ | $r_5$ | $r_7$ |
|-----------|---------|---------|---------|---------|
| 0 | 2.67975 | 0.99685 | 1.02740 | 3.74812 |
| 1 | 2.33074 | 0.99420 | 1.02775 | 3.74507 |
| 2 | 2.27572 | 0.99347 | 1.02812 | 3.74670 |
| 3 | 2.26738 | 0.99332 | 1.02818 | 3.74698 |

The third Riemann problem (1a in R&J) has the initial states $B_x = 5.0/\sqrt{4\pi}$ and

$$\vec{U}_{\mathrm{L}} = (1.0, 10.0, 0.0, 5.0/\sqrt{4\pi}, 0.0, 40.0),$$
$$\vec{U}_{\mathrm{R}} = (1.0, -10.0, 0.0, 0.0, 5.0/\sqrt{4\pi}, 0.0, 1.5),$$

where the relative cosmic ray pressures are given by $X_{\mathrm{L}} = 1.0$ and $X_{\mathrm{R}} = 0.5$. Again, we start the iteration with the eight initial parameters taken from the solution of the thermal shock tube: $r_2 = 2.67975$, $r_4 = 0.99685$, $r_5 = 1.02740$, $r_7 = 3.74812$, $B_{y2} = 3.8389$, $B_{y4} = 4.0380$, $B_{y7} = 5.4272$, and $B_{z4} = 0$. The Riemann solver then requires three Newton-Raphson iterations (see Table 5.8) to arrive at the solution given in Table 5.13a. The two fast shocks are weaker than in the purely thermal case while the jumps over the inner two wave fronts are virtually unaltered.

The comparison to the GADGET-2 snapshot at $t = 0.022$ in Figure 5.9 reveals a good agreement between our theoretical prediction and the simulation results. The wave speeds and the partial pressures of the two gas components are very accurately reproduced. We note that the numerical oscillations in the $B_y$-component are stronger than in the thermal shock tube.

The fourth shock tube test we perform is the modified Riemann problem 3b in Ryu & Jones in which the relative cosmic ray pressures $X_{\mathrm{L}} = 2.0$ and $X_{\mathrm{R}} = 1.0$ are inserted. This gives $B_x = 0.01$ and

$$\vec{U}_{\mathrm{L}} = (1.0, -1.0, 0.0, 0.0, 1.0, 0.0, 2.0),$$
$$\vec{U}_{\mathrm{R}} = (1.0, 1.0, 0.0, 0.0, 1.0, 0.0, 3.0),$$

We use the approximate thermal density jumps $r_2 = 0.5$, $r_4 = 1.0$, $r_5 = 1.0$, $r_7 = 0.5$. After some trial and error we find a good initial guess for the magnetic fields, given by $B_{y2} = 0.52$, $B_{y4} = -0.55$, $B_{y7} = -0.9$, and $B_{z4} = 0$. After three nested Newton-Raphson iterations (see Table 5.9) the states in Table 5.14a are obtained. The inhomogeneous relativistic pressure component induces an asymmetry in the wave speeds and compression ratios which becomes obvious in Table 5.14b. The former mirror-inverted strong rarefactions are weakened to different extents, the inner right-facing rarefaction has turned into a very weak shock wave.

The broken symmetry is nicely seen in Figure 5.10, where the numerical and the analytical solutions are plotted at $t = 0.07$. The prediction has roughly the same quality as in the thermal shock tube. The differences in the densities, pressures and tangential magnetic

Table 5.9: The sequence of iterations for the density jumps in Riemann problem 4

| Iteration | $r_2$ | $r_4$ | $r_5$ | $r_7$ |
|-----------|---------|---------|---------|---------|
| 0 | 0.50000 | 1.00000 | 1.00000 | 0.50000 |
| 1 | 0.56145 | 0.98669 | 1.01673 | 0.67841 |
| 2 | 0.56440 | 0.98134 | 1.02285 | 0.69162 |
| 3 | 0.56446 | 0.97970 | 1.02444 | 0.69284 |

Table 5.10: The sequence of iterations for the density jumps in Riemann problem 5

| Iteration | $r_2$ | $r_4$ | $r_5$ | $r_7$ |
|-----------|---------|---------|---------|---------|
| 0 | 0.58000 | 0.85000 | 1.80000 | 0.99500 |
| 1 | 0.61645 | 0.96111 | 2.24876 | 0.99365 |
| 2 | 0.61172 | 0.97221 | 2.63338 | 0.97826 |
| 3 | 0.60846 | 0.96914 | 2.95998 | 0.96913 |
| 4 | 0.60637 | 0.96487 | 3.25656 | 0.96325 |

field components are comparable. Interestingly, in the cosmic-ray modified shock tube, the disagreement in the wave speed is less severe for the weaker rarefaction on the right.

The last Riemann problem is the Brio & Wu shock tube modified through the inclusion of cosmic rays with the relative pressures $X_L = 0.5$ and $X_R = 0.3$. The left and right initial states become $B_x = 0.75$ and

$$\vec{U}_L = (1.0, 0.0, 0.0, 1.0, 0.0, 1.5),$$
$$\vec{U}_R = (0.125, 0.0, 0.0, 0.0, -1.0, 0.0, 0.13).$$

Setting the density jumps and magnetic fields to the thermal values inferred from Table 5.5a produces undefined wave speeds that cannot be restored even if we vary the initial parameters by a few percent. A look at the simulation result in Figure 5.11 reveals that the left-facing slow shock has turned into a rarefaction wave after going from the purely thermal to the two-fluid Riemann problem. This implies that for the speed of the leftwards propagating slow wave the alternative one of the two positive roots of equation (5.50) applies.

By default, the simulation outcome serves as an aid to orientation for the choice of initial parameters. We assume the values $r_2 = 0.58$, $r_4 = 0.85$, $r_5 = 1.8$, $r_7 = 0.995$, $B_{y2} = 0.52$, $B_{y4} = -0.55$, $B_{y7} = -0.9$, and $B_{z4} = 0$. This initial guess is already a good approximation to the numerical result. However, after the first Newton-Raphson iteration the density jump $r_5$ starts diverging (see Table 5.10). Even an extensive experimentation with the initial parameters did not improve the situation. We thus have to conclude that the algorithm is inapplicable of solving this special Riemann problem.

In Table 5.15a we give the analytical result for the eight zones of the shock tube after one Newton-Raphson iteration. From the simulation snapshot at $t = 0.07$ in Figure 5.11 we deduce that the true value of $r_5$ must not largely deviate from 1.8, but the high sensitivity

Table 5.11a: Solution of Riemann problem 1 (R&J 2a + cosmic rays)

| $\rho$ | $v_c$ | $v_y$ | $v_z$ | $B_y$ | $B_z$ | $p_{\text{th}}$ | $p_{\text{CR}}$ | $p$ |
|---|---|---|---|---|---|---|---|---|
| 1.0800 | 1.2000 | 0.0100 | 0.5000 | 1.0155 | 0.5642 | 0.9500 | 1.9000 | 2.8500 |
| 1.2971 | 0.7581 | 0.0526 | 0.5236 | 1.2306 | 0.6837 | 1.3455 | 2.4486 | 3.7941 |
| 1.2971 | 0.7581 | 0.1534 | 0.2869 | 1.3455 | 0.4141 | 1.3455 | 2.4486 | 3.7941 |
| 1.3008 | 0.7570 | 0.1464 | 0.2848 | 1.3391 | 0.4121 | 1.3460 | 2.4581 | 3.8040 |
| 1.4958 | 0.7569 | 0.1464 | 0.2848 | 1.3391 | 0.4121 | 2.0576 | 1.7464 | 3.8040 |
| 1.3553 | 0.7184 | −0.1791 | 0.1846 | 1.6603 | 0.5110 | 1.7318 | 1.5235 | 3.2552 |
| 1.3553 | 0.7184 | −0.0876 | −0.0438 | 1.5538 | 0.7769 | 1.7318 | 1.5235 | 3.2552 |
| 1.0000 | 0.0000 | 0.0000 | 0.0000 | 1.1284 | 0.5642 | 1.0000 | 1.0000 | 2.0000 |

Table 5.11b: Lagrangian wave speeds and Mach numbers of Riemann problem 1

| $W_{-\text{f}}$ | $W_{-\text{s}}$ | $W_{+\text{s}}$ | $W_{+\text{f}}$ |
|---|---|---|---|
| 2.85143 | 0.510749 | 0.556779 | 2.74004 |

to the parameters renders it difficult to find the root of equations (5.55) - (5.58). As in the thermal case, the compound wave structure, which consists of the rotational discontinuity and the rarefaction travelling at the same speed, appears as one single wave structure while the analytical solution displays two separate discontinuities (see section 5.1.5). For unknown reasons, the numerical oscillations in this Riemann problem are extremely strong.

### 5.2.3 Conclusions

We have derived a novel analytical solution to the MHD Riemann problem for a medium composed of a thermal gas and a relativistic cosmic ray component from the modified jump conditions for MHD shocks. The comparison with the numerical shock tubes performed with GADGET-2 reveal that we have obviously chosen the right ansatz for computing the

Table 5.12a: Solution of Riemann problem 2 (R&J 2b + cosmic rays)

| $\rho$ | $v_c$ | $v_y$ | $v_z$ | $B_y$ | $B_z$ | $p_{\text{th}}$ | $p_{\text{CR}}$ | $p$ |
|---|---|---|---|---|---|---|---|---|
| 1.0000 | 0.0000 | 0.0000 | 0.0000 | 1.6926 | 0.0000 | 1.0000 | 1.0000 | 2.0000 |
| 1.9111 | −2.0448 | 0.3287 | 0.0000 | 3.3586 | 0.0000 | 4.1107 | 2.4517 | 6.5624 |
| 1.9111 | −2.0448 | 0.2807 | 0.4809 | 3.2921 | 0.6648 | 4.1107 | 2.4517 | 6.5624 |
| 2.6794 | −2.2075 | −1.3573 | 0.1501 | 1.1924 | 0.2408 | 7.7247 | 3.9145 | 11.6390 |
| 0.0802 | −2.2075 | −1.3573 | 0.1501 | 1.1924 | 0.2408 | 7.9539 | 3.6853 | 11.6390 |
| 0.0869 | −1.9791 | 2.0409 | 0.8363 | 0.2391 | 0.0483 | 8.2846 | 4.1189 | 12.4040 |
| 0.0869 | −1.9791 | 2.0246 | 1.0000 | 0.2439 | 0.0000 | 8.2846 | 4.1189 | 12.4040 |
| 0.1000 | 0.0000 | 2.0000 | 1.0000 | 0.2821 | 0.0000 | 10.0000 | 5.0000 | 15.0000 |
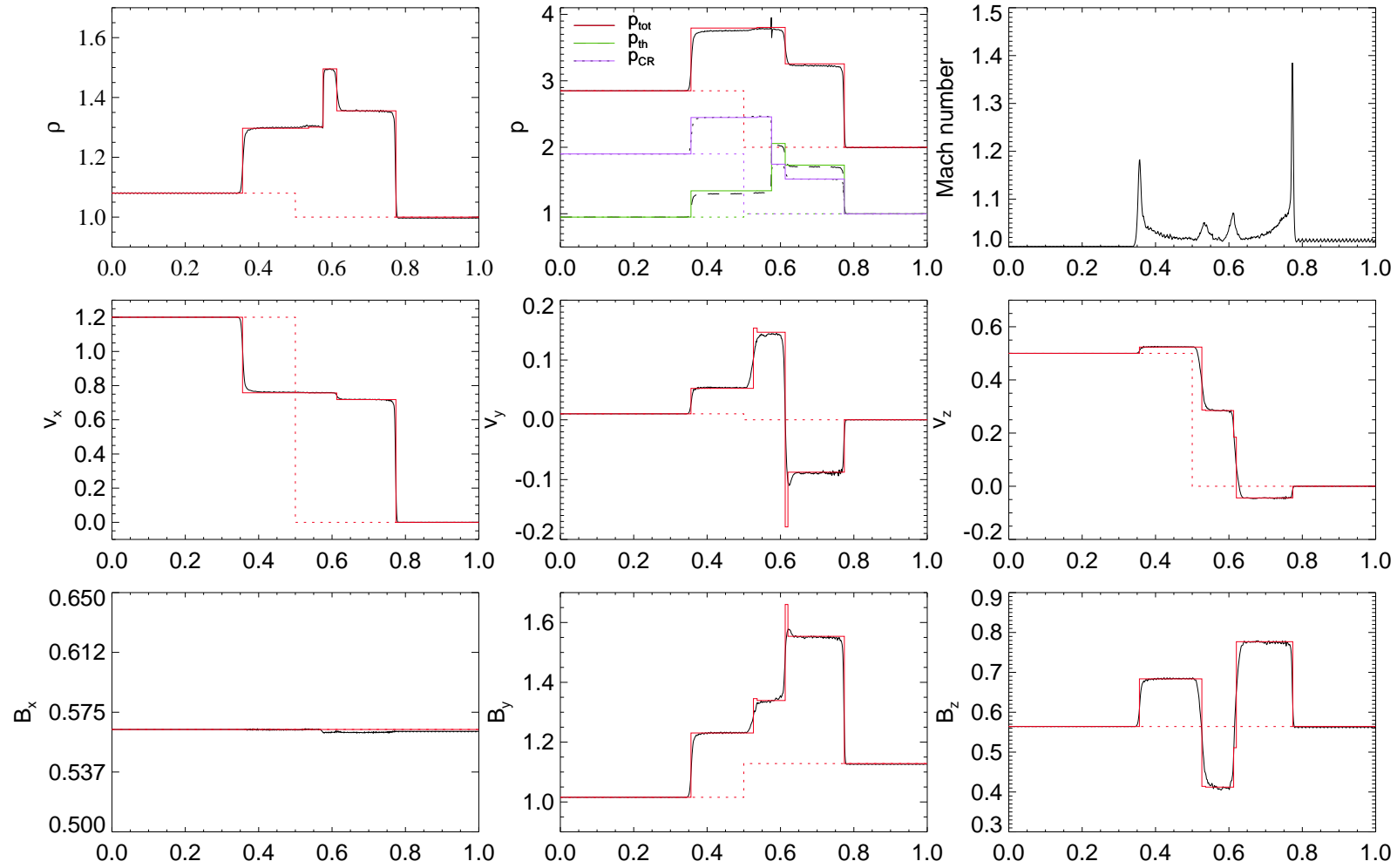
Figure 5.7: Riemann problem 1 (R&J 2a + cosmic rays) at $t = 0.1$ with waves from left to right: fast shock, rotational discontinuity, slow shock, contact discontinuity, slow shock, rotational discontinuity, fast shock
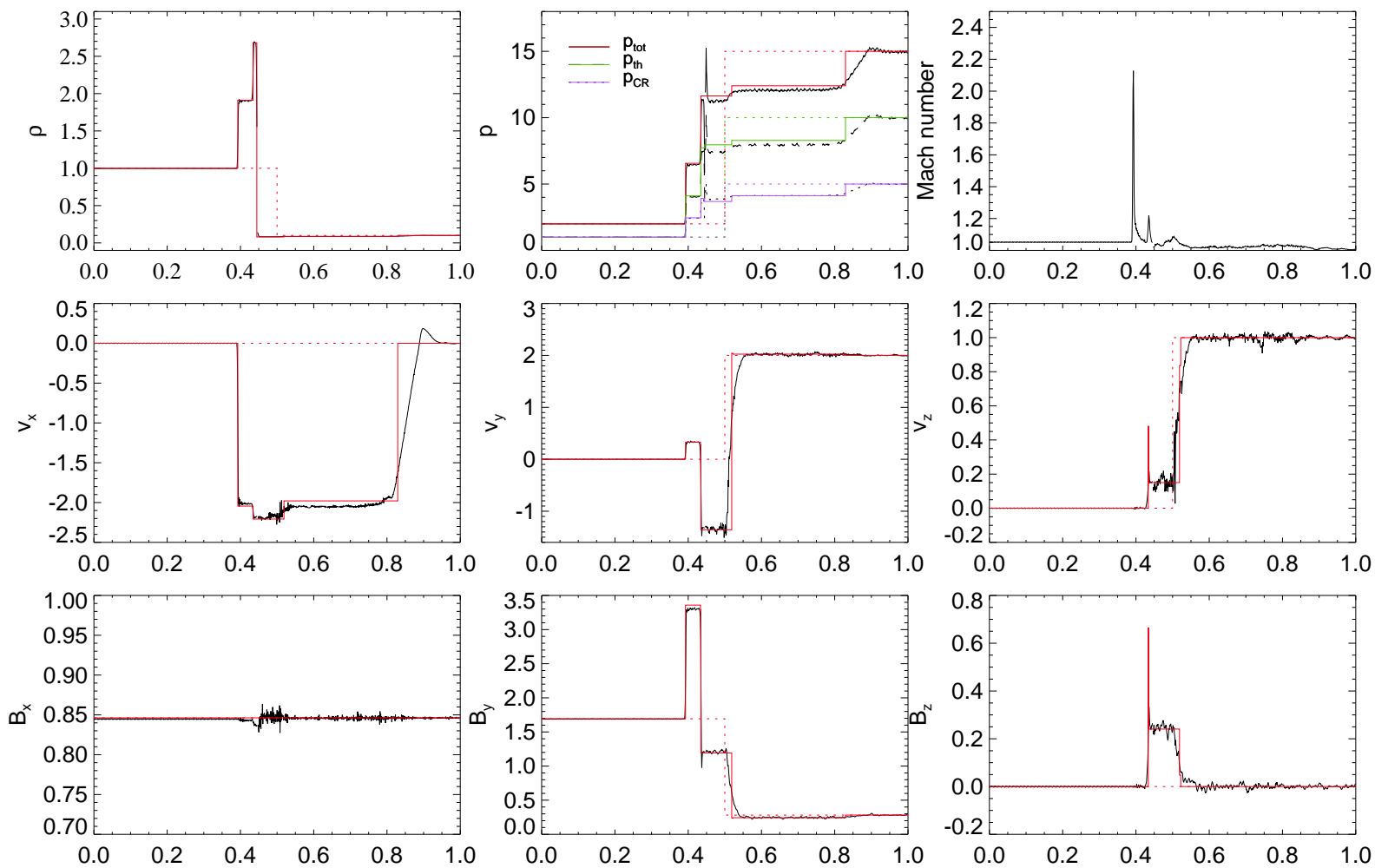
Figure 5.8: Riemann problem 2 (R&J 2b + cosmic rays) at $t = 0.025$ with waves from left to right: fast shock, rotational discontinuity, slow shock, contact discontinuity, slow rarefaction, rotational discontinuity, fast rarefaction
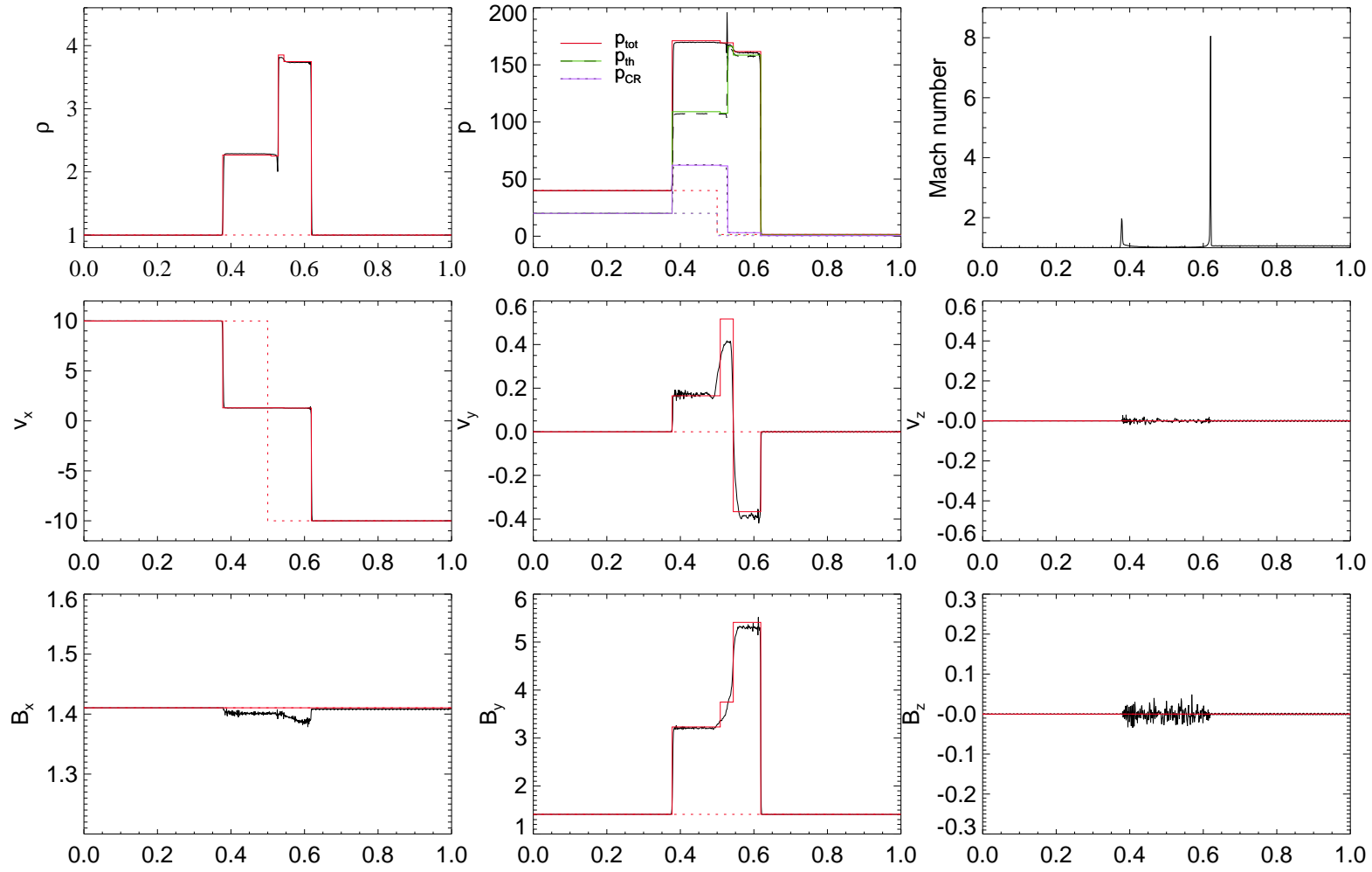
Figure 5.9: Riemann problem 3 (R&J 1a + cosmic rays) at $t = 0.022$ with waves from left to right: fast shock, slow rarefaction, contact discontinuity, slow shock, fast shock
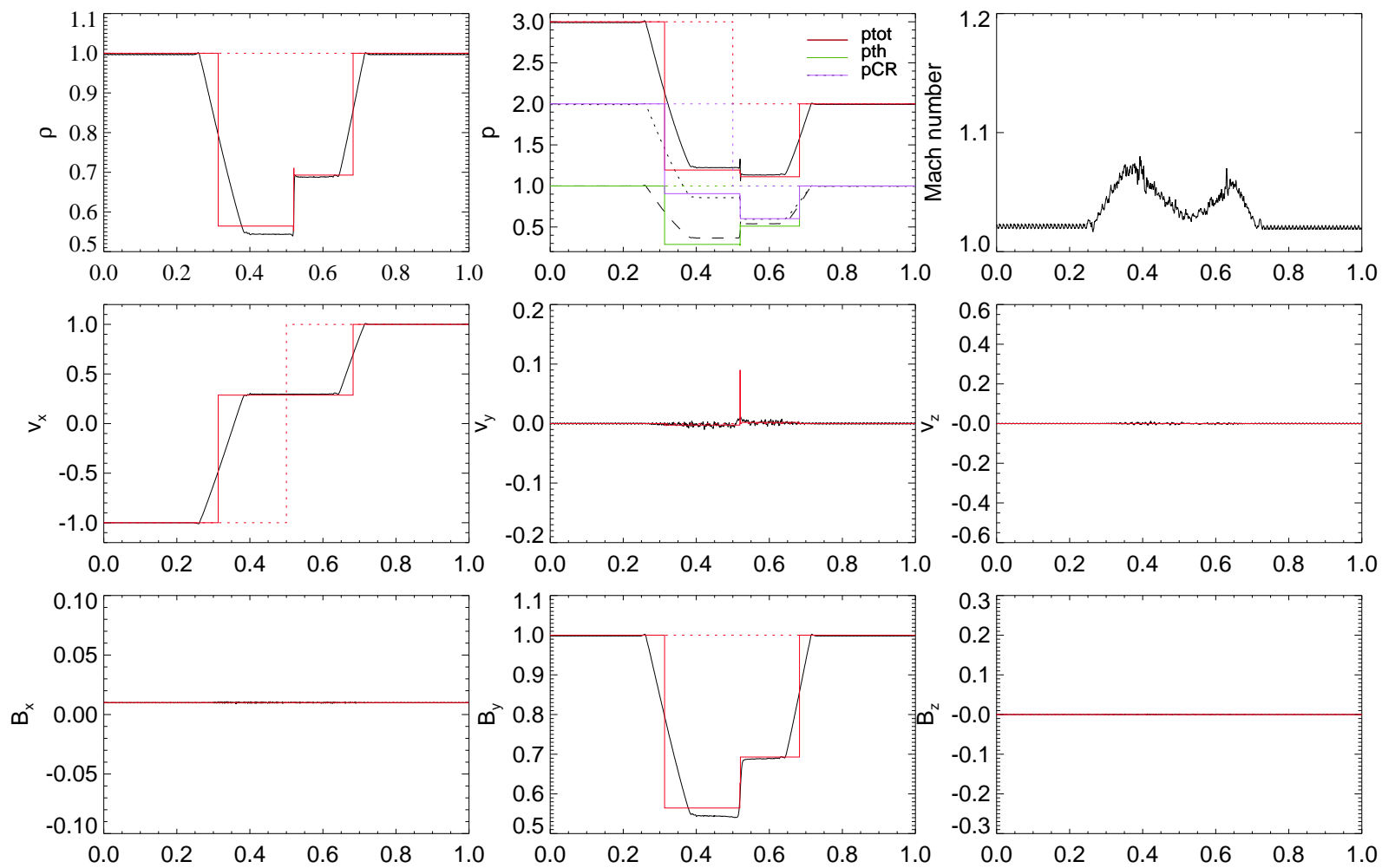
Figure 5.10: Riemann problem 4 (R&J 3b + cosmic rays) at $t = 0.07$ with waves from left to right: fast rarefaction, slow rarefaction, contact discontinuity, slow shock, fast rarefaction
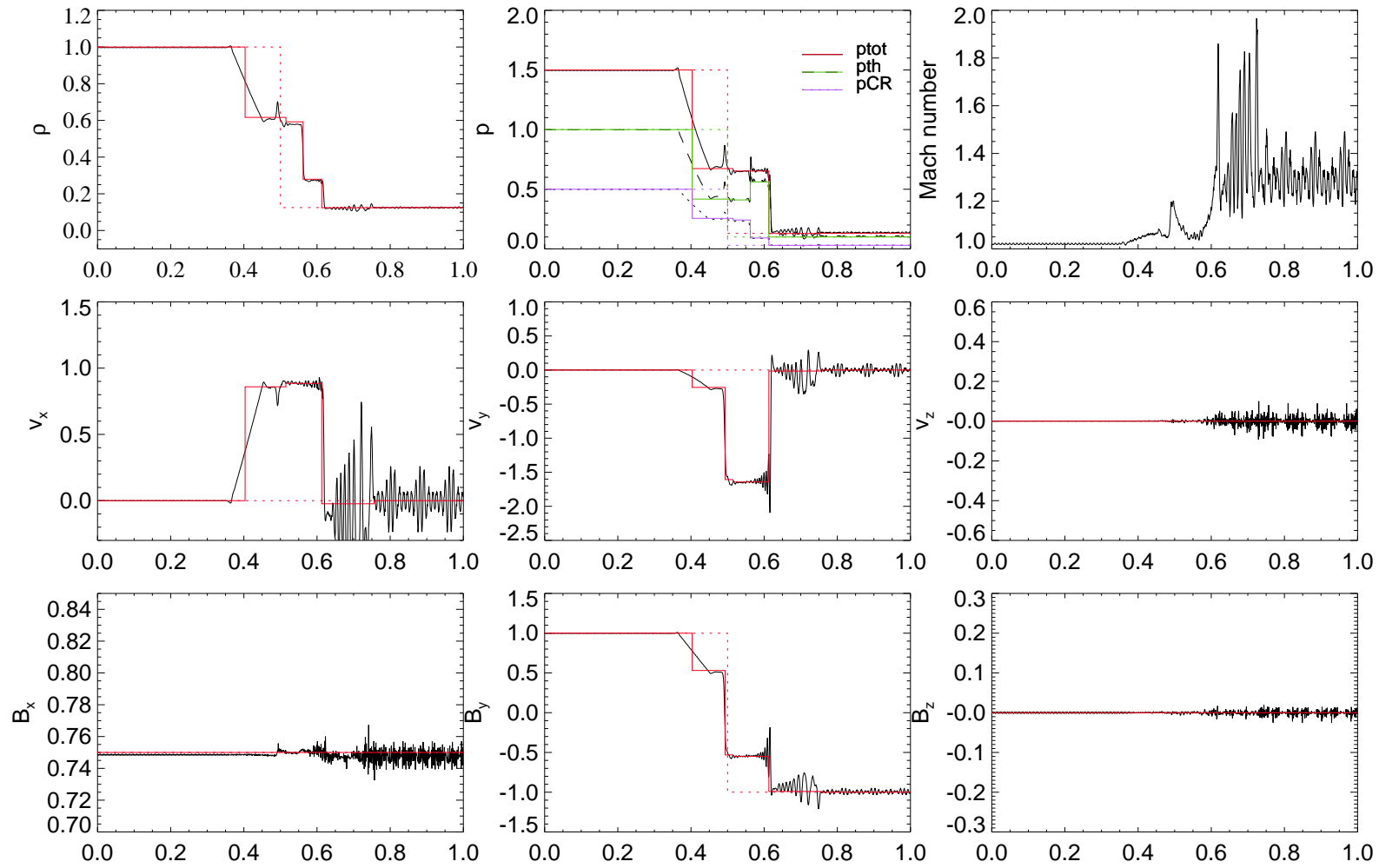
Figure 5.11: Riemann problem 5 (R&J 5a + cosmic rays) at $t = 0.07$ with waves from left to right: fast rarefaction, slow compound, contact discontinuity, slow shock, fast rarefaction

Table 5.12b: Lagrangian wave speeds and Mach numbers of Riemann problem 2

| $W_{-f}$ | $W_{-s}$ | $W_{+s}$ | $W_{+f}$ |
|---|---|---|---|
| 4.28907 | 1.08492 | 0.237414 | 1.31703 |

Table 5.13a: Solution of Riemann problem 3 (R&J 1a + cosmic rays)

| $\rho$ | $v_c$ | $v_y$ | $v_z$ | $B_y$ | $B_z$ | $p_{th}$ | $p_{CR}$ | $p$ |
|---|---|---|---|---|---|---|---|---|
| 1.0000 | 10.0000 | 0.0000 | 0.0000 | 1.4105 | 0.0000 | 20.0000 | 20.0000 | 40.0000 |
| 2.2674 | 1.3013 | 0.1651 | 0.0000 | 3.2320 | 0.0000 | 109.0100 | 62.1300 | 171.1400 |
| 2.2674 | 1.3013 | 0.1651 | 0.0000 | 3.2320 | 0.0000 | 109.0100 | 62.1300 | 171.1400 |
| 2.2522 | 1.3075 | 0.5175 | 0.0000 | 3.7503 | 0.0000 | 107.7650 | 61.5560 | 169.3200 |
| 3.8526 | 1.3075 | 0.5175 | 0.0000 | 3.7503 | 0.0000 | 166.0850 | 3.2361 | 169.3200 |
| 3.7470 | 1.2881 | −0.3665 | 0.0000 | 5.4108 | 0.0000 | 158.5500 | 3.1140 | 161.6600 |
| 3.7470 | 1.2881 | −0.3665 | 0.0000 | 5.4108 | 0.0000 | 158.5500 | 3.1140 | 161.6600 |
| 1.0000 | −10.0000 | 0.0000 | 0.0000 | 1.4105 | 0.0000 | 1.0000 | 0.5000 | 1.5000 |

Table 5.13b: Lagrangian wave speeds and Mach numbers of Riemann problem 3

| $W_{-f}$ | $W_{-s}$ | $W_{+s}$ | $W_{+f}$ |
|---|---|---|---|
| 15.5622 | 2.07397 | 2.64951 | 15.3974 |

Table 5.14a: Solution of Riemann problem 4 (R&J 3b + cosmic rays)

| $\rho$ | $v_c$ | $v_y$ | $v_z$ | $B_y$ | $B_z$ | $p_{th}$ | $p_{CR}$ | $p$ |
|---|---|---|---|---|---|---|---|---|
| 1.0000 | −1.0000 | 0.0000 | 0.0000 | 1.0000 | 0.0000 | 1.0000 | 2.0000 | 3.0000 |
| 0.5645 | 0.2870 | −0.0026 | 0.0000 | 0.5645 | 0.0000 | 0.2880 | 0.9060 | 1.1940 |
| 0.5645 | 0.2870 | −0.0026 | 0.0000 | 0.5645 | 0.0000 | 0.2880 | 0.9060 | 1.1940 |
| 0.5530 | 0.2873 | 0.0892 | 0.0000 | 0.6273 | 0.0000 | 0.2760 | 0.8806 | 1.1566 |
| 0.7098 | 0.2873 | 0.0892 | 0.0000 | 0.6273 | 0.0000 | 0.5345 | 0.6221 | 1.1566 |
| 0.6928 | 0.2870 | 0.0019 | 0.0000 | 0.6928 | 0.0000 | 0.5117 | 0.6016 | 1.1133 |
| 0.6928 | 0.2870 | 0.0019 | 0.0000 | 0.6928 | 0.0000 | 0.5117 | 0.6016 | 1.1133 |
| 1.0000 | 1.0000 | 0.0000 | 0.0000 | 1.0000 | 0.0000 | 1.0000 | 1.0000 | 2.0000 |

Table 5.14b: Lagrangian wave speeds and Mach numbers of Riemann problem 4

| $W_{-f}$ | $W_{-s}$ | $W_{+s}$ | $W_{+f}$ |
|---|---|---|---|
| 1.66796 | 0.00683877 | 0.00751065 | 1.60825 |

Table 5.15a: Solution of Riemann problem 5 (R&J 5a + cosmic rays)

| $\rho$ | $v_c$ | $v_y$ | $v_z$ | $B_y$ | $B_z$ | $p_{\text{th}}$ | $p_{\text{CR}}$ | $p$ |
|--------|--------|---------|--------|---------|--------|--------|--------|--------|
| 1.0000 | 0.0000 | 0.0000 | 0.0000 | 1.0000 | 0.0000 | 1.0000 | 0.5000 | 1.5000 |
| 0.6165 | 0.8589 | $-0.2547$ | 0.0000 | 0.5312 | 0.0000 | 0.4173 | 0.2559 | 0.6732 |
| 0.6165 | 0.8589 | $-1.6077$ | 0.0000 | 0.5312 | 0.0000 | 0.4173 | 0.2559 | 0.6732 |
| 0.5925 | 0.8850 | $-1.6427$ | 0.0000 | $-0.5497$ | 0.0000 | 0.4106 | 0.2422 | 0.6528 |
| 0.2793 | 0.8850 | $-1.6427$ | 0.0000 | $-0.5497$ | 0.0000 | 0.5615 | 0.0913 | 0.6528 |
| 0.1242 | $-0.0234$ | $-0.0157$ | 0.0000 | $-0.9905$ | 0.0000 | 0.0991 | 0.0297 | 0.1288 |
| 0.1242 | $-0.0234$ | $-0.0157$ | 0.0000 | $-0.9905$ | 0.0000 | 0.0991 | 0.0297 | 0.1288 |
| 0.1250 | 0.0000 | 0.0000 | 0.0000 | $-1.0000$ | 0.0000 | 0.1000 | 0.0300 | 0.1300 |

Table 5.15b: Lagrangian wave speeds and Mach numbers of Riemann problem 5

| $W_{-\text{f}}$ | $W_{-\text{s}}$ | $W_{+\text{s}}$ | $W_{+\text{f}}$ |
|--------|--------|--------|--------|
| 1.38052 | 0.397042 | 0.203172 | 0.456971 |

wave velocities of the compound fluid.

The initial guess for the eight parameters in (5.55) - (5.58) was constructed on the assumption that the overall structure of waves and magnetic fields is still preserved after the inclusion of the relativistic component. If possible, the parameters were thus set to the values found for the corresponding thermal shock tubes. Otherwise, the initial guess had to be figured out in a numerical simulation.

In the first four shock tube tests our Riemann solver steadily converged to a stable analytical solution within three to five nested iterations. For the first and third Riemann problem the computed states and velocities agreed well with the numerical solution. In the fourth test the deviations were at least in line with the accuracy of the analogous thermal shock tube. This achievement can be seen as a strong indication of the correct physical behaviour of the SPMHD implementation and the cosmic ray module.

Nevertheless, for the second Riemann problem, we obtained a solution that is apparently unphysical since it significantly differed from the simulation result. As explained in section 5.2.1, this might be due to the existence of multiple roots of the system of equations (5.55) - (5.58). It is also noticeable that five instead of three iterations for the density jumps were required which usually is a sign of a poor initial guess. We expect to find the correct wave speeds only if the initial guess lies sufficiently close to the physical solution.

Finally, the last Riemann problem, which is the cosmic ray-modified Brio & Wu shock tube, turned out to be unsolvable with our algorithm. Although we had chosen an initial guess that approximately reproduced the simulation result, one of the density jumps immediately started diverging after the first Newton-Raphson iteration. The problem might partly arise from the fact that the Brio & Wu shock tube contains a special wave feature that cannot be theoretically described in the thermal case either.

In summary, we succeeded in precalculating three out of five simulation results. We thus

conclude that our Riemann solver can be an appropriate tool for predicting the outcome of MHD shock tube simulations with a composite of a thermal and a relativistic gas performed with GADGET-2, provided we have a proper initial guess. The last restriction currently is the greatest shortcoming of the algorithm since an appropriate initial guess is a priori not known but has to be deduced from the corresponding thermal shock tube or the numerical result.

Most important, the fact that three of the simulation results exactly match the predicted Riemann solutions demonstrates that the interplay between the SPMHD implementation and the cosmic ray module results in a physically correct behaviour, even in the extreme case of equally large thermal, relativistic and magnetic energy densities. The code should thus properly trace the structure formation shocks in our cosmological simulations and calculate the resulting changes in the thermal and non-thermal energy components. Since, under the conditions given in clusters of galaxies, the contribution of the non-thermal components to the total energy in any case will be less than 10 %, we can neglect the errors introduced by the Mach number estimation.

# Cluster Simulations

<div style="text-align:right; font-size:3em; font-weight:bold;">6</div>

The bremsstrahlung emission from the hot intracluster gas with temperatures of $10^6$ to $10^8$ K makes clusters of galaxies the most luminous X-ray sources in the universe, with the exception of quasars. Thermal X-ray emission is thus a common observational property of all galaxy clusters. Since the amount and temperature of the intracluster plasma scales with the cluster mass, the X-ray luminosities and the masses of clusters are correlated (Reiprich & Böhringer 2002).

In contrast, large-scale synchrotron radiation from the ICM, caused by the existence of large scale magnetic fields and of a population of relativistic electrons, is only observed in a minor fraction of galaxy clusters. Giovannini et al. (2002) report that, in a complete cluster sample, 5 % of clusters have a central radio halo source and 6 % a peripheral relic source. The detection rate of diffuse radio sources increases with the cluster X-ray luminosity, reaching $\sim 35$ % in clusters with X-ray luminosities larger than $10^{45}\,\mathrm{erg\,s^{-1}}$ (in the ROSAT band).

Studies at X-ray energies provide evidence that all of these clusters are highly unrelaxed and show signatures of recent merger events. The connection to cluster mergers, which supply the energy to the amplification of the magnetic fields and the acceleration of the particles would at least in part explain the relative rarity of diffuse radio sources.

In this chapter we will investigate the details of the halo-merger connection through the comparison between the X-ray and radio emission of simulated clusters of galaxies and their light deflecting properties. First, we will introduce the cluster sample and respond to special features in their structure formation histories. In the subsequent section we will present the evolution of their X-ray luminosities as a function of redshift and discuss the morphologies of the surface brightness maps for selected merger events. Next, we will study the non-thermal properties of the clusters on the basis of their luminosities at a frequency of 1.4 GHz. Furthermore, we will compare X-ray and radio contour maps of merger events and discuss the associated morphologies. By the end of the section we will investigate the temporal correlation between enhanced X-ray and radio activity and try to establish a connection between both signatures. Finally, we will trace the merger history of the galaxy clusters on the basis of their strong lensing properties and search for analogies to their thermal and non-thermal evolution.

## 6.1 Numerical set-up

The galaxy cluster sample originates from the large cosmological simulation presented in Yoshida et al. (2001). This simulation assumed a flat $\Lambda$CDM cosmology with a present matter density parameter $\Omega_{\mathrm{m}} = 0.3$, a baryonic fraction of $\Omega_{\mathrm{B}} = 0.039$, and an energy density parameter $\Omega_{\Lambda} = 0.7$. The value of the Hubble constant in units of $100\,\mathrm{km\,s^{-1}Mpc^{-1}}$ is given by $h = 0.7$. The model universe comprised $512^3$ dark matter particles, each of mass $6.6 \cdot 10^{10}\,h^{-1}\,\mathrm{M_\odot}$, inside a cubic box of $479\,h^{-1}$ co-moving Mpc side length. The distribution of initial Gaussian density fluctuations was normalised to the present abundance of galaxy clusters assuming an amplitude $\sigma_8 = 0.9$ for the present day power-spectrum.

The dark matter halos in the cosmological simulation were identified as groups of particles that had the overdensity characteristic of virialised objects predicted by the spherical collapse model around local density maxima. By selecting massive dark matter halos with virial masses in the range $\sim 4 \cdot 10^{14}$ to $2.4 \cdot 10^{15}\,\mathrm{M_\odot}$, a number of suitable candidates for galaxy clusters were found (Tormen et al. 2004). The depicted areas were cut out of the simulation volume and re-simulated with a mass resolution of $2 \cdot 10^9\,\mathrm{M_\odot}$ to $6 \cdot 10^9\,\mathrm{M_\odot}$ per dark matter particle. The initial conditions for these clusters were produced using the "Zoomed Initial Conditions" (ZIC) technique described in Tormen et al. (1997), thereby re-sampling the initial density field and increasing the number of particles.

The newly generated initial conditions were evolved using the GADGET-2 code including gas physics, magnetic fields and the self-consistent cosmic ray model. All cluster simulations start at redshift $z = 60$ and end at $z = 0$. Snapshots were written at 141 output times, equally spaced in $\log(1 + z)$ between $z = 10$ and $z = 2.16$, and, in order to obtain a higher time resolution, with a finer spacing between $z = 2.16$ and $z = 0$.

## 6.2 The cluster sample

We study a sample of three galaxy clusters that span a mass range of $1.8 \cdot 10^{14}\,\mathrm{M_\odot}$ to $3.2 \cdot 10^{15}\,\mathrm{M_\odot}$ at $z = 0$. The two smaller objects, g51 and g72, are typical representatives of massive clusters that, besides being highly X-ray luminous, are expected to host large radio halos as a signature of dynamical activity (for a comparison with real galaxy clusters see e.g. Horner et al. 1999). The largest of the three objects, g8, belongs to the high-mass end of observed galaxy clusters. Despite its rather unspectacular formation history, due to its large amount of high-temperature thermal gas, g8 serves as a suitable test object in the study of the correlation between merger activity and radiative processes.

The galaxy clusters are identified with the most massive halo in each of the three simulations. The evolution of the main halo with time is traced by the means of its mass growth and increasing virial radius. In the following we summarise the formation history of the three galaxy clusters:

### g8
The evolution of the g8 cluster is characterised by smooth accretion and a few weak minor merger events. The smoothness of the accretion process is reflected in the evolution of
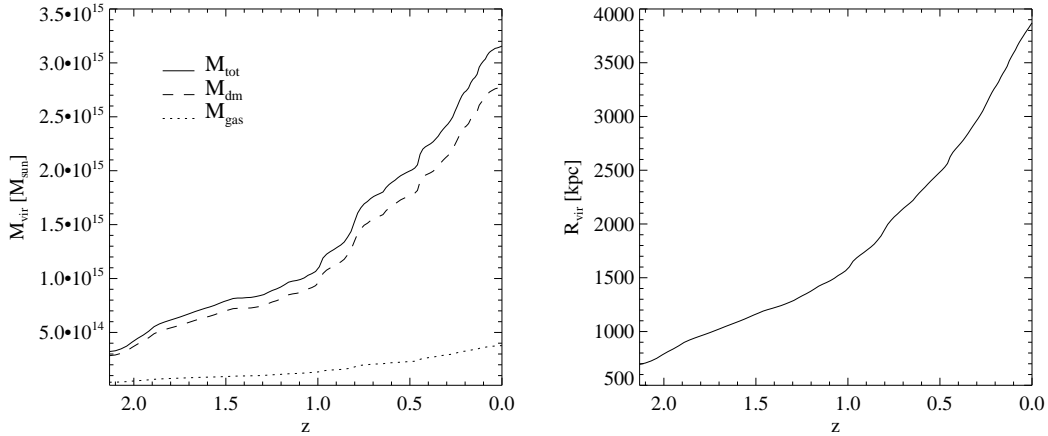
Figure 6.1: Evolution of the virial mass (left) and the virial radius (right) of the cluster g8 in the redshift interval $z = [2.13, 0.00]$. Shown are the total mass (solid line), the dark matter mass (dashed line), and the gas mass (dotted line).

the virial mass, plotted as a function of redshift in the left panel of Figure 6.1. The mass curve increases monotonically and does not exhibit any larger jumps. Yet most noticeable are the mass increases at $z \approx 0.8$ and $z \approx 0.5$. As can be seen in the right panel of Figure 6.1, the virial radius grows larger than $2.5 \, \mathrm{Mpc}$ at redshifts below $z = 0.5$, which makes the g8 cluster one of the most extended gravitationally bound objects that are observed today. The cluster is particularly interesting because of its large mass from which we can expect a high X-ray luminosity. Furthermore, even in the absence of major merger events, the infall of sub-halos in the mass range of $7.6 \cdot 10^{13} \, \mathrm{M_\odot}$ to $1.9 \cdot 10^{14} \, \mathrm{M_\odot}$ involves high-impact accretion shocks that amplify the intracluster magnetic fields and might significantly trigger the production of cosmic rays. We thus expect the appearance of a large scale radio halo above the detection limit.

**g51**

The g51 cluster goes through a major merger around $z \approx 1.1$ and some minor mergers after $z \lesssim 0.6$. The major merger is the prominent feature in the mass evolution curve of Figure 6.2, where the mass grows to a maximum value of $\sim 1 \cdot 10^{15} \, \mathrm{M_\odot}$ at $z \approx 1.15$ and subsequently drops by almost $10 \, \%$ at $z \approx 1.3$, before it rises again around $z \approx 1.4$. This run is characteristic for a sub-clump that traverses the main halo and, in a sort of pendular motion, is drawn back by gravity into the centre of the main halo. In the right panel of Figure 6.2 we see that the virial radius is only slightly affected by the merger event and keeps monotonically increasing all the time. Since $R_{\mathrm{vir}} \propto M_{\mathrm{vir}}^{1/3}$, we do not expect to see large jumps in the evolution of the virial radius. From the merger events we can anticipate reasonable magnetic energies and a strongly varying production of relativistic particles. Consequently, radio emission halos of fluctuating sizes and luminosities should
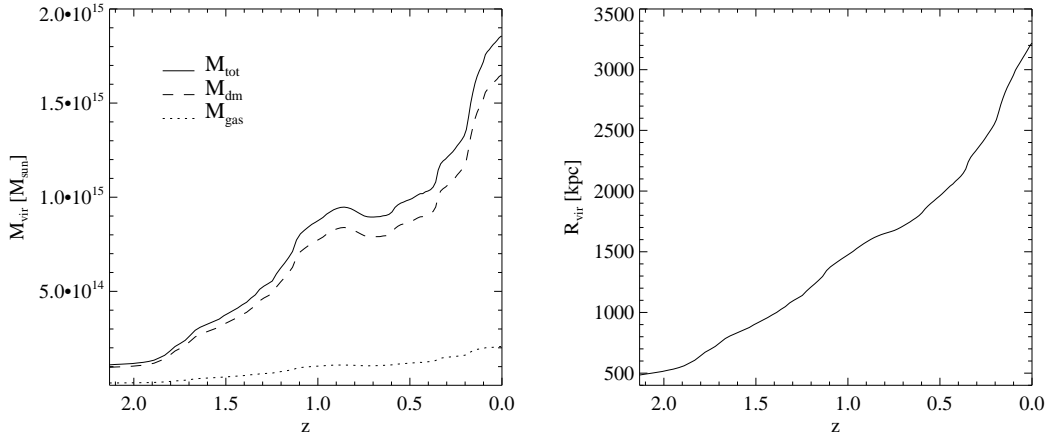
Figure 6.2: Evolution of the virial mass (left) and the virial radius (right) of the cluster
            g51 in the redshift interval $z = [2.13, 0.00]$. Shown are the total mass (solid
            line), the dark matter mass (dashed line), and the gas mass (dotted line).

be produced. With a final mass of $\sim 1.8\,\mathrm{M}_\odot$ and a size of $\sim 3\,\mathrm{Mpc}$ around $z = 0.1$, the
g51 cluster is larger than the average of galaxy clusters and should thus be a bright X-ray
source.

### g72

As can be seen from Figure 6.3, the g72 cluster has approximately the same final mass and
size as the g51 cluster. Nevertheless, g72 has a unique formation history due to two major
merger events, one at $z \lesssim 0.8$ and one in the late phase of its evolution at $z \lesssim 0.3$. For
both events we observe the characteristic steepening in the slope of the mass function. The
low redshift of the second merger event makes the g72 cluster well comparable to Abell
2256, a massive galaxy cluster at redshift $z \approx 0.06$ that is currently in the final stage of
a major merger. The corresponding X-ray and radio maps are presented in Section 3.3.3.
Due to the strong merger shocks in the formation history of g72, we expect to see large
increases in both, X-ray and radio emission.

## 6.3  X-ray emission

In the following, we will investigate how the X-ray luminosities of the simulated clusters
evolve in the course of structure formation and identify distinct features in their thermal
evolution that can be related to minor and major merger events. We will further search for
substructures and distortions in the X-ray brightness distributions that indicate sub-clump
interaction and check whether their morphologies can explain the observations.

   In order to generate X-ray maps that allow for the comparison to observational data,
the gas distributions of the simulated clusters were projected onto two-dimensional arrays
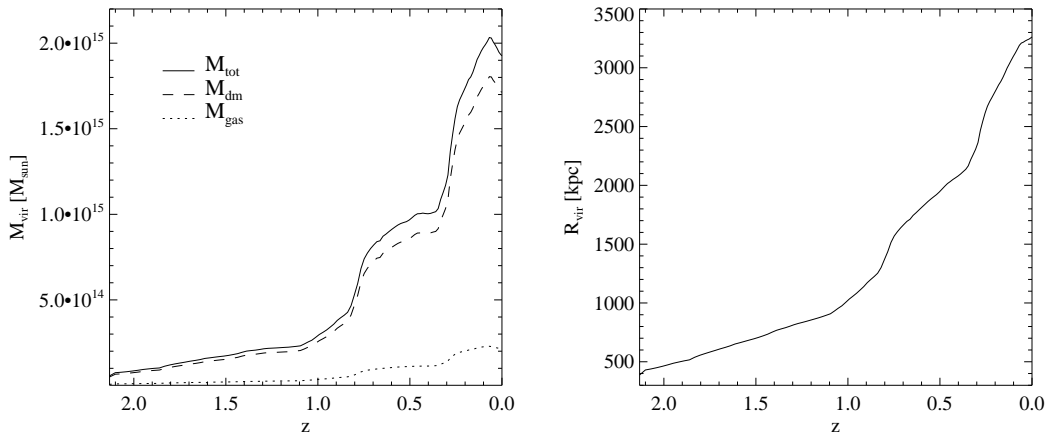
Figure 6.3: Evolution of the virial mass (left) and the virial radius (right) of the cluster g72 in the redshift interval $z = [2.13, 0.00]$. Shown are the total mass (solid line), the dark matter mass (dashed line), and the gas mass (dotted line).

of $1024^2$ pixels by integrating over the kernel function of each SPH particle along a specified line of sight. The projection was carried out for three different directions, hereafter specified as the $x$, $y$, and $z$-direction, respectively. The X-ray flux emitted by each pixel was determined using the MEKAL emission model in the spectral fitting analysis package XSPEC (Arnaud 1996). The model accounts for the continuum spectrum of an optically thin plasma whose electrons have a Maxwellian energy distribution (Mewe et al. 1985, 1986; Kaastra & Mewe 1993), including Fe L emission and the line emissions from several elements (Liedahl et al. 1995). Intergalactic absorption is described by the WABS model on the basis of Wisconsin cross-sections (Morrison & McCammon 1983). The X-ray fluxes were calculated for an effective bandpass of 0.6 - 20 keV, assuming a primordial hydrogen abundance and a mean hydrogen density of $1 \, \text{cm}^{-3}$. Total luminosities were obtained by integrating over the cluster's surface.

### 6.3.1 Luminosities

In Figure 6.4 we show the total X-ray luminosity of the g8 cluster as a function of redshift. In the course of structure formation the luminosity grows by a factor of $\sim 9$, from approximately $10^{45} \, \text{erg s}^{-1}$ at $z = 2.13$ to about $9 \cdot 10^{45} \, \text{erg s}^{-1}$ at $z = 0.006$. This trend clearly reflects the increasing mass and temperature of the ICM. The light curve is superimposed by several prominent peaks that indicate sudden luminosity boosts to up to $\gtrsim 200$ % of the initial luminosity. This strong and fast increase in thermal emissivity together with an equally fast decline suggests a sudden high compression of the medium as caused by a violent accretion shock with subsequent relaxation of the cluster. Looking at the left panel of Figure 6.1, we see that the luminosity peak around $z \lesssim 0.7$ indeed follows a steepening of the halo growth function at slightly higher redshifts. The same can be observed for the
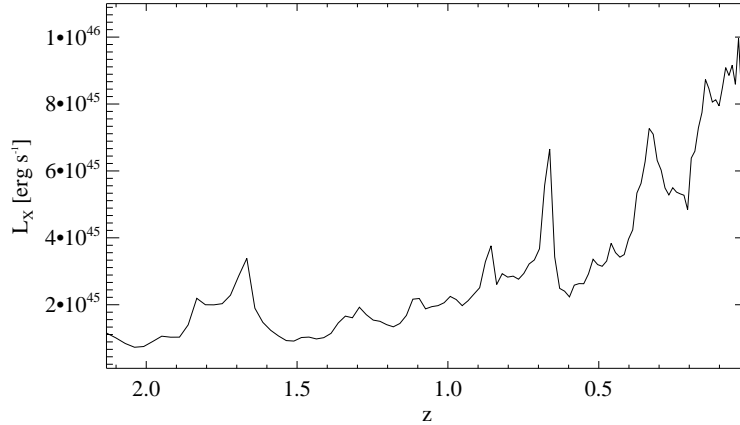
Figure 6.4: Simulated X-ray luminosity of the g8 cluster in units of $\mathrm{erg\,s^{-1}}$ as a function of redshift.

peaks at $z \approx 0.3$ and $z \approx 0.15$ which are apparently induced by an abrupt increase in cluster mass.

Figure 6.5 shows the X-ray luminosity of the g51 cluster. As in the example of g8, the luminosity increases with decreasing redshift, due to the thermal evolution of the ICM. The X-ray luminosity at the final redshift is smaller than that of g8 by a factor of $\sim 0.4$, due to the smaller cluster mass. However, the relative increase in X-ray luminosity is much stronger, about a factor of 20 between $z = 2.13$ and $z = 0.006$. The enhanced thermal emission is due to the higher dynamical activity of the g51 cluster. As in the case of the g8 cluster, a number of prominent peaks are superimposed to the luminosity curve in Figure 6.5. The largest peak occurs at $z \approx 0.1$ where the luminosity abruptly rises by about 100 %.

The evolution of the X-ray luminosity of cluster g72 is shown in Figure 6.6. It displays two large peaks in the wake of the major merger events around $z \approx 0.65$ and $z \approx 0.2$. The first merger leads to an increase in X-ray luminosity by a factor of 3, while during the second major merger, the luminosity temporarily grows to about six times the initial value before it drops again very rapidly. Over the remaining redshift range, the luminosity curve appears rather smooth without significant variation which is due to the smooth and sparse matter accretion at redshifts above $z \approx 1$. In total, we denote a growth in the X-ray luminosity from $10^{43}\,\mathrm{erg\,s^{-1}}$ to about $2 \cdot 10^{45}\,\mathrm{erg\,s^{-1}}$ from $z = 2.13$ to $z = 0.006$.

### 6.3.2 Morphologies

Studies of the X-ray morphologies are of major importance since the thermal gas bears the most evident signatures of cluster mergers. For the more detailed analysis of the cluster dynamics we pick out redshift intervals in the thermal history of the clusters that appear particularly interesting and investigate their associated X-ray morphologies.

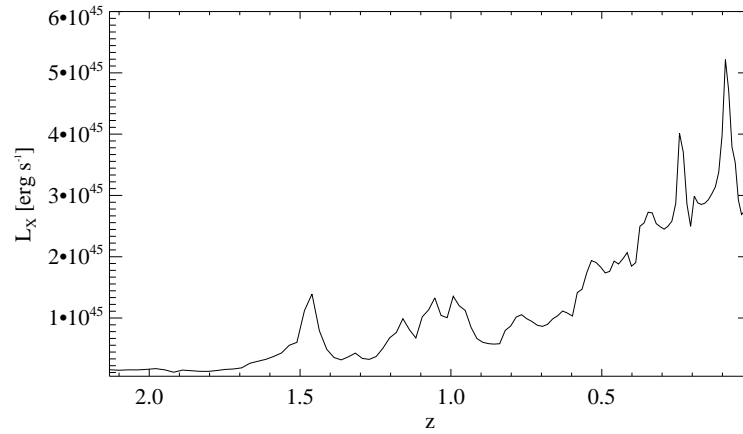The situation we select from the light curve of g8 corresponds to the broad peak in

Figure 6.5: Simulated X-ray luminosity of the g51 cluster in units of $\mathrm{erg\,s^{-1}}$ as a function of redshift.
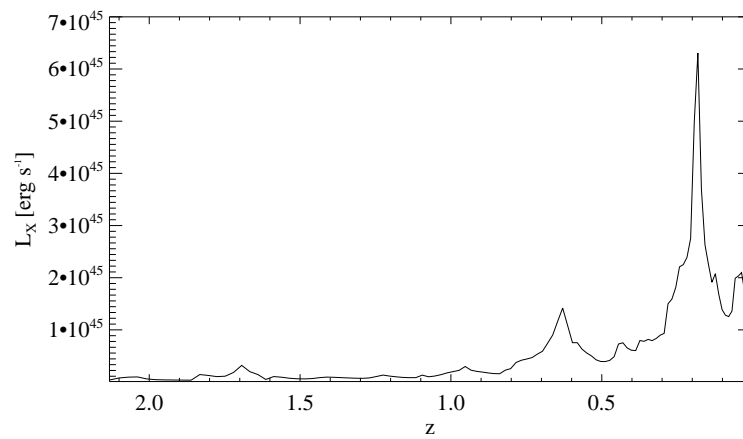


Figure 6.6: Simulated X-ray luminosity of the g72 cluster in units of $\mathrm{erg\,s^{-1}}$ as a function of redshift.

the redshift interval $z = [0.416, 0.268]$, where the curve displays a small bend in its slope before reaching the maximum value. The X-ray contours are shown in Figure 6.7. The maps were obtained from a projection along the $x$-axis and by plotting contour lines in the range $F_X = 10^{-13}$ - $5 \cdot 10^{-18}\,\mathrm{erg\,s^{-1}\,cm^{-2}}$ in a central cutout of $1\,\mathrm{Mpc}$ side length. The contour lines reveal the infall of two sub-clumps from opposite directions. One clump appears in the upper right panel of Figure 6.7, at redshift $z = 0.388$. It enters from the left border, a little bit above the main halo and rapidly merges with the cluster, while the second clump, already visible in the first panel, describes an orbital motion around the main halo before it transversely enters from downside. The second infall thereby induces the higher compression ratios since the clump propagates a long way through the low-density gas in the outer regions where it can produce shocks with high Mach numbers. The time-lag of the two mergers and their infall geometries could thus plausibly explain the luminosity peak in Figure 6.4.

In Figure 6.8 we take a closer look at the inner cluster dynamics around the most prominent X-ray peak at redshift $z \approx 0.9$ in the thermal history of g51. We present the X-ray morphologies in the redshift range $z = [0.124, 0.006]$, obtained by the projection along the $x$-axis and for a central cutout of $1\,\mathrm{Mpc}$ side length. The contours show lines of equal flux in the range $F_X = 10^{-6}$ - $10^{-12}\,\mathrm{erg\,s^{-1}\,cm^{-2}}$. Immediately before the X-ray luminosity reaches the overall maximum in Figure 6.5, a minor merger takes place at $z = 1.01$, visible in the upper right panel of Figure 6.8. A smaller clump falls in later around $z = 0.06$, visible in the last panel of the second row and in the first panel of the third row of Figure 6.8. This second infall prevents the cluster from immediate relaxation and can explain the slight broadening of the luminosity peak around half of the maximum.

In Figure 6.9 we present the X-ray contours of the thermal radiation at the time of the first major merger. Shown is a cutout of $1\mathrm{Mpc}^2$ size at the centre of the cluster and for redshifts $z = 0.731$ to $z = 0.550$. The line of sight is the $y$-axis. The g72 cluster is the upper halo in the first panel which at this time has an approximate mass of $6.9 \cdot 10^{14}\,\mathrm{M_\odot}$. The smaller clump, which is approaching from below, contains almost half of the main halo mass. The clumps hit each other with a slight offset in $x$-direction and thus spiral around each other in the centre. At $z = 0.630$ the cluster reaches the local emission maximum of $L_X \approx 5 \cdot 10^{45}\,\mathrm{erg\,s^{-1}}$ before its core gets disrupted due to the high angular momentum. The two sub-halos are catapulted into opposite directions, well visible in the last four panels of Figure 6.9.

Figure 6.10 shows X-ray maps of the second major merger in a projection along the $x$-axis. The infalling sub-clump comes from the upper right direction. It crosses the centre of g72 and moves past the main halo where it gets decelerated by the cluster's gravitational potential. This first crossing coincides with the highest peak in Figure 6.6, which indicates that the merger shock induces very strong compression and thus a high release of thermal energy. After the core passage, the X-ray morphology appears strongly distorted, displaying an elongated shape. The regression and final infall of the sub-clump are not depicted in Figure 6.10, but from the evolution of the total luminosities we see that it induces a second bright X-ray boost.
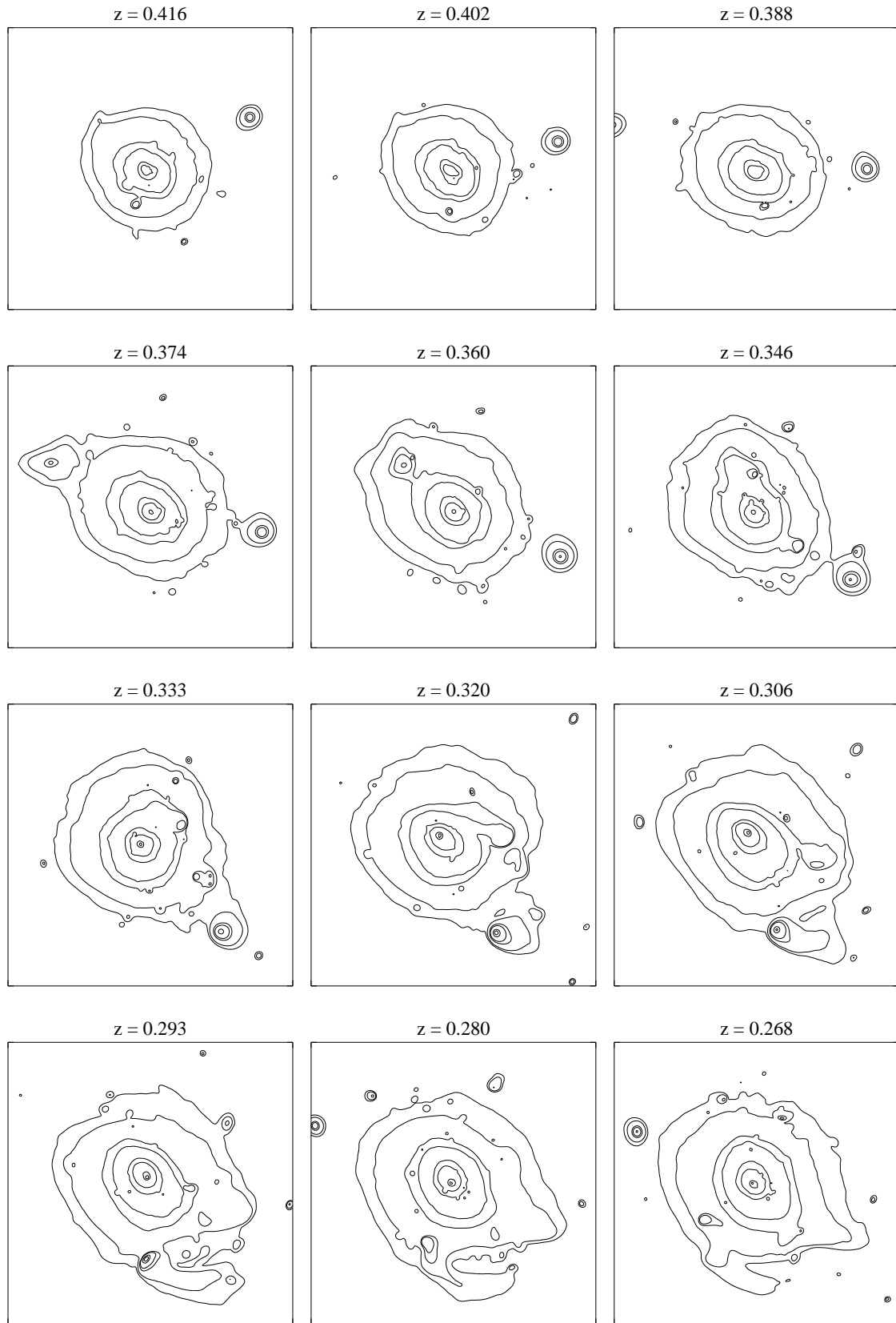
Figure 6.7: X-ray flux contours of the g8 cluster obtained from the projection along the $x$-axis within a region of $1\,\mathrm{Mpc}$ side length in the redshift interval $z = [0.416, 0.268]$. Contour levels are $5 \cdot 10^{-18}, 10^{-17}, 5 \cdot 10^{-17}, 10^{-16}, 5 \cdot 10^{-16}, 10^{-15}, 5 \cdot 10^{-15}, 10^{-14}, 5 \cdot 10^{-14}, 10^{-13}\,\mathrm{erg\,s^{-1}\,cm^{-2}}$.
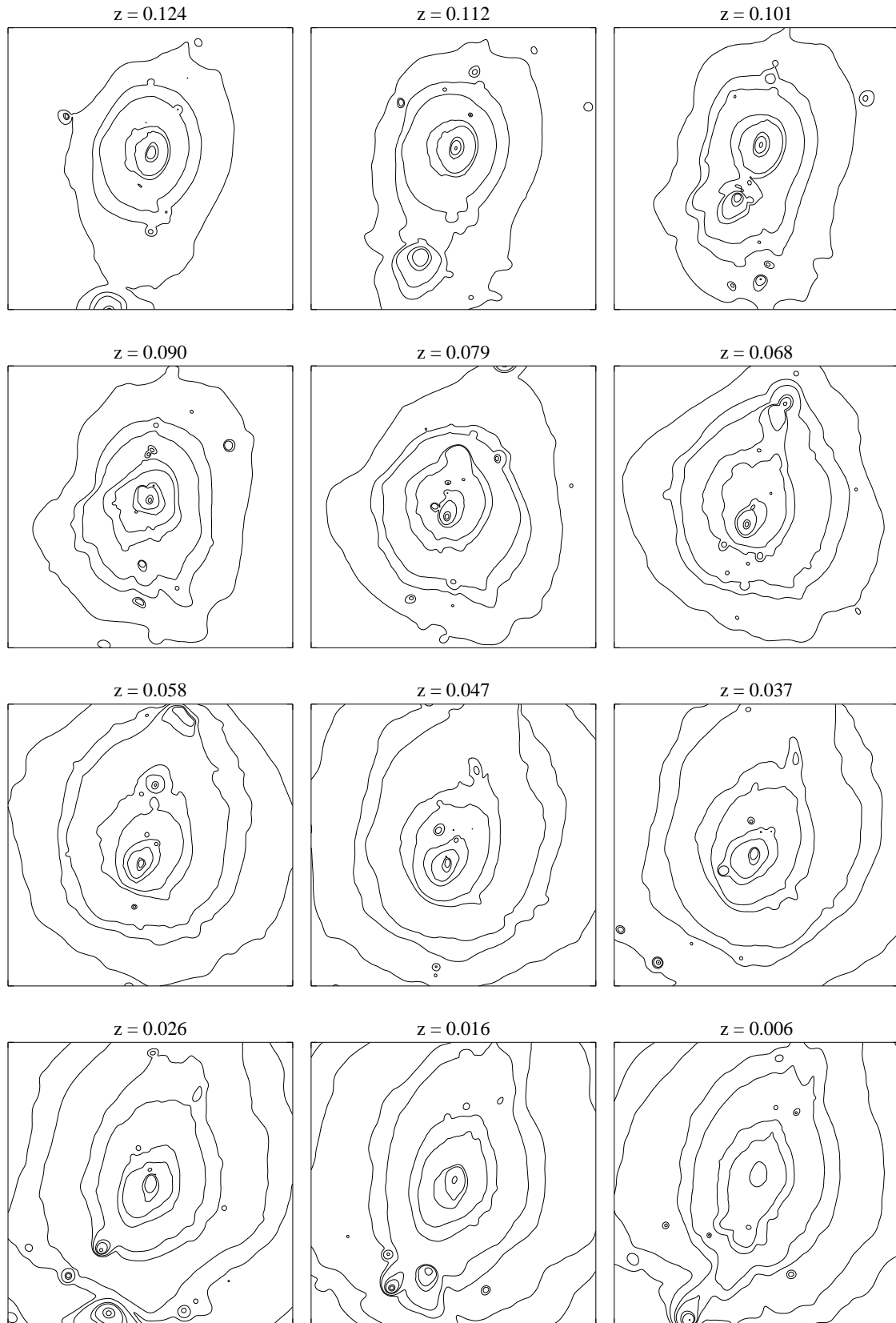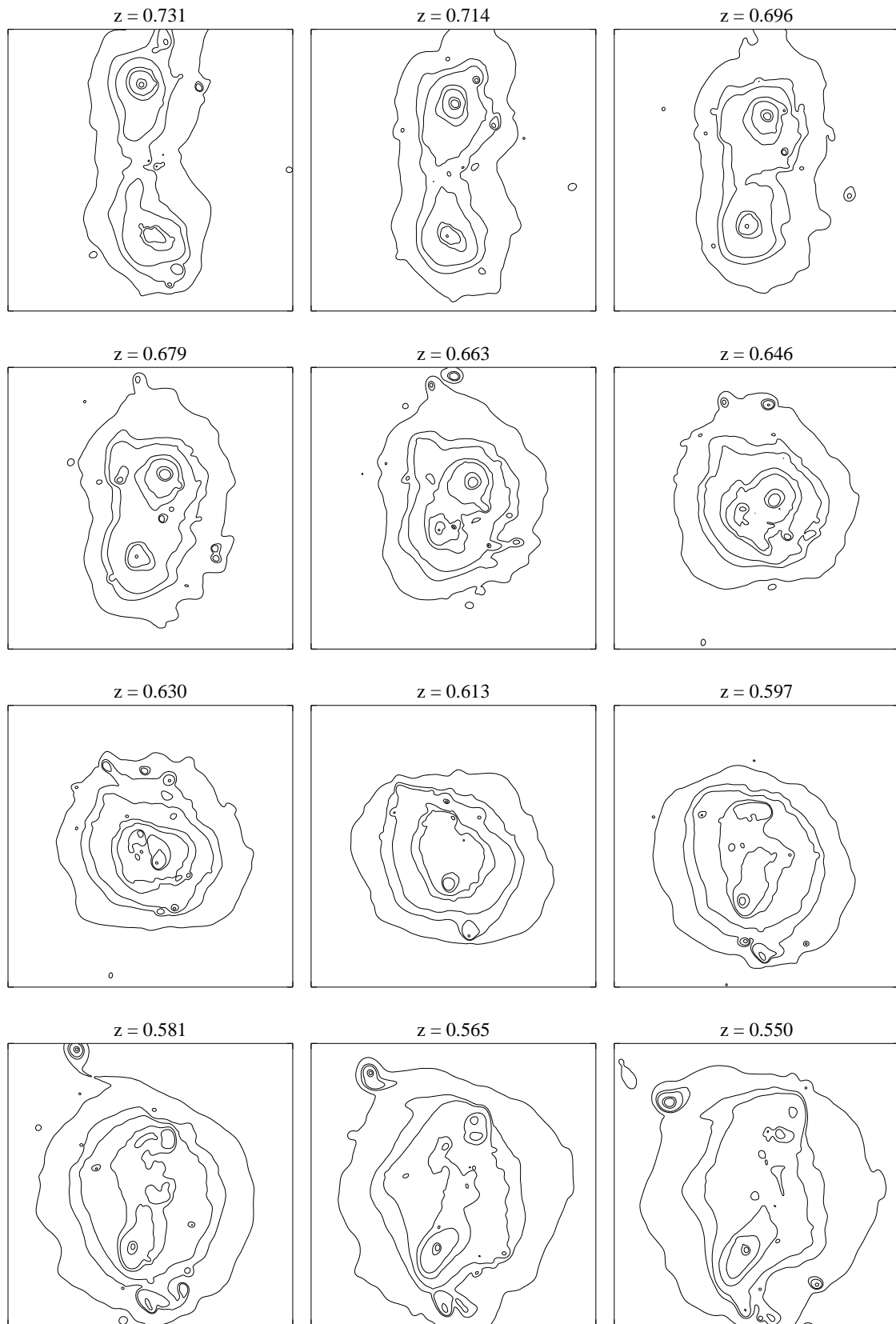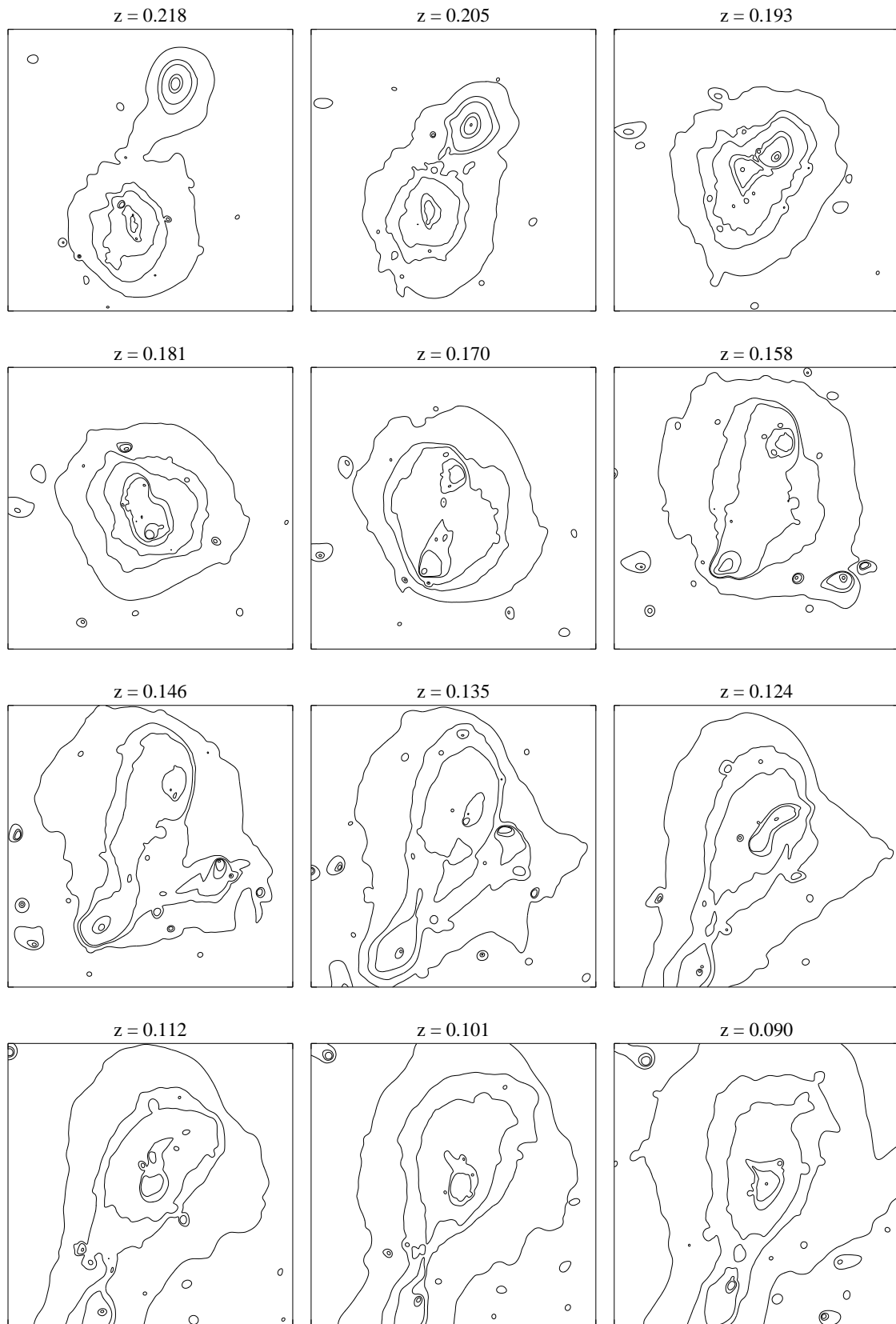
Figure 6.8: X-ray flux contours of the g51 cluster obtained from the projection along the $x$-axis within a region of $1\,\mathrm{Mpc}$ side length in the redshift interval $z = [0.124, 0.006]$. Contour levels are $10^{-17}, 5 \cdot 10^{-17}, 10^{-16}, 5 \cdot 10^{-16}, 10^{-15}, 5 \cdot 10^{-15}, 10^{-14}, 5 \cdot 10^{-14}, 10^{-13}, 10^{-12}\,\mathrm{erg\,s}^{-1}\,\mathrm{cm}^{-2}$.

Figure 6.9: X-ray flux contours of the g72 cluster obtained from the projection along the $y$-axis within a region of $1\,\mathrm{Mpc}$ side length in the redshift interval $z = [0.731, 0.550]$. Contour levels are $10^{-19}, 5 \cdot 10^{-19}, 10^{-18}, 5 \cdot 10^{-18}, 10^{-17}, 5 \cdot 10^{-17}, 10^{-16}, 5 \cdot 10^{-16}, 10^{-15}, 5 \cdot 10^{-15}, 10^{-14}, 5 \cdot 10^{-14}\,\mathrm{erg\,s^{-1}\,cm^{-2}}$.

Figure 6.10: X-ray flux contours of the g72 cluster obtained from the projection along the $x$-axis within a region of $1\,\mathrm{Mpc}$ side length in the redshift interval $z = [0.268, 0.135]$. Contour levels are $10^{-17}, 5 \cdot 10^{-17}, 10^{-16}, 5 \cdot 10^{-16}, 10^{-15}, 5 \cdot 10^{-15}, 10^{-14}, 5 \cdot 10^{-14}, 10^{-13}, 10^{-12}\,\mathrm{erg\,s^{-1}\,cm^{-2}}$.
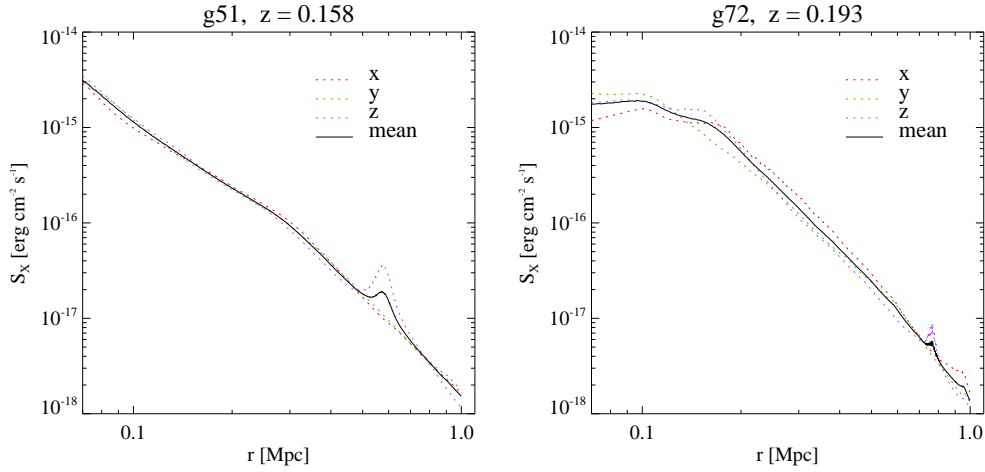
Figure 6.11: Azimuthally averaged X-ray profiles centered on the emission maximum for g51 and g72. Dotted lines show the profiles obtained for projections along the $x$ (red), $y$ (green), $z$-axis (purple). The black solid line represents the mean profile over all three projections.

### 6.3.3 Profiles

We reveal the different thermal characteristics of virialising and merging galaxy clusters by means of two exemplary X-ray profiles of the simulated clusters at different stages of their dynamical evolution.

Figure 6.11 shows the radially averaged X-ray profiles of the clusters g51 and g72 within a radius of 1 Mpc centered on the maxima of thermal emission. The profile of g51 is taken at $z = 0.158$ in a quiet phase between two minor merger events. The profile displays a piece-wise constant slope which becomes steeper at a distance of about 0.3 Mpc away from the centre. The small bump around $r = 0.6$ signals the beginning of the upcoming minor merger at $z \approx 0.1$.

The profile of g72 is taken at the time of the first core passage during the final major merger event. Due to the two the large sub-clumps in the centre of g72 the X-ray profile has flattened in a core region of radius $r \lesssim 02\,\mathrm{Mpc}$, while for larger radii the profile falls of with a single constant slope.

As Figure 6.11 reveals, the two clusters do not significantly differ in their peak thermal brightness but in the size of their X-ray luminous surface area. The large bright core in the profile of g72 is thus the reason for the strong in increase in X-ray luminosity.

## 6.4  Radio emission

The cosmic ray model implemented in GADGET-2 accounts for the production and radiation of secondary cosmic ray electrons - electrons that are injected all over the cluster volume due to hadronic collisions between cosmic ray nuclei and thermal ions in the ICM
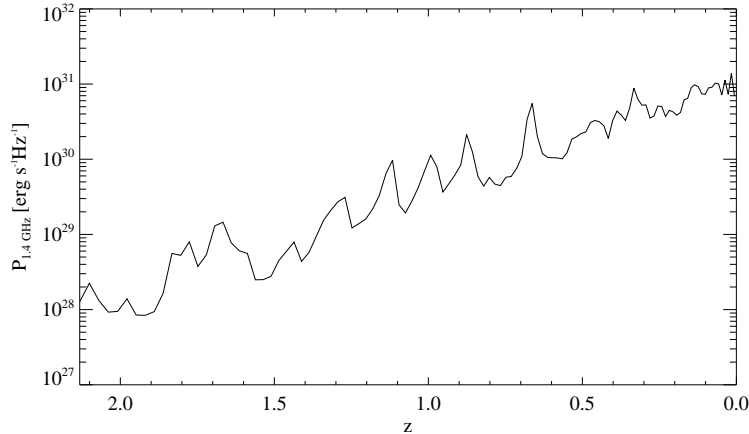
Figure 6.12: Radio synchrotron luminosity of the g8 cluster at 1.4 GHz

(see Sections 3.3.2 and 4.3). Not taken into consideration is the generation and radiation of primary cosmic ray electrons. The latter are populations of mildly relativistic electrons that get re-accelerated by accretion shocks and turbulence in the ICM. Primary electrons are believed to be the main source of the so-called radio relics, small irregular and highly polarised radio lobes observed in the cluster periphery.

Since the cosmic ray model neglects the re-acceleration of primary electrons, our simulated clusters might lack an important fraction of their synchrotron power. The synchrotron emission was calculated under the assumption of an isotropic distribution of magnetic field lines and electron pitch angles according to the formalism presented in Section 4.3.2. The magnetic fields of g8 and g51 were evolved starting from seed values $0.9 \cdot 10^{-8}$ G in order to obtain magnetic energies that constituted about 1 - 10 % of the thermal energy. The seed field of g72 was $0.9 \cdot 10^{-9}$ G and the magnetic energy had to be scaled up retrospectively by a factor $10^2$ in order to arrive at magnetic energies that are typically derived for radio-luminous clusters of galaxies.

### 6.4.1 Luminosities

In Figure 6.12 we show the radio luminosity of the g8 cluster at 1.4 GHz as a function of redshift. The plot displays a large number of pronounced radio peaks imposed on a regular and very steep increase of the luminosity over three orders of magnitude between $z = 2.13$ and $z = 0.006$. The peaks indicate boosts in the synchrotron emissivity by factors of 3 to 10, with a trend towards stronger magnification at higher redshifts. This trend may be due to the fact that the gas densities inside the cluster are lower at higher redshifts and therefore on average stronger shocks are produced. Comparing Figures 6.12 and 6.4, most radio peaks seem to have an X-ray counterpart, although sometimes the X-ray peaks appear slightly shifted towards lower redshifts. This is in accordance with the temporal sequence of lumpy matter accretion during which the strongest shocks are produced when
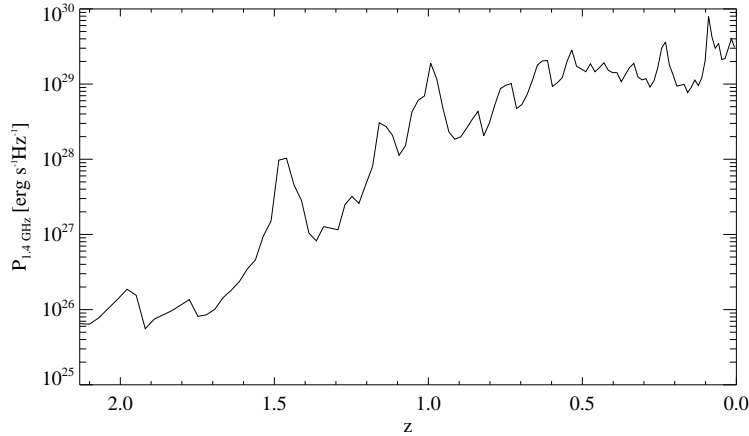
Figure 6.13: Radio synchrotron luminosity of the g51 cluster at 1.4 GHz

an infalling clump crosses the outer, low-density layers of the ICM whereas the rise in temperature is largest when the clump has reached the centre of the cluster.

The synchrotron power emitted at 1.4 GHz of cluster g51 is shown in Figure 6.13. The luminosity grows by four orders of magnitude from $z = 2.13$ and $z = 0.006$. The first crossing of the sub-clump in the major merger event induces a large broad peak around $z \approx 1$ where the radio luminosity instantaneously rises by a factor 10. After the end of the major merger, around $z \approx 0.5$, the overall luminosity at first declines and later rises again around $z \approx 0.1$. In this region, we observe two more large peaks due to minor mergers events, one at $z \approx 2.3$ and one around $z \approx 0.1$. The second merger triggers the emission maximum with a total luminosity of $P_{1.4\mathrm{GHz}} \approx 10^{30} \mathrm{erg\,s^{-1}\,Hz^{-1}}$.

Figure 6.14 shows the radio luminosity of the g72 cluster at 1.4 GHz for redshifts $z = 2.13$ to $z = 0.006$. The increase in radio luminosity by about five orders of magnitude from $\sim 4 \cdot 10^{25}$ to $2.4 \cdot 10^{30}$ Jy arcmin$^{-2}$ is the strongest for all three clusters, and serves as a proof of the hypothesis that merging clusters of galaxies produce the strongest radio emission. The two major merger events around $z \approx 0.65$ and $z \approx 0.2$ hence trigger the strongest release of radio emission. Remarkably, in the second major merger process, the first and the second infall of the sub-clump produce equally large peak luminosities of about $10^{31} \mathrm{erg\,s^{-1}\,Hz^{-1}}$. Several other radio peaks appear in Figure 6.14 that have only very weakly pronounced X-ray counterparts. The low X-ray and high synchrotron peaks can be explained by the fact that the clumps that merge with the cluster at those high redshifts cannot heat up the ICM significantly, due to their low masses. Nevertheless, since the gas density at this time is very low, the clumps produce shocks of considerable strength that subsequently lead to an amplification of the magnetic field and to enhanced cosmic ray production.
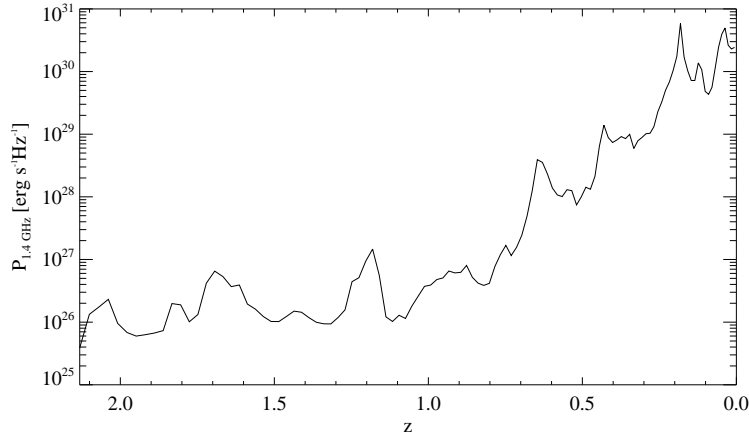
Figure 6.14: Radio synchrotron luminosity of the g72 cluster at 1.4 GHz

## 6.4.2 Morphologies

In order to investigate how matter accretion affects the shape of the radio halo we study contour plots of the synchrotron flux at 1.4 GHz for the situations selected in Section 6.3.2. To allow for a direct comparison with the X-ray morphologies the radio contours are overlaid onto the associated X-ray surface brightness maps. For a better readability, we only show five X-ray contour levels.

In Figure 6.15 we present the radio morphologies of the minor merger event in the g8 cluster at redshifts between $z = 0.416$ and $z = 0.268$. The synchrotron emission is seen to be centred on the maximum of X-ray emission over the whole sequence. In the upper three panels of the plot the radio halo exhibits a spherical shape with irregular boundaries. As the two sub-clumps are approaching the cluster, the radio halo gets distorted and appears slightly elongated along the direction of infall. The contour lines in front of the clump first flatten and then arch inwards as the medium is compressed by the ram pressure of the shock front. This effect is well visible at $z = 0.374$ and at $z = 0.320$ where the radio luminosity ultimately reaches an emission maximum of $\lesssim 10^{30}\,\mathrm{Jy\,arcmin}^{-2}$. The radio boost is thus strongest before the clump has merged with the cluster core. This effect explains why the radio halos of dynamically active galaxy clusters often display an irregular shape.

The X-ray characteristics of the final merger event in the formation history of g51 were described in the last section. We take a closer look at the associated radio morphologies. Figure 6.16 shows the combined radio and X-ray maps in the redshift range $z = [0.124, 0.006]$. The radio halo in the second and third panel is significantly elongated along the direction of infall. The flattening and bending of the contour lines is more pronounced than in the radio maps of cluster g8. This is of course due to the stronger shocks induced by the infall of the relatively large sub-clump. In the subsequent two panels we

can observe how the radio halo gets back into a spherical shape as the cluster starts virial-ising. The shapes of the radio and X-ray contours thereby evolve similarly. The relaxation process is disrupted by the infall of smaller sub-clumps and the halo gets distorted again, thereby increasing its overall size. In the last picture, we again see a flattening of the outermost contour line. All in all we can conclude that the distortion of the radio halo becomes more pronounced for the infall of larger sub-clumps. We thus expect to see an even stronger effect in case of a major merger event.

In Figure 6.17 we show the radio and X-ray contour maps of the first major merger of g72. Before the collision we observe two separate and faint radio halos which are centered on the thermal emission maxima. While the clump is approaching the cluster centre the radio emission intensifies and the two distinct halos merge into one single, elongated radio structure. The rich substructure during the core passage between $z = 0.663$ and $z = 0.613$ suggests that the ICM is violent, filled with shocks, strong currents, and turbulence. While the clump is running out of the cluster core, we see a finger-like structure evolving perpendicular to the direction of outflow. Except for that particular feature, the overall radio and X-ray morphology display a great similarity.

The radio morphologies of the second major merger event are shown in Figure 6.18. The selected redshift interval and the line of sight are the same as for the X-ray maps shown earlier. Again we can observe that the radio halo expands and flattens towards the direction of infall, thereby reflecting the ram pressure caused by the motion of the sub-clump. We see significant substructure in the radio emission which exhibits a high level of turbulence in the ICM. At $z = 0.193$ the radio emission reaches the overall maximum in surface brightness with about $5 \cdot 10^{31}$ Jy arcmin$^{-2}$. There is an obvious analogy to the merger geometry of Abell 2256. The shape of the central radio halo is very similar with the one difference that our secondary cosmic ray electron model is not capable of reproducing the rhombic radio lobe in the wake of the shock front, visible in the upper right corner of Figure 3.9. This striking feature in the radio emission of Abell 2256 is evidently caused by primary electrons that got re-accelerated by the turbulent motion behind the shock front. Nevertheless, the remarkable similarity between the simulation and the observation strongly supports the applicability of our numerical models. After the sub-clump has crossed the centre of the main halo, the radio halo gets significantly enlarged by the outgoing shock front. In doing so it traces the morphology of the thermal emission. In the last six panels the radio halo has reached an approximate overall size of about 1 Mpc which corresponds to the average size of observed radio halos.

### 6.4.3 Profiles

In this section we present the radio profiles of the clusters g51 and g72 in order to disclose the differences in the non-thermal properties of relaxing and merging galaxy clusters.

Figure 6.19 shows the azimuthally averaged radio profiles of g51 and g72 at redshifts $z = 0.158$ and $z = 0.193$. Most remarkably, the peak brightness of the radio halo in g72 is about a factor 7 higher than that of the radio halo in g51. Both profiles display a flattening of the core region and similar slopes outside $r \approx 0.2$ Mpc with a slightly steeper decline
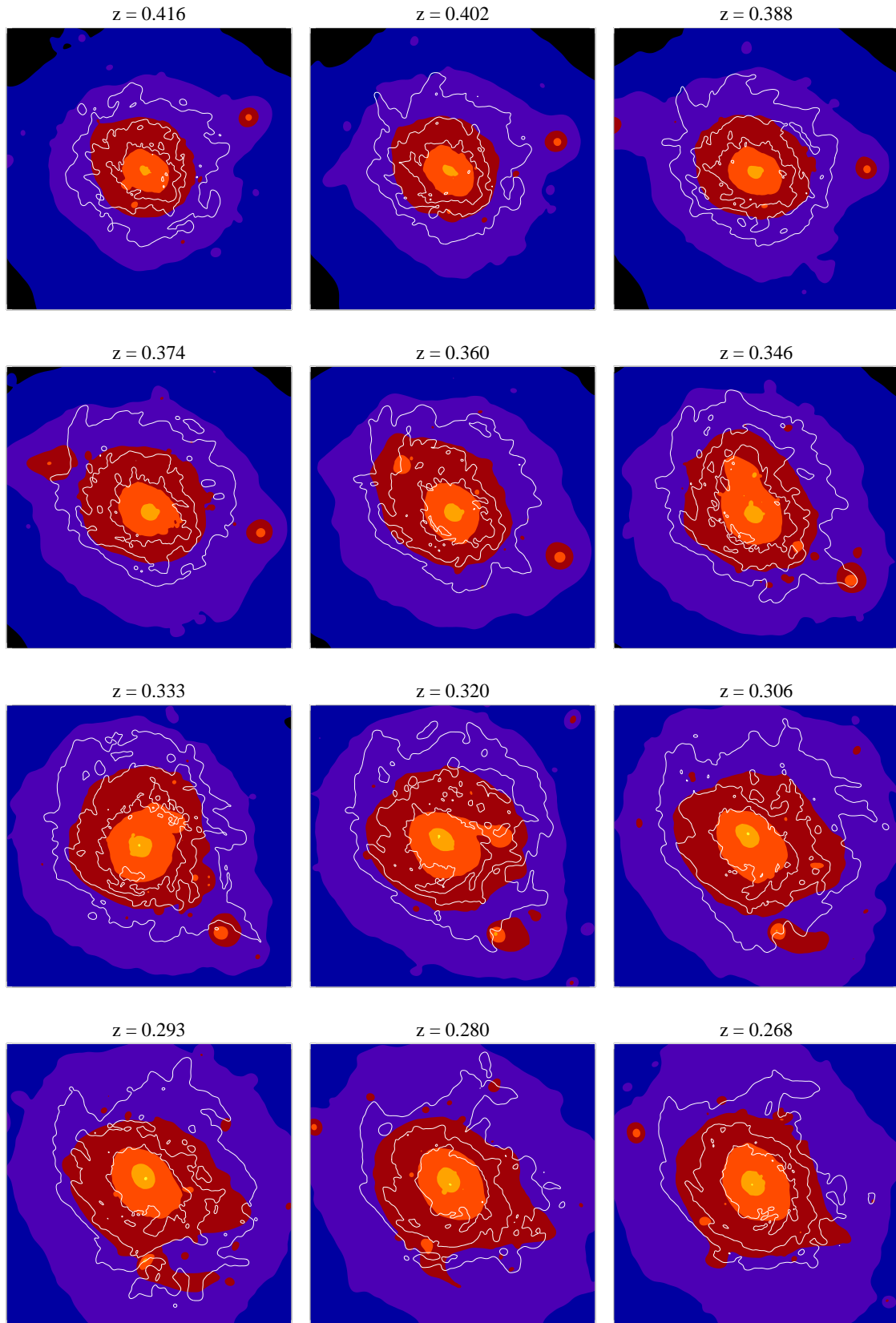
Figure 6.15: Overlay of the radio contours at $S_{1.4\mathrm{GHz}} = [10^{-6}, 10^{-5}, 10^{-4}]\,\mathrm{Jy\,arcmin^{-2}}$ and the X-ray surface brightness contour maps of the g8 cluster. The maps were obtained from the projection along the $x$-axis within a region of $1\,\mathrm{Mpc}$ side length in the redshift interval $z = [0.416, 0.268]$.
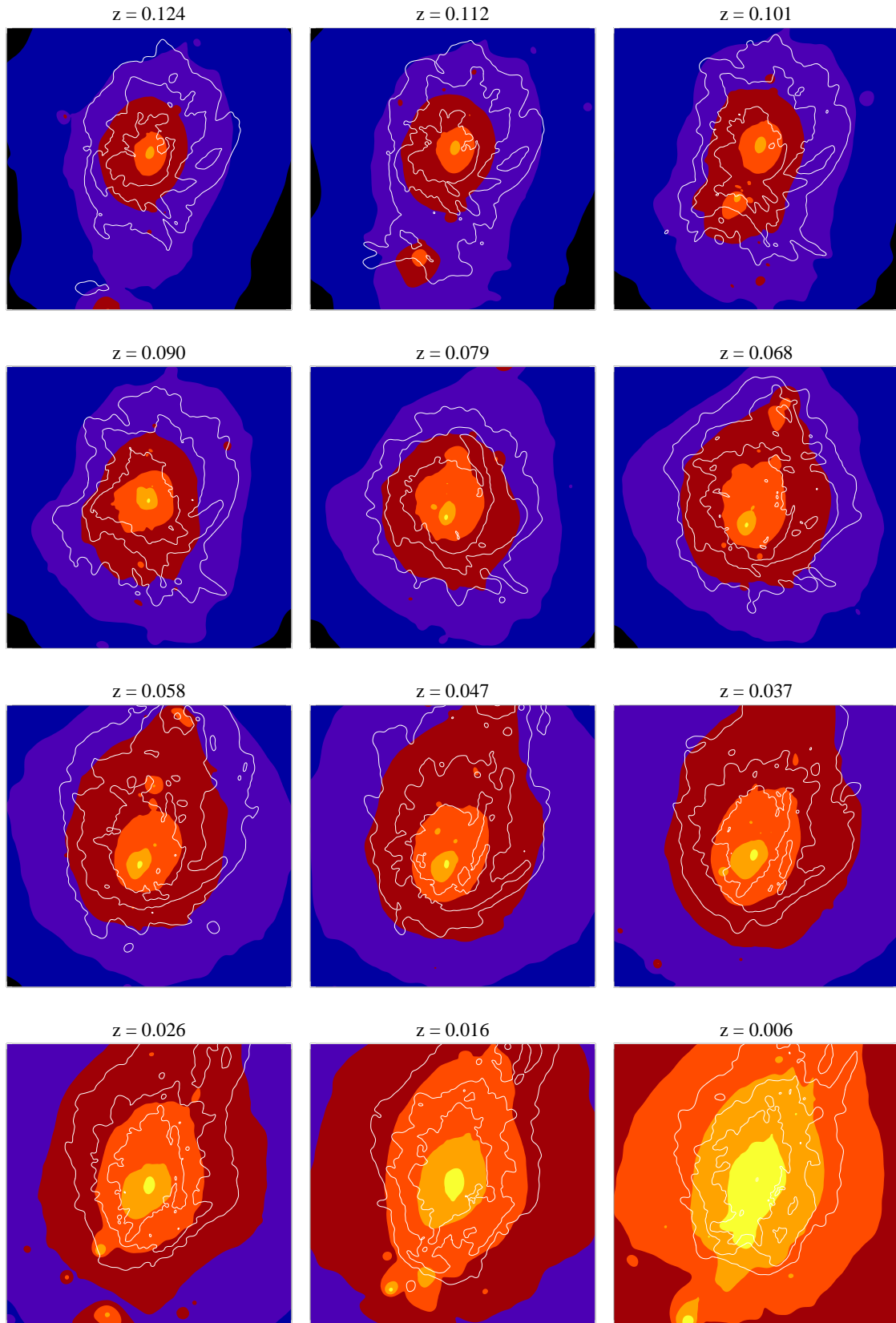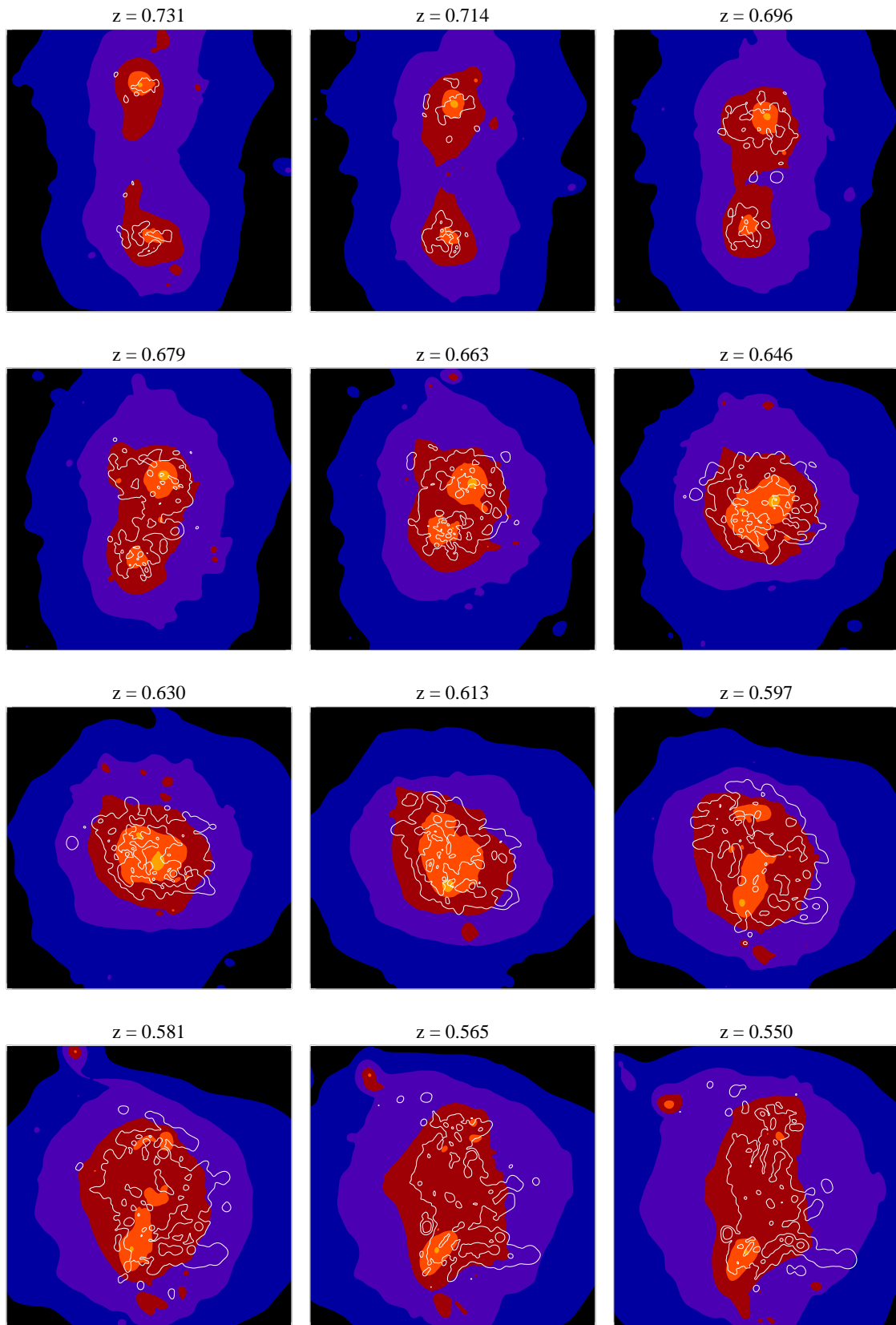
Figure 6.16: Overlay of the radio contours at $S_{1.4\,\mathrm{GHz}} = [10^{-7}, 10^{-6}, 10^{-5}]\,\mathrm{Jy\,arcmin^{-2}}$ and the X-ray surface brightness contour maps of the g51 cluster. The maps were obtained from the projection along the $x$-axis within a region of $1\,\mathrm{Mpc}$ side length in the redshift interval $z = [0.124, 0.006]$.
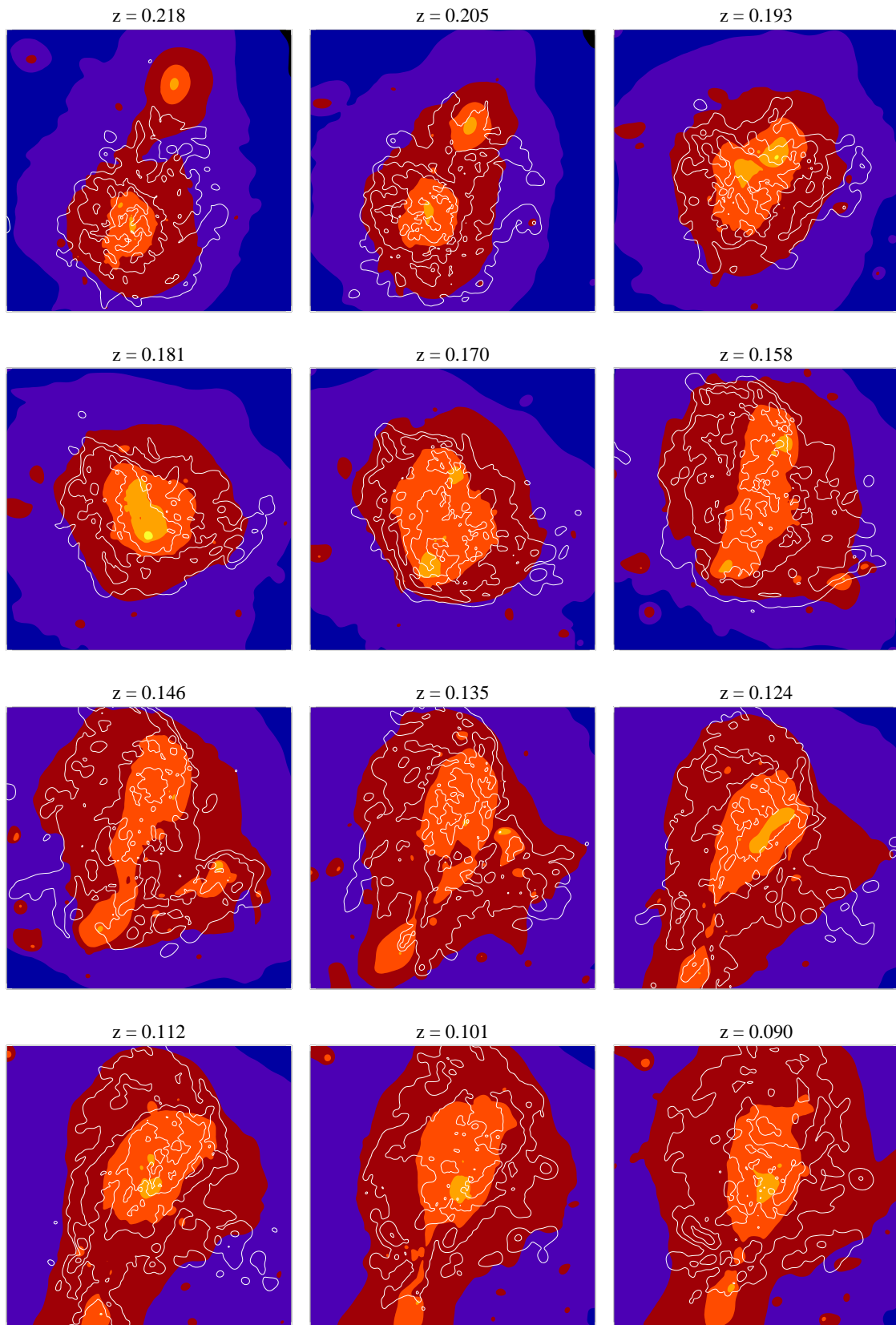
Figure 6.17: Overlay of the radio contours at $S_{1.4\text{GHz}} = [10^{-7}, 10^{-6}, 10^{-5}] \, \text{Jy arcmin}^{-2}$ and the X-ray surface brightness contour maps of the g72 cluster. The maps were obtained from the projection along the $y$-axis within a region of $1 \, \text{Mpc}$ side length in the redshift interval $z = [0.731, 0.550]$.

Figure 6.18: Overlay of the radio contours at $S_{1.4\mathrm{GHz}} = [10^{-6}, 10^{-5}, 10^{-4}]\,\mathrm{Jy\,arcmin}^{-2}$ and the X-ray surface brightness contour maps of the g72 cluster. The maps were obtained from the projection along the $x$-axis within a region of $1\,\mathrm{Mpc}$ side length in the redshift interval $z = [0.218, 0.090]$.
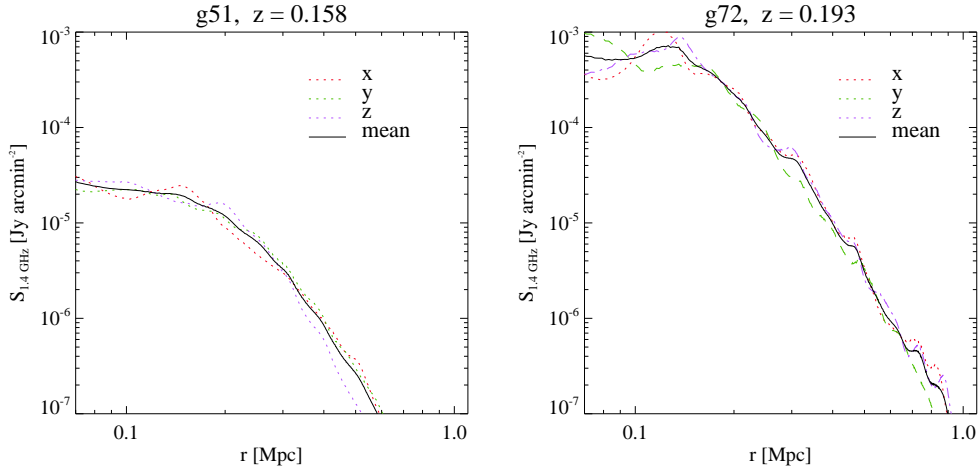
Figure 6.19: Azimuthally averaged radio profiles at 1.4 GHz centered on the emission max-
imum for g51 and g72. Dotted lines show the profiles obtained for projections
along the $x$ (red), $y$ (green), $z$-axis (purple). The black solid line represents
the mean profile over all three projections.

in the surface brightness in g72. The bumps close to the centre and in the outskirts of
the radio profile in g72 signals that the radio halo has a clumpy and very irregular shape
which is also obvious in Figure 6.18.

The high surface brightness of g72 leads to a peak in the radio luminosity which is about
a factor 15 larger than that of g51 at the specified redshifts. The faintness of the radio
halo of g51 might explain why diffuse radio emission is not detected in galaxy clusters that
do not exhibit signs of recent merger events.

## 6.5  Radio - X-ray comparison

So far there seems to be convincing evidence that diffuse radio sources are preferentially
associated with high X-ray luminous clusters that undergo strong mergers. In order to give
additional support to this theory we present a more systematic study of the correlation
between merger activity and radiative processes in our sample of simulated clusters.

Figures 6.20, 6.21, and 6.22 show the luminosity evolution of the g8, the g51, and the
g72 cluster respectively. Both functions are shown in logarithmic scaling. In all three
clusters the two curves exhibit striking similarities in the positions of the luminosity peaks
as well as in their relative height.

A few exceptions can be seen for example in the light curves of g51 where, around the
redshift $z = 1$, two peaks appear in the X-ray emission while in the radio power only
one broad peak can be seen. Furthermore, around $z \approx 1.25$ there is a small bump in the
radio distribution which has no counterpart in X-ray. The same feature can be seen in the
emission characteristics of g8 at $z \approx 1.3$ and $z \approx 0.45$ where we observe two distinct peaks
in the X-ray emission but only one single maximum in the radio brightness. Also, in both
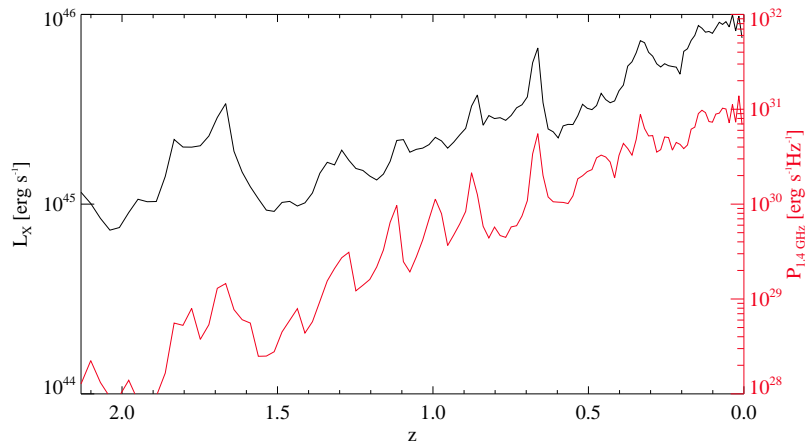
Figure 6.20: X-ray (black line) to radio (red line) comparison in the redshift interval $z = [2.13, 0.006]$ for the simulation of the g8 cluster.
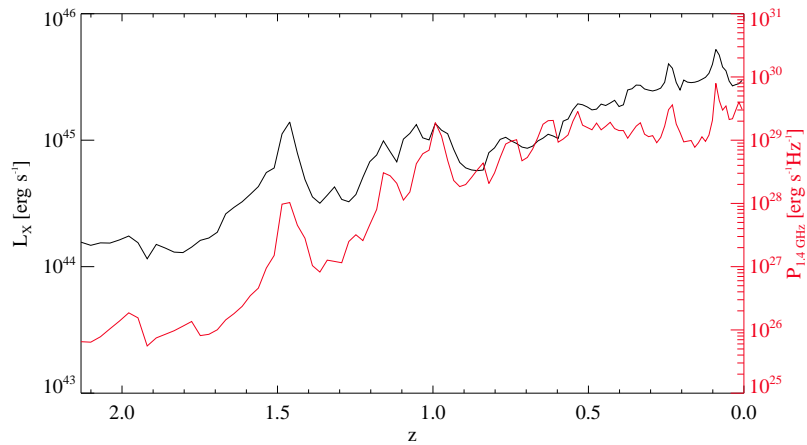


Figure 6.21: X-ray (black line) to radio (red line) comparison in the redshift interval $z = [2.13, 0.006]$ for the simulation of the g51 cluster.
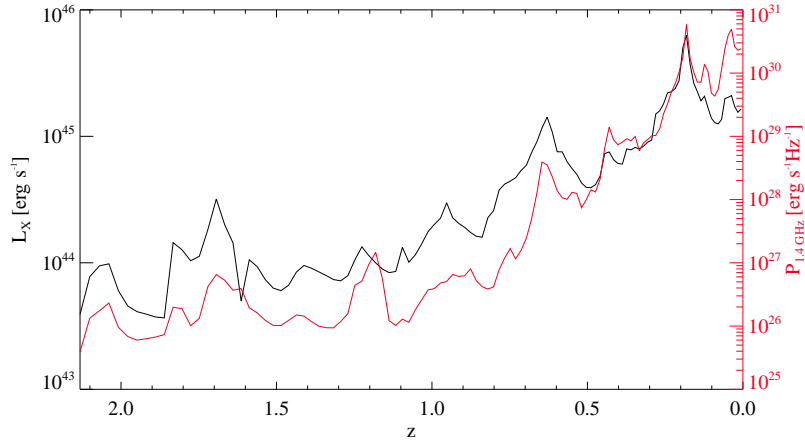
Figure 6.22: X-ray (black line) to radio (red line) comparison in the redshift interval $z = [2.13, 0.006]$ for the simulation of the g72 cluster.

clusters g8 and g51, the light curves appear less correlated at higher redshifts. However, since high redshifts correspond to extremely large distances and low gas densities galaxy clusters at those redshifts cannot be observed.

The X-ray luminosity curve of the g72 cluster is clearly dominated by the two major merger events. The situation is more ambiguous for the radio power which displays a few more quite prominent peaks such as the maxima at $z = 1.2$ and $z = 0.06$. As mentioned earlier, we assume that the much smaller X-ray boosts at early times are due to low gas densities and temperatures, a physical fact that can also explain the pronounced radio peaks between $z = 1.2$ and $z = 0.8$ in the rather smooth accretion history of g8. The relatively small X-ray boost in the late formation history of g72 could be due to the fact that the merging sub-clump has already lost a part of its mass during the first crossing and therefore the final infall does not trigger an equally strong X-ray boost in thermal emission. Looking back at the last panels in Figure 6.18 we see that the whole cluster core is indeed disrupted and the final merging is split into a number of smaller mergers.

In order to further quantify the temporal correlation between the radio power and the X-ray luminosity for each cluster we calculate the cross correlation function

$$\xi(\tau) = \langle (P_{1.4\mathrm{GHz}} - \langle P_{1.4\mathrm{GHz}} \rangle)(t + \tau)(L_\mathrm{X} - \langle L_\mathrm{X} \rangle)(t) \rangle, \tag{6.1}$$

which is obtained by calculating the correlation coefficients of the two signatures for a shifting by a certain number $\tau$ of intervals in time $t$. Time in this respect means intervals of constant $\log(z + 1)$ which is the time interval between two GADGET-2 snapshots. The mean values $\langle P_{1.4\mathrm{GHz}} \rangle$ and $\langle L_\mathrm{X} \rangle$ were calculated by averaging over a total of nine snapshots including the current snapshot and the four preceding and subsequent snapshots respectively. For the four first and last snapshots the averages were accordingly calculated with a smaller sample of luminosities. By this means we subtracted the average upgrowth of both quantities. The cross correlation functions were computed for a shifting of 20 output times in both directions, where the minus sign refers to a shifting of the X-ray
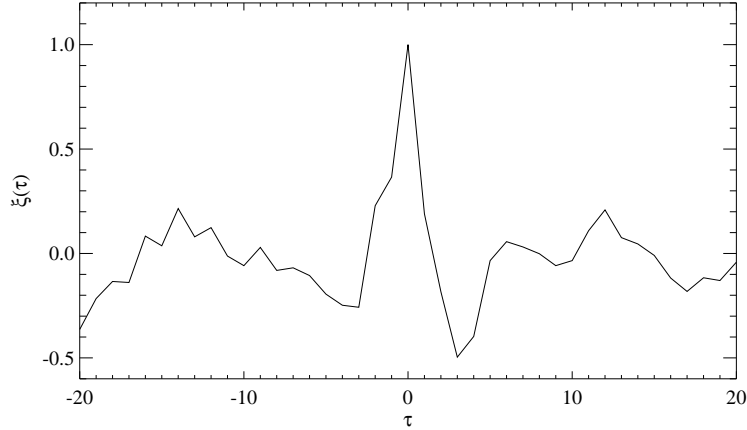
Figure 6.23: Cross-Correlation coefficient of the radio and X-ray luminosities of the g8 cluster as a function of shiftings in $\log(1+z)$. Negative values correspond to a shifting of $L_X$ towards earlier times with respect to $P_{1.4\text{GHz}}$ while positive values correspond to shifting to later times.

luminosity to earlier times with respect to the radio emission and the plus sign refers to a shifting in the opposite direction.

Figures 6.23, 6.24, and 6.25 show the results of the calculation for each of the three clusters. For a clearer presentation, the correlation functions are normalised to one. In Figure 6.23 the cross correlation function of the g8 cluster yields a very clear result. The central peak at $\tau = 0$ dominates the function thus proving that the two observables are correlated. The cross correlation functions of g51 and g72 are more ambiguous. The maxima at $\tau = 0$ are largest, but nevertheless, some of the lateral peaks are very pronounced. In Figure 6.24 we see four peaks that occur symmetrically at $\tau = \pm 7$ and $\tau = \pm 13$ and have approximately the same height. In Figure 6.25 two large lateral maxima appear at $\tau = -6$ and $\tau = -12$ and two smaller ones at $\tau = 7$ and $\tau = 13$.

There is a simple explanation for these results: The two peaks at $z = 1.16$ and $z = 1.01$ in the light curves of g51 in Figure 6.24 are separated by seven output intervals while the very pronounced peak at $z = 1.46$ is 13 output times away from $z = 1.16$. Consequently, the overlapping of the three peaks give large contributions to the cross-correlation coefficient of the g51 cluster at $\tau = \pm 7$ and $\tau = \pm 13$. The same effect applies for the cross-correlation function of cluster g72 where it leads to feigned correlations for shiftings of $\tau = -7, -13$ and $\tau = 6, 12$.

The cross-correlation analysis thus provides convincing evidence that the thermal and non-thermal components in the simulated galaxy clusters are correlated and consequently lead to simultaneous bursts in X-ray and radio emission.
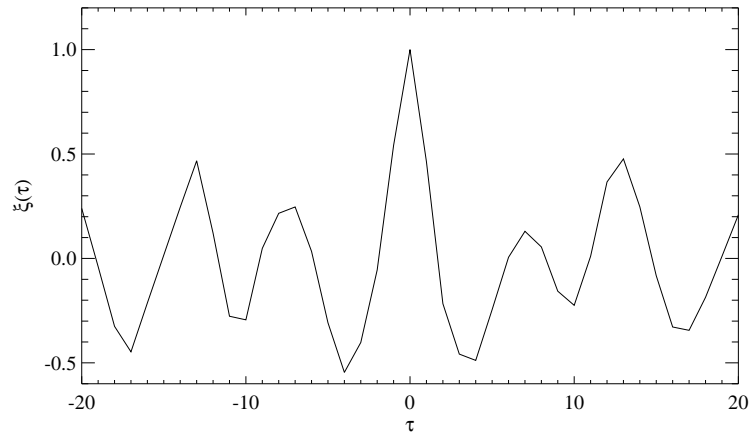
Figure 6.24: Cross-Correlation coefficient of the radio and X-ray luminosities of the g51 cluster as a function of shiftings in $\log(1+z)$. Negative values correspond to a shifting of $L_X$ towards earlier times with respect to $P_{1.4\mathrm{GHz}}$ while positive values correspond to shifting to later times.
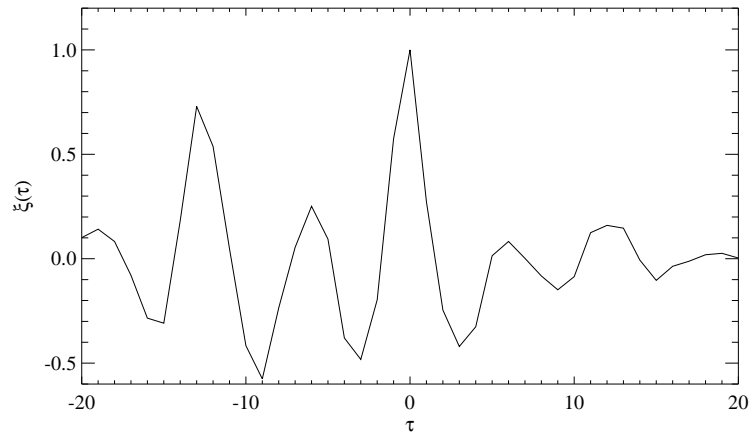


Figure 6.25: Cross-Correlation coefficient of the radio and X-ray luminosities of the g72 cluster as a function of shiftings in $\log(1+z)$. Negative values correspond to a shifting of $L_X$ towards earlier times with respect to $P_{1.4\mathrm{GHz}}$ while positive values correspond to shifting to later times.

## 6.6 Strong lensing cross sections

Galaxy clusters act as gravitational lenses on the light emitted by background sources. Since the light deflection angles depend on the matter distribution inside the lens, the lensing properties of the simulated clusters are strongly affected by mass accretion and merger activity. Consequently, we expect to see a temporal correlation between the increase of the radio and X-ray emission, triggered by accretion shocks and the increase of temperature in the ICM, and the light deflecting properties of the underlying dark matter distribution. In what follows we will introduce the strong lensing cross section $\sigma_{7.5}$ which will serve as a measure for the light deflecting power of the simulated clusters in the course of their evolution.

The strong lensing cross section $\sigma_{7.5}$ is defined by the sum of the statistical weights of sources that produce images with $L/W \geq 7.5$. If there is more than one such image for a source, the statistical weights are multiplied by the number of images. The corresponding area is expressed in co-moving Mpc. The strong lensing cross section is particularly useful for tracing the accretion history of the simulated clusters since it increases when a sub-halo crosses the cluster core during a merger (Torri et al. 2004; Meneghetti et al. 2005). Consequently, if there is a correlation between merger events and the boost in X-ray and radio luminosity we must observe a simultaneous increase in the strong lensing cross section and the radio and X-ray brightness.

The numerical routines for calculating the strong lensing cross sections were kindly provided by Ewald Puchwein who designed the algorithm in order to investigate the impact of gas physics on strong cluster lensing in a sample of four galaxy clusters, including g8, g51, and g72. We will give a brief summary of the numerical method, details are found in Puchwein et al. (2005).

The surface mass density $\Sigma$ of each cluster is obtained by projecting all dark matter particles that are located inside a sphere of co-moving radius $3\,h^{-1}\,\mathrm{Mpc}$ around the cluster centre onto an equidistant grid of $4096^2$ grid cells. From the projected mass map the convergence $\kappa$ and its Fourier transform $\hat{\kappa}$ are calculated. In Fourier space, the Poisson equation (3.71) takes the simple linear form

$$\hat{\psi} = -\frac{2}{k^2}\hat{\kappa}\,,\tag{6.2}$$

from which we derive the Fourier transform of the lensing potential $\hat{\psi}$ and subsequently transform it back to the real value $\psi$. However, due to the non-periodicity of the convergence field, the discrete Fourier algorithm gives accurate results only in a narrow region around the cluster centre. The error can be reduced by calculating the Fourier transform of a perfectly periodic, two-dimensional array of cluster point masses with periodicity $6\,h^{-1}\,\mathrm{Mpc}$, and then subtracting the same array with one point mass missing at the position of the original cluster. The remaining error can then be neglected in the central $1024^2$ cells of the grid which serve as the lensing plane.

A number of elliptical sources with an equivalent radius of 0.5 arcsec was placed at the source plane, which was held fixed at $z = 1.5$. To obtain an adequate number of arcs, the density of sources close to the caustics was particularly high. Statistical weights

were assigned to the sources according to the areas represented. This method was first introduced by Miralda-Escude (1993b,a) as a tool for the statistical analysis of lensed images. A detailed description for non-analytic models is given in Bartelmann & Weiss (1994) and Bartelmann et al. (1995).

Using the deflection angles calculated from the lensing potential $\hat{\psi}$, one can trace back the path of a light ray from a grid point in the lens plane to a point in the source plane and check whether it matches one of the specified sources. As described in Meneghetti et al. (2000), the images are approximated by simple geometrical figures such as ellipses, circles, rectangles or rings with a specified length-to-width ratio $L/W$.

Figure 6.26 shows the strong lensing cross section as a function of redshift for all three projections of g8. Also shown as the dotted lines is the radio luminosity at 1.4 GHz. All three cross sections display the prominent peaks around $z \approx 0.7$ and $z \lesssim 0.5$, as well as several minor maxima which indicate enhanced dynamical activity. In the comparison with the radio luminosity we see that to each maximum in the cross section we can assign a peak in the synchrotron emission of the cluster. In the upper panel, which corresponds to the line of sight along the $x$-axis, we can identify the infall of the two clumps which we described earlier. The plot reveals that the radio maximum lies exactly between the two sub-mergers when the shock compression is the strongest. The effect is even better visible for the projection along the $y$-axis, as shown in the lower panel.

In Figure 6.27 we compare the strong lensing cross sections of the g51 cluster with its radio luminosity at 1.4 GHz. Remarkably, the impact of matter infall on the strong lensing cross section of g51 greatly depends on the line of sight. While the merger at $z \approx 2.3$ in the second panel leads to an increase of the cross section by more than 100 %, it leaves no marks in the first panel. The same happens for the spike at $z \approx 0.5$ in the last panel, which is not present in the other two projections. Nevertheless, we observe a small radio peak at the same redshift which is obviously connected to the infall. Also for the other peaks in the cross sections, there is an obvious correlation with phases of enhanced radio activity of the ICM in g51.

The strong lensing cross sections of the g72 cluster are very narrowly peaked around the final major merger at $z \approx 0.19$. Furthermore visible are the two core passages of a sub-halo around $z \approx 0.67$ and $z \approx 0.48$ which both times leads to a strong increase of the cross section of the first panel, while in the other two panels only the second core passage is pronounced. The radio luminosity follows the trend of the cross section very accurately over the entire redshift range which is a clear proof of the connection between merger activity and augmented synchrotron emission.

## 6.7 Conclusions

On the basis of numerical simulations of three different galaxy clusters we have shown that the hierarchical evolution of galaxy clusters via mergers of sub-clumps with the main halo produces a variety of observational signatures such as a strong increase in radiative power, elongated and clumpy X-ray emission and extended and irregular radio synchrotron halos.
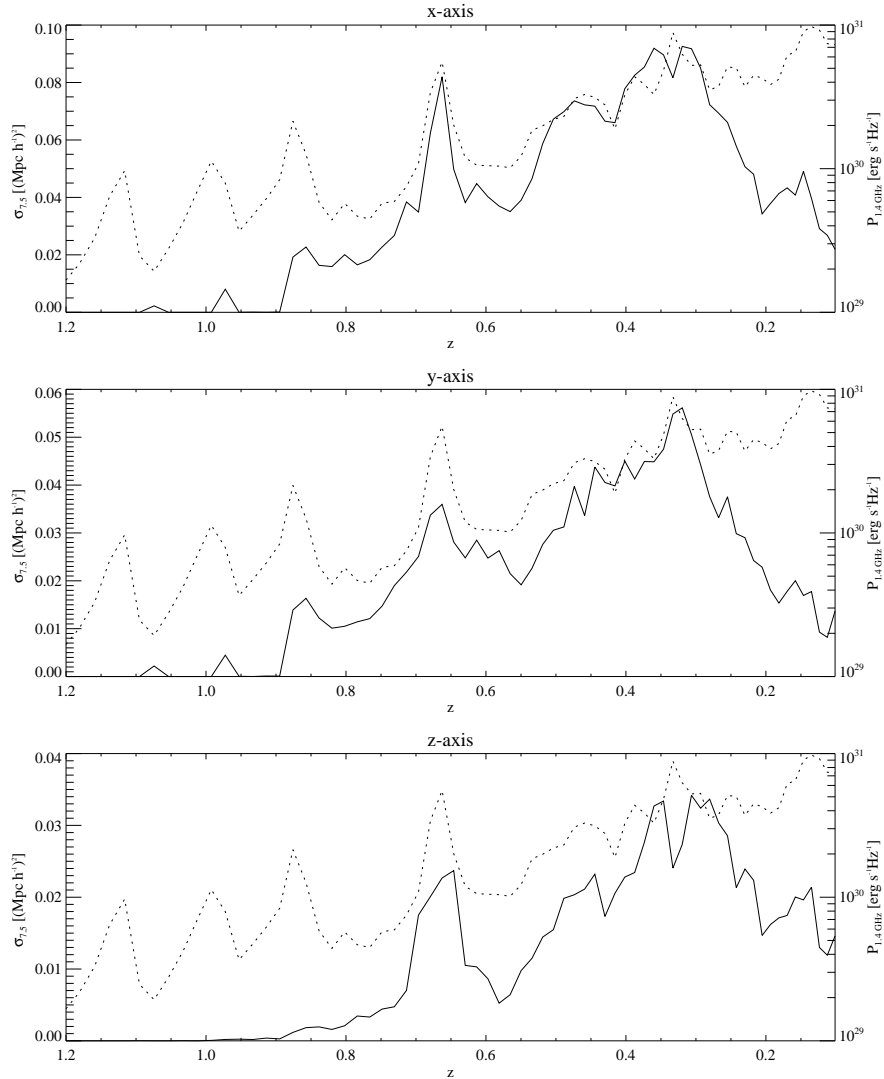
Figure 6.26: Strong lensing cross sections for projections along the $x$, $y$, and $z$-axis of the simulations of the g8 cluster. The cluster is shifted within the redshift interval $z = [0.08, 1.20]$ while the source is fixed at $z = 1.5$. Overplotted as the dotted lines is the radio luminosity at 1.4 GHz as a function of redshift.
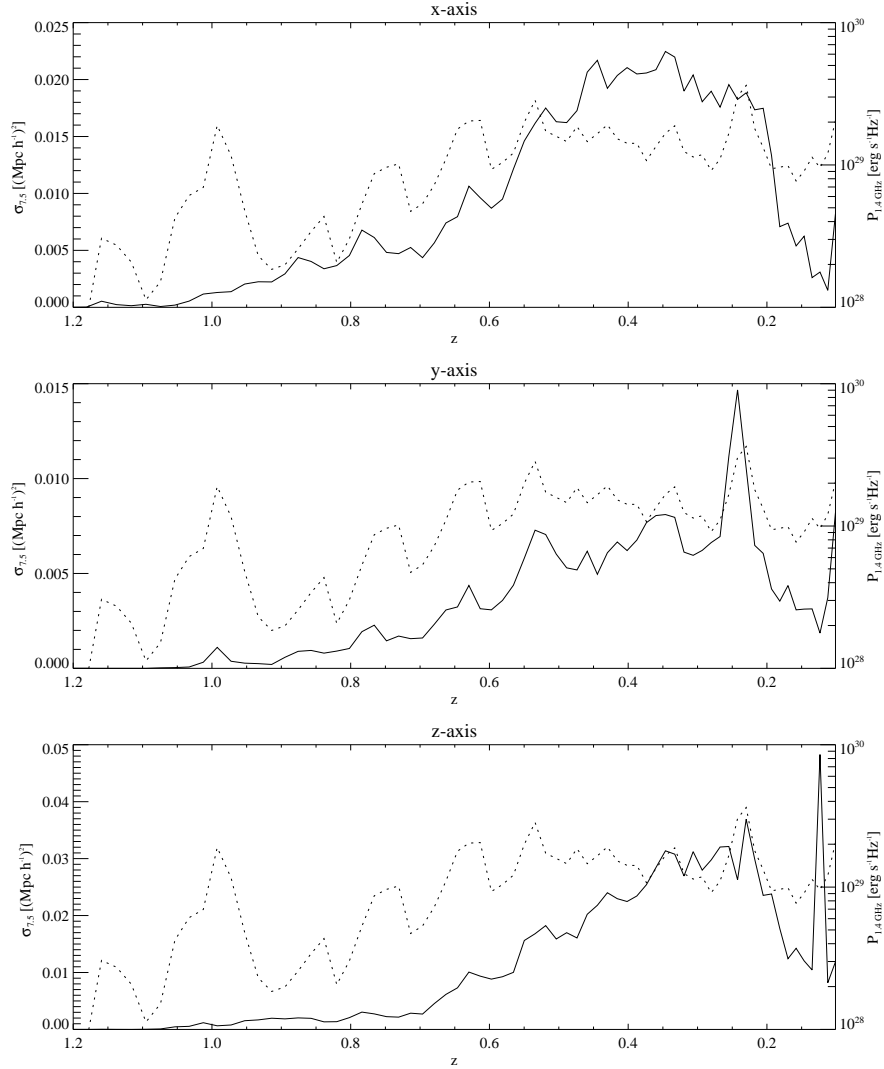
Figure 6.27: Strong lensing cross sections for projections along the $x$, $y$, and $z$-axis of the simulations of the g51 cluster. The cluster is shifted within the redshift interval $z = [0.08, 1.20]$ while the source is fixed at $z = 1.5$. Overplotted as the dotted lines is the radio luminosity at 1.4 GHz as a function of redshift.

Figure 6.28: Strong lensing cross sections for projections along the $x$, $y$, and $z$-axis of the simulations of the g72 cluster. The cluster is shifted within the redshift interval $z = [0.08, 1.20]$ while the source is fixed at $z = 1.5$. Overplotted as the dotted lines is the radio luminosity at 1.4 GHz as a function of redshift.
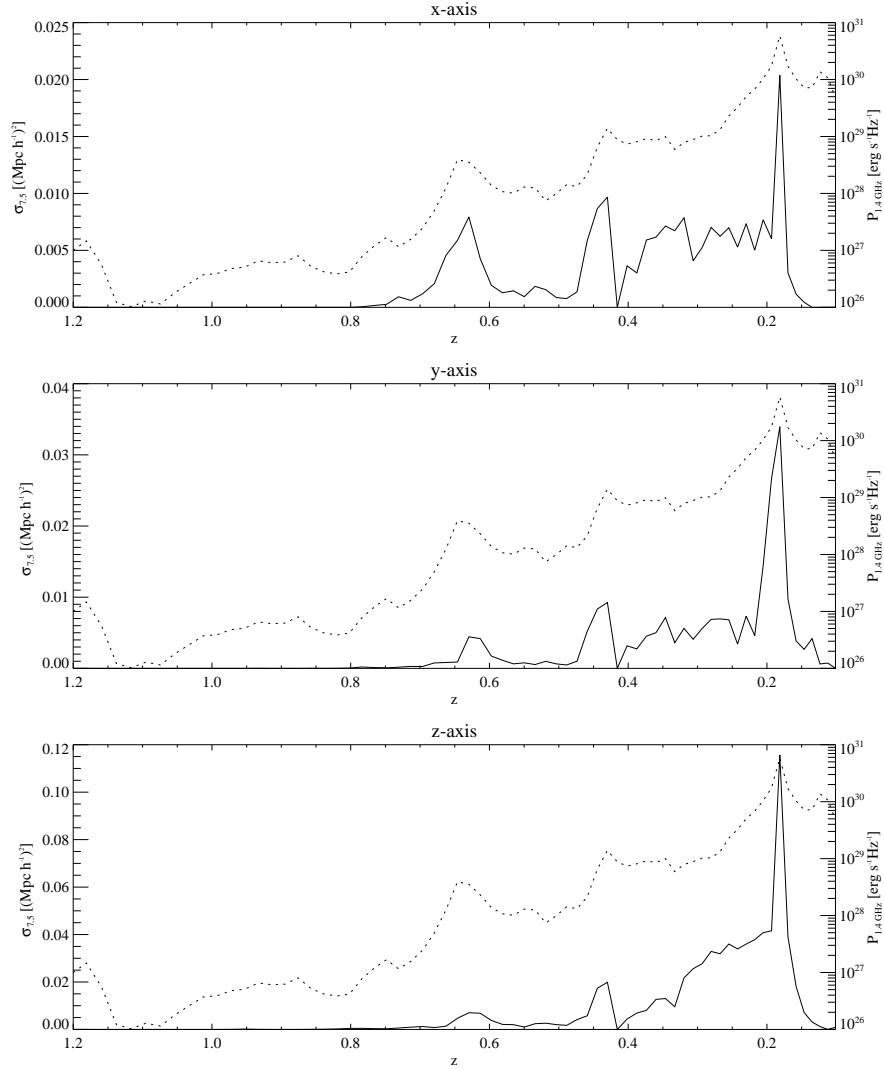
The temporal evolution of the X-ray and radio power of the cluster sample suggests that the presence of strong and diffuse thermal and non-thermal emission in the ICM is related to the existence of strong minor and major merger events. Further support comes from our study of selected X-ray and radio maps in which we discovered morphological similarities between the thermal gas distribution and the structure of radio halos.

The direct comparison of the X-ray and radio luminosities revealed the strong correlation between thermal and non-thermal activity of the simulated clusters over a wide range of redshifts. Verification was obtained by calculating the cross-correlation functions of both signatures.

Finally, through a comparison of the strong lensing cross sections with the radio luminosity functions we have demonstrated that the radio properties of the simulated galaxy clusters are strictly connected to their structure formation histories. The presence of non-thermal components such as relativistic particles and magnetic fields is thus found to be related to the existence of minor and major merger events.

# Summary and conclusions 7

There is strong observational evidence that the presence of diffuse, large-scale radio halos in massive and unrelaxed clusters of galaxies correlates with a high X-ray luminosity. The radio emission which is not associated to single galaxies but to the intracluster medium has a synchrotron origin. According to the standard scenario, the synchrotron emission is produced by the gyration of relativistic electrons, so-called cosmic rays, in the magnetised plasma of the clusters. The existence of cosmic rays and magnetic fields in galaxy clusters has been proven independently.

One goal of this thesis was to test the combined performance of the magnetic field implementation and the self-consistent cosmic ray model in GADGET-2, a massively parallel tree-SPH code designed and released by Volker Springel. After successful testing, the modules were employed in simulations of the formation of galaxy clusters. The purpose of these simulations was to prove the existence of a correlation between the emission and the dynamical state of the clusters.

In the first part of this thesis, amongst other things, we summarised our current knowledge about intracluster magnetic fields and the origin of cosmic rays. We emphasised the importance of cluster mergers, being the most energetic triggers of field amplification and particle acceleration in the intracluster medium. Furthermore, we presented the radiation mechanisms that lead to the observed large-scale radio and X-ray emission.

In the second part of this thesis we gave an introduction to smoothed particle hydrodynamics, the numerical method for modelling baryonic gas physics in GADGET-2. We described its application to magnetohydrodynamics. We furthermore introduced the self-consistent cosmic ray model developed by Ensslin, Pfrommer, and Jubelgas.

To provide the theoretical basis for the performance tests with the magnetic field implementation and the cosmic ray model, we introduced the MHD Riemann problem which serves as a standard test problem for MHD codes. As a first step we implemented the analytical MHD Riemann solver presented by Dai and Woodward. To check its operational reliability, we reproduced five shock tube problems presented in the paper. We furthermore checked the solutions against shock tube simulations with GADGET-2. The tests showed an accurate agreement between the analytical and numerical solutions.

To account for the presence of cosmic rays we developed a novel analytical solution to the MHD Riemann problem for a composite of a thermal gas and cosmic rays. We upgraded the analytical Riemann solver to the solving of the MHD Riemann problem

with the composite gas. We then repeated the five shock tube calculations presented earlier, including a cosmic ray pressure component that constituted 30 - 200 % of the thermal gas pressure. The shock tube calculations were performed with the analytical Riemann solver and with GADGET-2. Our results are summarised in the following:

- The MHD Riemann problem in the two-fluid case involves the solution of a system of four equations with eight unknowns. This can be done using an iterative scheme. One needs to supply initial values for the density jumps over the four magnetosonic wave fronts and the corresponding tangential components of the magnetic field.

- By means of the two-fluid Riemann solver we accurately predicted two out of five simulation results. For a third Riemann problem the agreement of the theoretical and simulated results was satisfactory. In one case, the Riemann solver converged to a different solution, due to an unfitting initial guess for at least one of the parameters. The last Riemann problem, which was the cosmic-ray modified Brio and Wu shocktube, could not be solved with our Riemann solver. The algorithm is not suited for this particular Riemann problem which is known to exhibit a special wave phenomenon.

- The successful theoretical prediction of the results of three shocktube simulations with GADGET-2 was taken as a strong indicator for the correct physical behaviour of the code. Since all shock tube tests included high cosmic ray pressures that were far beyond the expected relativistic pressures in the cosmological simulations, we suppose that the magnetic field implementation and the cosmic ray model can be used simultaneously when modelling the formation of galaxy clusters.

- The Mach number finder in GADGET-2 does not account for the magnetic pressure in magnetohydrodynamic shocks. In the numerical shocktube calculations we observed a mean deviation of 10 - 15 % between the theoretical and simulated Mach numbers for a purely thermal gas. Since the shock strength estimation in GADGET-2 is suited to the inclusion of cosmic rays, the errors in the Mach numbers should be similar for shocktube calculations in a composite of cosmic rays and a thermal gas. In cosmological simulations, this error can be completely neglected since the magnetic energy makes up only 1 - 10 % of the thermal energy in galaxy clusters.

After the validation through the shock tube tests, we performed simulations of the structure formation of three different galaxy clusters, including magnetic fields and cosmic rays. In a post-processing procedure we calculated the thermal bremsstrahlung emission from the intracluster gas and the synchrotron energy losses of the secondary cosmic ray electron population at a frequency of 1.4 GHz. We furthermore computed the strong lensing cross sections of all three galaxy clusters. On the basis of these observables we discussed the evolution of the thermal and non-thermal emission and its connection to merger activity. We obtained the following results:

- In all three galaxy clusters we observed a strong increase in X-ray luminosity between redshifts $z = 2.13$ and $z = 0.006$. In one cluster with a rather smooth accretion

history, the X-ray brightness raised by a factor of 9 in the specified redshift range. In contrast, the thermal luminosity of a cluster with two major mergers in the same time grew by a factor of $\sim$37. In all three clusters, strong luminosity boosts occurred during the accretion of larger sub-clumps. Depending on the relative size of the infalling sub-clumps, the peak luminosities reached up to 200 - 300 % of the mean value.

- In the same redshift interval, $z = [2.13, 0.006]$, the radio luminosity at 1.4 GHz in the cluster sample grew by three to five orders of magnitude, with the larger increases for a higher merger activity. Locally, the radio luminosity evolution displayed strong peaks which coincided with the occurrence of strong shocks in the intracluster gas. The shocks induced an increase of the radio emissivity by about one order of magnitude.

- We found that the X-ray and radio maps have similar morphologies and display significant substructure during strong merger events. Furthermore, due to the ram pressure of large shock fronts, the surface brightness and overall size of the radio halos increased significantly. These effects are consistent with the observation and can plausibly explain why large-scale radio emission so far has only been detected in galaxy clusters that show signs of recent major merger events.

- In a systematic comparison of the X-ray and radio luminosities we could verify that the X-ray and radio observables of the simulated clusters are correlated in time. A comparison of the synchrotron luminosity and the strong lensing cross sections of the clusters furthermore proved that the radio boosts are strictly connected to merger activity.

Our results give strong support to the hypothesis of a correlation between large-scale radio emission and merger activity as inferred from the observations. We note that a secondary cosmic ray electron population can only in part explain the radio morphologies of real galaxy clusters. We expect to obtain more realistic radio halos if the production of primary cosmic ray electrons in the intracluster medium is taken into account as well.

# Bibliography

Abell, G. O. 1958, ApJS, 3, 211

Alpher, R. A., Bethe, H., & Gamow, G. 1948, Phys. Rev., 73, 803

Alpher, R. A. & Herman, R. C. 1949, Phys. Rev., 75, 1089

Arnaud, K. A. 1996, in Astronomical Society of the Pacific Conference Series, Vol. 101, Astronomical Data Analysis Software and Systems V, ed. G. H. Jacoby & J. Barnes, 17–+

Ascasibar, Y., Yepes, G., Müller, V., & Gottlöber, S. 2003, MNRAS, 346, 731

Balsara, D. S. 1998, ApJS, 116, 119

Barmin, A. A., Kulikovskiy, A. G., & Pogorelov, N. V. 1996, J. Comp. Phys., 126, 77

Bartelmann, M., Steinmetz, M., & Weiss, A. 1995, A&A, 297, 1

Bartelmann, M. & Weiss, A. 1994, A&A, 287, 1

Benz, W. & Hills, J. G. 1987, ApJ, 323, 614

Bergman, D. R. & Belz, J. W. 2007, J. Phys. G: Nucl. Part. Phys., 34, R359

Biermann, L. 1950, Zeit.Naturforschung, 5a, 65

Blandford, R. D. & Ostriker, J. P. 1978, ApJ, 221, L29

Børve, S., Omang, M., & Trulsen, J. 2001, ApJ, 561, 82

Bressaard, P. J. & van de Hulst, H. C. 1962, Rev. Mod. Phys., 34, 507

Brio, M. & Wu, C. C. 1988, J. Comp. Phys., 75, 400

Bullock, J. S., Kolatt, T. S., Sigad, Y., et al. 2001, MNRAS, 321, 559

Candia, J., Roulet, E., & Epele, L. N. 2002, Journal of High Energy Physics, 12, 33

Carilli, C. L. & Taylor, G. B. 2002, ARA&A, 40, 319

Carroll, S. M. 2004, Spacetime and geometry. An introduction to general relativity (Spacetime and geometry / Sean Carroll. San Francisco, CA, USA: Addison Wesley, ISBN 0-8053-8732-3, 2004, XIV + 513 pp.)

Cassano, R. & Brunetti, G. 2004, Journal of Korean Astronomical Society, 37, 583

Clarke, T. E. & Ensslin, T. A. 2006, AJ, 131, 2900

Clarke, T. E., Kronberg, P. P., Böhringer, H., & Enßlin, T. A. 2002, Highlights of Astronomy, 12, 537

Clowe, D., Bradač, M., Gonzalez, A. H., et al. 2006, ApJ, 648, L109

Colella, P. & Woodward, P. R. 1984, Journal of Computational Physics, 54, 174

Copeland, E. J. 2007, in American Institute of Physics Conference Series, Vol. 957, Particles, Strings, and Cosmology-PASCOS 2007, 21–29

Courant, R. & Friedrichs, K. O. 1976, Applied Mathematical Sciences, Vol. 21, Supersonic Flow and Shock Waves (Springer-Verlag)

Dai, W. & Woodward, P. R. 1994, J. Comp. Phys., 111, 354

Dennison, B. 1980, ApJ, 239, L93

Dermer, C. D. 1986a, ApJ, 307, 47

Dermer, C. D. 1986b, A&A, 157, 223

Dodelson, S. 2003, Modern cosmology (Modern cosmology / Scott Dodelson. Amsterdam (Netherlands): Academic Press. ISBN 0-12-219141-2, 2003, XIII + 440 p.)

Dolag, K., Bartelmann, M., & Lesch, H. 1999, A&A, 348, 351

Dolag, K., Bartelmann, M., & Lesch, H. 2002, A&A, 387, 383

Dolag, K., Evrard, A., & Bartelmann, M. 2001, A&A, 369, 36

Dolag, K. & Stasyszyn, F. A. 2008, ArXiv e-prints, 807

Dolag, K., Vazza, F., Brunetti, G., & Tormen, G. 2005, MNRAS, 364, 753

Eke, V. R., Navarro, J. F., & Steinmetz, M. 2001, ApJ, 554, 114

Ensslin, T. A., Pfrommer, C., Springel, V., & Jubelgas, M. 2006, ArXiv Astrophysics e-prints

Falle, S. A. E. G. & Komissarov, P. L. 2001, J. Plasma Phys., 65, 29

Feretti, L., Burigana, C., & Enßlin, T. A. 2004, New Astronomy Review, 48, 1137

Feretti, L., Gioia, I. M., & Giovannini, G., eds. 2002, Astrophysics and Space Science Library, Vol. 272, Merging Processes in Galaxy Clusters

Fermi, E. 1949, Phys. Rev., 75, 1169

Fujita, Y. & Takahara, F. 1999, ApJ, 519, L51

Fukushige, T. & Makino, J. 1997, ApJ, 477, L9+

Gaisser, T. K. 1990, Cosmic rays and particle physics (Cambridge and New York, Cambridge University Press, 1990, 292 p.)

Gaisser, T. K. & Stanev, T. 2009, Nuclear Physics A, 777, 98

Gal, R. R. 2006, ArXiv Astrophysics e-prints

Gingold, R. A. & Monaghan, J. J. 1977, MNRAS, 181, 375

Giovannini, G., Feretti, L., & Govoni, F. 2002, in IAU Symposium, Vol. 199, The Universe at Low Radio Frequencies, ed. A. Pramesh Rao, G. Swarup, & Gopal-Krishna, 149–+

Godunov, S. K. 1959, Matematicheskii Sbornik, 47, 271

Goldshmidt, O. & Rephaeli, Y. 1993, ApJ, 411, 518

Govoni, F. & Feretti, L. 2004, International Journal of Modern Physics D, 13, 1549

Grasso, D. & Rubinstein, H. R. 2001, Physics Reports, 348, 163

Greisen, K. 1966, Phys. Rev. Lett., 16, 748

Harari, D., Mollerach, S., & Roulet, E. 2006, ArXiv Astrophysics e-prints astro-ph/0609294

Hernquist, L. 1993, ApJ, 404, 717

Hess, V. F. 1912, Physikalische Zeitschrift, 13, 1084

Hinshaw, G., Weiland, J. L., Hill, R. S., et al. 2008, ArXiv e-prints, 803

Horner, D. J., Mushotzky, R. F., & Scharf, C. A. 1999, ApJ, 520, 78

Hugoniot, H. 1887, Journal de 1'Ecole Polytechnique, 57, 3

Hugoniot, H. 1889, Journal de 1'Ecole Polytechnique, 58, 1

Jeffrey, A. 1966, University mathematical texts, Vol. 33, Magnetohydrodynamics (Edinburgh: Oliver & Boyd)

Jones, C. & Forman, W. 1984, ApJ, 276, 38

Jones, C. & Forman, W. 1999, ApJ, 511, 65

Jubelgas, M., Springel, V., Enßlin, T., & Pfrommer, C. 2008, A&A, 481, 33

Kaastra, J. S. & Mewe, R. 1993, A&AS, 97, 443

Kang, H. & Jones, T. W. 2002, Journal of Korean Astronomical Society, 35, 159

Kang, H. & Jones, T. W. 2005, ApJ, 620, 44

Karzas, W. J. & Latter, R. 1961, ApJS, 6, 167

Kay, S. T. 2004, MNRAS, 347, L13

Kohlhörster, W. 1913, Physikalische Zeitschrift, 11, 1153

Kolanoski, H. 2007, Skript zur Vorlesung Einführung in die Astroteilchenphysik an der Humboldt Universität zu Berlin und DESY Zeuthen, http://www-zeuthen.desy.de/˜kolanosk/astro0607/skript.html

Komatsu, E., Dunkley, J., Nolta, M. R., et al. 2008, ArXiv e-prints, 803

Liedahl, D. A., Osterheld, A. L., & Goldstein, W. H. 1995, ApJ, 438, L115

Longair, M. S. 1981, High energy astrophysics (Cambridge and New York, Cambridge University Press, 1981. 420 p.)

Lucy, L. B. 1977, AJ, 82, 1013

Lynden-Bell, D. 1967, MNRAS, 136, 101

Mannheim, K. & Schlickeiser, R. 1994, A&A, 286, 983

Markevitch, M., Gonzalez, A. H., Clowe, D., et al. 2004, ApJ, 606, 819

Maughan, B. J., Jones, L. R., Ebeling, H., et al. 2003, ApJ, 587, 589

Maughan, B. J., Jones, L. R., Ebeling, H., & Scharf, C. 2004, MNRAS, 351, 1193

Meneghetti, M., Bartelmann, M., Dolag, K., et al. 2005, A&A, 442, 413

Meneghetti, M., Bolzonella, M., Bartelmann, M., Moscardini, L., & Tormen, G. 2000, MNRAS, 314, 338

Mewe, R., Gronenschild, E. H. B. M., & van den Oord, G. H. J. 1985, A&AS, 62, 197

Mewe, R., Lemen, J. R., & van den Oord, G. H. J. 1986, A&AS, 65, 511

Miniati, F. 2002, MNRAS, 337, 199

Miniati, F., Ryu, D., Kang, H., & Jones, T. W. 2001, ApJ, 559, 59

Miralda-Escude, J. 1993a, ApJ, 403, 497

Miralda-Escude, J. 1993b, ApJ, 403, 509

Monaghan, J. J. 1997, J. Comp. Phys., 136, 298

Monaghan, J. J. & Gingold, R. A. 1983, J. Comp. Phys., 52, 374

Monaghan, J. J. & Lattanzio, J. C. 1985, A&A, 149, 135

Moore, B., Quinn, T., Governato, F., Stadel, J., & Lake, G. 1999, MNRAS, 310, 1147

Morris, J. P. & Monaghan, J. J. 1997, J. Comp. Phys., 136, 41

Morrison, R. & McCammon, D. 1983, ApJ, 270, 119

Myuong, R. S. & Roe, P. L. 1997a, J. Plasma Phys., 58, 485

Myuong, R. S. & Roe, P. L. 1997b, J. Plasma Phys., 58, 521

Nagano, M. & Watson, A. A. 2000, Reviews of Modern Physics, 72, 689

Narayan, R. & Bartelmann, M. 1996, ArXiv Astrophysics e-prints

Navarro, J. F., Frenk, C. S., & White, S. D. M. 1996, ApJ, 462, 563

Navarro, J. F., Frenk, C. S., & White, S. D. M. 1997, ApJ, 490, 493

Padmanabhan, T. 1993, Structure formation in the universe (Cambridge ; New York : Cambridge University Press, 1993.)

Padmanabhan, T. 1999, ArXiv Astrophysics e-prints

Peacock, J. A., Cole, S., Norberg, P., et al. 2001, Nature, 410, 169

Peebles, P. J. E. & Dicke, R. H. 1968, ApJ, 154, 891

Penzias, A. A. & Wilson, R. W. 1965, ApJ, 142, 419

Perlmutter, S., Aldering, G., Goldhaber, G., et al. 1999, ApJ, 517, 565

Pfrommer, C. & Enßlin, T. A. 2004, A&A, 413, 17

Pfrommer, C., Enßlin, T. A., Springel, V., Jubelgas, M., & Dolag, K. 2007, MNRAS, 378, 385

Pfrommer, C., Springel, V., Enßlin, T. A., & Jubelgas, M. 2006, MNRAS, 367, 113

Phillips, G. J. & Monaghan, J. J. 1985, MNRAS, 216, 883

Price, D. J. & Monaghan, J. J. 2004, MNRAS, 348, 139

Puchwein, E., Bartelmann, M., Dolag, K., & Meneghetti, M. 2005, A&A, 442, 405

Randall, S. W., Sarazin, C. L., & Ricker, P. M. 2002, in Bulletin of the American Astronomical Society, Vol. 34, Bulletin of the American Astronomical Society, 1218–+

Rankine, W. J. M. 1870, Phil. Trans. Roy. Soc. London, 160, 277

Rees, M. J. 1989, The origin and cosmogonic implications of seed magnetic fields (Problems in Theoretical Physics and Astrophysics), 415–421

Reiprich, T. H. & Böhringer, H. 2002, ApJ, 567, 716

Riess, A. G., Filippenko, A. V., Challis, P., et al. 1998, AJ, 116, 1009

Rybicki, G. B. & Lightman, A. P. 1979, Radiative processes in astrophysics (New York, Wiley-Interscience, 1979. 393 p.)

Ryu, D. & Jones, T. W. 1995, ApJ, 442, 228

Sarazin, C. L. 1988, X-ray emission from clusters of galaxies (Cambridge Astrophysics Series, Cambridge: Cambridge University Press, 1988)

Sarazin, C. L. 1999, ApJ, 520, 529

Sarazin, C. L. 2004, Journal of Korean Astronomical Society, 37, 433

Schneider, P. 2006, Extragalactic Astronomy and Cosmology (Extragalactic Astronomy and Cosmology, by Peter Schneider. Berlin: Springer, 2006.)

Shapiro, P. R., Iliev, I. T., & Raga, A. C. 1999, MNRAS, 307, 203

Sigl, G. 2006, ArXiv Astrophysics e-prints astro-ph/0612240

Sod, G. A. 1978, J. Comp. Phys., 78, 1

Springel, V. 2005, MNRAS, 364, 1105

Springel, V. & Hernquist, L. 2002, MNRAS, 333, 649

Springel, V., Yoshida, N., & White, S. D. M. 2001, New Astronomy, 6, 79

Stone, J. M., Hawley, J. F., Evans, C. R., & Norman, M. L. 1992, ApJ, 388, 415

Suto, Y., Sasaki, S., & Makino, N. 1998, ApJ, 509, 544

Thomas, P. A. & Couchman, H. M. P. 1992, MNRAS, 257, 11

Tormen, G., Bouchet, F. R., & White, S. D. M. 1997, MNRAS, 286, 865

Tormen, G., Moscardini, L., & Yoshida, N. 2004, MNRAS, 350, 1397

Torri, E., Meneghetti, M., Bartelmann, M., et al. 2004, MNRAS, 349, 476

Trodden, M. & Carroll, S. M. 2004, ArXiv Astrophysics e-prints

Voit, G. M., Kay, S. T., & Bryan, G. L. 2005, MNRAS, 364, 909

Wang, L. & Steinhardt, P. J. 1998, ApJ, 508, 483

Webb, G. M. 1987, ApJ, 319, 215

White, S. D. M. 1996, in Cosmology and Large Scale Structure, ed. R. Schaeffer, J. Silk, M. Spiro, & J. Zinn-Justin, 349–+

Wiebel-Sooth, B., Biermann, P. L., & Meyer, H. 1998, A&A, 330, 389

Wu, C. C. 1990, J. Geophys. Res., 95, 8149

Yamamoto, T. & for the Pierre Auger Collaboration. 2007, ArXiv e-prints, 707

Yoshida, N., Sheth, R. K., & Diaferio, A. 2001, MNRAS, 328, 669

Zatsepin, G. T. & Kuz'min, V. A. 1966, ZhETF Pis'ma, 4, 114

Zwicky, F., Herzog, E., & Wild, P. 1968, Catalogue of galaxies and of clusters of galaxies (Pasadena: California Institute of Technology (CIT), 1961-1968)

# Acknowledgements

First of all I thank Prof. Dr. Matthias Bartelmann for offering this thesis topic to me and for guiding me through the past years. Im am very grateful for patiently answering my questions and for many fruitful and vivid discussions that helped me whenever I got stuck in a problem. I also thank him for encouraging me when it was necessary.

I owe thanks to Dr. Volker Springel for kindly providing me access to the inofficial version of GADGET-2. I am furthermore indebted to Dr. Klaus Dolag who gave me the initial conditions for the cluster simulations and who made other useful programs available to me. I thank Dr. Torsten Enßlin and Dr. Christoph Pfrommer for introducing me to cosmic ray physics and the numerical modelling with GADGET-2. I particularly thank Christoph for many useful discussions and for generously providing me some of his routines for the visualisation of the shock tube simulations.

Many thanks go to Prof. Dr. Ralf Klessen who agreed to be my second referee and to participate in my Ph.D. exam. He moreover showed great interest in my work and always took the time to listen to my problems. I also thank Prof. Dr. Eva Grebel and Prof. Dr. Max Camenzind for accepting to be in my defense commission.

I also thank Dr. Christian Fendt for helping me with IMPRS issues and for organising numerous barbecues and Christmas celebrations.

Special thanks go to Emanuel for doing a great job with the computer administration and for his readiness to help me whenever I had a computer problem. Without his help I would never have solved most of the problems I had with GADGET-2. He also kindly provided me his code for the projection of SPH particles.

I am very grateful to Ewald for allowing me to use his code for the computation of the strong lensing cross sections and for helping me with the evaluation.

Lots of thanks go to all my colleagues for the nice atmosphere at ITA and for many useful discussions about astrophysics, programming, and related topics. Furthermore, I very much enjoyed the coffee breaks, parties, dinners, and evenings in town, although, unfortunately, in the last months I could not join very often. I especially thank all the office mates I had during the last years, namely Gunter, Emanuel, Gregor, and Jean-Claude for inspiring remarks and relaxing conversations.

I thank my family for supporting me in every respect. Finally, I thank Sascha for his love and understanding, and the great fun we had during all the years.